Impact of protein functionality and processing on structure and texture of plant-based meat produced using extrusion and 3D printing

by

Shirin Sheikhizadeh

M.S., Islamic Azad University, Science and Research Branch, Tehran, Iran, 2021

AN ABSTRACT OF A DISSERTATION

submitted in partial fulfillment of the requirements for the degree

DOCTOR OF PHILOSOPHY

Department of Grain and Food Science
College of Agriculture

KANSAS STATE UNIVERSITY
Manhattan, Kansas

2026

Abstract

Driven by demand for sustainable meat alternatives, this research investigated how protein type, functionality and extrusion processing conditions influence the structure, texture and performance of plant-based meat produced using three distinct process technologies, viz., low moisture extrusion, high moisture extrusion and additive manufacturing. These three technologies and the quality of associated products, textured vegetable protein (TVP), high moisture meat analog (HMMA) and 3D printed plant-based meat, respectively, were the focus of this study.

Before evaluating the different process technologies and plant-based meat products, the functionality of various plant proteins was characterized because it strongly influenced structure development and product quality. Based on water absorption capacity (WAC) and rapid visco-analysis (RVA), soy protein isolate (SPI) and one type of soy protein concentrate (SPC1) were classified as cold swelling proteins due to their high WAC (SPI: 5.05-5.95 g/g; SPC1: 4.35 g/g) and/or low-temperature peak viscosity (30-42°C). In contrast, pea protein isolate (PPI), wheat gluten (WG), faba bean concentrate (FBC), lentil protein concentrate (LPC), and two other types of soy protein concentrate (SPC2 and SPC3) behaved as non-cold swelling ingredients, showing lower hydration and/or requiring higher temperatures to develop viscosity. Cold swelling proteins generally show high cross-linking and have greater film-forming ability, which leads to more expanded and porous plant-based meat structures, whereas non-cold swelling proteins are often associated with denser, more fibrous products. These functional differences helped explain variation in processing behavior, texture and final structure of TVP, HMMA, and 3D-printed plant-based meat.

The first part of this study focused on the processing of TVP products using low-moisture extrusion and examined faba- and lentil-based formulations processed under different screw speeds and in-barrel moisture (IBM) conditions. FBC was blended with SPI, PPI, or WG, and LPC with SPI or PPI. Specific mechanical energy (SME) ranged from 595.79 to 918.86 kJ/kg in faba-based formulations and from 660.24 to 804.96 kJ/kg in lentil-based formulations. Besides protein functionality, extrusion behavior and TVP structure and texture were also affected by screw speed and IBM. Increasing IBM or lower screw speed reduced SME. SPI-containing formulations generally had the highest SME because of their high viscosity during extrusion, followed by WG and PPI. Bulk density ranged from 140.4 to 275.2 g/L and 120.7 to 266.8 g/L for FBC- and LPC-based TVP products, respectively. SPI produced more porous, lower-density structures, whereas WG and PPI produced denser, more fibrous products; bulk density was negatively correlated with water holding capacity ($r = -0.93$ and -0.86 for FBC- and LPC-based TVP products, respectively). These results were in alignment with the protein functionality hypothesis based on cold swelling and non-cold swelling properties. Computer vision (CV) and machine learning (ML)-based fibrosity scores showed strong positive correlations with expert visual scores for both FBC- and LPC-based TVP products ($r = 0.95$ and 0.96, respectively), indicating close agreement between CV+ML-based and expert assessments of fibrous structure.

The second part of this study examined the processing of HMMA products using soy proteins and high moisture extrusion with a special cooling die and examined the influence of formulation and extrusion conditions on fibrous structure. A blended standard formulation (STD) consisting of SPC1, SPC2, SPI, tapioca starch, canola oil and salt was compared with a single-protein formulation (SP) consisting of SPC2, canola oil and salt, under different feed rate and barrel temperature conditions. STD showed greater hydration, lower gelation concentration, and

higher viscosity development than SP, consistent with the expected functionality differences between the formulations. Increasing barrel temperature reduced SME (from 685 to 537 kJ/kg in STD and from 745 to 542 kJ/kg in SP) due to lower melt viscosity. Increasing feed rate under low-temperature conditions increased die pressure, while SME changed only slightly. However, the low-feed, high-temperature condition produced the highest (up to 2.37) anisotropy index (AI; a measure of directional fiber alignment), supporting the hypothesis that stronger thermal treatment and longer residence time improved protein alignment and fibrous structure. Low-temperature conditions produced the firmest texture (hardness up to 183.72 N), showing that firmer products were not necessarily more fibrous. Visual fibrosity was higher in STD (7.35-8.11) than SP (4.02-6.75). These results supported the formulation hypothesis that STD showed stronger hydration and higher visual fibrosity, but AI did not differ significantly between STD and SP under matched processing conditions, indicating that processing conditions, particularly low-feed and high-temperature, were the main driver of structural anisotropy. Fiberlyzer, an image-based method that quantifies fibrousness from elongated structures in macro images, showed a strong positive correlation with AI ($r = 0.93$), and an expert-guided deep-learning model based on a modified ResNet-18 showed strong agreement with expert visual fibrosity scores ($r = 0.89$).

The third and final part of this study explored extrusion-based 3D printing of plant-based meat using PPI and SPI with different levels of methylcellulose (MC) and pea fiber (PF). SPI (cold swelling) hydrated faster than PPI (non-cold swelling) and produced plant protein ink with higher viscosity. SPI formulations were firmer, reaching hardness up to 23.47 N, likely because faster hydration and higher viscosity formed a stronger, more cohesive printed network. MC showed very high WAC (9.93 g/g) and increased viscosity, which helped to print filaments that

set quickly after deposition. However, at higher MC levels, this strong thickening made the ink overly viscous and elastic, limiting relaxation after extrusion and reducing dimensional stability, reflected by more negative dimensional distortion ratio (DDR) values (as low as -0.27), where DDR compares the measured printed dimensions with the intended design, and values closer to zero indicate better shape fidelity. In contrast, PF improved shape retention by providing more gradual water binding and physical support, reducing deformation and bringing DDR closer to 0.

This research showed that plant-based meat quality depends on the combination of plant protein functionality and processing. Across TVP, HMMA and 3D-printing products, differences in hydration, viscosity, moisture, temperature, screw speed and formulation shaped processing, structure, and texture, providing an improved theoretical and scientific framework and practical guidance for designing more consistent products.

Impact of protein functionality and processing on structure and texture of plant-based meat produced using extrusion and 3D printing

by

Shirin Sheikhizadeh

M.S., Islamic Azad University, Science and Research Branch, Tehran, Iran, 2021

A DISSERTATION

submitted in partial fulfillment of the requirements for the degree

DOCTOR OF PHILOSOPHY

Department of Grain and Food Science
College of Agriculture

KANSAS STATE UNIVERSITY
Manhattan, Kansas

2026

Approved by:

Major Professor
Dr. Sajid Alavi

Copyright

© Shirin Sheikhizadeh 2026.

Abstract

Driven by demand for sustainable meat alternatives, this research investigated how protein type, functionality and extrusion processing conditions influence the structure, texture and performance of plant-based meat produced using three distinct process technologies, viz., low moisture extrusion, high moisture extrusion and additive manufacturing. These three technologies and the quality of associated products, textured vegetable protein (TVP), high moisture meat analog (HMMA) and 3D printed plant-based meat, respectively, were the focus of this study.

Before evaluating the different process technologies and plant-based meat products, the functionality of various plant proteins was characterized because it strongly influenced structure development and product quality. Based on water absorption capacity (WAC) and rapid visco-analysis (RVA), soy protein isolate (SPI) and one type of soy protein concentrate (SPC1) were classified as cold swelling proteins due to their high WAC (SPI: 5.05-5.95 g/g; SPC1: 4.35 g/g) and/or low-temperature peak viscosity (30-42°C). In contrast, pea protein isolate (PPI), wheat gluten (WG), faba bean concentrate (FBC), lentil protein concentrate (LPC), and two other types of soy protein concentrate (SPC2 and SPC3) behaved as non-cold swelling ingredients, showing lower hydration and/or requiring higher temperatures to develop viscosity. Cold swelling proteins generally show high cross-linking and have greater film-forming ability, which leads to more expanded and porous plant-based meat structures, whereas non-cold swelling proteins are often associated with denser, more fibrous products. These functional differences helped explain variation in processing behavior, texture and final structure of TVP, HMMA, and 3D-printed plant-based meat.

The first part of this study focused on the processing of TVP products using low-moisture extrusion and examined faba- and lentil-based formulations processed under different screw speeds and in-barrel moisture (IBM) conditions. FBC was blended with SPI, PPI, or WG, and LPC with SPI or PPI. Specific mechanical energy (SME) ranged from 595.79 to 918.86 kJ/kg in faba-based formulations and from 660.24 to 804.96 kJ/kg in lentil-based formulations. Besides protein functionality, extrusion behavior and TVP structure and texture were also affected by screw speed and IBM. Increasing IBM or lower screw speed reduced SME. SPI-containing formulations generally had the highest SME because of their high viscosity during extrusion, followed by WG and PPI. Bulk density ranged from 140.4 to 275.2 g/L and 120.7 to 266.8 g/L for FBC- and LPC-based TVP products, respectively. SPI produced more porous, lower-density structures, whereas WG and PPI produced denser, more fibrous products; bulk density was negatively correlated with water holding capacity ($r = -0.93$ and -0.86 for FBC- and LPC-based TVP products, respectively). These results were in alignment with the protein functionality hypothesis based on cold swelling and non-cold swelling properties. Computer vision (CV) and machine learning (ML)-based fibrosity scores showed strong positive correlations with expert visual scores for both FBC- and LPC-based TVP products ($r = 0.95$ and 0.96, respectively), indicating close agreement between CV+ML-based and expert assessments of fibrous structure.

The second part of this study examined the processing of HMMA products using soy proteins and high moisture extrusion with a special cooling die and examined the influence of formulation and extrusion conditions on fibrous structure. A blended standard formulation (STD) consisting of SPC1, SPC2, SPI, tapioca starch, canola oil and salt was compared with a single-protein formulation (SP) consisting of SPC2, canola oil and salt, under different feed rate and barrel temperature conditions. STD showed greater hydration, lower gelation concentration, and

higher viscosity development than SP, consistent with the expected functionality differences between the formulations. Increasing barrel temperature reduced SME (from 685 to 537 kJ/kg in STD and from 745 to 542 kJ/kg in SP) due to lower melt viscosity. Increasing feed rate under low-temperature conditions increased die pressure, while SME changed only slightly. However, the low-feed, high-temperature condition produced the highest (up to 2.37) anisotropy index (AI; a measure of directional fiber alignment), supporting the hypothesis that stronger thermal treatment and longer residence time improved protein alignment and fibrous structure. Low-temperature conditions produced the firmest texture (hardness up to 183.72 N), showing that firmer products were not necessarily more fibrous. Visual fibrosity was higher in STD (7.35-8.11) than SP (4.02-6.75). These results supported the formulation hypothesis that STD showed stronger hydration and higher visual fibrosity, but AI did not differ significantly between STD and SP under matched processing conditions, indicating that processing conditions, particularly low-feed and high-temperature, were the main driver of structural anisotropy. Fiberlyzer, an image-based method that quantifies fibrousness from elongated structures in macro images, showed a strong positive correlation with AI ($r = 0.93$), and an expert-guided deep-learning model based on a modified ResNet-18 showed strong agreement with expert visual fibrosity scores ($r = 0.89$).

The third and final part of this study explored extrusion-based 3D printing of plant-based meat using PPI and SPI with different levels of methylcellulose (MC) and pea fiber (PF). SPI (cold swelling) hydrated faster than PPI (non-cold swelling) and produced plant protein ink with higher viscosity. SPI formulations were firmer, reaching hardness up to 23.47 N, likely because faster hydration and higher viscosity formed a stronger, more cohesive printed network. MC showed very high WAC (9.93 g/g) and increased viscosity, which helped to print filaments that

set quickly after deposition. However, at higher MC levels, this strong thickening made the ink overly viscous and elastic, limiting relaxation after extrusion and reducing dimensional stability, reflected by more negative dimensional distortion ratio (DDR) values (as low as -0.27), where DDR compares the measured printed dimensions with the intended design, and values closer to zero indicate better shape fidelity. In contrast, PF improved shape retention by providing more gradual water binding and physical support, reducing deformation and bringing DDR closer to 0.

This research showed that plant-based meat quality depends on the combination of plant protein functionality and processing. Across TVP, HMMA and 3D-printing products, differences in hydration, viscosity, moisture, temperature, screw speed and formulation shaped processing, structure, and texture, providing an improved theoretical and scientific framework and practical guidance for designing more consistent products.

Table of Contents

List of Figures

List of Tables

Acknowledgements

I would like to express my deepest gratitude to my advisor, Dr. Sajid Alavi, for his scientific guidance, constant encouragement, and unwavering support throughout my graduate studies. Without his mentorship, trust, and continuous support, I truly could not have completed this journey. I am especially grateful for the opportunity he gave me to pursue my studies and work toward a goal I had always dreamed of achieving. His trust opened the door for me to continue my education in another country and provided me with a valuable environment in which I was able to grow, learn, and connect with many knowledgeable and accomplished professionals. I will always be sincerely thankful to Dr. Alavi for making this important stage of my life possible.

I would also like to extend my sincere appreciation to my committee members, Dr. Sanjoy Das, Dr. Yonghui Li, and Dr. Davood Pourkargar, for their time, thoughtful feedback, and valuable guidance. Their support and expertise have been greatly appreciated.

I am also grateful to Mr. Eric Maichel for his support during the extrusion trials and for his assistance with production-related work throughout this research.

My sincere thanks also go to my lab mates, colleagues, and friends at the university for their help, kindness, and support along the way. Their encouragement and companionship made this journey much easier and more meaningful.

Finally, I would like to express my deepest love and gratitude to my mother and father. They have always been my greatest supporters, my constant source of encouragement, and the quiet strength behind every step of my life. Whatever I have achieved has been possible because of their endless love, sacrifices, and unwavering belief in me. It is because of them, and because of the love that has always surrounded me, that I was able to reach this stage.

Chapter 1 - Introduction

Plant-based meat alternatives have gained increasing attention as part of a broader transition toward more sustainable, resilient, and diversified food. Their growth has been driven by environmental, ethical, and health-related concerns, as well as the need for alternative protein sources that can help meet future food demands (Ali & Bharali, 2025; Boukid et al., 2022; McClements, 2022; Zahari et al., 2022). However, the long-term success of these products depends not only on sustainability and nutrition, but also on their ability to reproduce the sensory qualities of meat, especially texture and structure (Herz et al., 2021; Michel et al., 2021). In particular, the development of fibrous, meat-like texture remains one of the main technological barriers to wider consumer acceptance (Elzerman et al., 2011).

Extrusion is currently the most widely used and industrially scalable technology for structuring plant proteins into meat analogs. In low-moisture systems, extrusion is used to produce textured vegetable protein (TVP), a shelf-stable product that develops a chewy texture after rehydration and is widely used in products such as patties, nuggets, and sausages (Baune et al., 2022; Singh et al., 2024). In high-moisture processes, extrusion can produce high-moisture meat analogs (HMMAs) with more continuous and fibrous structures resembling whole-muscle meat (Dekkers et al., 2016). During extrusion, proteins are exposed to heat, shear, pressure, and moisture, which promote unfolding, aggregation, alignment, and phase separation, ultimately determining the internal structure and textural properties of the final product (Grabowska et al., 2014; Ferawati et al., 2021; Webb et al., 2023).

Although processing conditions such as temperature, moisture, screw speed, barrel temperature, and feed rate strongly influence product quality, ingredient functionality is equally important in controlling structure development (Chen et al., 2010; Osen et al., 2014; Riaz, 2000).

Texture formation depends on how proteins hydrate, swell, unfold, interact, and set during processing. For this reason, protein blending has become an important strategy in plant-based meat design, especially as the field expands beyond soy to include a wider range of pulse and cereal proteins (Baune et al., 2022; Flory et al., 2023; Ma et al., 2022). At the same time, predicting texture outcomes across different protein systems remains difficult, highlighting the need for practical frameworks that connect raw material functionality to extrusion behavior and final product structure (Grabowska et al., 2016).

One useful framework is to classify proteins according to hydration-related functionality, including water absorption, swelling behavior, gelation, and viscosity development. These properties are closely linked to molecular structure, surface chemistry, and processing history (Day, 2013). Based on these distinctions, plant proteins are often categorized as cold swelling or non-cold swelling systems. Cold swelling proteins show strong water affinity, early hydration, and rapid viscosity development, whereas non-cold swelling proteins generally require greater thermal input to unfold, hydrate, and form cohesive networks (Flory et al., 2023). This distinction helps explain differences in extrusion behavior and final product morphology. Previous studies have shown that proteins with stronger cold swelling behavior tend to produce more expanded and porous structures, while proteins with lower cold swelling capacity tend to form denser and more layered products (Flory et al., 2023; Webb et al., 2023a; Xiao et al., 2025).

This framework is particularly relevant as the plant-based meat industry increasingly explores pulse proteins such as lentil, pea, and faba bean. These ingredients are attractive because of their nutritional value, sustainability potential, and role in diversifying raw material supply (Kaale et al., 2023; Ma et al., 2022). Lentil has emerged as a promising pulse for next-generation meat analog, while faba bean protein has also gained interest as a sustainable but still

underutilized ingredient (Kaale et al., 2023; Thomsen et al., 2025). However, compared with soy and pea proteins, faba bean proteins generally show weaker hydration efficiency, water-holding capacity, and gelation behavior, making their successful application more formulation- and process-dependent (Thomsen et al., 2025).

Extrusion-based 3D food printing can also be considered a form of extrusion processing, because the material is forced under pressure through a die-like opening, in this case a nozzle, and deposited in a controlled manner to form a structure layer by layer. Beyond extrusion, similar formulation challenges also apply to extrusion-based 3D food printing. In a 3D food printer, materials are deposited layer by layer to create customized structures, and successful printing depends mainly on extrudability and shape stability after deposition (Dankar et al., 2018; Liu et al., 2017). As in extrusion, these properties are governed by the rheological and physicochemical behavior of the formulation or ink. Plant proteins such as pea protein isolate and soy protein isolate are commonly used because of their ability to form structured matrices, while hydrocolloids can improve cohesion, water management, and shape retention (Aghababaei et al., 2025; Bhuiyan et al., 2025). However, the combined effects of protein source and binder concentration on printing performance and post-print structure are still not fully understood (Dankar et al., 2018; Zhang et al., 2021; Shah et al., 2024).

Overall, the literature shows that the successful design of plant-based meat analogs depends on linking ingredient functionality to process response and final structure across multiple product platforms. Whether the target product is a low-moisture TVP, a fibrous HMMA, or a 3D-printed meat analog, protein source, hydration behavior, swelling characteristics, and formulation composition interact with processing conditions to determine structure development. Building on this principle, this dissertation examines plant-based meat

systems across four related applications: faba bean-based TVP, lentil-based TVP, soy-based HMMA, and extrusion-based 3D printing, to better understand how formulation and processing can be combined to improve structure, texture, and functional performance.

1.1 Chapter 2 Objectives

This chapter focuses on faba bean-based plant-based meat analogs and examines how blending faba bean concentrate with proteins that differ in functionality influences extrusion texturization. Specifically, this chapter investigates the effects of combining faba bean concentrate with pea protein isolate, soy protein isolate, and wheat gluten under different extrusion conditions defined by in-barrel moisture and screw speed. The objective is to determine how protein functionality and processing conditions interact to affect hydration behavior, extrusion responses, and final product structure and texture, and to provide insight into how faba bean protein can be more effectively used in structured meat analog applications.

1.2 Chapter 3 Objectives

Chapter 3 examines lentil-based textured vegetable protein (TVP) and evaluates the impact of replacing soy protein isolate with pea protein isolate in a lentil protein concentrate-based formulation. This chapter aims to determine how soy-to-pea substitution changes raw material hydration, thermal flow behavior, and extrusion performance, and how these changes influence final product structure and texture. By comparing SPI-rich and PPI-rich lentil blends, this chapter addresses how formulation design can be used to improve fibrosity, water holding capacity, and firmness in pulse-based TVP products.

1.3 Chapter 4 Objectives

Chapter 4 focuses on soy-based high-moisture meat analogs and investigates how formulation complexity and extrusion conditions shape fibrous structure development. Two HMMA formulations were compared: a standard blended formulation containing multiple soy ingredients and starch, and a simplified single-protein formulation based primarily on one soy protein concentrate. The objective of this chapter is to evaluate how formulation composition and processing conditions (feed rate and barrel temperature) affect raw material functionality, extrusion behavior, final texture, and fibrousness. In addition, this chapter examines whether image-based fibrousness measurements correspond with mechanical anisotropy, with the broader goal of improving objective evaluation of fiber formation in HMMA products.

1.4 Chapter 5 Objectives

This chapter extends the dissertation from extrusion texturization to extrusion-based 3D food printing. This chapter investigates the effects of plant protein type, methylcellulose concentration, and pea fiber inclusion on the printability and structural stability of plant-based meat formulations designed for 3D printing. Using pea protein isolate and soy protein isolate-based formulations, the chapter evaluates how compositional changes affect water absorption, viscosity development, gelation behavior, dimensional distortion after printing, and final texture. The objective is to clarify how formulation variables govern both flow during printing and structural integrity after deposition, thereby supporting the design of more stable and functional plant-based meat inks for 3D food printing applications.

1.5 References

Aghababaei, F., McClements, D. J., Pignitter, M., & Hadidi, M. (2025). Plant protein edible inks: Upgrading from 3D to 4D food printing. *Food Chemistry: X, 26*, 102280. https://doi.org/10.1016/j.fochx.2025.102280

Ali, A., & Bharali, P. (2025). The rise of plant-based meat alternatives: Challenges and perspectives. *Food Bioscience, 68*, 106640. https://doi.org/10.1016/j.fbio.2025.106640

Baune, M.-C., Terjung, N., Tülbek, M. Ç., & Boukid, F. (2022). Textured vegetable proteins (TVP): Future foods standing on their merits as meat alternatives. *Future Foods, 6*, 100181. https://doi.org/10.1016/j.fufo.2022.100181

Bhuiyan, M. H. R., Yeasmen, N., & Orsat, V. (2025). Plant-proteins based 3D meat analog printing: A review. *Food Chemistry, 482*, 144157. https://doi.org/10.1016/j.foodchem.2025.144157

Chen, F. L., Wei, Y. M., Zhang, B., & Ojokoh, A. O. (2010). System parameters and product properties response of soybean protein extruded at wide moisture range. *Journal of Food Engineering, 96*(2), 208–213. https://doi.org/10.1016/j.jfoodeng.2009.07.014

Dankar, I., Haddarah, A., Omar, F. E. L., Sepulcre, F., & Pujolà, M. (2018). 3D printing technology: The new era for food customization and elaboration. *Trends in Food Science & Technology, 75*, 231–242. https://doi.org/10.1016/j.tifs.2018.03.018

Day, L. (2013). Proteins from land plants – Potential resources for human nutrition and food security. *Trends in Food Science & Technology*. https://doi.org/10.1016/j.tifs.2013.05.005

Dekkers, B. L., Boom, R. M., & van der Goot, A. J. (2018). Structuring processes for meat analogs. *Trends in Food Science & Technology, 81*, 25–36. https://doi.org/10.1016/j.tifs.2018.08.011

Elzerman, J. E., Hoek, A. C., van Boekel, M. A. J. S., & Luning, P. A. (2011). Consumer acceptance and appropriateness of meat substitutes in a meal context. *Food Quality and Preference, 22*(3), 233–240. https://doi.org/10.1016/j.foodqual.2010.10.006

Ferawati, F., Zahari, I., Barman, M., Hefni, M., Ahlström, C., Witthöft, C., & Östbring, K. (2021). High-moisture meat analogs produced from yellow pea and faba bean protein isolates/concentrate: Effect of raw material composition and extrusion parameters on texture properties. *Foods, 10*(4), 843. https://doi.org/10.3390/foods10040843

Flory, J., Xiao, R., Li, Y., Dogan, H., Talavera, M. J., & Alavi, S. (2023). Understanding protein functionality and its impact on quality of plant-based meat analogs. *Foods, 12*(17), 3232. https://doi.org/10.3390/foods12173232

Grabowska, K. J., Zhu, S., Dekkers, B. L., de Ruijter, N. C. A., Gieteling, J., & van der Goot, A. J. (2016). Shear-induced structuring as a tool to make anisotropic materials using soy protein concentrate. *Journal of Food Engineering, 188*, 77–86. https://doi.org/10.1016/j.jfoodeng.2016.05.010

Herz, E., Herz, L., Dreher, J., Gibis, M., Ray, J., Pibarot, P., Schmitt, C., & Weiss, J. (2021). Influencing factors on the ability to assemble a complex meat analog using a soy-protein-binder. *Innovative Food Science & Emerging Technologies, 73*, 102806. https://doi.org/10.1016/j.ifset.2021.102806

Kaale, L. D., Siddiq, M., & Hooper, S. (2023). Lentil (Lens culinaris Medik) as nutrient-rich and versatile food legume: A review. *Legume Science, 5*(2), e169. https://doi.org/10.1002/leg3.169

Liu, Z., Chen, X., Dai, Q., Xu, D., Hu, L., Li, H., Hati, S., Chitrakar, B., Yao, L., & Mo, H. (2023). Pea protein-xanthan gum interaction driving the development of 3D printed dysphagia diet. *Food Hydrocolloids, 139*, 108497. https://doi.org/10.1016/j.foodhyd.2023.108497

Ma, Y., Schlangen, M., Potappel, J., Zhang, L., & van der Goot, A. J. (2024). Quantitative characterizations of visual fibrousness in meat analogs using automated image analysis. *Journal of Texture Studies, 55*(1), e12806. https://doi.org/10.1111/jtxs.12806

McClements, D. J., Weiss, J., Kinchla, A. J., Nolden, A. A., & Grossmann, L. (2021). Methods for testing the quality attributes of plant-based foods: Meat- and processed-meat analogs. *Foods, 10*(2), 260. https://doi.org/10.3390/foods10020260

Michel, F., Hartmann, C., & Siegrist, M. (2021). Consumers' associations, perceptions and acceptance of meat and plant-based meat alternatives. *Food Quality and Preference*. https://www.semanticscholar.org/paper/Consumers%E2%80%99-associations%2C-perceptions-and-acceptance-Michel-Hartmann/5850bdf8b73f42a256c16f75125365000d8744dc

Osen, R., Toelstede, S., Wild, F., Eisner, P., & Schweiggert-Weisz, U. (2014). High moisture extrusion cooking of pea protein isolates: Raw material characteristics, extruder responses, and texture properties. *Journal of Food Engineering, 127*, 67–74. https://doi.org/10.1016/j.jfoodeng.2013.11.023

Riaz, M. N. (Ed.). (2000). *Extruders in food applications*. CRC Press. https://doi.org/10.1201/9781482278859

Singh, R., Guerrero, M., Nickerson, M. T., & Koksel, F. (2024). Effects of extrusion screw speed, feed moisture content, and barrel temperature on the physical, techno-functional, and microstructural quality of texturized lentil protein. *Journal of Food Science, 89*(4), 2040–2053. https://doi.org/10.1111/1750-3841.16991

Thomsen, J., Rao, J., & Chen, B. (2025). Faba bean protein: Chemical composition, functionality, volatile compounds, and applications in food production. *Trends in Food Science & Technology, 156*, 104863. https://doi.org/10.1016/j.tifs.2024.104863

Webb, D., Dogan, H., Li, Y., & Alavi, S. (2023). Physico-chemical properties and texturization of pea, wheat and soy proteins using extrusion and their application in plant-based meat. *Foods, 12*(8), 1586. https://doi.org/10.3390/foods12081586

Xiao, R., Flory, J., Alavi, S., & Li, Y. (2025). Physicochemical and functional properties of plant proteins before and after extrusion texturization. *Food Hydrocolloids, 163*, 111119. https://doi.org/10.1016/j.foodhyd.2025.111119

Zahari, I., Östbring, K., Purhagen, J. K., & Rayner, M. (2022). Plant-based meat analogs from alternative protein: A systematic literature review. *Foods, 11*(18), 2870. https://doi.org/10.3390/foods11182870

Chapter 2 - Extrusion Texturization of Faba Bean-Based Plant-Based Meat: Effects of Protein Type and Extrusion Conditions

Abstract

Driven by demand for sustainable meat alternatives, this research investigated how protein type, functionality and extrusion processing conditions influence the structure, texture and performance of plant-based meat produced using low-moisture extrusion. Textured vegetable protein (TVP) based on faba bean concentrate, in combination with various supplemental plant proteins, was the focus of this study.

Before evaluating the different process technologies and plant-based meat products, the functionality of various plant proteins was characterized because it strongly influenced structure development and product quality. Based on water absorption capacity (WAC) and rapid visco-analysis (RVA), soy protein isolate (SPI) was classified as cold swelling protein due to its high WAC (5.95 g/g) and low-temperature peak viscosity (50 °C). In contrast, soy protein concentrate (SPC3), pea protein isolate (PPI), wheat gluten (WG) and faba bean concentrate (FBC) behaved as non-cold swelling ingredients, showing lower hydration and/or requiring higher temperatures to develop viscosity. Cold swelling proteins generally lead to more viscous melts and also exhibit high cross-linking and greater film-forming ability, which leads to more expanded and porous TVP structures; whereas non-cold swelling proteins are more often associated with denser, more fibrous products. These functional differences helped explain variation in processing behavior, texture and final structure of faba bean-based TVP.

FBC paired with different plant protein sources was processed using low-moisture extrusion and the impact of screw speeds and in-barrel moisture (IBM) on resultant TVP products was studied. FBC was blended with SPI, PPI or WG to obtain three distinct formulations. Specific mechanical energy (SME) ranged from 596 to 919 kJ/kg. The formulations containing SPI generally had the highest SME because of their high viscosity during extrusion, followed by WG and PPI. Bulk density of TVP products ranged from 140.4 to 275.2 g/L. SPI produced more porous, lower-density structures, whereas WG and PPI produced denser, more fibrous products; bulk density was negatively correlated with water holding capacity ($r = -0.93$). TVP texture data, such as hardness and other attributes, were found to be closely related to bulk density and WHC. These results were in alignment with the protein functionality hypothesis that was based on their cold swelling and non-cold swelling properties. Besides protein functionality, extrusion behavior and TVP structure and texture were also affected by screw speed and IBM. Higher IBM or lower screw speed reduced SME, which in turn impacted product bulk density and fibrosity. A prior developed image analysis algorithm based on a combination of computer vision (CV) and machine learning (ML) provided fibrosity scores showed strong positive correlations with expert visual scores for the FBC-based TVP products ($r = 0.95$), indicating close agreement between objective image processing and subjective expert assessments of fibrous structure of TVP products.

This research showed that the quality of TVP processed using low moisture extrusion depended on the combination of protein functionality and processing. Differences in hydration, viscosity, temperature, screw speed and formulation shaped processing, structure and texture, providing an improved theoretical and scientific framework and practical guidance for designing better quality plant-based meat products.

2.1 Introduction

Plant-based meat alternatives have gained increasing attention as part of a broader transition toward more sustainable and resilient food systems. Recent reviews emphasize that the growing consumption of plant-based meat products aligns with multiple Sustainable Development Goals (SDGs), including food security, public health, responsible consumption, climate action, and biodiversity preservation. While sustainability considerations continue to drive innovation in this sector, the technological challenge of replicating meat-like texture and structure using plant-derived proteins remains a central limitation to wider adoption (Ali and Bharali 2025).

Extrusion is currently the most widely applied and industrially scalable technology for structuring plant proteins into fibrous meat analogues. During extrusion, proteins are exposed to combined thermal energy, mechanical shear, and controlled moisture, leading to unfolding, aggregation, and alignment that collectively determine the internal structure and textural properties of the final product (Webb, Dogan, et al., 2023; Xiao et al., 2025). Although extrusion parameters such as temperature, moisture content, and screw configuration strongly influence product characteristics, recent studies highlight that the functional behavior of the protein ingredients themselves plays an equally critical role in governing structure development during extrusion (Flory et al., 2023; Webb, Dogan, et al., 2023).

The functional performance of plant proteins during processing is closely linked to their molecular structure, surface chemistry, and processing history. Plant proteins differ substantially in subunit composition, molecular size, amino acid profile, and bonding capacity, which in turn regulate solubility, hydration, unfolding, and aggregation behavior. Surface charge and the relationship between environmental pH and protein isoelectric point further influence hydration

by modulating electrostatic repulsion and accessibility of water-binding sites (Day 2013). These intrinsic characteristics establish the basis for differences in swelling and gelation behavior among plant protein ingredients.

Legume proteins provide clear examples of structurally driven functional diversity. Pea protein isolates are primarily composed of globulins, particularly 11S legumin and 7S vicilin, which exhibit different architectures. Legumin is a compact, disulfide-bonded protein that denatures and aggregates at elevated temperatures, whereas vicilin lacks disulfide bonds and possesses a more flexible, hydrophilic structure that facilitates hydration at lower temperatures (Stone et al., 2015; O'Kane et al., 2004). Comparative analyses of commercial pea protein isolates demonstrate that vicilin-rich proteins show higher solubility, higher water absorption, lower least gelation concentration, and more rapid viscosity development, while legumin-rich proteins exhibit delayed, heat-dependent swelling behavior (Webb, Dogan, et al., 2023). Soy protein isolate represents a distinct case in which industrial alkaline extraction and spray-drying induce partial denaturation of β-conglycinin (7S) and glycinin (11S), exposing functional groups that promote rapid hydration and viscosity development at ambient temperatures (Nishinari et al., 2014).

Wheat gluten is composed primarily of gliadin and glutenin proteins, which belong to the prolamin and glutelin families, respectively, and form viscoelastic networks stabilized by intermolecular disulfide bonding (Day 2013). Wheat gluten is widely recognized as a non-cold swelling protein ingredient. Comparative functional analyses show that gluten exhibits lower water absorption, higher least gelation concentration, and delayed viscosity development relative to soy and pea protein isolates, consistent with heat-dependent hydration and network formation (Webb, Dogan, et al., 2023).

Based on these functional distinctions, plant proteins are commonly categorized as cold swelling or non-cold swelling ingredients. Cold swelling proteins are characterized by strong water affinity, early hydration, low gelation thresholds, and rapid viscosity development without extensive thermal unfolding. In contrast, non-cold swelling proteins exhibit lower native hydration capacity and require thermal activation to unfold, hydrate, and form cohesive networks (Flory et al., 2023). This framework provides a mechanistic basis for understanding how different proteins respond to processing stresses before and during extrusion.

Faba bean protein has emerged as a promising but comparatively underutilized plant protein source. Thomsen et al. (2025) highlight that faba bean protein concentrates are rich in globulin storage proteins and offer advantages related to protein content and sustainability potential; however, their native functional performance is generally weaker than soy and pea proteins, particularly in terms of hydration efficiency, water-holding capacity, and gelation behavior. These limitations are attributed to the structural rigidity and thermal stability of faba bean globulins, which place faba bean protein within the category of non-cold swelling ingredients. As a result, faba bean protein often requires processing or formulation strategies to improve its performance in structured food applications.

Recent extrusion studies showed that the cold versus non-cold swelling framework has direct implications for structure development in protein blends. Flory et al. (2023) showed that low-moisture extrusion of blends containing different ratios of cold and non-cold swelling proteins produced pronounced differences in internal morphology, crosslinking behavior, and density, even under identical extrusion conditions. Similarly, Webb et al. (2023) reported that hydration kinetics and viscosity development govern water distribution and network formation during extrusion, leading to non-additive functional behavior in blended protein systems. Xiao et

al. (2025) further demonstrated that extrusion induces substantial conformational and bonding changes in protein blends, and that the extent of these transformations depends on the swelling characteristics of the constituent proteins rather than on total protein content alone.

Importantly, how cold and non-cold swelling proteins behave during extrusion is not determined by formulation alone, but is strongly influenced by processing conditions. In-barrel moisture content affects protein hydration, mobility, and the extent of molecular interactions, whereas screw speed governs shear intensity, residence time, and mechanical energy input. Together, these parameters shape protein unfolding, aggregation, and alignment during extrusion, ultimately controlling network formation and product structure

(Webb, Dogan, et al., 2023; Flory et al., 2023; Xiao et al., 2025). Consequently, the behavior of blended proteins during extrusion reflects an interplay between ingredient swelling characteristics and processing conditions, rather than a simple effect of formulation.

However, it is still unclear how these functional behaviors operate in protein blends, especially when cold or non-cold swelling proteins are combined with a base protein such as faba protein concentrate.

Based on the established differences between cold and non-cold swelling proteins, it was hypothesized that their incorporation into faba bean concentrate would differentially affect hydration, protein-protein interactions, and structure formation during extrusion. Specifically, cold swelling proteins, which hydrate and swell at lower temperatures, were expected to promote early water uptake and facilitate film-forming behavior, leading to a more expanded and porous structure with reduced fibrous texture. In contrast, non-cold swelling proteins, which require higher thermal input to fully hydrate and unfold, were expected to undergo more extensive shear-

induced denaturation within the extruder, resulting in stronger intermolecular interactions and enhanced fiber formation.

In terms of processing conditions, it was further hypothesized that low in-barrel moisture (IBM) content combined with high screw speed would generate higher shear and mechanical energy, favoring protein unfolding, alignment, and the development of a dense and fibrous structure. Conversely, high IBM and lower screw speed were expected to reduce shear intensity and increase plasticization, promoting expansion and leading to softer, more porous structures.

Together, these findings indicate that protein swelling behavior is not merely a descriptive functional property but a mechanistic driver of extrusion texturization. Despite this emerging understanding, systematic investigation of how faba bean protein interacts with different proteins under varying extrusion conditions, and how these combined effects influence structure development and functional properties, remains limited. Therefore, the objective of this study was to investigate the effects of blending faba bean concentrate with proteins exhibiting distinct swelling behaviors, in combination with controlled variations in IBM and screw speed, on physicochemical properties and extrusion texturization outcomes, to provide insight to support rational formulation and process design of plant-based meat analogues.

2.2 Materials and Methods

2.2.1 Ingredients and formulation

In this study, Faba bean concentrate (FBC; Ingredion Inc., Westchester, IL, USA) was used as a protein source in the formulation of plant-based meat analogues. Three formulations were examined, all centered on FBC as the primary protein ingredient.

The first formulation consisted of 45% FBC, 44% pea protein isolate (PPI; Puris Pea 870, PURIS Foods, Minneapolis, MN, USA), and 11% soy protein concentrate (SPC; ArconS; ADM, Quincy, IL, USA). The second formulation included 45% FBC, 44% soy protein isolate (SPI; Profam 974, Archer Daniels Midland Company, Abilene, KS, USA), and 11% SPC. The third formulation contained 45% FBC, 44% vital wheat gluten (Royal Ingredients Group B.V., Alkmaar, The Netherlands), and 11% SPC. These formulations were designed to examine how combining FBC with different protein sources influences overall formulation behavior, with particular attention to protein content and potential textural performance.

The protein contents of the individual ingredients, as reported by the manufacturers, were 60% for FBC, 80% for PPI, 90% for SPI, 82% for gluten, and 72% for SPC. These values were used to calculate the target protein content of each formulation.

The net protein content of the formulations varied, with values of 70.12%, 74.52%, and 71.30% for the first, second, and third formulations, respectively. This variation in protein content was achieved by adjusting the proportions of FBC and other protein sources in each formulation.

Each formulation was prepared in 300 lb batches, providing sufficient material for subsequent processing and analytical evaluations while maintaining consistency across production runs.

The formulations evaluated in this study demonstrate different approaches to incorporating FBC into plant-based meat and provide a basis for assessing how protein source selection influences formulation characteristics. The composition of each formulation and the corresponding net protein content are summarized in Table 2.1.

Table 2.1. Ingredient composition (%) of faba bean-based protein formulations used for extrusion

Ingredient (%)	Treatment 1	Treatment 2	Treatment 3
Faba bean Concentrate	45	45	45
Pea Protein Isolate	44		
Soy Protein Isolate		44	
Gluten			44
Soy Protein Concentrate	11	11	11
Net protein content %	70.1	74.5	71.3

2.2.2 Raw Material Analysis

2.2.2.1 Moisture Content

The moisture content of raw ingredients was assessed following the AACC 44-19.01 method. Duplicate samples, each weighing approximately 2 g, underwent a drying process at 135°C for 2 hours as per the described procedure.

2.2.2.2 Water Absorption Capacity (WAC)

WAC refers to the amount of water that protein can absorb. It is also referred to water binding capacity (Onyango, 2022)

The WAC of raw materials was measured for each treatment mix, along with the individual ingredients, to assess their functional properties and potential impact on the final product quality. The procedure was completed according to Webb et al. (2020). In brief, 2.5 g of the raw recipe was combined with 30 mL of water, followed by vortexing for 10 seconds. The samples were allowed to stand at room temperature for 30 minutes, with two additional

agitations during this period. Subsequently, they were centrifuged at 3900 RPM for 30 minutes, and the residual water was decanted. This test was performed in triplicate.

WAC was calculated using the following equation:

$$WAC\ \left(\frac{g_{water}}{g_{protein}}\right) = \frac{W_f - W_i}{W_i} \quad (2.1)$$

Where W_f is the weight of the sediment, and W_i is the initial weight of the sample.

2.2.2.3 Least Gelation Concentration (LGC)

The LGC was measured to evaluate the non-cold swelling ability of the protein ingredients and formulations. The procedure was adapted from Wang et al. (2007) and Kamani et al. (2024) with minor modifications. Protein suspensions of increasing concentration were prepared by mixing distilled water with the protein powders to obtain slurries ranging from 8% to 20% (w/v). Each slurry was made into a test tube and manually mixed to ensure uniform hydration. The tubes were then placed in a boiling water bath (90-100°C) for 1 hour, cooled with water for 10 minutes, and subsequently refrigerated for 2 hours. After cooling, each tube was inverted to assess gel formation. The LGC was defined as the lowest concentration at which the sample formed a stable, non-flowing gel. A sample that remained semi-solid without slipping down the tube was classified as a gel. All measurements were performed in duplicate. A lower LGC value reflects stronger heat-gelling capacity, which is consistent with proteins that exhibit delayed, heat-induced viscosity development during thermal processing. A lower LGC reflects stronger thermal gelling capacity, which is theoretically consistent with RVA profiles that exhibit a delayed, heat-induced rise in viscosity.

2.2.2.4 Rapid Visco Analyzer (RVA)

The thermal viscosity behavior of the protein ingredients and formulations was evaluated using a Rapid Visco Analyzer (RVA 4800, Perten Instruments, PerkinElmer, NSW, Australia), following the general procedures of AACC Method 76-21.02 STD1. RVA can identify viscosity development, both cold and non-cold swelling properties, indicated by changes in viscosity over time and with increasing temperature (Osen et al., 2014), which simulate functional transitions relevant to extrusion.

For each test, approximately 3.5 g of sample was weighed on a dry-matter basis, with the actual mass adjusted according to the inherent moisture content of the ingredient or formulation (14% w/v basis), and dispersed in 25 mL of distilled water. The slurry was equilibrated at 50°C while stirring at 960 rpm for 10 seconds, held at 50°C for an additional 50 seconds, then heated to 95°C under reduced shear (160 rpm). Samples were maintained at 95°C for 3 minutes and subsequently cooled to 50°C.

Viscosity was recorded continuously to generate a thermal viscosity curve for each material. Additional parameters, including the temperature and time at which viscosity began to rise, were also documented. All measurements were performed in duplicate.

2.2.2.5 Differential Scanning Calorimetry (DSC)

DSC is an analytical technique used to measure thermal transitions in materials, providing valuable insights into their thermal properties. DSC involves heating a sample and recording the energy required to maintain a controlled temperature increase. This method is widely used to determine transition temperatures, enthalpy changes, and heat capacities of materials, making it essential for characterizing phase change materials, polymers, and other

substances. The technique offers precise and reliable data, critical for research and development in various fields (Fatahi et al., 2022).

Thermal transitions in the protein samples were evaluated using a differential scanning calorimeter (DSC Q100 V9.9 Build 303, TA Instruments, New Castle, DE). The procedure followed was based on the method outlined by Brishti et al. (2020), with slight modifications to suit the specific requirements of this study.

Approximately 5-10 mg of raw sample materials and blends were weighed into stainless steel, high-volume pans and hermetically sealed with an O-ring in the lid. The samples were then heated from 0 °C at a rate of 10 °C per minute until reaching 250 °C, using an empty pan as a reference. The nitrogen purge flow was maintained at 50 mL per minute. Data were analyzed with the Universal Analysis Program, V4.5A (TA Instruments, New Castle, DE, USA), and the peak temperature and enthalpy of denaturation were recorded.

2.2.3 Extrusion Parameters and Calculations

Before extrusion, dry ingredient blends were prepared using a double-ribbon blender (Wenger Manufacturing, Sabetha, KS, USA) and mixed for 5 minutes to ensure uniformity. Blends were processed using a pilot scale co-rotating twin-screw extruder (TX-52, Wenger Manufacturing, Sabetha, KS, USA) with a 52-mm screw diameter and a length-to-diameter (L/D) ratio of 19.5. The extruder consisted of four temperature-controlled barrel zones, which were set to 30°C, 50°C, 80°C, and 110°C from the feed to the die end. A constant dry feed rate of 50 kg/h and a screw speed range from 323 to 455 rpm were used for all treatments.

An aggressive screw profile (Figure 2.1) was selected in order to generate the high shear and mechanical energy required for texturizing the plant proteins, consistent with approaches

described by Webb et al. (2020). The profile incorporated cut-flight elements, forward and reverse kneading blocks, and reduced-pitch conveying elements, which collectively increased barrel fill, restricted forward conveying, and promoted extensive deformation and crosslinking of the hydrated proteins. A ¼-inch venturi die was installed upstream of the final die openings to further elevate shear before the melt stream was channeled into two ¼-inch outlet dies (Figure 2.2). Extrudate was cut immediately at the die face using three rotating knives.

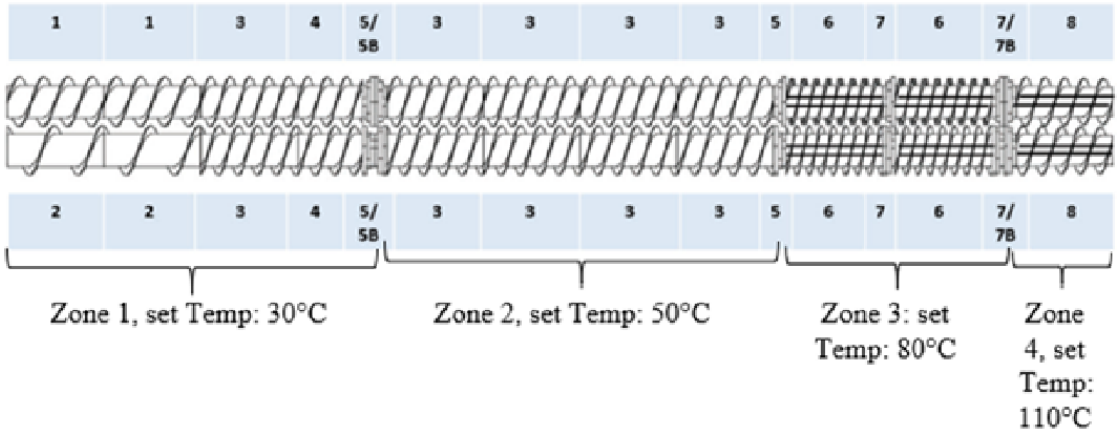

Figure 2.1. Screw Profile (Reproduced from Flory et al., 2023)

The screw profile consisted of the following elements: (1) full pitch, double, 9U; (2) full pitch, single, 9U; (3) ¾ pitch, double, 9U; (4) ¾ pitch, double, 6U; (5) forward KB (5B = backward); (6) ½ pitch, double, cut flight; (7) reverse KB (7B = backward); and (8) ¾ pitch, double, cut flight, cone.

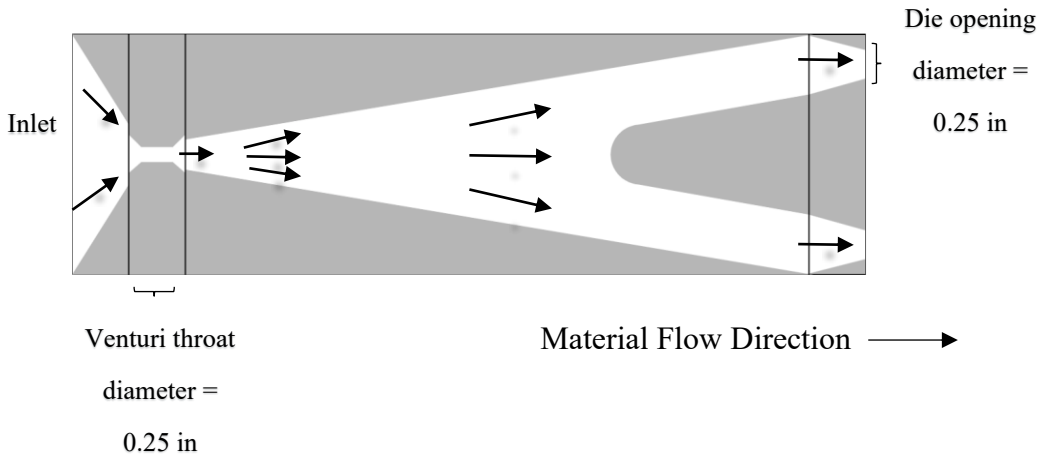

Figure 2.2. Venturi Die

Moisture levels were controlled by injecting water into the preconditioner and directly into the extruder barrel. Injection rates ranged from 1.4 to 9.2 kg/h, depending on the formulation and target hydration. In-barrel moisture (IBM) was calculated as:

$$IBM\ (\%wb) = \frac{(m_f \times (x_{wf}) + m_{wp} + m_{we})}{m_f + m_{wp} + m_{we}} \quad (2.2)$$

where X_{wf} is the moisture content of the dry feed material (expressed as wet basis fraction), and m_f, m_{wp} and m_{we} are the dry feed rate, water injection rate into the preconditioner, and water injection rate into the extruder (in kg/hr), respectively.

Steam injection was not used in any treatment. Temperatures were recorded at the preconditioner discharge, at each barrel head, and immediately before the die, while die pressure was monitored using an analog gauge.

For the experimental design, each formulation was processed using different combinations of in-barrel moisture (IBM) levels and screw speeds. For each formulation, three distinct IBM-screw speed conditions were adjusted during extrusion, resulting in a total of nine different treatments.

For each treatment, two types of products were collected. A portion of the extrudate was conveyed directly to a dual-pass dryer (Series 4800, Wenger Manufacturing) and dried at 113°C for 14 minutes, followed by 5 minutes of ambient cooling, to generate dried chunk samples. The remaining portion of the extrudate stream was diverted before the dryer and immediately milled in its undried state using a hammer mill (Fitzpatrick Co., Westwood, MA). The wet-milled product was packaged and stored frozen for later use in patty development and structural analyses.

During the extrusion process, specific mechanical energy (SME) represents the energy absorbed by the material due to the action of the screws. This can lead to different levels of protein cross-linking and texturization. SME also serves as an indicator of viscosity changes, as the screws require more energy to move the material as the viscosity in the extruder barrel increases. SME (in kJ/kg) was calculated using the following equation:

$$Specific\ Mechanical\ Energy\ \left(\frac{kJ}{kg}\right) = \frac{W - W_0}{m} \quad (2.3)$$

where W is motor power reading in kW, W_0 is the no-load motor power reading, and m is mass flow rate in kg/sec.

A data acquisition system was used to continuously monitor and record key processing variables throughout the extrusion runs. Parameters were logged at a one-second sampling rate and included down spot temperature (material exit from preconditioner), barrel zone temperatures, die temperature, bin feeder speed (RPM), preconditioner cylinder speed (RPM), extruder motor load, extruder screw speed (RPM), knife speed (RPM), water injection rates into both the extruder and preconditioner, and motor power (kW).

Bulk density was assessed during processing by filling a standardized 1-L container with extrudate and determining its mass. This measurement provided a rapid indication of product

expansion and overall texturization, allowing operators to adjust processing parameters when necessary. Lower bulk density values correspond to greater expansion, which is typically associated with a softer and more aerated structure.

2.2.4 Extrudate Analysis

2.2.4.1 Bulk Density

Bulk density, measured in grams per liter, was determined by filling a 1-liter cup with extrudate and recording its mass. Bulk density serves as a rapid means to assess the extent of expansion and texturization. A lower bulk density indicates more expansion, resulting in a porous structure in the final product.

2.2.4.2 Water Holding Capacity (WHC)

WHC is often correlated with bulk density, representing the ability of porous texturized extrudates to absorb and retain water. WHC determination involves immersing 15 grams of whole dried extrudates and also milled extrudates in excess water for 20 minutes at room temperature, followed by draining and allowing the hydrated extrudates to settle on a mesh metal screen for 5 minutes (Webb et al., 2020). Each test was performed with five replicates. The mass before and after hydration was measured to calculate the WHC using the provided equation:

$$WHC = \frac{m_{wet} - m_{dry}}{m_{dry}} \quad (2.4)$$

2.2.4.3 Texture Profile Analysis (TPA)

TPA was performed to characterize the mechanical texture properties of extruded products using a two-cycle compression test, which is designed to simulate the action of chewing

(Bourne, 2002). This approach allows quantification of key textural parameters derived from force-time curves, including hardness, springiness, and chewiness.

TPA measurements were conducted using a TA-XT2 Texture Analyzer (Texture Technologies Corp., Scarsdale, NY, USA), following procedures described by Webb et al. (2020). A cylindrical compression probe (25 mm diameter) was used for all tests. Samples were subjected to two consecutive compressions to 50% strain with a trigger force of 5 g. The pre-test and test speeds were set to 1 mm/s, and the post-test speed was set to 5 mm/s. Hardness was defined as the maximum force recorded during the first compression cycle. Springiness was calculated as the ratio of the recovered distance between the first and second compressions, and Chewiness was calculated as the ratio of the area under the second peak to the area under the first peak, multiplied by hardness and springiness (Bourne, 2002; McClements, 2021). All measurements were performed using ten replicates per sample.

TPA measurements were conducted on hydrated textured vegetable protein (TVP) chunks, uncooked patties prepared from rehydrated milled TVP without binders, and cooked patties formulated with binders.

For dried chunks, they were fully hydrated in tap water at room temperature for 20 minutes before testing. Excess water was removed for 5 minutes, and hydrated chunks were analyzed under the TPA conditions described above.

For patties prepared without binders, milled TVP was rehydrated in tap water for 20 minutes, followed by draining in a sieve for 5 minutes to remove excess water. The hydrated material was formed into patties with a diameter of 50 mm and a thickness of 10 mm and analyzed using the same TPA parameters.

For patties prepared with binders, milled TVP was combined with the additional ingredients listed in Table 2.2. A total mass of 91.5 g was used per patty. Patties were formed using a patty press to a uniform thickness of 10 mm and cooked on a preheated griddle without added oil for approximately 5 minutes until an internal temperature of 71°C was reached. For texture testing, a 50 mm diameter core was taken from the center of each patty, and TPA was performed under the same testing conditions described above.

Table 2.2. Patty formulation used for texture analysis of faba protein-based TVP.

Ingredient	Amount %	Manufacturer
Soy Sauce	3.00	Conagra Brands Canada Inc., Boisbriand, Quebec, Canada
Maggi Liquid Flavoring	0.30	Nestlé USA, Inc., Arlington, VA, USA
Worcester	0.33	The Kraft Heinz Company, Chicago, IL, USA
Liquid Smoke	0.06	The Colgin Companies, Dallas, TX, USA
Water	55.06	Municipal tap water, Manhattan, KS, USA
Texturized Vegetable Protein	24.64	-
Dry seasoning mix	2.22	o Beet Powder: The Dojo, LLC (Kate Naturals), Fountain Valley, CA, USA o Yeast flakes: Hoosier Hill Farm LLC (Saco Foods), Middleton, WI, USA o Porcini powder: Fresh & Wild Specialty Foods, Vancouver, WA, USA o Garlic, Onion, Pepper, Italian seasoning powder: Walmart Inc., Bentonville, AR, USA
Faba Bean Protein	7.41	Know-How Foods, Faribault, MN, USA
Methylcellulose HV	1.49	Modernist Pantry, LLC, Eliot, ME, USA
Coconut Oil	2.75	Amazon.com Services LLC, Seattle, WA, USA
Vegetable Oil	2.75	Associated Wholesale Grocers, Inc., Kansas City, KS, USA

2.2.4.4 Visual Analysis

To analyze the internal structure of the extruded textured vegetable protein products, high-resolution macro images were captured using a Nikon D750 digital camera equipped with a 105 mm macro lens and SB-R200 wireless remote flash. The imaging setup included a Kaiser Copy Stand RS1, two Dracast Camlux Pro LED light panels, and an 18% grey card as the background to ensure standardized lighting and color balance. Image acquisition was conducted using Capture One Pro for Mac (version 10.1.1.5, Phase One, Copenhagen, Denmark) software.

For final product imaging, samples were obtained using two complementary selection approaches. First, two pieces from each treatment were randomly selected after extrusion.

These samples were rehydrated in tap water for 30 minutes, drained for 5 minutes, and cut both longitudinally and transversely to reveal internal structure, yielding four images per treatment. In addition, to capture structural variation over processing time, one sample was randomly selected from each extrusion run at 0, 2, 4, 6, and 8 minutes. Each of these samples was sectioned only in the longitudinal direction, producing five additional images per treatment. In total, nine macro images were generated per treatment for structural evaluation.

2.2.4.5 Fibrosity Score

Fibrosity was additionally evaluated using image-based texture scores obtained from a previously developed computer vision framework for extruded plant-based meat products. In that framework, an unsupervised computer vision approach was used to quantify fibrousness from cross-sectional images based on extracted structural features, and a semi-supervised machine learning (CV+ML) approach was further developed to refine texture scoring using expert-labeled data. In the present study, these image-derived fibrosity scores were used as complementary

quantitative measures and were compared with expert visual scores to assess whether the automated methods captured similar treatment-related differences in fibrous structure (Bagheri et al., 2026).

2.2.5 Statistical Analysis

Statistical analyses were performed using one-way ANOVA to evaluate differences among treatments. Homogeneity of variances was assessed using Levene's test. When the assumption of equal variances was met, Fisher's one-way ANOVA was applied, followed by Tukey's HSD post-hoc test. When the homogeneity assumption was violated, Welch's one-way ANOVA was used with Games–Howell post-hoc comparisons. Statistical significance was defined at $p < 0.05$.

2.3 Results and Discussion

2.3.1 Raw Material Characteristics

2.3.1.1 Water Absorption Capacity (WAC)

WAC reflects the ability of proteins to absorb and retain water under ambient conditions and is commonly used as an indicator of protein-water interactions driven primarily by the availability of polar and charged sites on the protein surface. Higher WAC values generally indicate a greater affinity for water, which is associated with protein composition, structural state, and the extent to which water-accessible functional groups are exposed, indicating overall cold swelling properties of the proteins (Osen et al., 2014; Stone et al., 2015; Flory et al., 2023).

The WAC values measured for the individual protein ingredients are presented in Figure 2.3. FBC exhibited a WAC of approximately 1.10 g water/g protein, which is comparable to values reported for faba bean protein concentrates in recent studies (Toldrà et al., 2025). The relatively low WAC of FBC is likely related to its structural and compositional characteristics. Compared to more processed protein isolates, proteins in faba bean concentrate tend to retain a more native and less denatured structure, limiting the exposure of polar binding sites required for water interaction. In addition, the presence of non-protein components such as starch and fiber may physically restrict water accessibility within the matrix. Since water absorption is strongly influenced by protein unfolding, polarity, and solubility (Osen et al., 2014; Webb, Li, et al., 2023) the more compact and less modified structure of FBC likely contributes to its lower water absorption capacity.

PPI showed a substantially higher WAC (3.82 g/g) compared to FBC. Similar ranges for pea protein isolates have been reported previously and are attributed to protein structural modifications introduced during wet fractionation, which can increase the exposure of polar amino acid residues and enhance water binding (Osen et al., 2014; Stone et al., 2015). SPI exhibited the highest WAC among the individual proteins tested (5.95 g/g), indicating a strong capacity for water absorption. This behavior is consistent with the highly denatured and aggregated structure typically associated with soy protein isolates, which promotes extensive protein-water interactions.

Gluten displayed a low WAC (1.37 g/g), which aligns with its known functional behavior. Gluten proteins are rich in prolamins and glutelins, which exhibit limited water solubility and restrict water uptake under non-heated conditions (Shewry and Tatham 1997).

SPC showed an intermediate WAC (4.63 g/g), reflecting partial protein purification and functionality that lies between native concentrates and fully isolated protein systems.

Blended formulations exhibited WAC values that reflected the combined functional contributions of their constituent proteins. The formulation containing FBC and PPI showed a WAC of approximately 1.64 g/g, which was lower than PPI alone but higher than FBC, indicating a moderating effect of FBC on the water absorption behavior of the blend. A similar trend was observed for the FBC + SPI formulation (2.61 g/g), where the high water-binding capacity of SPI was partially reduced by the presence of FBC. In contrast, the FBC + gluten formulation exhibited a WAC (1.41 g/g) close to that of gluten, suggesting that gluten dominated the water absorption behavior of this blend.

Overall, these results demonstrate that WAC is strongly influenced by protein source and structural state, with isolates exhibiting greater water absorption than concentrates and native proteins. In blended systems, the measured WAC reflects the relative contribution of each protein component and their interaction within the mixture, rather than a simple additive effect.

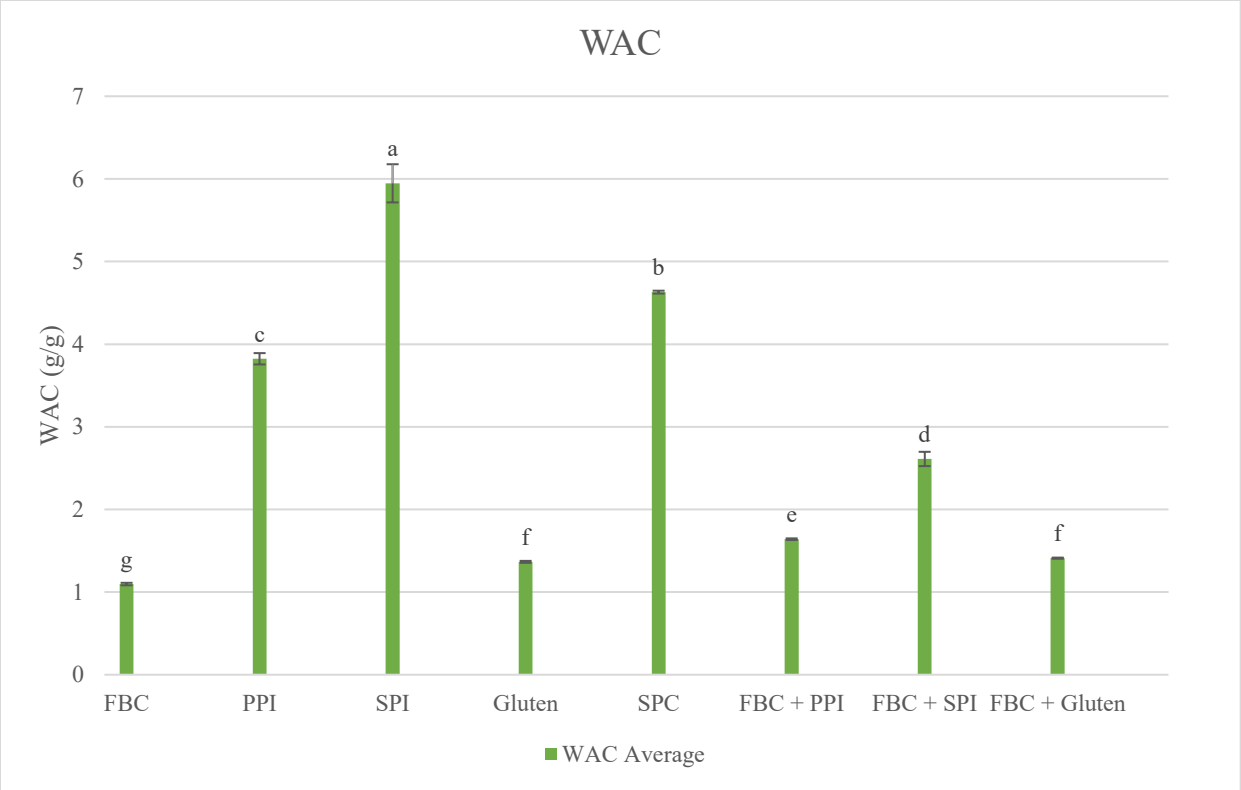

Figure 2.3. Water Absorption Capacity of Raw Material. Bars represent mean ± SD (n = 3). Different letters indicate significant differences among samples according to Tukey's post hoc test ($p < 0.05$)

2.3.1.2 Least Gelation Concentration (LGC)

LGC was used to evaluate the minimum protein concentration required to form a gel structure after heating and subsequent cooling, reflecting the ability of proteins to establish a stable network. Lower LGC values indicate stronger gelation capacity, whereas higher values suggest weaker network formation (Webb et al., 2023; Ribeiro et al., 2024).

In this study, LGC values for individual ingredients and blends ranged from 12% to 18% (Figure 2.4). Among individual ingredients, faba bean concentrate exhibited an LGC of 12%, consistent with previously reported values for faba bean proteins (Vogelsang-O'Dwyer et al., 2020). This relatively low LGC can be attributed to the composite nature of faba bean concentrate, which contains both protein and residual starch fractions that enhance water binding

and viscosity development during heating. In addition, faba proteins are relatively rich in the 11S globulin (legumin) fraction, which is known to exhibit higher thermal stability and stronger intermolecular interactions compared to 7S proteins. The higher sulfur-containing amino acid content of legumin further promotes disulfide bond formation, contributing to a more stable and cohesive gel network (Webb, Li, et al., 2023). SPC also showed a low LGC (12%), while SPI required a higher concentration (16%) to form a stable gel. This agrees with prior observations that protein isolates do not necessarily exhibit superior gelation performance despite higher purity, likely due to extensive aggregation during wet extraction (Ribeiro et al., 2024; Webb, Dogan, et al., 2023).

PPI showed the highest LGC (18%), indicating weaker gelation ability. This behavior has been reported for commercially produced pea protein isolates, which are often highly denatured during isolation, reducing effective protein-protein interactions required for gel network formation (Flory et al., 2023). For wheat gluten, an LGC of 14% was observed in the present study. This value is lower than the commonly reported range for native wheat gluten (approximately 16-22%) (Webb, Li, et al., 2023). However, reduced gelation concentrations have been reported under conditions where the gluten network is structurally modified. For example, recent work has shown that physical or enzymatic modification of the gliadin-glutenin complex can alter protein aggregation and facilitate gel formation at lower protein concentrations (Zadeike et al., 2025).

For blends, LGC values did not consistently align with those of the individual components. The FBC + PPI blend exhibited an LGC of 14%, while FBC + SPI and FBC + gluten blends showed LGC values of 16% and 18%, respectively. Notably, the inclusion of cold-

swelling proteins did not systematically reduce the LGC of the blends relative to the individual ingredients.

This indicates that when proteins were evaluated as blends rather than individual ingredients, the LGC values did not follow a simple additive trend based on the behavior of the constituent proteins. In several formulations, blends exhibited LGC values that were either higher or lower than expected from the individual components alone, indicating that gelation behavior emerges from interactions between protein fractions rather than from their independent contributions. Similar non-additive behavior has been reported for pea-soy protein isolate and concentrate systems, where protein-protein interactions, competition for water, and differences in hydration and aggregation during heating. These findings suggest that in mixed protein systems, gelation is governed by collective structural rearrangements and interfacial interactions rather than by the intrinsic gelling ability of each protein in isolation (Flory et al., 2023; Aslam et al., 2026).

Across all treatments, no variability was observed among replicates (standard deviation = 0). Consequently, LGC results are presented descriptively, and no inferential statistical analysis was performed.

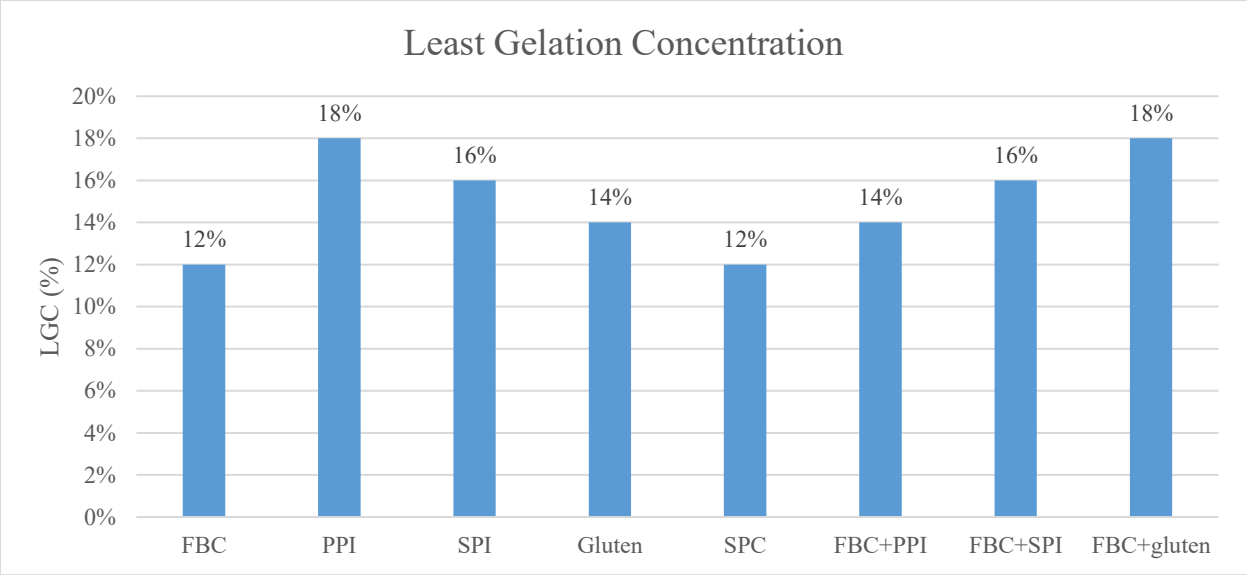

Figure 2.4. Least Gelation Concentration Results

2.3.1.3 Rapid Visco Analyzer (RVA)

RVA was used to characterize the viscosity development of individual proteins and blends during a controlled heating and shear cycle, providing insight into their cold and non-cold swelling behavior. Peak viscosity, temperature at peak viscosity, and time to reach peak viscosity, along with cold peak viscosity, defined as the maximum viscosity observed between 50 and 60 °C, and its corresponding temperature and time, are summarized in Table 2.3, and the corresponding RVA viscosity profiles are presented in Figures 2.5 and 2.6.

Clear differences were observed among the individual protein ingredients. SPI exhibited the highest peak viscosity (1001.5 ± 251.02 cP) and reached its peak immediately at the start of the test (0.3 min) and at the lowest temperature (50.33 °C), indicating extremely cold swelling behavior. This rapid viscosity development is consistent with previous reports that describe SPI as highly water soluble and capable of forming viscosity with minimal thermal input (Flory et al., 2023; Webb, Li, et al., 2023). PPI also displayed cold swelling characteristics, reaching its

peak viscosity (183 ± 16.9 cP) early in the heating cycle (2.93 min, 73.4 °C), although the magnitude of the viscosity was substantially lower than that of SPI. Variability in cold swelling intensity among pea protein isolates has been widely reported and is strongly influenced by protein solubility and processing history (Osen et al., 2014; Webb, Li, et al., 2023).

In contrast, FBC, gluten, and SPC exhibited lower peak viscosities and reached their peak viscosity later in the heating cycle, consistent with non-cold swelling behavior. FBC showed a low peak viscosity (43.5 ± 0.7 cP) occurring only after extended heating (6.4 min at 95 °C), indicating that the viscosity development depends on thermal energy. Similarly, gluten and SPC reached their peak viscosities at high temperatures (95 °C and 73.8 °C, respectively) and longer times, reflecting their lower water absorption and delayed solubilization, as previously observed for non-cold swelling and hydrophobic protein systems (Webb, Li, et al., 2023; Hong et al., 2022).

In contrast, FBC, gluten, and SPC exhibited lower peak viscosities and reached their peak viscosity later in the heating cycle, consistent with non-cold swelling behavior. FBC showed a low peak viscosity (43.5 ± 0.7 cP) occurring only after extended heating (6.4 min at 95 °C), indicating that the viscosity development depends on thermal energy. Similarly, gluten and SPC reached their peak viscosities at high temperatures (95 °C and 73.8 °C, respectively) and longer times, reflecting their lower water absorption and delayed solubilization, as previously observed for non-cold swelling and hydrophobic protein systems (Flory et al., 2023; Webb, Dogan, et al., 2023).

Blending FBC with cold swelling proteins altered the RVA profiles in an additive manner. The FBC + PPI blend exhibited a moderate peak viscosity (45.5 ± 0.7 cP) and an intermediate peak time (2.53 min), indicating that the cold swelling behavior of PPI was

dampened by the presence of FBC. Likewise, the FBC + SPI blend showed a markedly lower peak viscosity (126 ± 11.3 cP) than SPI alone and reached its peak later (2.37 min at 66.45 °C), despite SPI being strongly cold swelling when tested individually. These results suggest that interactions between protein components in blends limit water availability and delay viscosity development, contradicting a simple additive effect of individual protein functionalities. Similar competitive hydration effects in protein blends have been reported previously, where highly soluble proteins dominate viscosity behavior when alone but are constrained in mixed systems (Flory et al., 2023; Webb, Dogan, et al., 2023).

The FBC + gluten blend showed the lowest overall peak viscosity (27.5 ± 0.7 cP) and required extended heating to reach its maximum, indicating dominance of non-cold swelling behavior. This response aligns with the hydrophobic nature and low cold water solubility of gluten, which limits viscosity development under low shear, dilute conditions (Webb, Li, et al., 2023).

Overall, RVA results demonstrate that viscosity development is governed not only by the swelling behavior of individual proteins but also by competitive interactions in blends. Cold swelling proteins such as SPI and PPI dominate viscosity behavior when tested alone, but their functionality is substantially reduced when combined with non-cold swelling proteins, highlighting non-additive effects in protein blends. These findings support the combined use of RVA, WAC, and LGC as complementary tools for distinguishing cold and non-cold swelling protein systems and for interpreting functional behavior relevant to high moisture extrusion applications (Flory et al., 2023; Webb, Li, et al., 2023).

Cold peak viscosity values further supported this interpretation. SPI showed the highest cold peak viscosity (1001.5 ± 251.02 cP) at the earliest point in the cold range (50.33 ± 0.04 °C,

0.3 ± 0.05 min), while PPI and SPC showed relatively high cold peak viscosities near the upper end of the cold range (163 ± 4.2 and 138.5 ± 34.6 cP, respectively, at approximately 59 °C and 1.8 min). In the blends, FBC + SPI retained an intermediate cold peak viscosity (77 ± 12.7 cP at 59.2 ± 0 °C and 1.8 ± 0 min), whereas FBC, FBC + PPI, and FBC + gluten remained low, confirming that cold swelling behavior was reduced in blends.

Table 2.3. Rapid Visco Analyzer Results

Sample	Peak Viscosity (cP)	Temp at Peak Visc (°C)	Time at Peak Visc (min)	Cold Peak Visc (cP) – Between 50 and 60 °C	Temp at Cold Peak Visc (°C)	Time at Cold Peak Visc (min)
FBC	43.5 ± 0.7	95 ± 0	6.4 ± 0.19	19.5 ± 0.7	54.5 ± 5.7	1.1 ± 0.9
PPI	183 ± 16.9	73.4 ± 0	2.93 ± 0	163 ± 4.2	59.3 ± 0.1	1.8 ± 0
SPI	1001.5 ± 251.02	50.33 ± 0.04	0.3 ± 0.05	1001.5 ± 251.02	50.33 ± 0.04	0.3 ± 0.05
Gluten	69 ± 2.8	95 ± 0	6.6 ± 0.6	64.5 ± 17.7	53.9 ± 5.06	1.23 ± 0.61
SPC	143 ± 32.5	73.8 ± 7.4	2.97 ± 0.61	138.5 ± 34.6	59.2 ± 0.04	1.8 ± 0
FBC + PPI	45.5 ± 0.7	68.6 ± 0	2.53 ± 0	21 ± 0	52. 6 ± 3.1	1.03 ± 0.6
FBC + SPI	126 ± 11.3	66.45 ± 0.7	2.37 ± 0.05	77 ± 12.7	59.2 ± 0	1.8 ± 0

FBC + Gluten	27.5 ± 0.7	95 ± 0	6.07 ± 0.5	19 ± 1.4	50.5 ± 0.2	0.93 ± 0.3

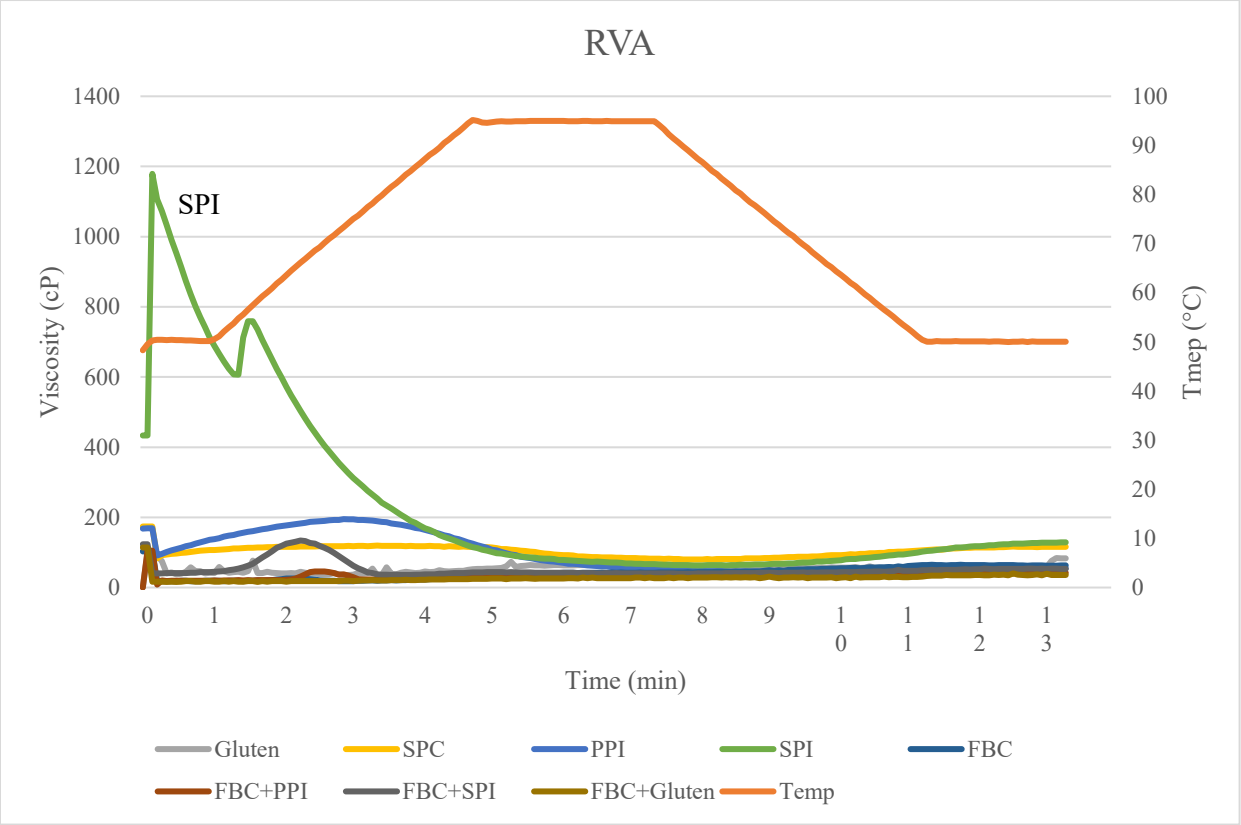

Figure 2.5. Rapid Visco Analyzer (all raw materials, with emphasis on the differences between SPI and the other raw materials)

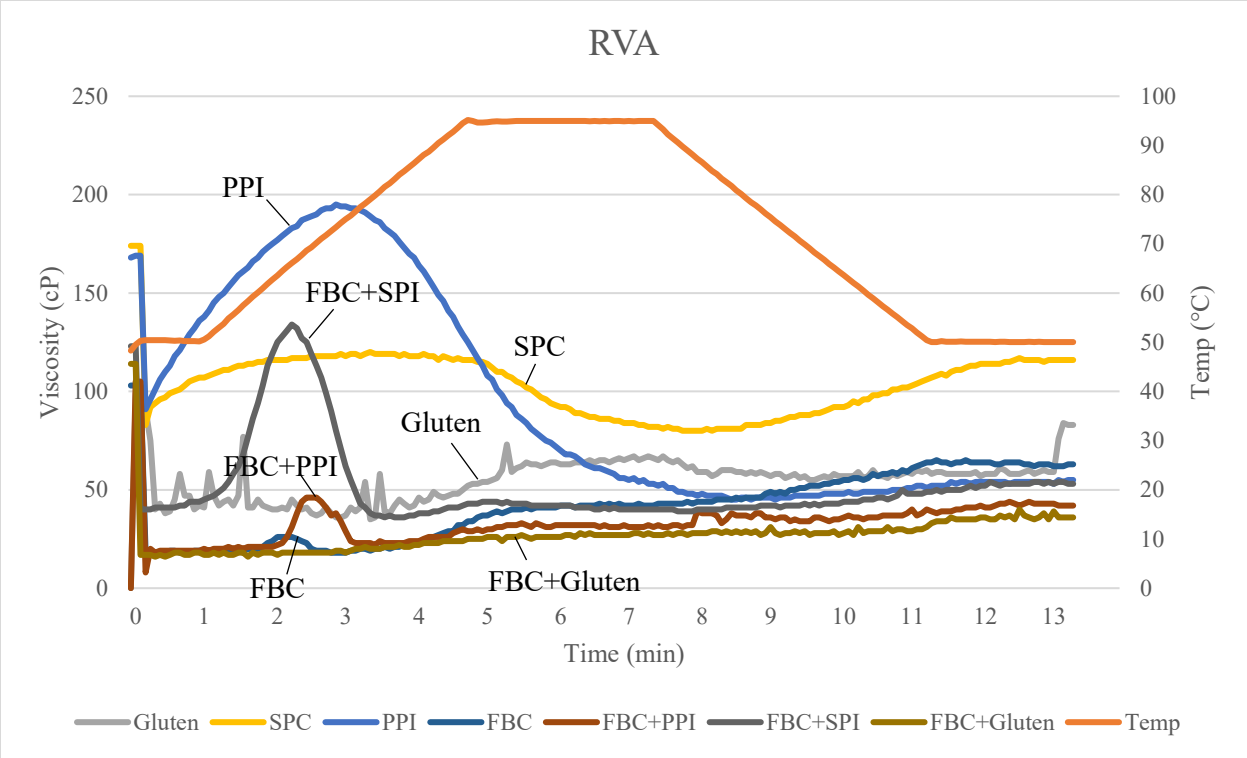

Figure 2.6. Rapid Visco Analyzer (raw materials, except SPI)

2.3.1.4 Differential Scanning Calorimetry (DSC)

DSC was used to characterize the thermal denaturation behavior of individual protein ingredients and their blends. Onset temperature (T_{onset}), peak denaturation temperature (T_m), and end temperature (T_{end}) were extracted from the thermograms. Measurements were performed in duplicate (n = 2); therefore, results are reported descriptively as mean ± standard deviation without inferential statistical analysis.

The individual proteins exhibited distinct thermal behaviors (Table 2.4). SPI showed the highest peak denaturation temperature (203.27 ± 0.23 °C), followed closely by PPI (199.88 ± 0.35 °C) and SPC (199.13 ± 9.29 °C), indicating high thermal stability. FBC exhibited an intermediate denaturation temperature (187.64 ± 1.40 °C), whereas gluten showed the lowest thermal stability, with a peak denaturation temperature of 172.38 ± 13.23 °C. These trends are

consistent with previous DSC studies on globular plant proteins and wheat gluten (Osen et al., 2014; Webb, Li, et al., 2023; Plattner et al., 2024).

Blending FBC with other proteins changed the thermal behavior relative to the individual components, indicating non-additive interactions. The FBC + SPI blend maintained a high denaturation temperature (196.35 ± 1.48 °C), closely resembling SPI, suggesting dominance of SPI in the thermal response. In contrast, the FBC + PPI blend showed a substantially reduced denaturation temperature (180.62 ± 12.85 °C), despite the high thermal stability of both individual proteins. The FBC + gluten blend also exhibited reduced and highly variable denaturation temperatures (181.07 ± 19.67 °C). These results suggest non-additive interactions between protein fractions in the blends, where the presence of one protein moderates the functional contribution of the other.

In addition to the DSC results, the WAC data showed a similar pattern of ingredient-dependent and non-additive functional behavior. SPI exhibited the highest water absorption capacity, followed by SPC and PPI, while FBC and gluten showed the lowest WAC values. This trend generally agrees with the DSC results, where SPI, PPI, and SPC showed relatively high peak denaturation temperatures, suggesting that proteins with greater thermal stability and hydration capacity may contribute more strongly to water binding and viscosity development. However, the blends did not follow a simple additive pattern. Although SPI alone showed the highest WAC, the FBC + SPI blend exhibited a substantially lower WAC than SPI, indicating that the hydration behavior of SPI was moderated when blended with FBC. Similarly, the FBC + PPI and FBC + gluten blends showed lower WAC values than their higher WAC individual components, consistent with the reduced or more variable denaturation temperatures observed in DSC. These results suggest that blending changed both thermal transitions and water binding

capacity, likely due to competition for water, changes in protein hydration, and protein-protein interactions within the mixes.

Such non-additive thermal responses have been previously reported in mixed biopolymer systems and attributed to phase separation, competition for water, and altered protein-protein interactions during heating (Li et al., 2014). Similar trends have also been observed in pea protein isolate and concentrate, where proteins with lower denaturation temperatures exhibit enhanced non-cold swelling behavior and faster thermal transitions (Plattner et al., 2024).

Overall, DSC results demonstrate that protein blends cannot be characterized only based on the thermal properties of their individual components. Instead, interactions between protein fractions play a critical role in determining denaturation behavior, which may have an effect on processing, such as extrusion and texturization.

The combined interpretation of RVA, LGC, WAC, and DSC results highlights clear differences between cold swelling and non-cold swelling proteins. Proteins exhibiting stronger hydration and cold swelling behavior, particularly SPI and PPI, showed relatively high WAC values and reached peak viscosity early during RVA testing, consistent with their greater solubility and ability to develop viscosity without extensive thermal input, as reported previously (Flory et al., 2023; Webb, Li, et al., 2023). In contrast, proteins classified as non-cold swelling, including gluten, showed lower or delayed functional responses, requiring additional thermal energy to swell and gel, which aligns with their lower WAC values, higher LGC values, and broader or lower denaturation responses observed in DSC (Plattner et al., 2024; Webb, Li, et al., 2023). Importantly, protein blends did not exhibit additive behavior across these measurements. Instead, RVA profiles showed reduced peak viscosities and shifts in the time required to reach peak viscosity, LGC values reflected moderated gelation behavior, WAC values showed reduced

water binding capacity compared with the higher WAC individual proteins, and DSC results revealed shifts and increased variability in denaturation temperatures. Such non-additive responses are consistent with previously reported competitive interactions for water, differences in protein solubility, and phase interactions in mixed protein systems, where one fraction can interfere with or dominate the functional response of another rather than contributing independently (Li et al., 2014; Webb, Li, et al., 2023).

Table 2.4. Differential Scanning Calorimetry Results

	Onset Temperature (°C)	Peak Denaturation Temperature (°C)	End Temperature (°C)
FBC	176.87 ± 0.77	187.64 ± 1.4	198.25 ± 2.47
PPI	172.14 ± 0.12	199.88 ± 0.35	216 ± 1.41
SPI	171.58 ± 1.32	203.27 ± 0.23	218 ± 1.41
Gluten	158.89 ± 20.36	172.38 ± 13.23	196.5 ± 0.71
SPC	176.68 ± 14.6	199.13 ± 9.29	216 ± 9.9
FBC + PPI	166.34 ± 12.32	180.62 ± 12.85	189.5 ± 19.09
FBC + SPI	173.06 ± 2.56	196.35 ± 1.48	212.25 ± 0.35
FBC + Gluten	162.47 ± 10.14	181.07 ± 19.67	193.5 ± 24.75

2.3.2 Extrusion Parameters and Calculations

Optimization of extrusion parameters is indeed crucial for developing high-quality plant-based meat alternatives, as the process fundamentally determines the final product's fibrous

structure, texture, and mouthfeel. By carefully controlling variables like temperature, moisture content, screw speed, and die design, manufacturers can transform a dough-like protein mixture into a product that mimics the properties of animal muscle. This optimization process is essential for achieving the desired chewiness and appearance that appeal to consumers (Aghagholizadeh & Amiri Rigi, 2025).

Various factors, such as the type of extruder, processing temperature profile, screw configuration, and type of die, influence the protein restructuring. Corotating twin-screw extruders provide mixing, heat transfer, and pumping behaviors suited to handling short process windows efficiently, such as dispersions with water, low or high viscosity protein solutions (melts). The design or arrangement of the screw elements is largely responsible for their function, such as metering, intensive mixing and heat transfer, filling, and metering compressing (Martin 2016). Changing the screw configuration (the forward and reverse elements) also affects the SME and mechanical energy dissipation, comparatively higher for combinations of mixing and reverse elements than for forwarding and mixing elements only (Pietsch et al., 2017).

SME, calculated using the wattmeter method, showed pronounced variation across the nine extrusion treatments and reflected the combined influence of IBM, screw speed, and formulation (Table 2.5 and Figure 2.7).

Within the FBC + PPI formulations, SME exhibited a clear inverse relationship with IBM. As IBM increased from 29.73 to 37.40 and 40.34, SME decreased progressively from 751.38 to 623.35 and 595.79 kJ/kg, respectively. Importantly, this reduction occurred despite an increase in screw speed from 357 rpm to 455 rpm, indicating that IBM exerted a stronger influence on SME than screw speed in this formulation. This behavior aligns with previous

extrusion studies showing that higher IBM lowers melt viscosity and mechanical resistance, thereby reducing the mechanical energy required during processing (Guerrero et al., 2025).

The role of screw speed became more apparent when IBM was held relatively constant. For the FBC + SPI formulation at low IBM (approximately 35.5), decreasing screw speed from 455 rpm to 323 rpm led to a decrease in SME from 918.86 to 795.85 kJ/kg. A comparable pattern was observed for FBC + gluten at high IBM (around 37), where SME decreased from 820.33 kJ/kg at 351 rpm to 753.6 kJ/kg at 455 rpm. These comparisons indicate that, under similar IBM conditions, higher screw speeds increase SME by intensifying mechanical input and shear within the extruder barrel, consistent with prior findings in pulse protein extrusion systems (Guerrero et al., 2025; Samard and Ryu 2019).

In addition to processing parameters, formulation-dependent differences in SME were evident. At comparable screw speeds (455 rpm) and similar IBM levels (35-37), SME varied substantially among protein blends. The FBC + SPI blend exhibited the highest SME (918.86 kJ/kg), followed by FBC + gluten (885.77 kJ/kg), whereas FBC + PPI showed markedly lower SME (623.35 kJ/kg). This trend can be attributed to differences in rheological behavior during extrusion, where SPI typically exhibits higher viscosity, leading to greater resistance to flow and increased mechanical energy input. In contrast, PPI generally has lower viscosity, resulting in reduced shear and consequently lower SME. These differences suggest that protein composition and matrix interactions influence the mechanical response of the melt, altering resistance to flow and energy dissipation during extrusion, as previously reported for mixed proteins (Samard and Ryu 2019; Guerrero et al., 2025).

Die pressure measurements further supported the trends observed for SME and provided additional insight into flow resistance during extrusion (Table 2.5). In general, formulations

processed at higher IBM exhibited lower die pressures, consistent with reduced melt viscosity and mechanical resistance. For example, within the FBC + PPI formulations, increasing IBM from 29.73 to 40.34 was accompanied by a marked reduction in die pressure from 575 to 300 psi, paralleling the observed decrease in SME.

At comparable IBM levels, variations in die pressure reflected both screw speed and formulation effects. While higher screw speeds tended to increase mechanical energy input, the magnitude of die pressure response was strongly formulation-dependent, indicating differences in melt strength and flow behavior among protein blends. Similar relationships between SME and die pressure have been reported in high-moisture extrusion systems, where die pressure acts as an indirect indicator of material viscosity and structural resistance under shear(Samard and Ryu 2019; Guerrero et al., 2025).

Die temperature showed a similar trend to SME across treatments, suggesting a positive relationship between mechanical energy input and melt temperature. In general, higher SME values were associated with higher die temperatures, while lower SME values corresponded to lower die temperatures. This pattern indicates that increased mechanical energy dissipation during extrusion contributes to higher thermal energy at the die.

Overall, the combined trends in SME and die pressure indicate that IBM plays a dominant role in governing flow softening and reducing mechanical resistance during extrusion. When IBM is comparable, increases in screw speed lead to higher SME by intensifying mechanical input and shear. However, the magnitude of both SME and die pressure responses is strongly formulation-dependent, reflecting differences in protein interactions and melt resistance to deformation within the die. These findings highlight the importance of considering IBM,

screw speed, and ingredient interactions simultaneously when interpreting extrusion energy requirements and material flow behavior.

Table 2.5. Screw Speed, IBM, SME, Die Pressure, and Die Temperature data across extrusion treatments.

	FBC + PPI (low IBM, Low rpm)	FBC + PPI (Med IBM, High rpm)	FBC + PPI (High IBM, High rpm)	FBC + SPI (Low IBM, High rpm)	FBC + SPI (Low IBM, Low rpm)	FBC + SPI (High IBM, Low rpm)	FBC + Glu (Low IBM, High rpm)	FBC + Glu (High IBM, High rpm)	FBC + Glu (High IBM, Low rpm)
Screw Speed (RPM)	357	455	455	455	323	365	455	455	351
IBM (%wb)	29.73	37.40	40.34	35.68	35.49	39.48	35.32	37.37	36.97
SME (kJ/kg)	751.38	623.35	595.79	918.86	795.85	808.63	885.77	820.33	753.60
Die Pressure (psi)	575	400	300	250	425	650	550	550	550
Die Temp (°C)	149	143	131	164	151	150	168	161	149

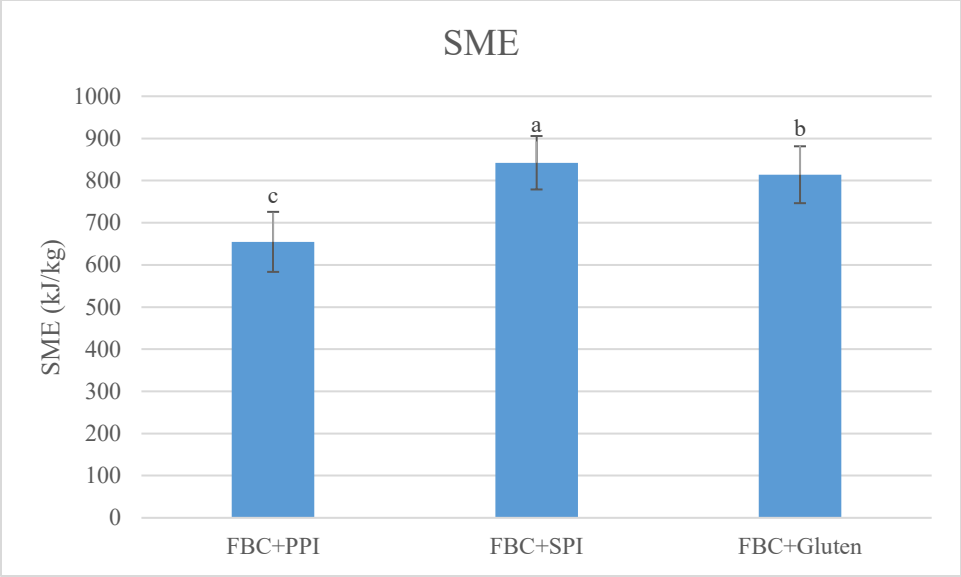

Figure 2.7. SME by Formulation

2.3.3 Extrudate Analysis

2.3.3.1 Bulk Density

Bulk density varied significantly among the nine extrusion treatments and reflected the combined effects of formulation, IBM, and screw speed (Table 2.6 and Figure 2.8). Because bulk density is inversely related to product expansion, lower values indicate greater porosity and gas retention within the extruded matrix (Webb, Dogan, et al., 2023). Clear formulation-dependent trends were observed, with blends containing higher proportions of cold swelling proteins exhibiting lower bulk density relative to formulations dominated by non-cold swelling protein fractions.

Among the formulations, FBC + SPI treatments consistently produced the lowest bulk density values (140-185 g/L), whereas FBC + PPI and FBC + gluten treatments showed substantially higher bulk densities, reaching up to 275 g/L under high IBM conditions. These

results align with prior findings that cold swelling proteins, such as SPI, possess superior film-forming and gas-holding capabilities during extrusion, which promote protein crosslinking and expansion (Webb, Dogan, et al., 2023). In contrast, non-cold swelling proteins and protein-starch mixtures tend to disrupt the continuity of the protein network, limiting expansion and increasing bulk density.

Processing conditions further modulated these formulation effects. Within the FBC + PPI system, increasing IBM from 29.73% to 40.34% led to a progressive increase in bulk density, suggesting reduced expansion under higher moisture conditions. Similar trends were observed in the gluten-containing formulations, where higher IBM was associated with higher bulk density despite comparable screw speeds. These observations are consistent with reports that increased moisture can reduce melt elasticity and gas retention capacity, particularly when protein crosslinking is limited (Webb, Li, et al., 2023).

When considered alongside SME results, the bulk density trends suggest that mechanical energy input alone does not govern expansion behavior. Although higher SME can enhance structural development, Webb, Dogan, et al. (2023) demonstrated that protein crosslinking capacity, closely associated with cold swelling behavior, is a primary driver of expansion in texturized protein systems. Accordingly, formulations combining strong cold swelling, film-forming proteins with sufficient mechanical input, exhibited lower bulk density and greater expansion, whereas blends lacking these functional characteristics showed higher bulk density regardless of SME magnitude.

In addition, bulk density showed a general inverse relationship with SME across treatments. Formulations with higher SME, particularly the FBC + SPI blends, tended to exhibit lower bulk density, indicating greater expansion. In contrast, treatments with lower SME, such as

FBC + PPI at higher IBM, showed higher bulk density, reflecting limited expansion. This suggests that while SME contributes to structural development, its effect on expansion is strongly modulated by protein functionality.

A similar inverse trend was observed between die temperature and bulk density. Treatments with higher die temperatures generally exhibited lower bulk density, whereas lower die temperatures were associated with denser structures. This pattern indicates that increased thermal and mechanical energy together increase expansion, although the extent of this effect remains dependent on the formulation's ability to form a continuous film, gas-holding network.

Overall, the bulk density results indicate that formulation effects, particularly the presence of cold swelling proteins with high film-forming ability, dominate expansion behavior, while processing parameters such as IBM and screw speed modulate these effects by influencing melt rheology and energy dissipation. Consistent with this, bulk density also showed inverse relationships with SME and die temperature, indicating that greater mechanical and thermal energy inputs generally promote expansion when supported by appropriate protein functionality. This highlights the importance of considering protein functionality and processing conditions simultaneously when interpreting expansion and structural development in extrusion systems (Guerrero et al., 2025).

Table 2.6. Bulk Density of final products. Different letters indicate significant differences among formulations based on Tukey's HSD test ($p < 0.05$)

	FBC + PPI (low IBM, Low rpm)	FBC + PPI (Med IBM, High rpm)	FBC + PPI (High IBM, High rpm)	FBC + SPI (Low IBM, High rpm)	FBC + SPI (Low IBM, Low rpm)	FBC + SPI (High IBM, Low rpm)	FBC + Gluten (Low IBM, High rpm)	FBC + Gluten (High IBM, High rpm)	FBC + Gluten (High IBM, Low rpm)
Bulk Density	238.3 ± 5.81^{g}	264.5 ± 4.08^{g}	275.2 ± 5.08^{g}	140.4 ± 3.99^{a}	159 ± 3.76^{b}	184.9 ± 2.16^{c}	221.8 ± 3.09^{d}	250 ± 5.7^{e}	269.5 ± 5.1^{f}

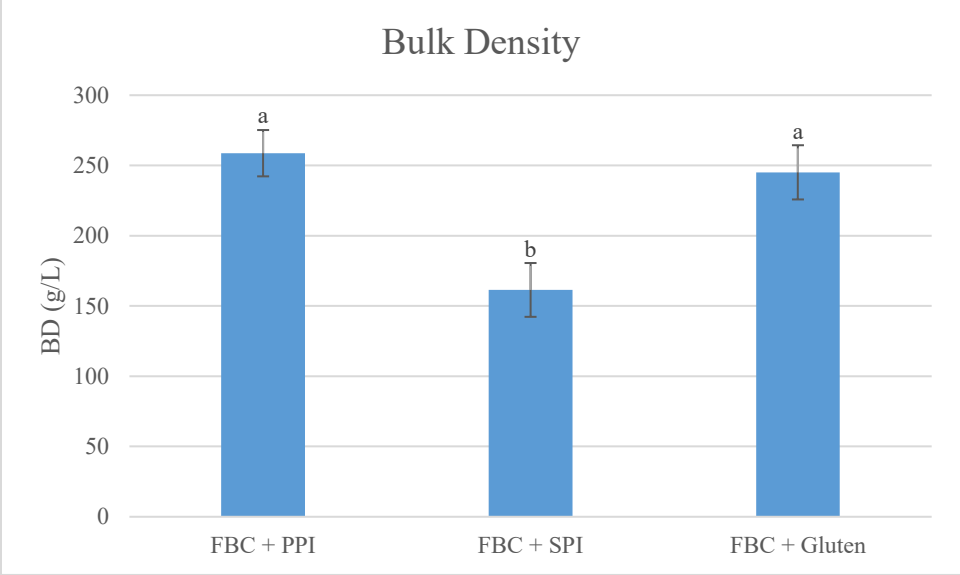

Figure 2.8. Bulk Density by Formulation

2.3.3.2 Water Holding Capacity (WHC)

WHC of a material represents its hydration properties and indicates the amount of water it can absorb at the macromolecular level (McClements et al., 2021). WHC differed significantly among formulations and followed consistent trends for both chunks and milled samples (Figures

2.9 and 2.10; Table 2.7). Across all formulations, WHC of milled samples was higher than that of chunks, while preserving the same relative ranking among treatments. This behavior is consistent with previous reports showing that milling increases exposed surface area and opens internal void spaces, thereby increasing water absorption capacity without changing the intrinsic material trends (van Esbroeck et al., 2024).

Among formulations, FBC + SPI treatments exhibited the highest WHC values in both chunk (370-417%) and milled (427-485%) forms, indicating highly expanded and porous structures. FBC + PPI showed intermediate WHC values (152-178% for chunks and 135-272% for milled samples), suggesting partial expansion and a less open internal structure compared to SPI-based extrudates. In contrast, FBC + gluten formulations consistently exhibited the lowest WHC (134-155% for chunks and 126-181% for milled samples) and reflecting denser and more layered structures. These differences align with prior studies demonstrating that WHC is primarily governed by extrudate structure, rather than protein content alone (Webb, Li, et al., 2023; Flory et al., 2023). Specifically, texturized products with more open and porous internal structures are able to absorb and retain greater amounts of water, whereas denser and more compact structures restrict water uptake and retention.

The observed WHC trends closely mirrored bulk density results, with treatments exhibiting higher bulk density showing lower WHC, and vice versa. This inverse relationship between bulk density and WHC has been consistently reported for texturized vegetable proteins and reflects differences in expansion and internal pore structure (Webb, Li, et al., 2023; Flory et al., 2023). In the present study, this structural relationship was further supported by a strong negative correlation between bulk density and WHC ($r=-0.93$, Figure 2.11), indicating that increased expansion and porosity were directly associated with enhanced water retention

capacity. Similar inverse relationships between bulk density, porosity, and WHC have been reported in legume and protein-based extrudates, where more expanded, porous structures provide greater void space for water absorption (van Esbroeck et al., 2024).

From a formulation perspective, the high WHC of FBC + SPI treatments is consistent with the behavior of cold swelling proteins, which are known to exhibit strong film-forming and water-binding capabilities during extrusion. Cold swelling proteins promote protein networking and gas holding capacity, leading to greater expansion and a more porous structure, which in turn enhances WHC (Flory et al., 2023). FBC + PPI formulations exhibited intermediate WHC and bulk density values, indicating a balance between expansion and structural compaction. This behavior suggests partial protein networking and moderate pore formation, consistent with proteins where cold swelling functionality is present but less dominant than in SPI-rich matrices. Such intermediate structures have been reported to result in moderate water retention. In contrast, the incorporation of wheat gluten led to denser, more compact structures with reduced porosity, limiting water uptake and retention, as previously observed for gluten-rich extrudates (Webb, Dogan, et al., 2023; Flory et al., 2023).

Processing effects further modulated WHC within each formulation. For FBC + SPI blends, IBM and higher SME were associated with higher WHC, particularly in chunk samples. This observation is consistent with literature suggesting that increased mechanical input can enhance protein structuring and gas retention when cold swelling proteins dominate the matrix, thereby increasing porosity and water retention (Webb, Dogan, et al., 2023; Flory et al., 2023). However, when IBM increased, WHC decreased despite comparable or higher screw speeds, indicating that excessive moisture reduced expansion and pore stability, as previously reported for legume-based extrudates (Guerrero et al., 2025).

Overall, these results demonstrate that WHC is primarily governed by extrudate structure, which is jointly influenced by protein functionality (cold versus non-cold swelling behavior), bulk density, and extrusion conditions. Formulations rich in cold swelling proteins exhibited higher expansion, lower bulk density, and consequently higher WHC, particularly when accompanied by sufficient mechanical energy input. In contrast, gluten-rich formulations produced denser structures with reduced water retention. These findings are fully consistent with previous studies linking WHC to porosity, expansion, and protein swelling behavior rather than extrusion energy alone (Flory et al., 2023; van Esbroeck et al., 2024).

Table 2.7. Water Holding Capacity of milled and chunk final products. Different letters indicate statistically significant differences among formulations based on one-way ANOVA followed by a Games-Howell post hoc test, applied due to violation of homogeneity of variances ($p < 0.05$)

	FBC + PPI (low IBM, Low rpm)	FBC + PPI (Med IBM, High rpm)	FBC + PPI (High IBM, High rpm)	FBC + SPI (Low IBM, High rpm)	FBC + SPI (Low IBM, Low rpm)	FBC + SPI (High IBM, Low rpm)	FBC + Gluten (Low IBM, High rpm)	FBC + Gluten (High IBM, High rpm)	FBC + Gluten (High IBM, Low rpm)
WHC – Chunk (%)	178.2 ± 11.5^{g}	177.3 ± 6.11^{g}	152.2 ± 2.71^{g}	417.2 ± 5.02^{a}	370.8 ± 3.82^{b}	241.9 ± 8.71^{c}	155.1 ± 3.85^{d}	134.2 ± 9.57^{d}	135.4 ± 5.4^{e}
WHC – Milled (%)	272.2 ± 12.75^{f}	181.9 ± 4.71^{f}	134.5 ± 4.05^{g}	484.6 ± 5.07^{a}	426.9 ± 8.15^{b}	260.8 ± 17.33^{c}	181.1 ± 7.08^{d}	150.3 ± 0.97^{e}	126.4 ± 4.44^{e}

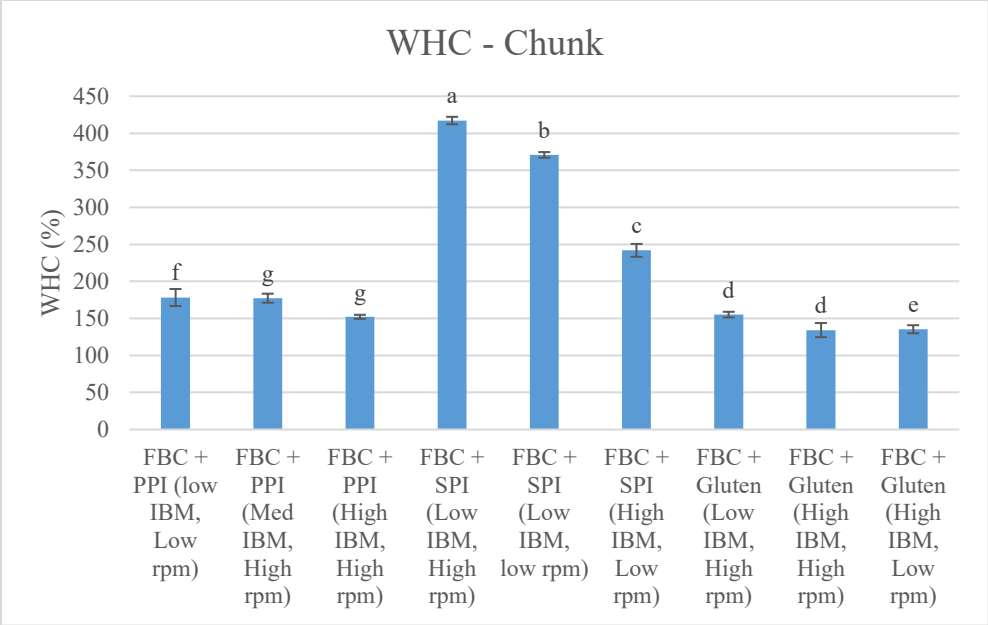

Figure 2.9. Water Holding Capacity for Chunk Samples. Bars represent mean ± standard deviation. Different letters indicate statistically significant differences among formulations based on one-way ANOVA followed by Games-Howell post hoc test ($p < 0.05$)

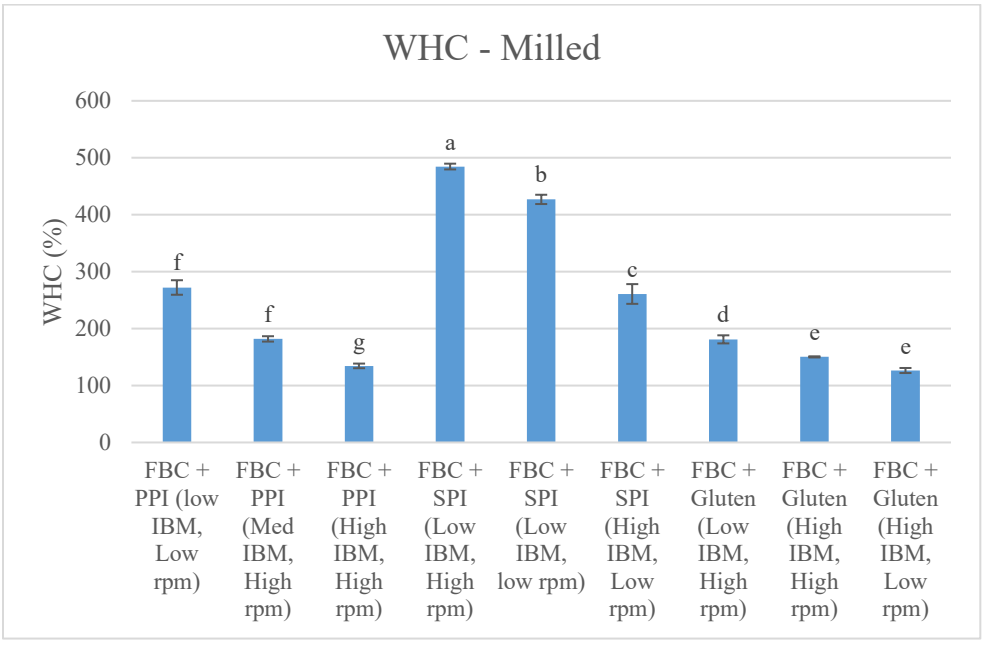

Figure 2.10. Water Holding Capacity for Milled Samples. Bars represent mean ± standard deviation. Different letters indicate statistically significant differences among formulations based on one-way ANOVA followed by Games-Howell post hoc test ($p < 0.05$).

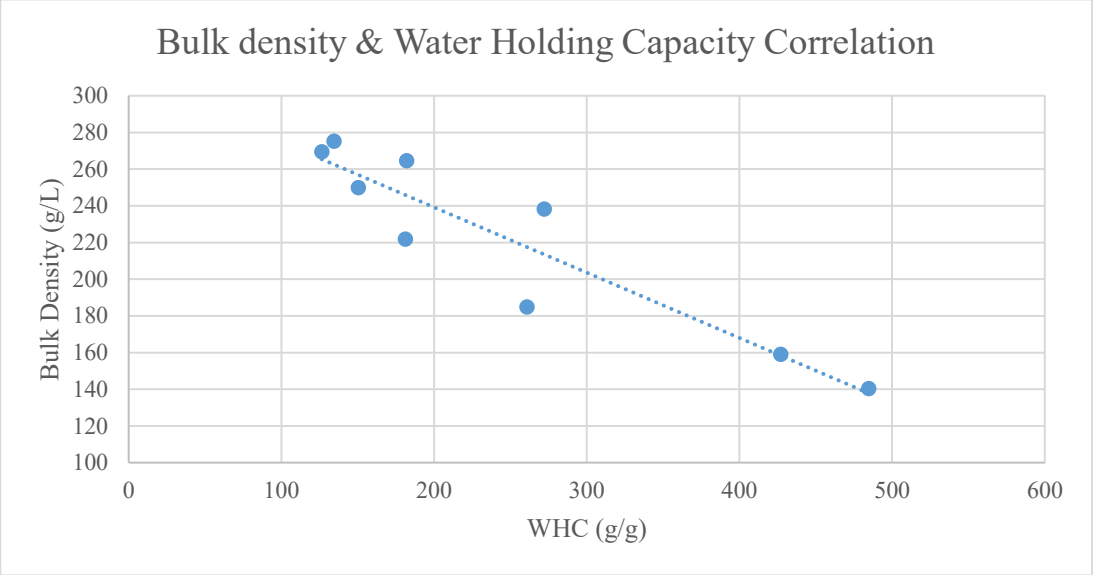

Figure 2.11. Water Holding Capacity and Bulk Density Correlation. A strong negative correlation was observed (r = - 0.93)

2.3.3.3 Texture Profile Analysis (TPA)

TPA was used to evaluate the mechanical behavior of hydrated extrudates as it relates to their internal structure and hydration properties. Textural attributes such as hardness, springiness, and chewiness are closely linked to protein functionality, bulk density, and water holding capacity, and collectively reflect the resistance of the protein matrix to deformation during mastication (Hong et al., 2022; Florry et al., 2023).

Across all formulations, texture parameters varied significantly with protein type, processing conditions, and product form (chunk, patty without binder, and patty with binder) (Tables 2.8 to 2.10). For chunk samples, hardness ranged from 3.74 to 10.41 N, with FBC + SPI treatments generally exhibiting lower hardness compared to FBC + PPI and FBC + gluten formulations. In contrast, gluten-containing treatments tended to show higher hardness values, consistent with the formation of denser and more compact protein networks. These trends align

with previous studies showing that cold swelling protein systems promote expanded, porous structures with lower resistance to compression, whereas non-cold swelling proteins, such as wheat gluten, produce stronger, layered structures that increase hardness (Flory et al., 2023; Webb, Li, et al., 2023).

Textural behavior closely mirrored hydration properties. Treatments with higher WHC consistently exhibited lower chunk hardness, while low WHC, high-density samples were significantly harder. This relationship was supported by a strong negative correlation (Figure 2.12) between chunk hardness and WHC (r=-0.70), indicating that increased water retention and porosity directly contributed to softer textures. Similar inverse relationships between hardness, WHC, and bulk density have been widely reported for texturized vegetable proteins and plant-based meat analogues (Hong et al., 2022; Webb et al., 2020).

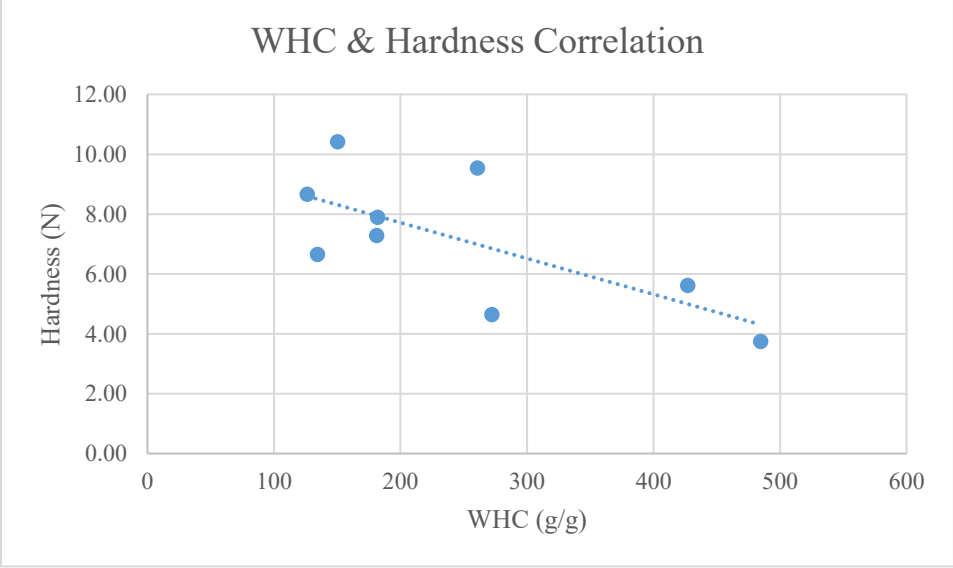

Figure 2.12. Water Holding Capacity and Hardness Correlation (r = - 0.7)

Product form further influenced texture. Patties prepared without binders (milled hydrated TVP) generally showed reduced hardness compared to chunk samples due to structural disruption during grinding and reshaping. In contrast, the addition of binders substantially increased hardness and chewiness across all formulations, reflecting enhanced matrix cohesion and load transfer within the hydrated patty system, as previously observed for binder-stabilized plant-based meat products (Webb, Li, et al., 2023).

Springiness values were relatively high across all chunk and patty samples, with limited differentiation among formulations. This lack of pronounced differences is consistent with earlier reports indicating that springiness is less sensitive to formulation changes under similar compression conditions and is strongly influenced by testing geometry and sample heterogeneity (Flory et al., 2023). Chewiness followed trends similar to hardness, as expected given its dependence on hardness, with denser and gluten-rich formulations exhibiting higher chewiness, while highly expanded, high-WHC treatments produced softer, less chewy textures.

Table 2.8. Texture Profile Analysis Results – Hardness. Different letters indicate significant differences among treatments based on appropriate post-hoc multiple comparison tests

Treatment	Hardness (N) - Chunk	Hardness (N) – Patty without Binder	Hardness (N) – Patty with Binder
FBC + PPI (low IBM, Low rpm)	4.64 ± 1.74 ^{d}	10.05 ± 1.75 ^{a}	45.75 ± 10.79 ^{a}
FBC + PPI (Med IBM, High rpm)	7.89 ± 4.26 ^{ab}	9.7 ± 1.78 ^{a}	17.25 ± 3.44 ^{c}
FBC + PPI (High IBM, High rpm)	6.65 ± 2.72 ^{abc}	10.06 ± 2.07 ^{a}	9.8 ± 3.84 ^{c}
FBC + SPI (Low IBM, High rpm)	3.74 ± 1.32 ^{d}	4.33 ± 1.59 ^{c}	27.49 ± 5.34 ^{b}
FBC + SPI (Low IBM, low rpm)	5.62 ± 1.66 ^{c}	5.45 ± 1.19 ^{bc}	26.8 ± 6.82 ^{b}
FBC + SPI (High IBM, Low rpm)	9.54 ± 2.62 ^{b}	5.13 ± 0.93 ^{bc}	23.49 ± 6.14 ^{b}
FBC + Gluten (Low IBM, High rpm)	7.28 ± 1.9 ^{c}	5.45 ± 1.35 ^{b}	15.25 ± 6.36 ^{c}

FBC + Gluten (High IBM, High rpm)	10.41 ± 5.39 [a]	6.47 ± 0.96 [b]	21.62 ± 10.91 [bc]
FBC + Gluten (High IBM, Low rpm)	8.66 ± 5.26 [ab]	6.83 ± 1.05 [b]	29.06 ± 16.73 [ab]

Table 2.9. Texture Profile Analysis Results – Springiness. Different letters indicate significant differences among treatments based on appropriate post-hoc multiple comparison tests

Treatment	Springiness % - Chunk	Springiness % – Patty without Binder	Springiness % – Patty with Binder
FBC + PPI (low IBM, Low rpm)	83.71 ± 6.73 [a]	84.25 ± 3. 64 [b]	65.19 ± 6.25 [a]
FBC + PPI (Med IBM, High rpm)	88.51 ± 5.03 [a]	88.09 ± 3.2 [ab]	47.49 ± 5.61 [c]
FBC + PPI (High IBM, High rpm)	88.42 ± 3.55 [a]	87.23 ± 2.41 [ab]	43.52 ± 9.47 [c]
FBC + SPI (Low IBM, High rpm)	89.76 ± 2.96 [a]	86.79 ± 2.87 [ab]	66.04 ± 3.97 [a]
FBC + SPI (Low IBM, low rpm)	89.58 ± 2.04 [a]	89.8 ± 1.7 [a]	69.45 ± 6.42 [a]
FBC + SPI (High IBM, Low rpm)	88.31 ± 2.38 [a]	89.56 ± 3.75 [a]	62.54 ± 9.82 [ab]
FBC + Gluten (Low IBM, High rpm)	92.52 ± 3.11 [a]	86.19 ± 1 [ab]	56.06 ± 7.66 [bc]
FBC + Gluten (High IBM, High rpm)	88.44 ± 5.6 [a]	88.45 ± 3.69 [ab]	58.38 ± 8.47 [bc]
FBC + Gluten (High IBM, Low rpm)	87.03 ± 4.05 [a]	88.64 ± 4.04 [ab]	63.47 ± 12.88 [ab]

Table 2.10. Texture Profile Analysis Results – Chewiness. Different letters indicate significant differences among treatments based on appropriate post-hoc multiple comparison tests

Treatment	Chewiness - Chunk	Chewiness – Patty without Binder	Chewiness – Patty with Binder
FBC + PPI (low IBM, Low rpm)	2.49 ± 0.72 [b]	6.22 ± 1.19 [a]	9.86 ± 4.61 [a]
FBC + PPI (Med IBM, High rpm)	5.37 ± 2.88 [ab]	6.42 ± 1.3 [a]	1.8 ± 0.9 [d]
FBC + PPI (High IBM, High rpm)	4.15 ± 1.84 [ab]	6.24 ± 1.4 [a]	0.9 ± 0.66 [d]
FBC + SPI (Low IBM, High rpm)	2.71 ± 0.98 [b]	3.07 ± 1.15 [b]	7.1 ± 1.98 [b]

FBC + SPI (Low IBM, low rpm)	4.02 ± 1.23 [ab]	3.94 ± 0.89 [b]	7.18 ± 2.33 [b]
FBC + SPI (High IBM, Low rpm)	6.40 ± 1.73 [a]	3.63 ± 0.8 [b]	4.9 ± 2.12 [c]
FBC + Gluten (Low IBM, High rpm)	4.97 ± 1.24 [a]	3.4 ± 0.88 [b]	2.38 ± 1.5 [ac]
FBC + Gluten (High IBM, High rpm)	6.46 ± 3.27 [a]	4.2 ± 0.56 [b]	4.77 ± 4.49 [c]
FBC + Gluten (High IBM, Low rpm)	4.65 ± 2.4 [ab]	4.51 ± 0.79 [b]	7.6 ± 7.39 [ab]

2.3.3.4 Visual Analysis

Visual Analysis of hydrated extrudate showed clear formulation-dependent differences in internal structure, consistent with previously reported effects of protein functionality on texturization behavior (Table 2.11). Distinct contrasts were observed among FBC + SPI, FBC + PPI, and FBC + gluten treatments in terms of porosity, layering, and fiber structure.

The FBC + SPI formulations exhibited the most porous internal structure, interconnected pores, and limited visible lamination. Similar porous morphologies have been reported for cold swelling protein systems dominated by soy and pea proteins, which possess strong gelling and film-forming abilities that promote melt extensibility and gas retention during extrusion (Flory et al., 2023; Flory and Alavi 2024). These proteins are known to form expanded matrices with high internal void volume, leading to a more cellular appearance rather than a layered fibrous structure (Webb, Dogan, et al., 2023). Although sponge-like and cavitary cross-sections have been reported at lower extrusion moisture levels in some proteins (Lin et al., 2022), the present results indicate a contrasting trend. In this study, lower IBM consistently resulted in higher bulk density across all formulations, reflecting reduced expansion and a more compact internal structure.

In contrast, FBC + gluten treatments displayed a distinctly layered and fibrous structure, with aligned lamellae and reduced open pore space. This morphology is consistent with wheat gluten, which contains gliadin and glutenin fractions capable of forming extensive intra and

intermolecular disulfide bonding. These elastic protein films favor lamination and fiber alignment rather than expansion, resulting in denser and more anisotropic structures (Flory and Alavi 2024; Flory et al., 2023). Similar laminated morphologies have been widely reported for non-cold swelling proteins and gluten-rich formulations, where thin protein layers dominate over cellular pore formation (Webb, Dogan, et al., 2023). Such layered architectures visually resemble fibrous meat-like structures but lack the open void network observed in cold swelling protein matrices.

The FBC + PPI formulations showed structural features that fell between those of SPI and gluten-based samples. Visually, these extrudates displayed a mix of partial porosity and noticeable layering. Compared to SPI, PPI-based samples were less expanded and contained fewer interconnected pores, but they were also less laminated than the gluten formulations. This intermediate appearance is consistent with previous work showing that pea protein isolate has moderate gel-forming ability, stronger than many plant proteins but weaker than soy, which can lead to mixed cellular and laminated structures depending on processing conditions (Flory et al., 2023; Webb, Dogan, et al., 2023).

Across all formulations, longitudinal sections revealed strong anisotropy aligned with the direction of material flow through the extruder, whereas transverse sections provided clearer visual separation between porous and laminated structures. This directional anisotropy is characteristic of extruded protein systems and reflects differences in phase rheology and hydration behavior of protein fractions as the material is sheared and stretched in the screws and die (Webb, Dogan, et al., 2023; Dekkers et al., 2018).

Overall, the visual analysis shows a clear structural pattern across formulations. FBC + SPI produced the most expanded and porous structure, FBC + gluten showed a dense, layered,

and fibrous structure, and FBC + PPI fell between these two extremes. These visual differences are consistent with previous studies showing that protein swelling behavior and film-forming ability strongly influence porosity, layering, and anisotropy in texturized vegetable proteins (Flory et al., 2023; Webb, Dogan, et al., 2023; Lin et al., 2022), and they align well with the formulation-dependent trends observed in bulk density, water-related properties, and texture.

Table 2.11. Macro Images of hydrated chunk final products

Final Products		Horizontal Cut	Horizontal Cut	Longitudinal Cut	Longitudinal Cut
FBC+ PPI	Low IBm, Low rpm	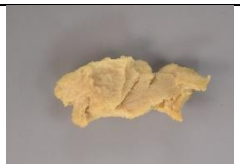	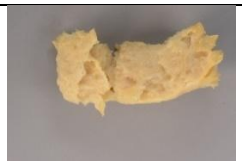	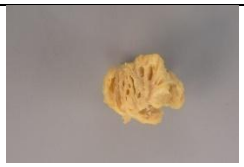	
	Med IBM, High rpm				
	High IBM, High rpm		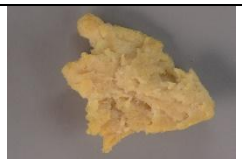	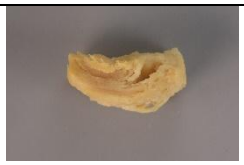	
FBC+ SPI	Low IBM,	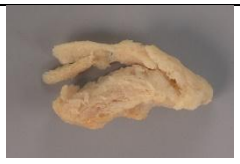			

	High rpm				
	Low IBM, Low rpm		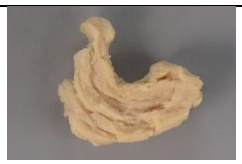		
	High IBM, Low rpm				
FBC + Gluten	Low IBm, High rpm				
	High IBM, High rpm				
	High IBM, Low rpm	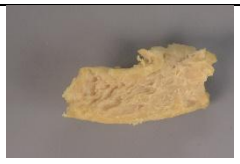			

2.3.3.5 Fibrosity Score

The treatment-level fibrosity scores showed clear differences among formulations and were consistent with the structural patterns observed in the visual analysis of the extrudates. SPI-based formulations, which exhibited more porous and expanded internal structures, generally showed lower fibrosity scores. In contrast, gluten-based samples displayed the highest fibrosity, reflecting their more layered and aligned internal structure. PPI-based treatments showed intermediate values, which align with their mixed morphology combining both porous and laminated features.

Fibrosity scores obtained from the computer vision-based (CV) and machine learning-based (ML) methods (Bagheri et al., 2026) were compared with expert visual scores (Table 2.12). The computer vision-based scores showed very limited variation across treatments and did not reflect the observed differences in structure. As a result, the correlation with expert scores was weak and slightly negative ($r=-0.24$), indicating that the unsupervised CV approach was not sensitive to treatment-level changes in fibrousness (Figure 2.13).

In contrast, the computer vision and machine learning-based (CV+ML) scores showed a strong positive correlation with expert evaluation ($r=0.95$) and closely followed the same trends across formulations (Figure 2.14). Specifically, treatments identified as highly fibrous by visual analysis and expert scoring, such as gluten-based samples, were also assigned higher scores by the CV+ML model, while more porous samples, particularly SPI-based treatments, received lower scores. This suggests that the semi-supervised CV+ML approach was able to better capture meaningful structural differences and align more closely with human perception of fibrousness. These findings are consistent with recent work showing that image-based fibrosity evaluation

can be further extended using deep neural network models trained on expert-scored plant-based meat images (Aljishi et al., 2026).

Table 2.12. Fibrosity Scores Across Treatments. Fibrosity scores were obtained from expert visual, computer vision-based, and machine learning-based evaluations.

Treatments	Expert Score	CV Score	CV+ML Score
FBC + PPI (low IBM, Low rpm)	6.56 ± 1.01	7.76 ± 0.93	6.42 ± 0.64
FBC + PPI (Med IBM, High rpm)	6.44 ± 0.88	7.62 ± 0.99	6.59 ± 0.72
FBC + PPI (High IBM, High rpm)	6.78 ± 1.39	7.66 ± 0.92	7.03 ± 0.85
FBC + SPI (Low IBM, High rpm)	6.11 ± 1.62	7.68 ± 0.94	6.34 ± 1.03
FBC + SPI (Low IBM, Low rpm)	7.11 ± 1.17	7.50 ± 1.07	6.88 ± 0.66
FBC + SPI (High IBM, Low rpm)	3.78 ± 1.99	7.44 ± 1.22	5.15 ± 1.44
FBC + Gluten (Low IBM, High rpm)	6.33 ± 1.01	7.46 ± 1.19	6.33 ± 0.48
FBC + Gluten (High IBM, High rpm)	6.67 ± 1.5	7.28 ± 1.34	6.50 ± 0.9
FBC + Gluten (High IBM, Low rpm)	7.78 ± 0.83	7.05 ± 1.6	6.92 ± 0.68

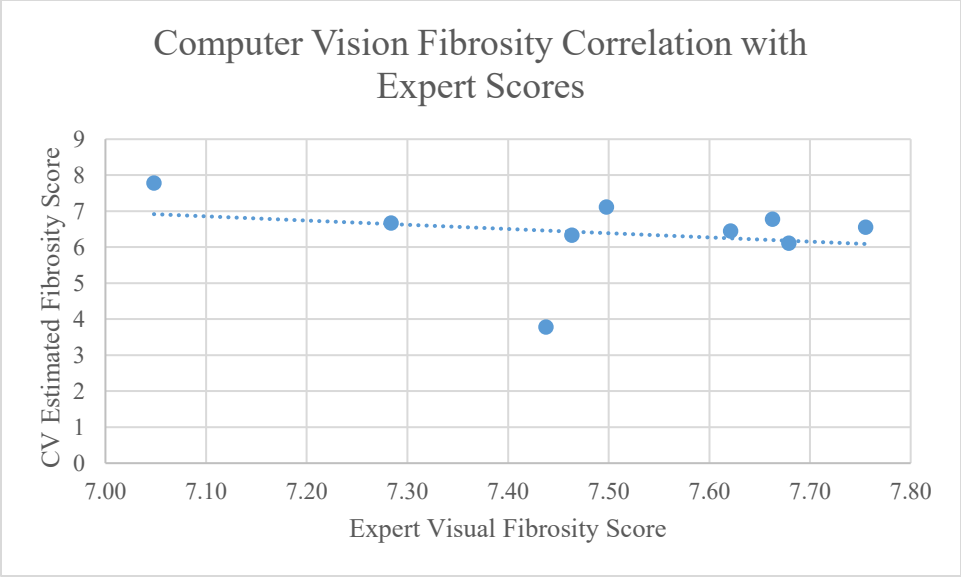

Figure 2.13. Scatter plot of computer vision-based fibrosity scores versus expert visual scores (r = - 0.24).

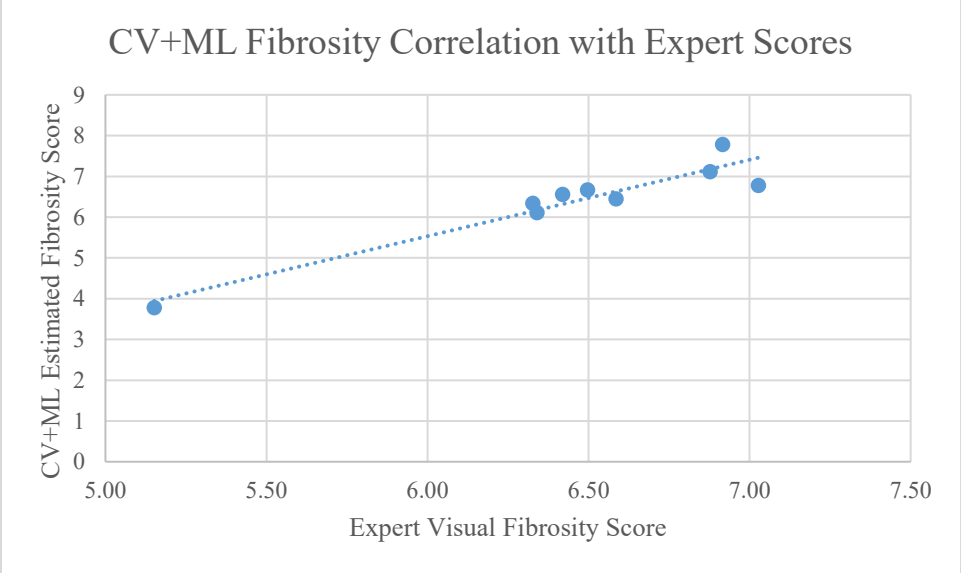

Figure 2.14. Scatter plot of computer vision + machine learning-based fibrosity scores versus expert visual scores (r = 0.95).

2.4 Conclusion

This study shows that the texture development of faba bean–based meat analogs during extrusion is driven mainly by how the proteins hydrate and swell, while processing conditions modulate these effects rather than determining them on their own. Formulations containing cold swelling proteins, particularly soy protein isolate, expanded more during extrusion and resulted in products with lower bulk density, higher water-holding capacity, and softer textures. In contrast, non-cold swelling proteins such as wheat gluten produced denser, more layered structures with greater mechanical strength, while pea protein isolate led to intermediate structural and textural characteristics.

Across all formulations, protein blends did not behave as simple combinations of their individual components. Instead, competition for water and protein–protein interactions played a central role in shaping structure development. In-barrel moisture was the dominant factor influencing melt viscosity and energy input, whereas screw speed primarily adjusted shear intensity depending on formulation. Together, these findings highlight that successful structuring of faba bean–based meat analogs relies on aligning protein functionality with extrusion conditions, and that protein swelling behavior is a key mechanistic driver of extrusion texturization.

2.5 References

Aghagholizadeh, R., & Rigi, A. A. (2025). High-moisture extrusion in plant-based meat: Challenges and emerging trends. *Journal of Food Process Engineering, 48*(4), e70107. https://doi.org/10.1111/jfpe.70107

Ali, A., & Bharali, P. (2025). The rise of plant-based meat alternatives: Challenges and perspectives. *Food Bioscience, 68*, 106640. https://doi.org/10.1016/j.fbio.2025.106640

Aljishi, A., Sheikhizadeh, S., Das, S., & Alavi, S. (2026). Estimating fibrosity scores of plant-based meat products from images: A deep neural network approach. *Foods, 15*(4), 665. https://doi.org/10.3390/foods15040665

Aslam, R., Sheikhizadeh, S., Alavi, S., Zhou, W., & Maqsood, S. (2026). Mechanistic evaluation of pea-soy protein isolate and concentrate based high moisture meat analogues: Evaluation of protein blends and extrudate quality. *Journal of Food Engineering, 406*, 112802. https://doi.org/10.1016/j.jfoodeng.2025.112802

Bagheri, A., Sheikhizadeh, S., Alavi, S., & Pourkargar, D. B. (2026). An integrated time series modeling and computer vision framework for predictive structure characterization of extruded plant-based meat products. *Artificial Intelligence in Agriculture, 16*(2), 854–872. https://doi.org/10.1016/j.aiia.2026.03.010

Bourne, M. C. (2002). Texture, viscosity, and food. *Food Texture and Viscosity*. https://doi.org/10.1016/B978-012119062-0/50001-2

Brishti, F. H., Chay, S. Y., Muhammad, K., Ismail-Fitry, M. R., Zarei, M., Karthikeyan, S., & Saari, N. (2020). Effects of drying techniques on the physicochemical, functional, thermal,

structural and rheological properties of mung bean (Vigna radiata) protein isolate powder. *Food Research International, 138*, 109783. https://doi.org/10.1016/j.foodres.2020.109783

Day, L. (2013). Proteins from land plants – Potential resources for human nutrition and food security. *Trends in Food Science & Technology, 32*(1), 25–42. https://doi.org/10.1016/j.tifs.2013.05.005

Dekkers, B. L., Boom, R. M., & van der Goot, A. J. (2018). Structuring processes for meat analogues. *Trends in Food Science & Technology, 81*, 25–36. https://doi.org/10.1016/j.tifs.2018.08.011

Fatahi, H., Claverie, J., & Poncet, S. (2022). Thermal characterization of phase change materials by differential scanning calorimetry: A review. *Applied Sciences, 12*(23), 12019. https://doi.org/10.3390/app122312019

Flory, J., & Alavi, S. (2024). Use of hydration properties of proteins to understand their functionality and tailor texture of extruded plant-based meat analogues. *Journal of Food Science, 89*(1), 245–258. https://doi.org/10.1111/1750-3841.16804

Flory, J., Xiao, R., Li, Y., Dogan, H., Talavera, M. J., & Alavi, S. (2023). Understanding protein functionality and its impact on quality of plant-based meat analogues. *Foods, 12*(17), 3232. https://doi.org/10.3390/foods12173232

Guerrero, M., Stone, A. K., Singh, R., Lui, Y. C., Koksel, F., & Nickerson, M. T. (2025). Effect of extrusion conditions on the characteristics of texturized vegetable protein from a faba bean protein mix and its application in vegan and hybrid burgers. *Foods, 14*(4), 547. https://doi.org/10.3390/foods14040547

Hong, S., Shen, Y., & Li, Y. (2022). Physicochemical and functional properties of texturized vegetable proteins and cooked patty textures: Comprehensive characterization and correlation analysis. *Foods, 11*(17), 2619. https://doi.org/10.3390/foods11172619

Kamani, M. H., Liu, J., Fitzsimons, S. M., Fenelon, M. A., & Murphy, E. G. (2024). Determining the influence of fava bean pre-processing on extractability and functional quality of protein isolates. *Food Chemistry: X, 21*, 101200. https://doi.org/10.1016/j.fochx.2024.101200

Li, S., Wei, Y., Fang, Y., Zhang, W., & Zhang, B. (2014). DSC study on the thermal properties of soybean protein isolates/corn starch mixture. *Journal of Thermal Analysis and Calorimetry, 115*(2), 1633–1638. https://doi.org/10.1007/s10973-013-3433-4

Lin, Q., Pan, L., Deng, N., Sang, M., Cai, K., Chen, C., Han, J., & Ye, A. (2022). Protein digestibility of textured-wheat-protein (TWP) -based meat analogues: (I) Effects of fibrous structure. *Food Hydrocolloids, 130*, 107694. https://doi.org/10.1016/j.foodhyd.2022.107694

Martin, C. (2016). Twin screw extruders as continuous mixers for thermal processing: A technical and historical perspective. *AAPS PharmSciTech, 17*(1), 3–19. https://doi.org/10.1208/s12249-016-0485-3

McClements, D. J., Weiss, J., Kinchla, A. J., Nolden, A. A., & Grossmann, L. (2021). Methods for testing the quality attributes of plant-based foods: Meat- and processed-meat analogs. *Foods, 10*(2), 260. https://doi.org/10.3390/foods10020260

Nishinari, K., Fang, Y., Guo, S., & Phillips, G. O. (2014). Soy proteins: A review on composition, aggregation and emulsification. *Food Hydrocolloids, 39*, 301–318. https://doi.org/10.1016/j.foodhyd.2014.01.013

O'Kane, F. E., Happe, R. P., Vereijken, J. M., Gruppen, H., & van Boekel, M. A. J. S. (2004). Heat-induced gelation of pea legumin: Comparison with soybean glycinin. *Journal of Agricultural and Food Chemistry, 52*(16), 5071–5078. https://doi.org/10.1021/jf035215h

Osen, R., Toelstede, S., Wild, F., Eisner, P., & Schweiggert-Weisz, U. (2014). High moisture extrusion cooking of pea protein isolates: Raw material characteristics, extruder responses, and texture properties. *Journal of Food Engineering, 127*, 67–74. https://doi.org/10.1016/j.jfoodeng.2013.11.023

Pietsch, V. L., Emin, M. A., & Schuchmann, H. P. (2017). Process conditions influencing wheat gluten polymerization during high moisture extrusion of meat analog products. *Journal of Food Engineering, 198*, 28–35. https://doi.org/10.1016/j.jfoodeng.2016.10.027

Plattner, B. J., Hong, S., Li, Y., Talavera, M. J., Dogan, H., Plattner, B. S., & Alavi, S. (2024). Use of pea proteins in high-moisture meat analogs: Physicochemical properties of raw formulations and their texturization using extrusion. *Foods, 13*(8), 1195. https://doi.org/10.3390/foods13081195

Ribeiro, G., Piñero, M.-Y., Parle, F., Blanco, B., & Roman, L. (2024). Optimizing screw speed and barrel temperature for textural and nutritional improvement of soy-based high-moisture extrudates. *Foods, 13*(11), 1748. https://doi.org/10.3390/foods13111748

Samard, S., & Ryu, G.-H. (2019). Physicochemical and functional characteristics of plant protein-based meat analogs. *Journal of Food Processing and Preservation, 43*(10), e14123. https://doi.org/10.1111/jfpp.14123

Shewry, P. R., & Tatham, A. S. (1997). Disulphide bonds in wheat gluten proteins. *Journal of Cereal Science, 25*(3), 207–227. https://doi.org/10.1006/jcrs.1996.0100

Stone, A. K., Karalash, A., Tyler, R. T., Warkentin, T. D., & Nickerson, M. T. (2015). Functional attributes of pea protein isolates prepared using different extraction methods and cultivars. *Food Research International, Grain Legumes - Science, Technology and Impacts on Human Health, 76*, 31–38. https://doi.org/10.1016/j.foodres.2014.11.017

Thomsen, J., Rao, J., & Chen, B. (2025). Faba bean protein: Chemical composition, functionality, volatile compounds, and applications in food production. *Trends in Food Science & Technology, 156*, 104863. https://doi.org/10.1016/j.tifs.2024.104863

Toldrà, M., Parés, D., Barnés-Calle, C., Gou, P., & Fulladosa, E. (2025). Techno-functional and physico-chemical properties of high moisture extrudates from faba bean (Vicia faba) protein concentrate using different extrusion conditions. *LWT, 225*, 117898. https://doi.org/10.1016/j.lwt.2025.117898

van Esbroeck, T., Sala, G., Stieger, M., & Scholten, E. (2024). Effect of structural characteristics on functional properties of textured vegetable proteins. *Food Hydrocolloids, 149*, 109529. https://doi.org/10.1016/j.foodhyd.2023.109529

Vogelsang-O'Dwyer, M., Petersen, I. L., Joehnke, M. S., Sørensen, J. C., Bez, J., Detzel, A., Busch, M., Krueger, M., O'Mahony, J. A., Arendt, E. K., & Zannini, E. (2020). Comparison of faba bean protein ingredients produced using dry fractionation and isoelectric precipitation: Techno-functional, nutritional and environmental performance. *Foods, 9*(3), 322. https://doi.org/10.3390/foods9030322

Wang, J.-S., Zhao, M.-M., Yang, X.-Q., Jiang, Y.-M., & Chun, C. (2007). Gelation behavior of wheat gluten by heat treatment followed by transglutaminase cross-linking reaction. *Food Hydrocolloids, 21*(2), 174–179. https://doi.org/10.1016/j.foodhyd.2006.03.006

Webb, D., Dogan, H., Li, Y., & Alavi, S. (2023). Physico-chemical properties and texturization of pea, wheat and soy proteins using extrusion and their application in plant-based meat. *Foods, 12*(8), 1586. https://doi.org/10.3390/foods12081586

Webb, D., Li, Y., & Alavi, S. (2023). Chemical and physicochemical features of common plant proteins and their extrudates for use in plant-based meat. *Trends in Food Science & Technology, 131*, 129–138. https://doi.org/10.1016/j.tifs.2022.11.006

Webb, D., Plattner, B. J., Donald, E., Funk, D., Plattner, B. S., & Alavi, S. (2020). Role of chickpea flour in texturization of extruded pea protein. *Journal of Food Science, 85*(12), 4180–4187. https://doi.org/10.1111/1750-3841.15531

Xiao, R., Flory, J., Alavi, S., & Li, Y. (2025). Physicochemical and functional properties of plant proteins before and after extrusion texturization. *Food Hydrocolloids, 163*, 111119. https://doi.org/10.1016/j.foodhyd.2025.111119

Zadeike, D., Zvirdauskiene, R., & Basinskiene, L. (2025). Gluten functionality modification: The effect of enzymes and ultrasound on the structure of the gliadin–glutenin complex and gelling properties. *Molecules, 30*(14), 3036. https://doi.org/10.3390/molecules30143036

Chapter 3 - Extrusion Processing of Lentil-Based TVP: Impact of Soy and Pea Protein Replacement on Product Structure and Texture

Abstract

Driven by demand for sustainable meat alternatives, this research investigated how protein type, functionality and extrusion processing conditions influence the structure, texture and performance of plant-based meat produced using low-moisture extrusion. Textured vegetable protein (TVP) based on lentil concentrate, in combination with various supplemental plant proteins, was the focus of this study.

Before evaluating the different process technologies and plant-based meat products, the functionality of various plant proteins was characterized because it strongly influenced structure development and product quality. Based on water absorption capacity (WAC) and rapid visco-analysis (RVA), soy protein isolate (SPI) was classified as a cold swelling protein due to its high WAC (5.48 g/g) and low-temperature peak viscosity (30 °C). In contrast, pea protein isolate (PPI), wheat gluten (WG), and lentil protein concentrate (LPC) behaved as non-cold swelling ingredients, showing lower hydration and/or requiring higher temperatures to develop viscosity. Cold swelling proteins generally lead to more viscous melts and also exhibit high cross-linking and greater film-forming ability, which leads to more expanded and porous TVP structures; whereas non-cold swelling proteins are more often associated with denser, more fibrous products. These functional differences helped explain variation in processing behavior, texture and final structure of lentil-based TVP.

LPC paired with different plant protein sources was processed using low-moisture extrusion and the impact of screw speeds and in-barrel moisture (IBM) on resultant TVP products was studied. LPC was blended with SPI or PPI to obtain two distinct formulations. Specific mechanical energy (SME) ranged from 660 to 805 kJ/kg. The formulations containing SPI generally had the highest SME because of their high viscosity during extrusion, followed by PPI. Bulk density of TVP products ranged from 120.7 to 266.8 g/L. SPI produced more porous, lower-density structures, whereas PPI produced denser, more fibrous products; bulk density was negatively correlated with water holding capacity ($r = -0.86$). TVP texture data, such as hardness and other attributes, were found to be closely related to bulk density and WHC. These results were in alignment with the protein functionality hypothesis that was based on their cold swelling and non-cold swelling properties. Besides protein functionality, extrusion behavior and TVP structure and texture were also affected by screw speed and IBM. Higher IBM or lower screw speed reduced SME, which in turn impacted product bulk density and fibrosity. A prior developed image analysis algorithm based on a combination of computer vision (CV) and machine learning (ML) provided fibrosity scores showed strong positive correlations with expert visual scores for lentil-based TVP products ($r = 0.96$), indicating close agreement between objective image processing and subjective expert assessments of fibrous structure of TVP products.

This research showed that the quality of TVP processed using low moisture extrusion depended on the combination of protein functionality and processing. Differences in hydration, viscosity, temperature, screw speed and formulation shaped processing, structure, and texture, providing an improved theoretical and scientific framework and practical guidance for designing better quality plant-based meat products.

3.1 Introduction

Plant-based alternatives are gaining momentum as more consumers reduce or avoid animal-based foods for environmental, ethical, and health reasons, and the success of these products depends strongly on achieving parity in texture and flavor with conventional meat (Boukid et al., 2022; Herz et al., 2021). Textured vegetable protein (TVP) is one of the main building blocks used to create meat analogues (such as patties, nuggets, sausages), and it is typically produced by structuring plant protein and water into a porous, shelf-stable material (low-moisture TVP) that becomes chewy and juicy after rehydration (Baune et al., 2022; Singh et al., 2024). Because texture formation depends on how proteins hydrate, unfold, interact, and set during extrusion, researchers and product developers increasingly use protein blending strategies (e.g., soy, wheat, pea, and pulses) to expand the range of achievable textures and improve overall product quality (Baune et al., 2022; Flory et al., 2023; Ma et al., 2022). However, it is also well recognized that comparing and predicting texture outcomes across new protein systems is difficult, and there remains a need for practical, standardized ways to evaluate raw material functionality and connect it to extrusion behavior and final product structure (Flory et al., 2023a; Grabowska et al., 2016; Mattice and Marangoni 2020; Yuliarti, Kiat Kovis, and Yi 2021). One promising framework is to characterize proteins based on hydration-related functionality (such as water absorption, gelling behavior, viscosity development, and flow temperature) and relate these properties to the internal architecture and texture of extruded products. Prior work indicates that proteins with higher water absorption and cold swelling behavior tend to show greater crosslinking potential and produce more porous, less layered TVP structures, while low cold swelling or non-cold swelling proteins tend to form denser, more

layered structures (Flory et al., 2023). This functional distinction is relevant as the industry looks beyond soy, given limitations such as allergen concerns and other constraints, and explores pulse proteins (including lentil and pea) as scalable alternatives with strong nutritional and sustainability value (Barbana and Boye 2013; Kaale, Siddiq, and Hooper 2023; Ma et al., 2022). Lentil, in particular, is increasingly recognized as a nutrient-dense pulse with growing production and broad application potential, making lentil-based protein products an attractive target for developing next-generation plant-based meat ingredients (Barbana and Boye 2013; Kaale et al., 2023).

In this study, lentil-based TVP was developed using lentil protein concentrate (LPC) as the base ingredient, while soy protein isolate (SPI) was progressively replaced with pea protein isolate (PPI) to investigate how protein substitution influences extrusion behavior and final product structure and texture. Although previous studies have shown that cold swelling and non-cold swelling proteins can produce different structures and textures during extrusion, it is still unclear whether these functional behaviors are maintained in blends. Limited information is available on how progressively replacing one protein with another in an LPC-based formulation changes the relationship between raw material functionality, extrusion behavior, and final product properties.

The aim of this research was to determine how replacing SPI with PPI in an LPC-based formulation changes raw material hydration and thermal flow behavior relevant to extrusion, as well as extrusion responses and resulting product structure and texture. The research goal was to link the functional properties of the protein blends, including their hydration and thermal flow behavior, to the development of structure and texture during extrusion.

Based on the functional framework distinguishing cold swelling versus non-cold swelling proteins, and the established links between internal structure, bulk density, hydration, and the mechanical behavior of TVP, it was hypothesized that progressively replacing SPI with PPI would shift the overall formulation from the functional behavior associated with SPI toward that associated with PPI. Accordingly, SPI-rich formulations were expected to show stronger cold swelling hydration behavior and produce more expanded, porous structures with lower bulk density, resulting in higher water holding capacity and softer texture. In contrast, PPI-rich formulations were expected to form denser, more layered structures with higher bulk density, lower water holding capacity, and firmer texture (van Esbroeck et al., 2024; Flory et al., 2023a).

By examining both raw material functionality and extrusion outcomes, this study helps explain how formulation affects structure and texture development in lentil-based TVP, supporting improved design of plant-based meats.

3.2 Materials and Methods

3.2.1 Ingredients and formulation

In this study, lentil protein concentrate (LPC) was used as the base protein ingredient in all formulations for the development of plant-based meat. LPC (VITESSENC Pulse 2550 Protein; Ingredion Inc., Westchester, IL, USA) contains 55% protein on a dry basis and was selected due to its nutritional value and increasing interest in lentil-based protein products for meat analogue applications (Kaale et al., 2023). Four formulations (F1-F4) were designed, each containing 42% LPC, while varying the proportions of additional protein sources to examine their combined effects on formulation behavior.

Soy protein isolate (SPI; Profam 974, Archer Daniels Midland Company, Abilene, KS, USA; 90% protein db) and pea protein isolate (PPI; Puris Pea 870, PURIS Foods, Minneapolis, MN, USA; 80% protein db) were incorporated at different ratios across formulations. Vital wheat gluten (Royal Ingredients Group B.V., Alkmaar, The Netherlands; 82% protein db) was included at a constant level (23%) in all formulations to support structure formation and textural development during extrusion processing (Jia et al., 2020).

The first contained a higher proportion of SPI (35%) and no PPI, whereas F4 represented the opposite end of the formulation range, with the highest PPI content (35%) and no SPI. Formulations F2 and F3 served as intermediate blends, with gradually decreasing SPI and increasing PPI levels. This formulation strategy allowed for controlled evaluation of how switching SPI with PPI, while maintaining a constant LPC and gluten level, influences the processing performance. A similar protein blending approach has been reported in previous studies (Webb et al., 2020), highlighting the role of mixed proteins in modulating texture and functionality in extruded plant-based products.

Based on the protein contents provided by the manufacturers, the calculated net protein content of the formulations ranged from 70.0% to 73.5% (Table 3.1). F1 exhibited the highest protein content (73.5%), followed by F2 (72.5%), F3 (71.0%), and F4 (70.0%).

Formulations F1 (LPC + 35% SPI) and F4 (LPC + 35% PPI) were prepared in 250 lb. batches and processed using pilot-scale extrusion. In contrast, formulations F2 (LPC + 25% SPI + 10% PPI) and F3 (LPC + 10% SPI + 25% PPI) were prepared at laboratory scale and processed using a lab-scale extruder to conduct additional complementary tests. This approach allowed the middle formulations to be tested efficiently, while pilot-scale runs were used for the two end-point blends with the highest SPI or highest PPI.

The composition of each formulation and the net protein content are summarized in Table 3.1.

Table 3.1. Ingredient composition of lentil-based formulations

Protein Sources (%)	F1	F2	F3	F4
Lentil Protein Concentrate	42	42	42	42
Soy Protein Isolate	35	25	10	-
Pea Protein Isolate	-	10	25	35
Gluten	23	23	23	23
Net protein content %	73.5	72.5	71	70

3.2.2 Raw Material Analysis

3.2.2.1 Moisture Content

The moisture content of raw ingredients was assessed following the AACC 44-19.01 method. Duplicate samples, each weighing approximately 2 g, underwent a drying process at 135°C for 2 hours as per the described procedure.

3.2.2.2 Water Absorption Capacity (WAC)

WAC was determined according to the method described by Webb et al. (2023). Briefly, 2.5 g of each sample was placed into centrifuge tubes, and 30 mL of deionized water was added. The mixtures were vortexed for 30 s to ensure proper dispersion and then allowed to stand at room temperature for 30 min, with intermittent agitation during this period. Samples were subsequently centrifuged at 3000 × g for 30 min, after which the supernatant was carefully decanted. The WAC was calculated as grams of water retained per gram of dry sample.

WAC was calculated using the following equation:

$$WAC\ \left(\frac{g_{water}}{g_{protein}}\right) = \frac{W_f - W_i}{W_i} \quad (3.1)$$

Where W_f is the weight of the sediment, and W_i is the initial weight of the sample.

3.2.2.3 Least Gelation Concentration (LGC)

LGC was determined following the method described by Sathe and Salunkhe (1981), with slight modifications. Protein slurries were prepared by dispersing the samples in 10 ml distilled water to obtain concentrations ranging from 8% to 20% (w/v), into a clean, dry glass test tube and manually mixed to ensure uniform hydration. The test tubes were then heated in a boiling water bath (90-100 °C) for 1 h, followed by cooling under running water for 10 min. Subsequently, the samples were refrigerated at 4 °C for 2 h. The LGC was defined as the lowest protein concentration at which the gel remained intact and did not flow or slip upon inversion of the test tube.

3.2.2.4 Rapid Visco Analyzer (RVA)

The thermal viscosity behavior of individual protein ingredients and formulations was characterized using a Rapid Visco Analyzer (RVA 4800, Perten Instruments). Measurements were conducted in accordance with the general framework of AACC Method 76-21.02 (STD1). The RVA was used to monitor viscosity changes as a function of time and temperature, allowing assessment of both cold and non-cold swelling behavior. These viscosity transitions provide insight into functional changes relevant to extrusion processing (Osen et al., 2014).

For each analysis, approximately 3.5 g of sample (dry basis) was weighed, with the exact mass adjusted based on the inherent moisture content of each ingredient or formulation to achieve a 14% (w/v) solids concentration. Samples were dispersed in 25 mL of distilled water

and loaded into the RVA canister. The slurry was initially equilibrated at 30 °C under high shear (960 rpm) for 10 s, followed by a holding period of 50 s at the same temperature. The sample was then heated to 95 °C under reduced shear (160 rpm), held at 95 °C for 2 min and 30 seconds, and subsequently cooled back to 30 °C between 7:12 and 11:00 min and finally held at 30 °C from 11:00 to 13:00 min.

Viscosity was recorded continuously throughout the heating and cooling cycle to generate thermal viscosity profiles for each sample. All measurements were performed in triplicate.

3.2.2.5 Phase Transition Analysis (PTA)

PTA was employed to characterize the thermal softening and flow behavior of the protein-based formulations and was performed following the procedures described by Webb et al. (2020) and Webb, Dogan, et al. (2023), with minor modifications. Measurements were conducted using a Phase Transition Analyzer (Wenger Manufacturing) to determine the softening temperature and flow point temperature of both raw and moderately extruded materials.

For PTA of raw materials, samples were adjusted to 24% moisture content. Approximately 2 g of each formulation was loaded into the PTA chamber and compressed using a blank die to 120 bar for 15 s. The sample was then subjected to a constant pressure of 100 bar while being heated at a rate of 8 °C/min, starting from an initial temperature of approximately 5-7 °C. The softening point was identified during this heating phase. Subsequently, a 2 mm capillary die was installed under the sample, and the material was again compressed to 120 bar for 15 s, followed by 100 bar during continued heating. The onset of material flow through the

capillary die was detected by a change in compressing rod displacement, and the corresponding temperature was recorded as the flow point temperature.

To evaluate the effect of moderate thermo-mechanical shear on flow behavior, the same formulations were processed by lab-scale extrusion prior to PTA testing. Extrusion was carried out using a Micro-18 twin-screw extruder (American Leistritz, Somerville, NJ, USA), selected to impart sufficient shear to initiate protein crosslinking without inducing extensive macromolecular degradation typically associated with high energy pilot-scale extrusion. Before extrusion, raw materials were adjusted to 28% moisture content and processed at a throughput of 2 kg/h and a screw speed of 487 rpm. Barrel temperature zones were set to 30, 40, 55, 95, 100, and 110 °C. A circular die with a diameter of 3.5 mm was used to shape the extrudates.

The extruded material was collected without drying, ground to a particle size of 250 μm using a Wiley mill, rehydrated to 24% moisture content, and analyzed by PTA using the same parameters applied to the raw materials. Comparing flow point temperatures before and after moderate shear treatment provided insight into the development of protein networking before pilot-scale extrusion.

All four formulations (LPC + 35% SPI, LPC + 35% PPI, LPC + 25% SPI + 10% PPI, and LPC + 10% SPI + 25% PPI) were evaluated under both raw and extruded conditions. Each PTA measurement was performed in triplicate.

3.2.3 Extrusion Parameters and Calculations

Before extrusion, the dry ingredient blends were prepared in a double-ribbon blender (Wenger Manufacturing, Sabetha, KS, USA) and mixed for 5 min to obtain a uniform mixture. The blends (LPC + 35% SPI and LPC + 35% PPI) were then processed using a pilot-scale

corotating twin screw extruder (TX-52, Wenger Manufacturing, Sabetha, KS, USA) equipped with 52-mm screws (L/D = 19.5). The extruder included four temperature-controlled barrel zones. From the feeder to the die, the zone set temperatures were 30°C, 50°C, 80°C, and 110°C. A constant dry feed rate of 50 kg/h was used for all runs, and screw speed was adjusted within 306 - 456 rpm depending on the treatment.

A high-shear screw configuration was selected to promote protein texturization, following the general approach reported by Webb et al. (2020). The screw profile included cut-flight conveying elements as well as forward and reverse kneading blocks to increase barrel fill, limit forward conveying, and intensify mixing of the hydrated proteins (see Figure 2.1). To further increase shear near the die, a ¼-inch venturi die was installed upstream of the final die outlets, and the melt stream was then directed into two ¼-inch outlet dies (see Figure 2.2). The extrudate was cut at the die using a three-knife rotating cutter.

Moisture was controlled by injecting water into the preconditioner (approximately 9 kg/h for all treatments) and by adding additional water directly into the extruder barrel (6.2 - 15.3 kg/h, depending on the treatment). In-barrel moisture (IBM, % wet basis) was calculated as:

$$IBM\ (\%wb) = \frac{(m_f \times (x_{wf}) + m_{ps} + m_{pw} + m_{es} + m_{ew})}{m_f + m_{ps} + m_{pw} + m_{es} + m_{ew}} \quad (3.2)$$

Where m_f is the dry feed rate, X_{wf} is the moisture content of the dry feed material (expressed as wet basis fraction), and m_{ps} and m_{pw} are the steam and water injection rate into the preconditioner; also, the m_{es} and mew are the steam and water injection rate into the extruder (in kg/h), respectively.

Steam was not applied in any treatment (m_{ps}, m_{es} = 0). Temperatures were recorded at the preconditioner discharge, at each barrel head, and immediately before the die. Die pressure was monitored using an analog gauge.

For the experimental plan, each formulation was run under multiple combinations of IBM and screw speed. Three IBM-screw speed conditions were set for each formulation, resulting in a total of six extrusion treatments across the study.

Two product streams were collected for each treatment. One portion of the extrudate was conveyed to a dual-pass dryer (Series 4800, Wenger Manufacturing) and dried at 113°C for 14 min, followed by 5 min of ambient cooling, to produce dried chunk samples. The remaining portion was diverted before drying and milled using a hammer mill (Fitzpatrick Co., Westwood, MA). This wet-milled material was packaged and stored frozen for later patty preparation and structural analyses.

Specific mechanical energy (SME) was used to describe the mechanical energy input delivered to the material (dry-feed basis) by the screws, which is closely linked to melt viscosity and the extent of texturization during processing. SME (kJ/kg) was calculated as:

$$Specific\ Mechanical\ Energy\ \left(\frac{kJ}{kg}\right) = \frac{W - W_0}{m} \quad (3.3)$$

where W is motor power reading in kW, W_0 is the no-load motor power reading, and m is mass flow rate in kg/sec.

A data acquisition system continuously recorded processing variables at a 1-s sampling rate. Logged parameters included downspot temperature (material temperature at preconditioner discharge), barrel zone temperatures, die temperature, bin feeder speed (rpm), preconditioner cylinder speed (rpm), motor load, screw speed (rpm), knife speed (rpm), water addition rates to the preconditioner and extruder, and motor power (kW).

Bulk density was measured during extrusion by filling a standardized one-liter container with extrudate and recording its mass. This quick check was used as an indicator of product

expansion and overall structure development during processing. Lower bulk density generally reflected greater expansion and a lighter, more porous texture.

3.2.4 Extrudate Analysis

3.2.4.1 Bulk Density

Bulk density, measured in grams per liter, was determined by filling a one-liter cup with extrudate and recording its mass. Bulk density serves as a rapid means to assess the extent of expansion and texturization. A lower bulk density indicates more expansion, resulting in a porous structure in the final product.

3.2.4.2 Water Holding Capacity (WHC)

WHC is related to bulk density and reflects how extrudates can absorb and retain water. To measure WHC, 15 g of both whole dried extrudates and milled samples were soaked in excess water for 20 minutes at room temperature. The samples were then drained and placed on a metal mesh screen for 5 minutes to remove excess water (Webb et al., 2020). Each measurement was conducted in five replicates. WHC was calculated based on the difference between the sample mass before and after hydration using the equation below:

$$WHC = \frac{m_{wet} - m_{dry}}{m_{dry}} \quad (3.4)$$

3.2.4.3 Texture Profile Analysis (TPA)

TPA was used to evaluate the mechanical texture properties of the extruded products. A two-cycle compression test was applied to mimic the chewing process and to obtain force-time

curves from which textural parameters were calculated (Bourne, 2002). The primary parameters evaluated were hardness, springiness, and chewiness.

All TPA measurements were performed using a TA-XT2 Texture Analyzer (Texture Technologies Corp., Scarsdale, NY, USA) following the general procedures described by (Webb et al., 2020). A cylindrical compression probe with a diameter of 25 mm was used for all tests. Samples were compressed twice to 50% of their original height with a trigger force of 5 g. The pre-test and test speeds were set to 1 mm/s, while the post-test speed was set to 5 mm/s. Hardness was defined as the maximum force recorded during the first compression cycle. Springiness was calculated as the ratio of the recovered distance between the first and second compressions. Chewiness was calculated as the product of hardness and springiness multiplied by the ratio of the area under the second compression curve to that of the first (Bourne 2002; McClements et al., 2021). Ten replicates were analyzed for each sample.

TPA was conducted on three sample types: hydrated textured vegetable protein (TVP) chunks, uncooked patties prepared from rehydrated milled TVP without binders, and cooked patties formulated with binders.

For TVP chunks, dried samples were fully hydrated in tap water at room temperature for 20 min. Excess surface water was removed by draining for 5 min, after which the hydrated chunks were analyzed under the TPA conditions described above.

For patties prepared without binders, milled TVP was rehydrated in tap water for 20 min and then drained in a sieve for 5 min to remove excess water. The hydrated material was shaped into patties with a diameter of 50 mm and a thickness of 10 mm, and texture measurements were performed using the same TPA settings.

For patties prepared with binders, milled TVP was mixed with the additional ingredients listed in Table 3.2. Each patty had a total mass of 91.5 g and was formed using a patty press to a uniform thickness of 10 mm. Patties were cooked on a preheated griddle without added oil for approximately 5 min until an internal temperature of 71 °C was reached. For texture analysis, a 50 mm diameter core was taken from the center of each cooked patty and analyzed under the same TPA conditions.

Table 3.2. Patty formulation used for texture analysis of lentil-based TVP

Ingredient	Amount %	Manufacturer
Soy Sauce	3.00	Conagra Brands Canada Inc., Boisbriand, Quebec, Canada
Maggi Liquid Flavoring	0.30	Nestlé USA, Inc., Arlington, VA, USA
Worcester	0.33	The Kraft Heinz Company, Chicago, IL, USA
Liquid Smoke	0.06	The Colgin Companies, Dallas, TX, USA
Water	55.06	Municipal tap water, Manhattan, KS, USA
Texturized Vegetable Protein	24.64	-
Dry seasoning mix	2.22	o Beet Powder: The Dojo, LLC (Kate Naturals), Fountain Valley, CA, USA o Yeast flakes: Hoosier Hill Farm LLC (Saco Foods), Middleton, WI, USA o Porcini powder: Fresh & Wild Specialty Foods, Vancouver, WA, USA o Garlic, Onion, Pepper, Italian seasoning powder: Walmart Inc., Bentonville, AR, USA
Faba Bean Protein	7.41	Know-How Foods, Faribault, MN, USA
Methylcellulose HV	1.49	Modernist Pantry, LLC, Eliot, ME, USA
Coconut Oil	2.75	Amazon.com Services LLC, Seattle, WA, USA
Vegetable Oil	2.75	Associated Wholesale Grocers, Inc., Kansas City, KS, USA

3.2.4.4 Visual Analysis

The internal structure of the extruded textured vegetable protein products was examined using high-resolution macro imaging. Images were captured with a Nikon Z 7II digital camera fitted with a 105 mm NIKKOR Z macro lens and a Godox MF-R76N TTL macro ring flash. A Kaiser RS1 copy stand and an 18% grey card were used to maintain consistent lighting and color balance across all images. Image acquisition was performed using Capture One software.

For each treatment, 68 TVP pieces were randomly selected from time-based production series (four pieces per 17 series). Before imaging, dried TVP chunks were rehydrated in tap water for 30 min, drained for 5 min, and then cut longitudinally to expose the internal structure for visual evaluation.

3.2.4.5 Fibrosity Score

Fibrosity was also evaluated using image-based texture scores derived from a developed framework for analyzing extruded plant-based meat products. This framework included two approaches: an unsupervised computer vision (CV) method that quantified fibrousness directly from cross-sectional images based on structural features, and a semi-supervised machine learning (CV+ML) method that improved the scoring by incorporating expert-labeled data.

In this study, these image-derived fibrosity scores were used as complementary quantitative indicators of structure and were compared with expert visual scores to determine whether the automated approaches captured similar differences in fibrousness across treatments (Bagheri et al., 2026).

3.2.5 Statistical Analysis

Statistical analyses were conducted using one-way ANOVA to compare treatment effects. Variance homogeneity was evaluated with Levene's test. For datasets meeting the equal-variance assumption, a standard one-way ANOVA was performed, followed by Tukey's HSD post-hoc test. When this assumption was not satisfied, Welch's one-way ANOVA was applied in conjunction with Games-Howell post-hoc comparisons. Differences were considered statistically significant at $p < 0.05$.

3.3 Results and Discussion

3.3.1 Raw Material Characteristics

3.3.1.1 Water Absorption Capacity (WAC)

Water absorption characteristics play an important role in improving both food formulation and processing parameters, particularly in manufacturing processes that involve controlled water addition, such as extrusion cooking (De Angelis et al., 2023). The observed differences in WAC among the protein ingredients reflect variations in protein structure, polarity, and degree of denaturation. Water absorption is primarily governed by the availability of polar sites capable of interacting with water molecules, as well as protein unfolding, which exposes additional hydrophilic residues (Osen et al., 2014).

As shown in Figure 3.1, significant differences in WAC were observed among the protein ingredients and blends. The high WAC of SPI observed in this study (5.48 ± 0.003 g/g) exceeds values reported by Brishti et al. (2017) (3 g/g), but is consistent with reports showing that soy

protein functionality is highly sensitive to processing history and protein denaturation. Heat induced unfolding has been shown to increase the number of accessible polar sites, thereby enhancing water absorption capacity. Similar high WAC values for soy-based formulations have also been reported by Aslam et al. (2026) where soy protein exhibited greater water absorption than pea protein-based formulations.

PPI exhibited a moderate WAC (2.86 ± 0.056 g/g), comparable to the value reported by (Tang et al., 2021) (3.5 g/g). Previous studies have demonstrated a positive relationship between heat-induced denaturation and water absorption in pea protein isolates (Sumner, Nielsen, and Youngs 1981), suggesting that differences in drying or extraction conditions may account for the slight discrepancies between studies.

LPC showed a relatively low WAC (1.15 ± 0.048 g/g), which aligns closely with values reported for dry-fractionated red lentil concentrates (0.9 - 1.07 g/g) by Pulivarthi et al. (2025). The low WAC of LPC compared to isolates likely reflects its lower protein purity and reduced exposure of hydrophilic residues due to minimal processing. In contrast, lentil protein isolates have been reported to exhibit substantially higher WAC values (up to 3.66 g/g), highlighting the strong influence of extraction method on functional properties.

Vital wheat gluten exhibited WAC values (1.32 ± 0.003 g/g) within the range reported by Schopf et al. (2021) (1.17 - 1.90 g/g), consistent with its relatively compact, elastic protein network and limited availability of polar binding sites.

Blending LPC with 35% SPI significantly enhanced water absorption capacity (2.38 ± 0.050 g/g), suggesting a synergistic effect driven by the highly hydrophilic nature of soy proteins. The increase in WAC for the LPC + 35% SPI blend indicates that soy protein can partially compensate for the lower hydration capacity of lentil proteins. When SPI content was

reduced and partially replaced with pea protein, intermediate WAC values were observed. Specifically, the LPC + 25% SPI + 10% PPI formulation exhibited a WAC of 1.78 ± 0.022 g/g, while further decreasing SPI to 10% and increasing PPI to 25% resulted in a WAC of 1.52 ± 0.035 g/g, reflecting a progressive decline in hydration capacity with decreasing soy protein content. In contrast, the LPC + 35% PPI blend showed only a modest improvement in WAC (1.48 ± 0.007 g/g) relative to LPC alone, consistent with the lower intrinsic WAC of pea protein compared to soy.

These results support previous findings that protein functionality is influenced by amino acid composition, polarity, subunit structure, and processing history (Hong, Shen, and Li 2022).

The hydration behavior of protein ingredients has been used to distinguish cold swelling and non-cold swelling proteins. Flory et al. (2023) proposed that materials exhibiting high water uptake (WAC > 4 g/g) demonstrate cold swelling behavior, whereas lower values indicate non-cold swelling characteristics or limited hydration under ambient conditions. In the present study, SPI suggests greater cold swelling potential. In contrast, the low WAC values observed for LPC and gluten indicate more restricted hydration behavior, consistent with proteins that require thermal or mechanical energy to enhance water uptake.

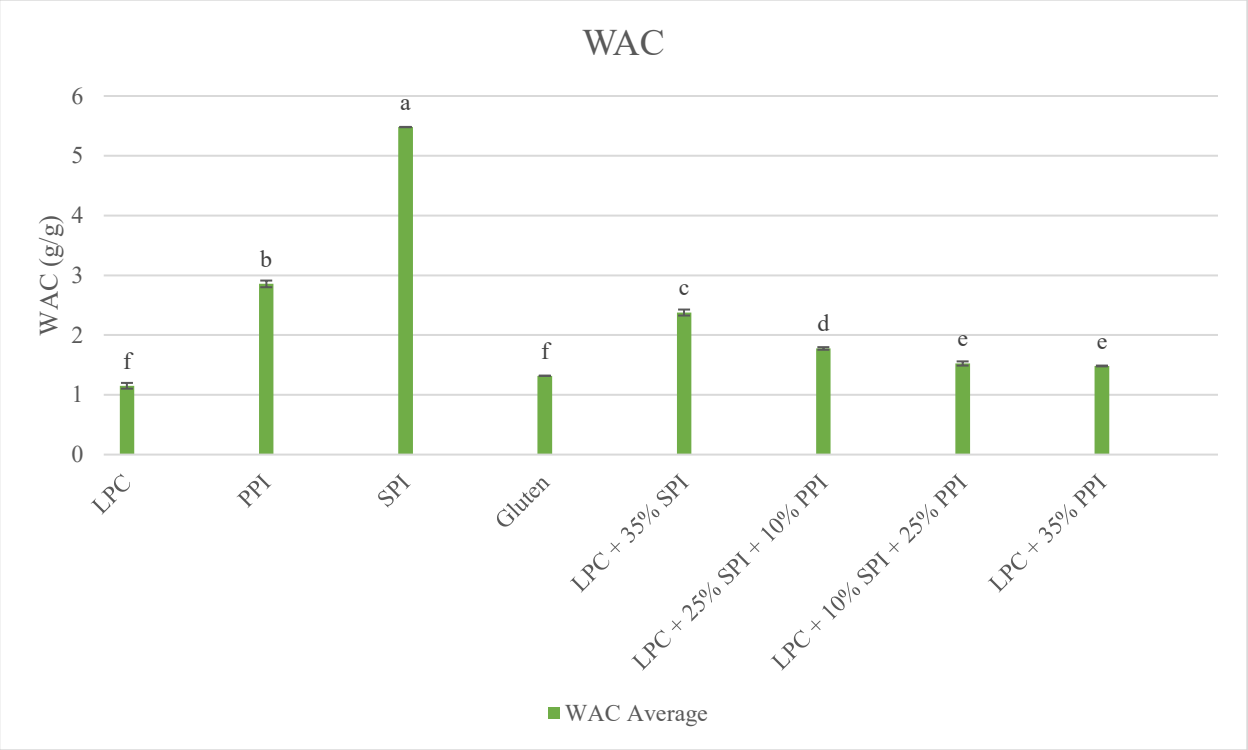

Figure 3.1. Water Absorption Capacity Results. Bars represent mean ± SD (n = 3). Different letters indicate significant differences among samples according to Tukey's post hoc test ($p < 0.05$)

3.3.1.2 Least Gelation Concentration (LGC)

Gelation of food proteins is associated with the formation of a three-dimensional crosslinked network of unfolded protein molecules capable of entrapping water (Brishti et al., 2017). The LGC is commonly used as an index of gelling ability, with lower values indicating a greater capacity to form a self-supporting gel (Boye et al., 2010). Protein gelation typically occurs when heating above the denaturation temperature causes unfolding, followed by aggregation during cooling, driven primarily by hydrophobic interactions and, in some cases, disulfide bond formation (Jarpa-Parra 2018).

LGC of the protein ingredients and lentil-based blends is shown in Figure 3. Among the single protein sources, wheat gluten exhibited the lowest LGC (12%, w/v), indicating the

strongest gel-forming ability, followed by SPI with an LGC of 14% w/v. In contrast, PPI showed the highest LGC (18% w/v), reflecting the weakest gelation capacity. LPC presented an intermediate LGC of 16% w/v. Both lentil-soy and lentil-pea blends exhibited an LGC of 16%, identical to that of LPC.

Pulse proteins, such as lentil and pea, generally exhibit weaker gelation behavior compared to soy, and reported LGC values for lentil proteins range from 8 to 14%, depending on the extraction method and composition (Jarpa-Parra 2018). The higher LGC observed here for LPC (16%) suggests limited network formation, possibly due to lower protein purity and reduced availability of reactive hydrophobic and sulfhydryl groups.

The higher LGC of PPI (18%) relative to SPI (14%) agrees with previous findings by Ma et al. (2022) who reported that pea protein required higher concentrations than soy protein to form stable gels, reflecting weaker intermolecular interactions and a greater degree of denaturation during commercial isolation. Such extensive denaturation can damage protein-protein interactions and reduce gel strength, thereby increasing the minimum concentration required for gel formation.

From a structural classification perspective, Flory et al. (2023) proposed that LGC can be used to differentiate cold and non-cold swelling proteins, with lower LGC values indicating proteins capable of maintaining a gel network through heating and cooling cycles. In this framework, the relatively low LGC of SPI and gluten suggests stronger resistance to shear thinning and greater stability of the gel network, properties that are beneficial for texture development in meat analogues. In contrast, the higher LGC of PPI is consistent with the idea that some commercially processed pea proteins, despite being cold swelling, may exhibit reduced gelling efficiency due to extensive denaturation and weakened protein-protein interactions.

Blending lentil protein with SPI or PPI and with different ratios did not improve gelation capacity, as all blends (LPC + 35% SPI, LPC + 25% SPI + 10% PPI, LPC + 10% SPI + 25% PPI, and LPC + 35% PPI) showed LGC values similar to LPC (16%). This indicates that the incorporation of lentil protein diluted the gel-forming ability of SPI and did not compensate for the poor gelling performance of PPI. This behavior suggests that lentil proteins may interfere with the formation of a continuous three-dimensional network, likely due to differences in molecular weight distribution, amino acid composition, and the balance between hydrophobic and covalent interactions (Brishti et al., 2017; Jarpa-Parra 2018).

Overall, the LGC results showed that gluten and SPI possess higher gelation capacity, while lentil and pea proteins require higher concentrations to form stable gels. This has direct implications for structuring in lentil-based TVP, where higher protein loading or additional structuring strategies may be required to achieve a continuous and stable network.

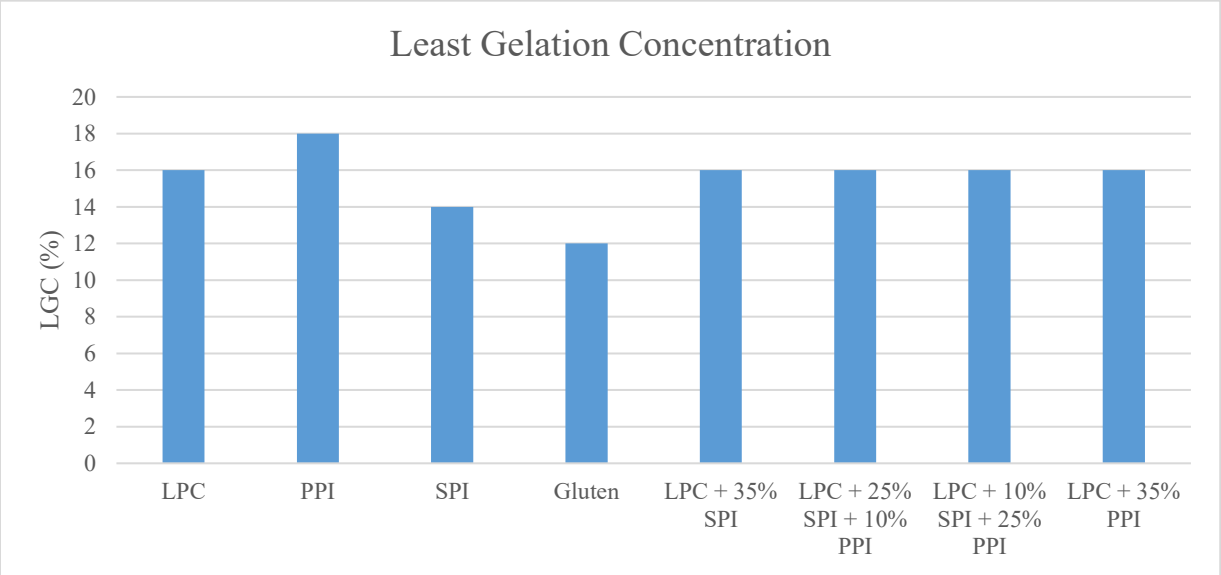

Figure 3.2. Least Gelation Concentration Results. The standard deviation was zero for all samples.

3.3.1.3 Rapid Visco Analyzer (RVA)

RVA was used to evaluate viscosity development during a controlled heating, holding, and cooling cycle and to infer whether the proteins behave as cold swelling or non-cold swelling materials. In general, cold swelling behavior is reflected by an early viscosity peak (typically before 4 min), whereas viscosity increases occurring later in the run are more indicative of non-cold swelling or heat-induced aggregation phenomena (Flory et al., 2023). Based on peak time and peak temperature (Table 3.3; Figures 3.3 to 3.5), the individual ingredients showed clearly different viscosity behaviors.

SPI showed a strong cold swelling behavior, reaching an exceptionally high peak viscosity very early in the run (1608.67 ± 573.47 cP at 30.07 ± 0.03 °C; 0.40 ± 0.04 min). This type of early, high viscosity is consistent with cold swelling globular proteins that rapidly hydrate and form a viscous network under shear at relatively low temperature (Flory et al., 2023a). In contrast, LPC, PPI, and gluten all reached their peak viscosity later and at the highest temperature stage of the profile (95 °C). LPC showed a moderate peak viscosity (156 ± 52.5 cP at 5.8 ± 0.2 min), while PPI (60.5 ± 12.7 cP at 5.6 ± 0.38 min) and gluten (47 ± 2.6 cP at 7.1 ± 0.12 min) remained relatively low throughout the cycle, with their maximum viscosity occurring only after substantial heating.

This heat-driven viscosity for lentil is consistent with reports that lentil proteins show a sharp change in viscosity around their denaturation region (around 75 °C), where unfolding and aggregation increase resistance to flow (Barbana and Boye 2013). In addition, for pulse-based ingredients, RVA viscosity can be strongly influenced by residual carbohydrates (such as starch) and by interactions among starch, protein, and fiber. Higher starch content typically yields higher peak viscosity due to granule swelling, while low starch protein isolates often show reduced or

even negligible pasting behavior. Therefore, the moderate peak viscosity of LPC (relative to PPI and gluten) is probably given that lentil concentrates has carbohydrate that can contribute to viscosity development during heating (Abdel-Aal et al., 2019; Pulivarthi et al., 2025).

Unlike the individual SPI, the blends did not show additive behavior, and in several cases, the peak viscosities were lower than expected based on the SPI component. Specifically, LPC + 35% SPI showed a very low peak viscosity (51.3 ± 7.1 cP) and reached that peak at an intermediate temperature (73 °C) and earlier time (3.4 min). Similarly, LPC + 35% PPI exhibited a low peak viscosity (38.33 ± 6.66 cP) at 76.67 ± 4.16 °C and 3.6 ± 0.35 min. Two mixed SPI + PPI formulations peaked at the highest temperature stage (95 °C), but showed different viscosity: LPC + 25% SPI + 10% PPI had the lowest peak viscosity overall (31.67 ± 2.08 cP), whereas LPC + 10% SPI + 25% PPI unexpectedly showed a much higher peak viscosity (126 ± 11.3 cP).

The cold peak values further confirmed that SPI was the only ingredient with pronounced cold swelling behavior. SPI showed a very high cold peak viscosity of 1608.67 ± 573.47 cP at 30.07 ± 0.03 °C and 0.40 ± 0.04 min, indicating rapid viscosity development at lowest temperature before substantial heating occurred. In contrast, LPC, PPI, and gluten showed much lower cold peak viscosities, ranging from 20.67 to 31.67 cP, suggesting limited cold swelling capacity. A similar trend was observed for most blends, where cold peak viscosities remained low despite the inclusion of SPI or PPI. LPC + 35% SPI, LPC + 25% SPI + 10% PPI, and LPC + 35% PPI showed cold peak viscosities of 29.00 ± 2.65, 23.67 ± 2.08, and 23.67 ± 6.35 cP, respectively, while LPC + 10% SPI + 25% PPI showed the lowest cold peak viscosity of 2.33 ± 1.15 cP. These results indicate that the strong cold swelling behavior of SPI was not retained in the lentil-based blends, likely due to ingredient interactions and competition for water during the early stage of the RVA profile.

This non-additive behavior is consistent with the idea that viscosity development in mixed proteins is governed not only by the intrinsic viscosity of each ingredient but also by interactions and competition for available water. In starch-protein blends, proteins can increase viscosity by concentrating the effective starch phase by water competition or decrease viscosity by forming a barrier around starch granules and limiting swelling. The direction depends on protein type and interaction mechanisms (Teobaldi et al., 2025). Related work also shows that increasing SPI inclusion in starchy blends can reduce peak viscosity and other RVA parameters because SPI competes for water and interferes with swelling or gelatinization of the carbohydrate fraction (Akinwale et al., 2017). In this study, for the lentil-based blends, the presence of multiple protein types likely changed hydration kinetics and aggregation behavior, producing viscosity profiles that do not follow a simple weighted average.

The earlier peak temperatures observed for LPC + 35% SPI (73 °C) and LPC + 35% PPI (77 °C), and the very low peak viscosity values of these blends, indicate that this behavior most likely reflects that in mixed starch-protein blends, proteins may compete with carbohydrates for available water and restrict swelling and molecular mobility within the matrix, leading to reduced or shifted viscosity peak (Akinwale et al., 2017; Teobaldi et al., 2025).

The contrasting behavior of the two SPI and PPI blended ratios (31.67 vs. 126 cP) may reflect differences in how the protein and the residual carbohydrate organize during heating and shear. One possible interpretation is that higher PPI inclusion (25%) in LPC + 10% SPI + 25% PPI promoted a matrix that allowed greater swelling or viscosity build-up during the highest temperature (95 °C), whereas the LPC + 25% SPI + 10% PPI produced a more restrictive matrix (lower peak) that limited swelling. These effects are consistent with the interaction framework

proposed for starch–protein mixtures, water competition, and protein thermal transitions that change mobility and energy transfer during gelatinization or aggregation (Teobaldi et al., 2025).

Overall, the RVA results align with the functional trends observed in WAC and LGC, but they also show that high water uptake does not necessarily match with high RVA peak viscosity in blends. SPI had the highest WAC and the lowest LGC among the tested plant proteins, indicating strong hydration and gel-forming ability, which can promote high viscosity under low temperature shear. Nevertheless, in blends, viscosity peaks were suppressed, highlighting that hydration and gelation behaviors can be affected by ingredient interactions and water competition across components. Therefore, RVA provides complementary evidence that lentil-based formulations exhibit complex viscosity behavior that is not predictable from single-ingredient performance.

Table 3.3. Rapid Visco Analyzer Results

Sample	Peak Viscosity (cP)	Temp at Peak Visc (°C)	Time at Peak Visc (min)	Cold Peak Visc (cP) – Between 30 and 60 °C	Temp at Cold Peak Visc (°C)	Time at Cold Peak Visc (min)
LPC	156 ± 52.5	95 ± 0	5.8 ± 0.2	28.67 ± 5.13	30.3 ± 0.35	0.76 ± 0.37
SPI	1608.67 ± 573.47	30.07 ± 0.03	0.4 ± 0.04	1608.67 ± 573.47	30.07 ± 0.03	0.4 ± 0.04

PPI	60.5 ± 12.7	95 ± 0	5.6 ± 0.38	31.67 ± 3.06	30.12 ± 0.03	0.4 ± 0
Gluten	47 ± 2.6	95 ± 0	7.1 ± 0.12	20.67 ± 1.15	30.35 ± 0.35	0.9 ±0.4
LPC + 35% SPI	51.3 ± 7.1	73 ± 0	3.4 ± 0	29 ± 2.65	30.92 ± 0.85	1.04 ± 0.2
LPC + 25% SPI + 10% PPI	31.67 ± 2.08	95 ± 0	5 ± 0.37	23.67 ± 2.08	30.08 ± 0.03	0.56 ± 0.27
LPC + 10% SPI + 25% PPI	126 ± 11.3	95 ± 0	5.7 ± 0.18	2.33 ± 1.15	31.1 ± 1.69	0.7 ± 0.5
LPC + 35% PPI	38.33 ± 6.66	76.67 ± 4.16	3.6 ± 0.35	23.67 ± 6.35	30.07 ± 0.06	0.5 ± 0.15

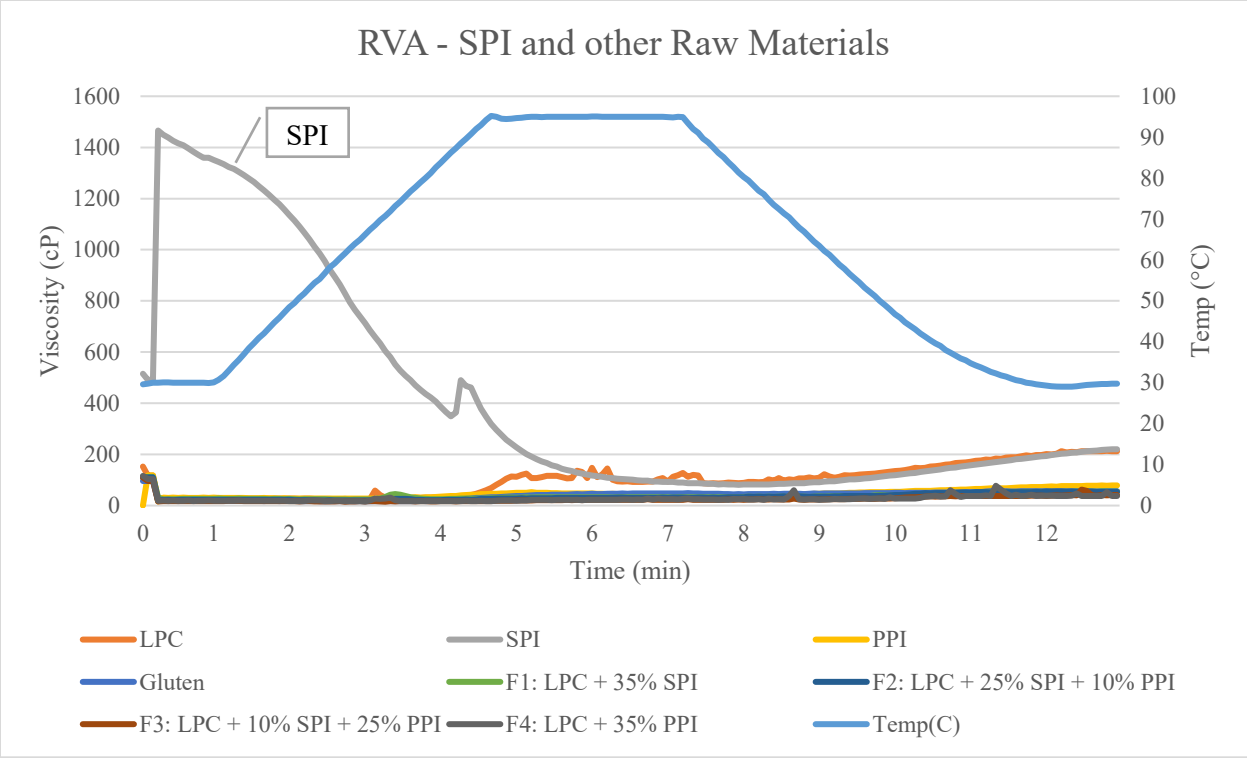

Figure 3.3. Rapid Visco Analyzer (all raw materials, with emphasis on the differences between SPI and the other raw materials)

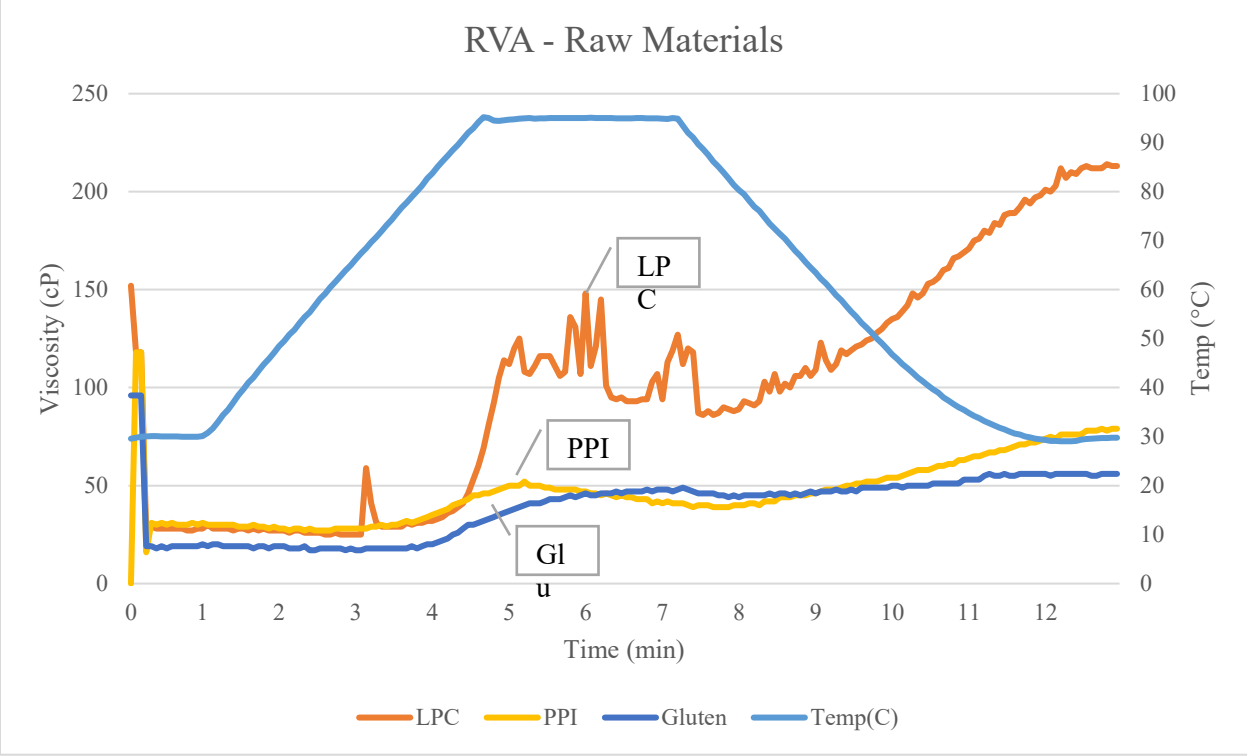

Figure 3.4. Rapid Visco Analyzer (individual raw materials, except SPI)

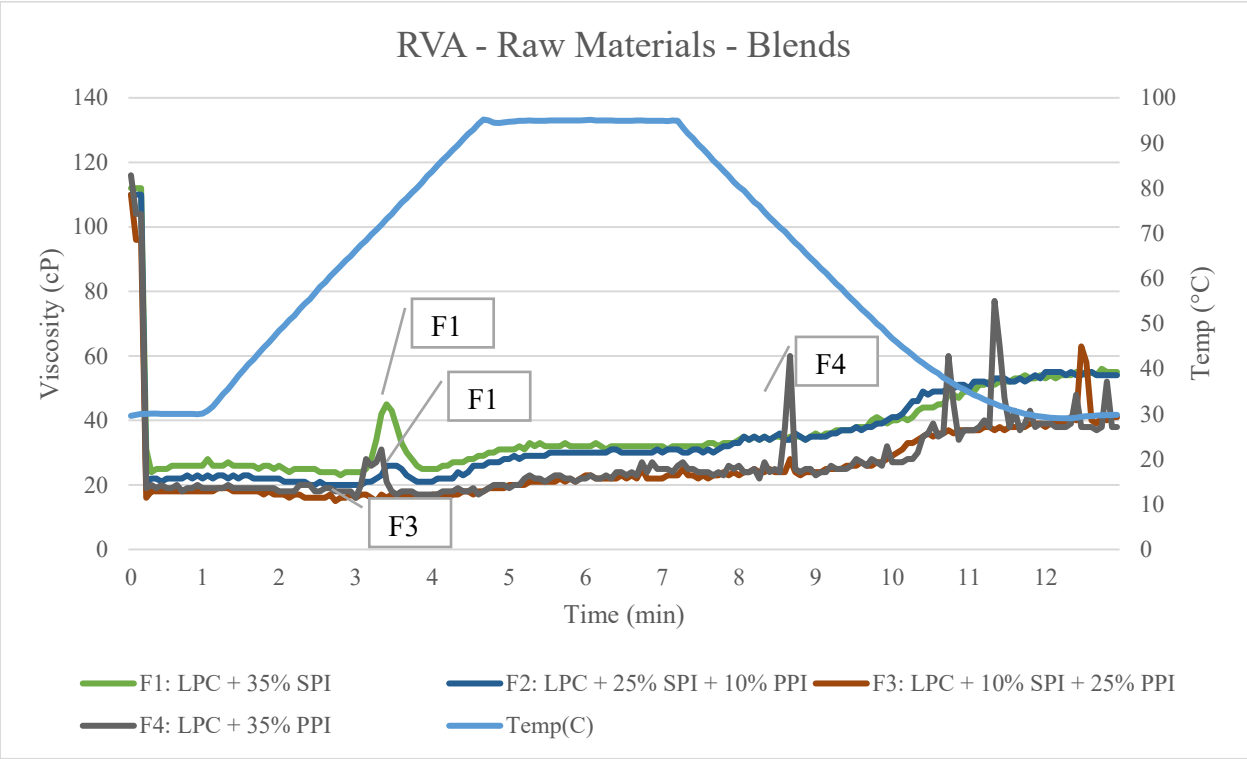

Figure 3.5. Rapid Visco Analyzer (Blends)

3.3.1.4 Phase Transition Analysis (PTA)

Phase transition analysis showed differences in flow temperature (Tf) among raw and lab-scale extruded materials (Table 3.4 and Figure 3.6). In the raw materials, Tf decreased as the proportion of PPI increased, from 36.8 °C in the SPI-rich formulation to 29.2 °C in the PPI-rich formulation. Because PTA flow temperature reflects resistance to flow and melt viscosity, lower Tf values indicate that materials become sufficiently plasticized and flowable at lower temperatures (Karkle, Alavi, and Dogan 2012). In contrast, a higher Tf indicates that more thermal energy is required before the material begins to flow, reflecting greater resistance to flow

during processing (Webb et al., 2023). Therefore, PTA provides a practical indication of the energy required for structural softening and flow.

The reduction in Tf with increasing PPI suggests that PPI-rich formulation became flowable at lower temperatures than SPI-rich blends. This may be related to differences in protein structure, water interaction, and viscosity development during heating. Similar relationships have been reported in protein and biopolymers, where formulation changes alter melt viscosity and flow behavior (Karkle et al., 2012; Webb et al., 2020). In the present study, the WAC results also showed higher water absorption for SPI than PPI, suggesting that SPI may have bound more water in blends. This could reduce water availability for the PPI fraction and affect plasticization and network formation during extrusion.

Lab-scale extrusion produced formulation-specific changes in Tf rather than a uniform increase. The change in flow temperature after extrusion, expressed as $\Delta Tf = Tf_{extruded} - Tf_{raw}$, further highlighted these differences (Figure 3.6). Positive ΔTf values were observed for the SPI-rich formulation (+3.7 °C) and the PPI-rich formulation (+4.8 °C), suggesting increased resistance to flow after processing. In contrast, the intermediate formulations showed little or negative change, with the largest decrease observed for the LPC + 10% SPI + 25% PPI formulation (7.8 °C). This agrees with previous PTA work showing that the change in Tf from raw to extruded material can be used as an indicator of protein networking or crosslinking potential, but that not all proteins increase Tf after moderate-energy extrusion (Webb et al., 2023).

These results can be explained by the balance between protein unfolding, denaturation, crosslinking, and structural breakdown during extrusion. Heat and shear can unfold proteins and partially denature them, exposing reactive groups. However, unfolding and denaturation alone do

not necessarily increase molecular weight or flow resistance. A higher apparent molecular weight and stronger resistance to flow occur only when unfolded or denatured proteins form stable intermolecular networks or crosslinks. If crosslinking is limited or if softening and macromolecular breakdown dominate, the material may become easier to flow and Tf may decrease. This interpretation is consistent with Webb et al. (2023), who reported that moderate extrusion may produce limited networking in some proteins and that this effect can be outweighed by degradation during extrusion and grinding.

The decrease in Tf for the LPC + 10% SPI + 25% PPI formulation therefore does not necessarily indicate an error in the PTA result. Rather, it suggests that under the lab-scale extrusion conditions used here, this formulation did not develop enough network strength to increase resistance to flow. Since Tf reflects melt viscosity and resistance to flow, a reduction in structural strength would be expected to lower Tf (Karkle et al., 2012). PTA also measures the temperature at which the overall blend begins to flow under pressure; therefore, in complex formulations, the measured Tf reflects the structure or component that mainly controls flow after processing (Plattner, Strahm, and Rausch, 2001).

Overall, the PTA results indicate that protein composition strongly influenced raw-material flow behavior, with increasing PPI lowering Tf. After lab-scale extrusion, changes in Tf depended on whether protein network formation or softening effects were more dominant. The increases in Tf for the SPI-rich and PPI-rich formulations suggest some crosslinking potential, while the unchanged or lower Tf values in the intermediate blends suggest limited network strengthening. Thus, protein denaturation alone was not sufficient to increase flow temperature; rather, increases in Tf depended on the extent to which denatured proteins formed stable intermolecular networks during extrusion (Plattner et al., 2001; Webb et al., 2023).

Table 3.4. Phase Transition Analysis Results

Treatments	Condition	Flow Temp (°C)
0% PPI: 35%SPI	Raw	36.8 ± 2.6
	Crosslinked	40.5 ± 7.2
10% PPI: 25%SPI	Raw	35.2 ± 2.3
	Crosslinked	35.6± 3.3
25% PPI: 10%SPI	Raw	32.8 ± 6.2
	Crosslinked	25.0± 4.0
35% PPI: 0%SPI	Raw	29.2 ± 2.8
	Crosslinked	34.0 ± 5.3

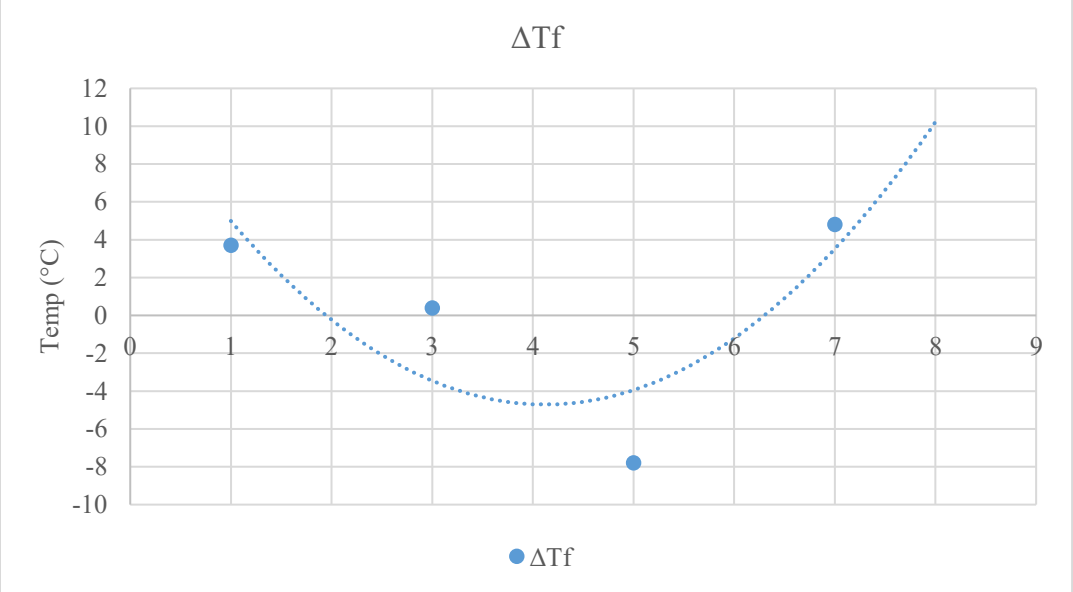

Figure 3.6. Effect of lab-scale extrusion on PTA flow temperature (ΔTf)

3.3.2 Extrusion Parameters and Calculations

In protein extrusion, IBM and screw speed are two primary levers used to control the thermo-mechanical environment inside the extruder. IBM directly determines melt viscosity and molecular mobility, while screw speed governs the magnitude of shear, friction, and mechanical energy input. Adjusting these parameters allows modulation of flow resistance, energy dissipation, and pressure development, which together shape protein texturization and structuring during extrusion (Baune et al., 2022). Table 3.6 summarizes screw speed, IBM, SME, die pressure, and die temperature across all treatments.

SME reflects the mechanical energy transferred from the extruder to the material and is shaped by both operating conditions (especially screw speed) and the rheology of the melt, which is strongly influenced by moisture and temperature. In general, increasing screw speed tends to increase SME through the screw speed, while increasing temperature or moisture can reduce viscosity and thereby reduce resistance-related responses such as torque and die pressure (Lyu et al., 2022; Singh et al., 2024).

Across the six runs, SME ranged from 660.24 to 804.96 kJ/kg, screw speed from 306 to 456 rpm, IBM from 30.12 to 38.3% wb, die pressure from 263 to 550 psi, and die temperature from 130.7 to 141.7 °C. The data show the expected dominant role of screw speed on SME, but also show that IBM can reshape the resistance (seen in die pressure), so SME does not behave as a simple one-factor outcome. This multi-parameter dependency is typical in extrusion, where moisture, temperature, screw configuration and operation, and raw material behavior determine the process state (Baune et al., 2022; Kantrong et al., 2018).

Across both SPI and PPI-based formulations, screw speed showed a clear influence on SME. Conditions operated at higher screw speeds (456 rpm) consistently produced higher SME

values compared with runs conducted at lower screw speeds (306-356 rpm). This behavior agrees with previous reports showing that increasing screw speed increases mechanical energy transfer even when torque or pressure decreases, because the screw speed term can dominate the SME calculation (Lyu et al., 2022; Singh et al., 2024). Accordingly, the lowest SME observed in the dataset (660 kJ/kg) occurred under reduced screw speed despite relatively high die pressure, confirming that energy input and flow resistance do not necessarily scale together.

Die pressure appeared to reflect melt resistance more directly than SME. Several conditions exhibited high die pressure together with moderate or even low SME, while other runs showed low pressure but high SME. Such conditions are common in extrusion processes where SME represents total mechanical energy input, whereas die pressure reflects resistance to flow at the die exit (Singh et al., 2024). High die temperatures further contributed to this behavior, so the condition showing the lowest pressure also exhibited the highest die temperature, consistent with viscosity reduction at higher temperatures, facilitating melt flow while SME remained high due to high screw speed (Guerrero et al., 2025).

An observation in the present data is that increasing IBM did not always lead to the expected decrease in SME. Generally, higher moisture acts as a plasticizer, increasing molecular mobility and reducing melt viscosity, which tends to lower torque, pressure, and SME (Ikuse et al., 2024; Singh et al., 2024).

This contradiction can be explained by the combined effects of barrel fill, shear transfer, and material structuring within the extruder. Increased feed rates (dry feed rate and extruder water) and changes in material flow conditions can increase barrel fill and enhance material-screw interaction, which may increase motor torque even when melt viscosity decreases locally (Unlu and Faller 2002). Thus, SME can remain high or even increase due to the dominant effect

of screw speed, while die pressure simultaneously decreases because higher moisture lowers melt viscosity and facilitates flow through the die.

Material composition likely further contributed to this behavior. Higher moisture can increase molecular mobility and facilitate protein chain rearrangement during thermo-mechanical processing (Baune et al., 2022; Ikuse et al., 2024). Under extrusion shear and temperature, gluten proteins undergo disulfide bond-related polymerization, reflected in reduced free sulfhydryl groups and denser network formation (Jia et al., 2020). Therefore, moisture may support these structural transitions by enabling molecular reorganization.

These mechanisms explain why IBM-driven viscosity reduction did not always lead to lower SME. SME reflected the balance between viscosity, barrel fill effects, shear, and protein network formation. Similar different responses of SME to moisture content have been reported, where SME first increases and then decreases depending on the combined influence of shear rate, viscosity, and residence time (Kantrong et al., 2018).

Comparison between SPI and PPI-based formulations under similar screw speed conditions showed that material-dependent rheology influenced extrusion responses. PPI blends generally exhibited higher die pressures than SPI blends, indicating greater resistance to flow at the die under comparable operating conditions. In contrast, the LPC+SPI formulation showed a slightly but significantly higher SME than the LPC+PPI formulation, with values of approximately 746 and 737 kJ/kg, respectively (Figure 3.7). These contrasting responses suggest that protein source affected different aspects of material behavior, with PPI increasing resistance to flow at the die, while SPI required greater overall mechanical energy during processing. Such differences are consistent with the sensitivity of extrusion behavior to raw material composition, protein interactions, and moisture-dependent melt plasticization (Ikuse et al., 2024).

Overall, the results showed that screw speed primarily controls SME, while IBM and temperature more directly influence melt resistance and die pressure. However, because extrusion responses emerge from interacting thermal, mechanical, and structural processes, deviations from simplified moisture viscosity expectations are possible in protein extrusion (Baune et al., 2022).

Table 3.5. Screw Speed, IBM, SME, and Die Pressure and Temp Data

	LPC + SPI (High IBM, High rpm)	LPC + SPI (Low IBM, High rpm)	LPC + SPI (Low IBM, Low rpm)	LPC + PPI (Low IBM, High rpm)	LPC + PPI (High IBM, Low rpm)	LPC + PPI (High IBM, High rpm)
Screw Speed (RPM)	411	456	306	456	356	456
IBM (%wb)	38.3	33.55	35.35	30.12	33.14	34.1
SME (kJ/kg)	742.32	804.96	693.36	764.64	660.24	787.68
Die Pressure (psi)	450	263	550	550	550	500
Die Temp (°C)	131.9 ± 2.2	141.7 ± 3.4	130.7 ± 2.2	132.2 ± 2.6	131.5 ± 4.1	133.3 ± 4.4

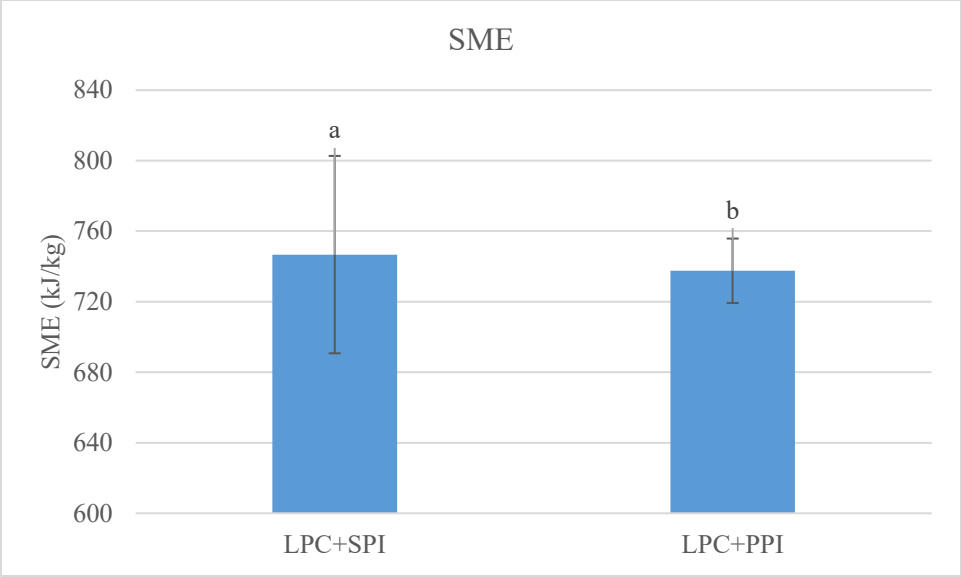

Figure 3.7. Mean SME values were significantly different between samples, as indicated by Welch's one-way ANOVA, $p < .001$.

3.3.3 Extrudate Analysis

3.3.3.1 Bulk Density

Bulk density (BD) is a structural indicator of extrudate expansion and internal porosity, where greater expansion and a higher number of air cells generally correspond to lower BD (Table 3.6). Also, BD captures how processing conditions and protein functionality jointly shape the compactness of the final TVP structure (Kantrong et al., 2018; Lyu et al., 2022).

Across formulations, BD ranged from 120.69 ± 21.09 to 266.75 ± 6.34 g/L, indicating variation in the degree of expansion and wall compaction among runs. From a processing standpoint, BD is also commercially relevant because it affects packaging and transport efficiency, while mechanistically reflecting changes in melt rheology and structure setting during extrusion (Singh et al., 2024).

When bulk density was considered from a formulation perspective, a clear difference was observed between the two proteins (Figure 3.8). The LPC + PPI formulations showed significantly higher bulk density than the LPC + SPI formulations, indicating that the PPI-based products developed a denser and more compact structure, while the SPI-based products were generally lighter and more expanded. This difference suggests that the formulation itself played an important role in determining the final structure of the extrudates. These results support the idea that protein source influences bulk density through its effects on melt behavior, film-forming ability and expansion.

Within the LPC + SPI formulations, BD was lowest for the Low IBM, High rpm condition (130.81 ± 5.93 g/L), whereas BD increased under Low IBM, Low rpm (164.38 ± 6.25 g/L) and remained similarly higher in High IBM, High rpm (164.81 ± 11.8 g/L). This pattern is consistent with screw speed promoting expansion through higher shear and a stronger pressure drop-driven flash off at the die exit, which tends to increase porosity and reduce BD. However, the higher IBM likely made the melt softer, so bubbles formed at the die exit were less stable and partially collapsed, which reduced expansion and kept BD similar to the low screw speed condition (Kantrong et al., 2018; Singh et al., 2024).

The SPI with the highest SME also showed one of the lowest BD values, supporting the idea that higher mechanical input can facilitate pore formation and expansion, depending on melt viscosity and how efficiently steam bubbles nucleate and stabilize during exit (Lyu et al., 2022).

From a material standpoint, SPI-rich systems are often discussed as having stronger film forming ability, which can support a more open, porous matrix, yielding lower BD under favorable shear and moisture conditions. This aligns with the broader observation that BD is

fundamentally structure-driven and tracks the balance between bubble formation and collapse during setting (Flory et al., 2023; Lyu et al., 2022).

In contrast, the LPC + PPI formulations showed a wider BD range, with the High IBM, Low rpm condition producing the highest BD (266.75 ± 6.34 g/L). This result is consistent with reduced screw speed limiting expansion, while a more compact structure can form when bubble growth is insufficient or bubbles collapse before being stabilized (Kantrong et al., 2018).

At matched high rpm (456 rpm), BD remained lower for the Low IBM, High rpm (120.69 ± 21.09 g/L), but increased for High IBM, High rpm (184.63 ± 16.35 g/L), suggesting that moisture and rheology interactions can shift the expansion outcome even when screw speed is held constant. In extrusion, higher moisture can reduce viscosity, which helps the material flow more easily but can also cause bubbles to collapse after exiting the die, leading to higher bulk density even when expansion conditions are favorable (Kantrong et al., 2018).

The higher bulk density in the two PPI formulations likely reflects differences in how each protein system stabilizes its internal structure during extrusion. Bulk density and water holding capacity often vary together because both depend on pore structure. More compact, layered matrices show higher density and less internal open space, while more porous structures show lower density. In this context, proteins with stronger cold swelling behavior, such as SPI, tend to form more porous structures, whereas non-cold swelling systems more often produce denser, layered products, leading to higher bulk density (Flory et al., 2023a).

Overall, these results suggest two main points; increasing screw speed generally lowers bulk density by promoting greater expansion, and also, the final density still depends on the protein type and moisture level, which determine whether the expanded structure remains stable

or partially collapses, so bulk density does not always follow a simple trend across all formulations and conditions (Kantrong et al., 2018; Lyu et al., 2022; Singh et al., 2024).

Table 3.6. Bulk Density of Lentil-Based Final Products. Means followed by different letters indicate significant differences among formulations based on the Games-Howell post-hoc test ($p < 0.05$).

Formulation	LPC + SPI (High IBM, High rpm)	LPC + SPI (Low IBM, High rpm)	LPC + SPI (Low IBM, Low rpm)	LPC + PPI (Low IBM, High rpm)	LPC + PPI (High IBM, Low rpm)	LPC + PPI (High IBM, High rpm)
Bulk Density (g/L)	164.81 ± 11.8 [b]	130.81 ± 5.93 [c]	164.38 ± 6.25 [b]	120.69 ± 21.09 [c]	266.75 ± 6.34 [a]	184.63 ± 16.35 [b]

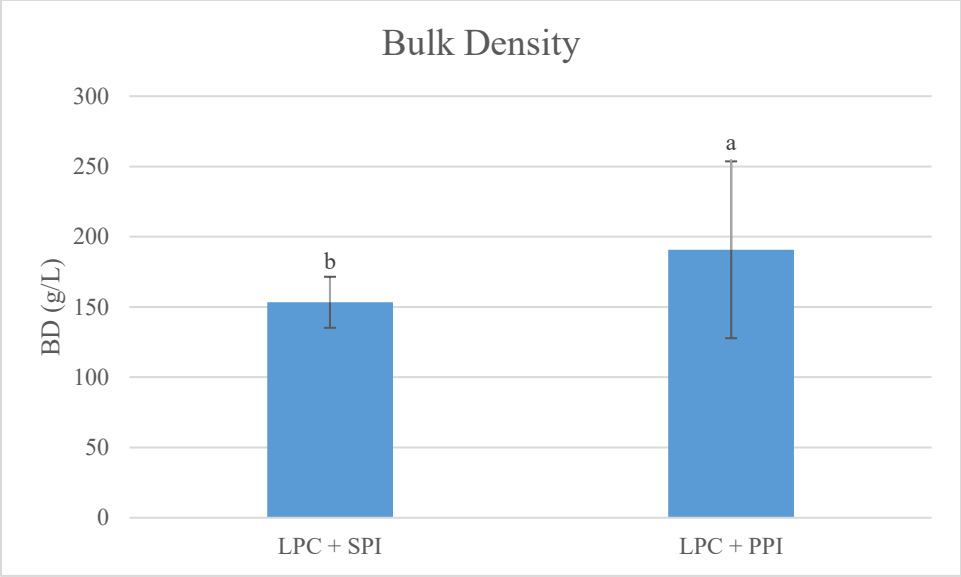

Figure 3.8. Effect of formulation on bulk density. Values are presented as mean ± SD; different letters indicate a significant difference ($p < 0.05$).

3.3.3.2 Water Holding Capacity (WHC)

WHC describes the ability of TVP to absorb and retain water and is strongly influenced by the internal structure of the final extrudate. In this study, a strong negative correlation was observed between WHC and bulk density ($r = -0.86$), indicating that products with lower bulk density generally retain more water (Figure 3.9). Lower bulk density is typically associated with greater expansion and a more porous internal structure, which allows water to penetrate and remain within the extrudate matrix. This relationship is consistent with previous studies identifying internal porosity and bulk density as major factors controlling WHC in TVP products (van Esbroeck et al., 2024; Flory et al., 2023a; Webb et al., 2023).

To simplify the comparison between formulations, WHC values were averaged across the extrusion conditions evaluated for each formulation. When WHC values were averaged across the extrusion conditions evaluated for each formulation, no significant difference was observed between LPC + SPI and LPC + PPI in either chunk or milled form ($p > 0.05$; Figure 3.10). For chunk samples, the mean WHC was 259.24 ± 55.60% for LPC + SPI and 241.19 ± 63.62% for LPC + PPI. For milled samples, the corresponding values were 305.30 ± 56.15% and 260.63 ± 71.16%, respectively. Although LPC + SPI showed higher mean WHC in both forms, the differences were not statistically significant.

In contrast, significant differences were observed among the individual formulation-extrusion condition treatments, as presented in the Appendix (Appendix Table A.1, Appendix Figures A.1 and A.2). The larger variation among these treatments, compared with the similar overall means of the two formulations, indicates that extrusion conditions had a greater influence on WHC than protein formulation alone. Changes in processing conditions likely altered expansion, porosity, and wall compactness, which affected the ability of the extrudates to absorb

and retain water. The strong negative correlation between WHC and bulk density further supports this explanation (Figure 3.9).

Milled samples also showed higher mean WHC than chunk samples for both formulations (Figure 3.10). Milling increases the available surface area and disrupts parts of the internal structure, which may expose additional water-binding sites and make internal pores more accessible to water. A similar effect has been reported for TVP products following particle-size reduction (van Esbroeck et al., 2024).

Overall, the results indicate that LPC + SPI and LPC + PPI had comparable WHC when averaged across the tested extrusion conditions. However, the significant differences among the individual treatments show that processing conditions and the resulting extrudate structure were more important in controlling water retention than the type of protein alone. This is consistent with previous studies emphasizing the role of porosity, bulk density, and internal structure in the hydration behavior of TVP products (van Esbroeck et al., 2024; Flory et al., 2023; Webb et al., 2023).

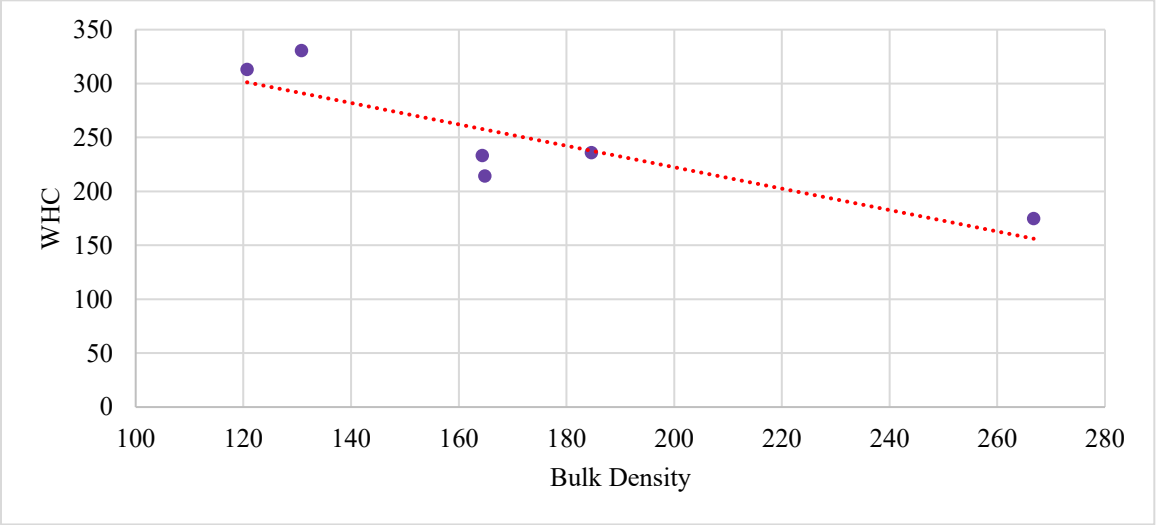

Figure 3.9. Water Holding Capacity and Bulk Density Correlation (Correlation Coefficient: - 0.86)

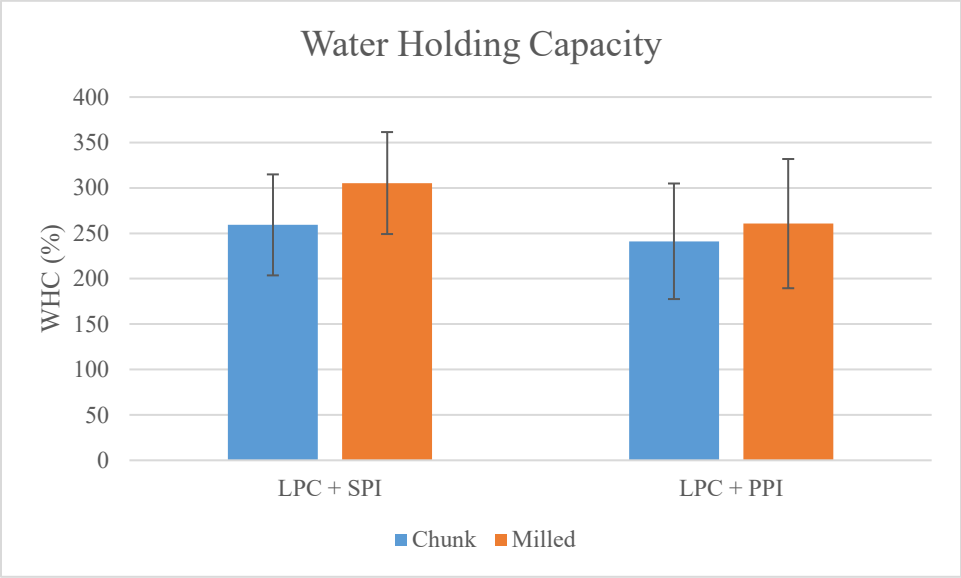

Figure 3.10. Water holding capacity of LPC + SPI and LPC + PPI formulations in chunk and milled forms. Bars represent mean ± standard deviation. No significant difference was observed between formulations within either product form ($p > 0.05$)

3.3.3.3 Texture Profile Analysis (TPA)

Texture Profile Analysis was conducted to evaluate the mechanical behavior of lentil-based texturized products and their corresponding patties, as texture attributes such as hardness, springiness, and chewiness are closely linked to protein network formation, bulk density, and water-holding capacity (WHC), and collectively reflect resistance to deformation during mastication (Flory et al., 2023; Lee et al., 2022). Across all treatments, texture parameters were influenced by product form (chunk vs. patty without binder), binder addition, protein type (SPI vs. PPI), and extrusion condition (IBM and screw speed) (Figures 3.13 to 3.16). To present the effect of protein formulation more clearly, the results were averaged across the extrusion conditions evaluated for each formulation. Detailed comparisons among the individual formulation-extrusion condition treatments are provided in the Appendix (Appendix Tables A.2 to A.4).

In chunk form, LPC + SPI and LPC + PPI showed mean hardness values of 5.61 ± 2.99 and 4.08 ± 3.25 N, respectively, with no significant difference between the formulations (Figure 3.13). However, chunk hardness was related to the structural properties of the extrudates. Hardness showed a moderate positive correlation with bulk density (r = 0.51; Figure 3.11) and a negative correlation with WHC (r = -0.66; Figure 3.12). These relationships indicate that denser structures tended to be firmer, while products with greater water retention tended to be softer. Similar relationships have been reported for TVP products, where compact structures provide greater resistance to compression, whereas more porous and hydrated structures generally show lower hardness (Flory et al., 2023b; Webb et al., 2023).

After the chunks were ground and formed into patties without binder, LPC + PPI showed significantly greater hardness than LPC + SPI, with values of 9.04 ± 3.14 and 5.72 ± 0.78 N, respectively (Figure 3.13). This result suggests that the difference between the protein formulations became more apparent after the original extrudate structure was disrupted. Grinding produces a more uniform matrix and may allow the inherent binding and network-forming properties of the proteins to contribute more directly to patty texture. In contrast, no significant difference was observed between the formulations after binder addition. Mean hardness increased to 27.16 ± 7.88 N for LPC + SPI and 30.50 ± 11.02 N for LPC + PPI. The large increase in hardness for both formulations reflects the formation of a more cohesive patty structure, consistent with previous reports that binders strengthen the matrix of plant-based patties (Webb et al., 2023).

Chewiness followed a pattern similar to hardness (Figure 3.14), which was expected because chewiness is strongly influenced by hardness and elastic recovery (Novaković and Tomašević 2017). In chunk form, LPC + SPI had significantly greater chewiness than LPC +

PPI, with mean values of 3.86 ± 1.99 and 2.40 ± 1.93 N, respectively. After patties were formed without binder, the pattern was reversed, and LPC + PPI showed significantly greater chewiness than LPC + SPI (5.23 ± 1.81 versus 3.83 ± 0.60 N). This change was consistent with the higher hardness observed for the PPI-based patties without binder. After binder addition, chewiness increased to 6.97 ± 2.85 N for LPC + SPI and 7.14 ± 4.10 N for LPC + PPI, with no significant difference between the formulations. The similar values indicate that the binder produced a more cohesive structure and reduced the textural differences associated with protein formulation.

Springiness was high in both chunk formulations, although LPC + SPI showed significantly greater springiness than LPC + PPI (89.94 ± 4.79 versus 84.54 ± 5.37%; Figure 3.15). The same pattern was observed in patties without binder, where LPC + SPI had significantly greater springiness than LPC + PPI (87.42 ± 2.84 versus 82.99 ± 4.03%). The higher springiness of LPC + SPI may be associated with its more porous and elastic internal structure, which allowed greater recovery after compression. These results indicate that the SPI-based products recovered slightly more after compression when no binder was present. Springiness can be influenced by protein network elasticity as well as sample structure and geometry (Flory et al., 2023b; Maung, Gu, and Ryu 2021). Binder addition produced a clear numerical reduction in springiness for both formulations, resulting in values of 63.34 ± 7.15% for LPC + SPI and 60.00 ± 10.37% for LPC + PPI. No significant difference was observed between the formulations after binder addition. The simultaneous increase in hardness and chewiness and decrease in springiness suggests that the binder created a firmer and more cohesive matrix with more restricted elastic recovery. This pattern is consistent with previous studies of plant-based patties, where binder increased structural strength while reducing springiness (Singh et al., 2024; Webb et al., 2023).

Overall, formulation affected texture differently depending on product form. Differences between LPC + SPI and LPC + PPI were more evident in chunks and patties without binder, whereas no significant formulation differences remained after binder addition for hardness, chewiness, or springiness. This indicates that the binder became the dominant factor controlling the final patty texture and reduced the influence of protein formulation. At the individual treatment level, extrusion conditions also produced significant textural differences, as shown in the Appendix. Together with the correlations between chunk hardness, bulk density, and WHC, these results show that final texture was controlled by the combined effects of protein formulation, extrusion-induced structure, and binder addition rather than by protein type alone.

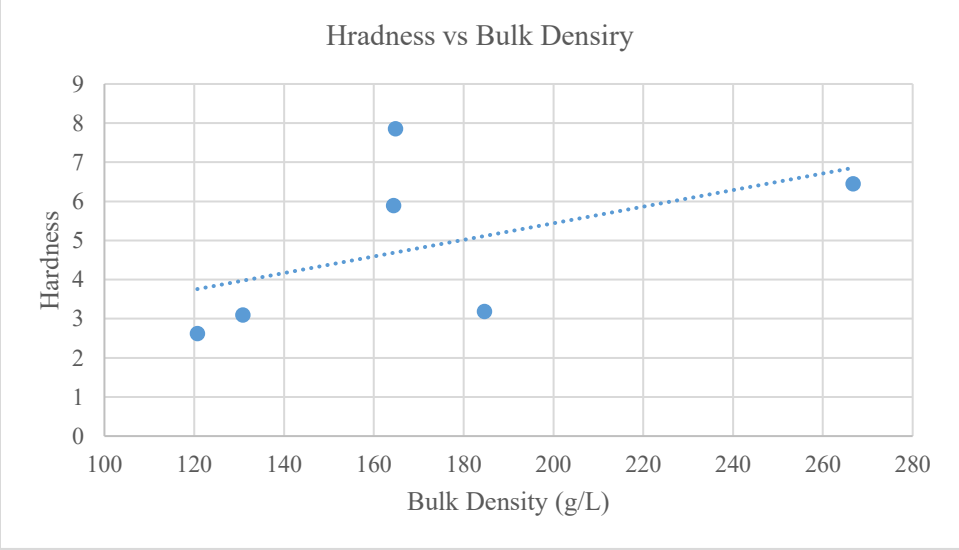

Figure 3.11. Hardness vs. Bulk Density Correlation (r = 0.51)

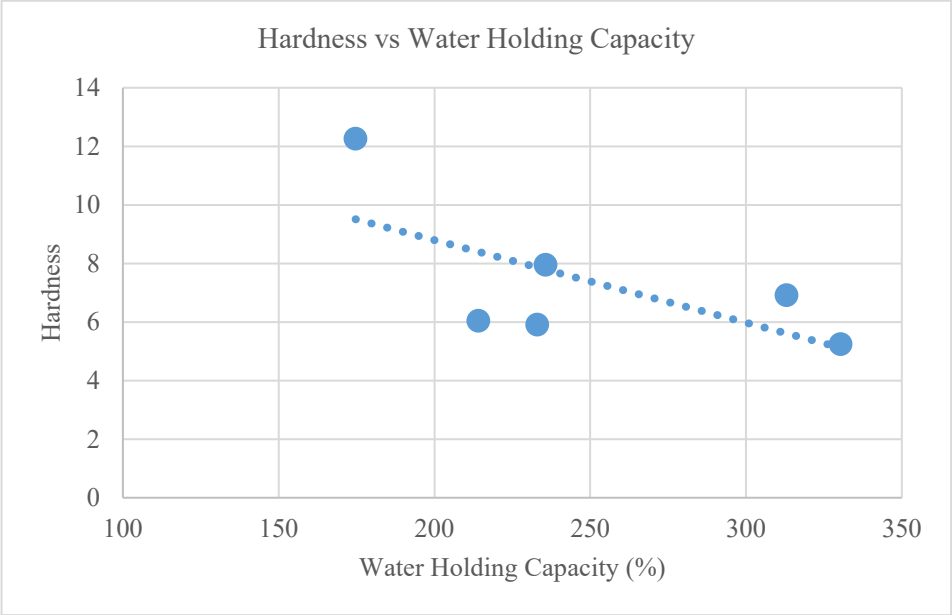

Figure 3.12. Hardness vs. Water Holding Capacity Correlation (r = - 0.66)

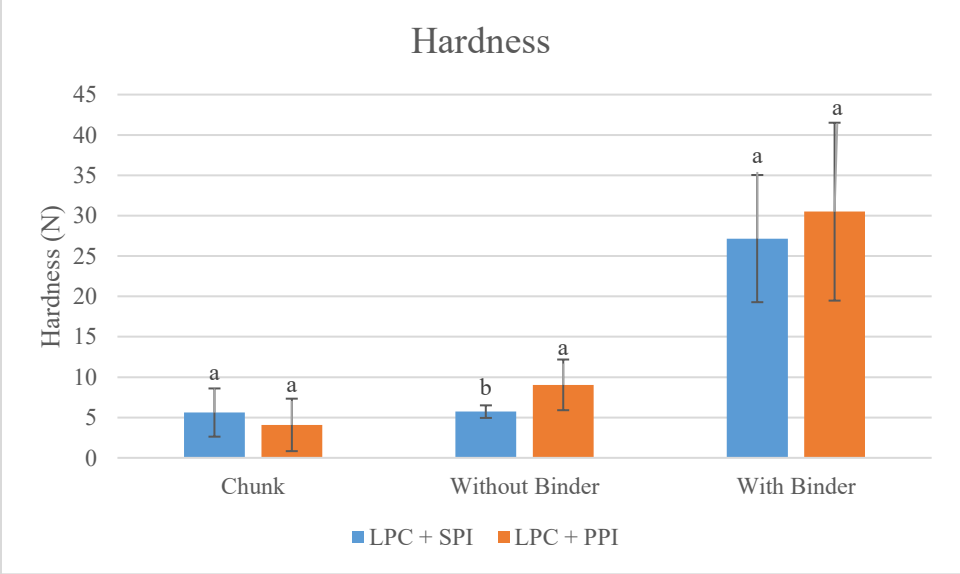

Figure 3.13. Hardness of LPC + SPI and LPC + PPI products in chunk, patty without binder, and patty with binder forms. Bars represent mean ± standard deviation. Different letters indicate significant differences between formulations within each product form ($p < 0.05$).

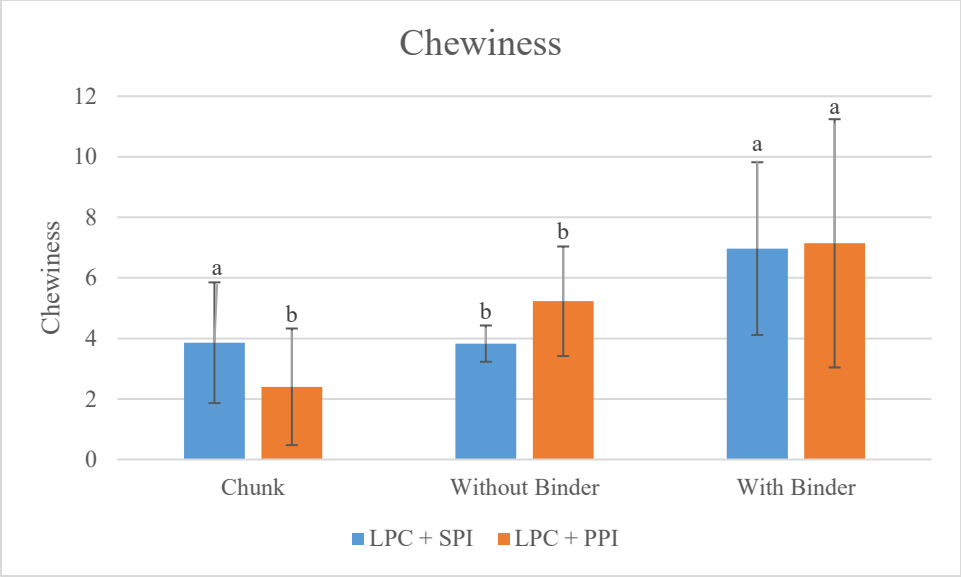

Figure 3.14. Chewiness of LPC + SPI and LPC + PPI products in chunk, patty without binder, and patty with binder forms. Bars represent mean ± standard deviation. Different letters indicate significant differences between formulations within each product form ($p < 0.05$).

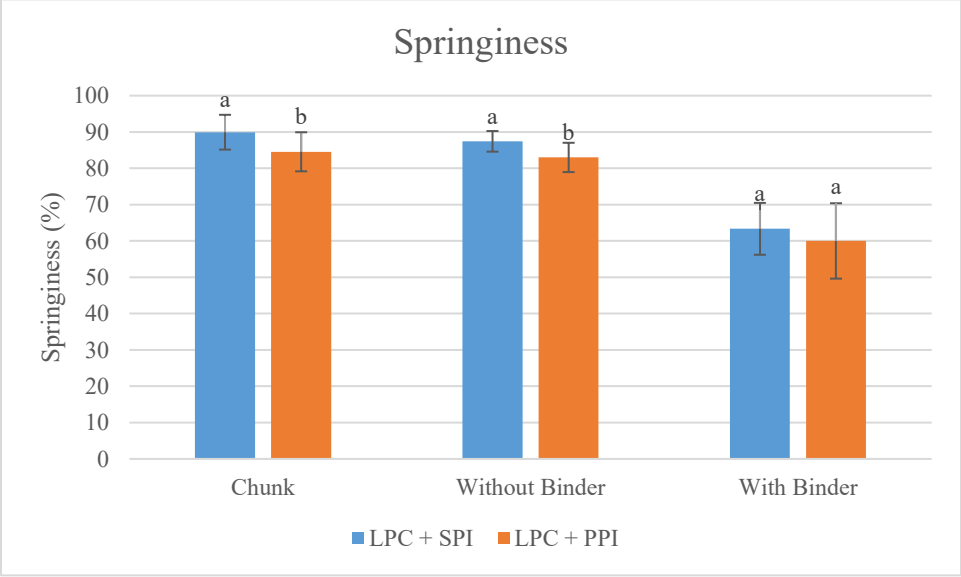

Figure 3.15. Springiness of LPC + SPI and LPC + PPI products in chunk, patty without binder, and patty with binder forms. Bars represent mean ± standard deviation. Different letters indicate significant differences between formulations within each product form ($p < 0.05$).

3.3.3.4 Visual Analysis

Visual analysis of the longitudinally cut extrudates showed that both LPC + SPI and LPC + PPI developed fiber-like structures along the extrusion direction (Figure 3.16). Representative images were selected for each formulation, while the complete set of images for the individual formulation-extrusion condition treatments is provided in the Appendix (Appendix Figure A.3). Fibrosity expert scores, measured on a scale from 1 (porous) to 10 (fibrous), were averaged across the extrusion conditions evaluated for each formulation. The mean expert score was 6 ± 0.65 for LPC + SPI and 6.13 ± 0.11 for LPC + PPI (Table 3.7), indicating a similar overall level of fiber development between the two formulations. However, the SPI treatments showed a wider range of scores, from 5.60 to 6.75, whereas the PPI treatments showed a narrower range of 6.06 to 6.26. This suggests that the visual structure of the SPI-based products was more responsive to changes in extrusion conditions, while the PPI-based products maintained a more consistent appearance. Detailed treatment-level scores are provided in the Appendix (Appendix Table A.5).

Overall, the close average scores suggest that protein formulation alone did not produce a large difference in fibrosity. Instead, extrusion conditions appeared to influence the balance between porous and layered structures, particularly in the SPI-based products. This agrees with previous studies showing that extrusion produces longitudinal fiber-like structures through protein denaturation and crosslinking, while the degree of alignment and porosity depends on the thermo-mechanical environment (Lyu et al., 2022; Singh et al., 2024). Differences in protein swelling behavior may also contribute to the observed morphology, as cold swelling proteins tend to develop a more cellular or porous structure, whereas non-cold swelling proteins may form denser and more layered matrices (Flory and Alavi 2024; Webb et al., 2023).

	Representative Image
LPC+SPI	
LPC+PPI	

Figure 3.16. Representative longitudinal images of hydrated LPC + SPI and LPC + PPI chunks.

Table 3.7. Mean fibrosity expert scores of LPC + SPI and LPC + PPI formulations averaged across the evaluated extrusion conditions.

Sample	Fibrosity Expert Score
LPC + SPI	6 ± 0.65
LPC + PPI	6.13 ± 0.11

3.3.3.5 Fibrosity Score

Fibrosity scores obtained from the computer vision and machine learning (CV+ML) model and computer vision (CV) approach were compared with expert visual scores across the six formulation-extrusion condition treatments. Expert scores were based on section 3.3.4.2. All six treatments were retained for the correlation analysis to capture the variation created by the different extrusion conditions, while the scores were also averaged within each formulation to provide a simpler overall comparison (Table 3.8). Detailed treatment-level scores are provided in the Appendix.

The formulation-level results showed close expert fibrosity scores for LPC + SPI and LPC + PPI, with mean values of 6 ± 0.65 and 6.13 ± 0.11, respectively. The CV+ML model produced similarly close scores for the two formulations, with values of 6.06 ± 0.47 for LPC + SPI and 6.11 ± 0.12 for LPC + PPI. In contrast, the CV approach produced a higher mean score for LPC + SPI than for LPC + PPI and showed considerably greater variation within the PPI formulation.

Across the individual treatments, CV+ML scores showed a very strong positive correlation with expert visual scores ($r = 0.96$; Figure 3.18). This close relationship indicates that the CV+ML model captured the structural features used by the experts when evaluating fibrous alignment and overall morphology. In contrast, CV scores showed little relationship with expert scores ($r = -0.13$; Figure 3.17), suggesting that the CV metric did not consistently reflect the visual differences recognized by the experts.

Overall, the agreement between the formulation-level averages and the strong treatment-level correlation shows that theCV+ ML model provided a closer representation of expert fibrosity assessment than the CV approach. The detailed results also indicate that extrusion

conditions created differences among individual treatments, particularly within the SPI-based samples, although the two formulations had similar average expert and ML fibrosity scores (Appendix, Table A.6).

Table 3.8. Mean fibrosity scores of LPC + SPI and LPC + PPI formulations obtained from expert visual, computer vision, and machine learning evaluations.

Treatments	Expert Score	CV Score	CV+ML Score
LPC + SPI	6 ± 0.65	6.54 ± 0.12	6.06 ± 0.47
LPC + SPI	6.13 ± 0.11	5.56 ± 1.53	6.11 ± 0.12

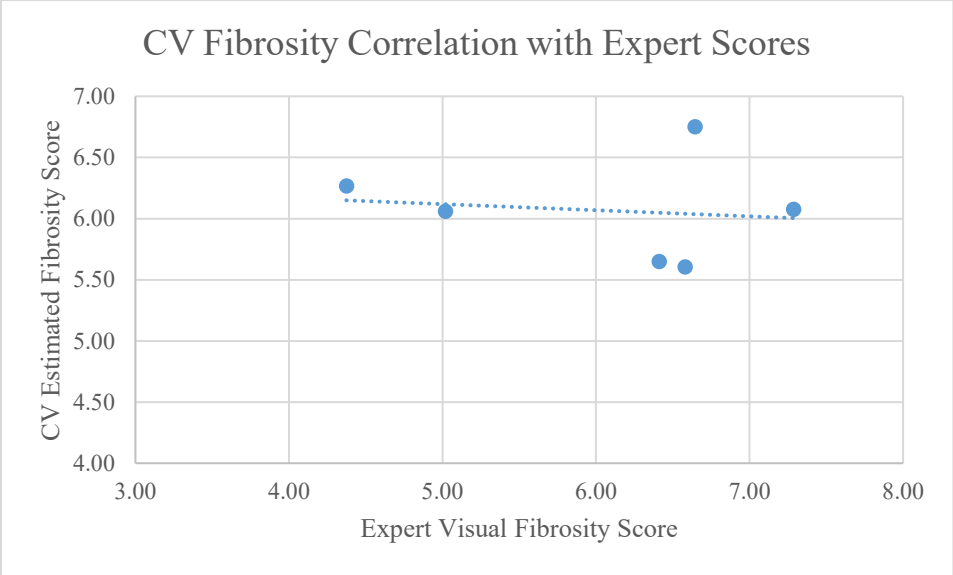

Figure 3.17. Scatter plot of computer vision-based fibrosity scores versus expert visual scores (r = - 0.13).

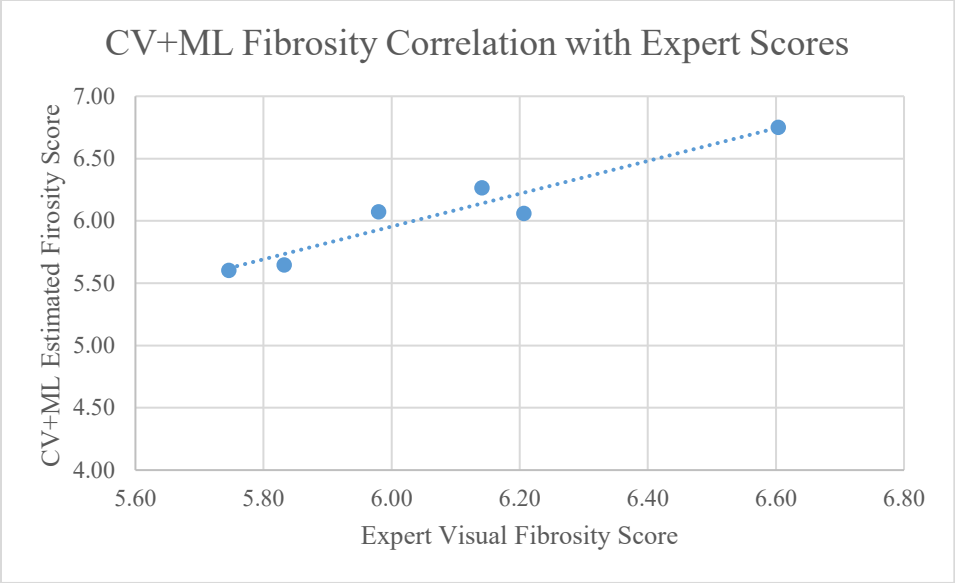

Figure 3.18. Scatter plot of computer vision + machine learning-based fibrosity scores versus expert visual scores (r = 0.96).

3.4 Conclusion

This study shows that replacing SPI with PPI in an LPC-based TVP system changes both raw material functionality and final product structure, and the effects are expressed through bulk density and WHC rather than SME alone. At the ingredient level, SPI had substantially higher WAC and a clear cold-swelling RVA response, while PPI and LPC showed more heat-dependent, lower viscosity behavior. When these proteins were blended with LPC and gluten, hydration and viscosity responses were not simply additive, highlighting that water competition and ingredient interactions shape functional behavior in mixed protein formulations.

Across pilot-scale extrusion conditions, the product outcomes reinforced that structure is the key to the relationship between formulation, processing, and texture. Bulk density varied widely across treatments and was strongly correlated with WHC; More expanded, lower density products retained more water, while denser structures retained less. Texture results followed the

same logic. Chunk and patty textures tracked structural compactness and hydration capacity, with denser and low WHC treatments producing firmer products and more expanded and higher WHC treatments producing softer textures. Binder addition dominated final patty texture by increasing hardness and chewiness and reducing springiness, but even after adding the binder, products that were already denser after extrusion still ended up firmer than the others.

Overall, the SPI-rich formulations tend to support more open, water-retentive structures, while PPI-rich formulations are more prone to compact structures unless processing conditions promote stable expansion. More importantly, the work showed that combining raw material screening tools (WAC, LGC, RVA, PTA) with simple structural metrics (BD, WHC) and texture testing provides a useful, standardized path to predict TVP quality. This helps reduce trial-and-error in formulation and supports more targeted development of next generation lentil-based meat ingredients with textures that better match consumer expectations.

3.5 References

Abdel-Aal, E.-S. M., Ragaee, S., Rabalski, I., Warkentin, T., & Vandenberg, A. (2019). Nutrient content and viscosity of Saskatchewan-grown pulses in relation to their cooking quality. *Canadian Journal of Plant Science*, *99*(1), 67–77. https://doi.org/10.1139/cjps-2018-0140

Akinwale, T. E., Shittu, T. A., Adebowale, A. A., Adewuyi, S., & Abass, A. B. (2017). Effect of soy protein isolate on the functional, pasting, and sensory acceptability of cassava starch-based custard. *Food Science & Nutrition*, *5*(6), 1163–1169. https://doi.org/10.1002/fsn3.507

Aslam, R., Sheikhizadeh, S., Alavi, S., Zhou, W., & Maqsood, S. (2026). Mechanistic evaluation of pea-soy protein isolate and concentrate based high moisture meat analogues: Evaluation of protein blends and extrudate quality. *Journal of Food Engineering*, *406*, 112802. https://doi.org/10.1016/j.jfoodeng.2025.112802

Bagheri, A., Sheikhizadeh, S., Alavi, S., & Pourkargar, D. B. (2026). An integrated time series modeling and computer vision framework for predictive structure characterization of extruded plant-based meat products. *Artificial Intelligence in Agriculture*, *16*(2), 854–872. https://doi.org/10.1016/j.aiia.2026.03.010

Barbana, C., & Boye, J. I. (2013). In vitro protein digestibility and physico-chemical properties of flours and protein concentrates from two varieties of lentil (Lens culinaris). *Food & Function*, *4*(2), 310–321. https://doi.org/10.1039/C2FO30204G

Baune, M.-C., Terjung, N., Tülbek, M. Ç., & Boukid, F. (2022). Textured vegetable proteins (TVP): Future foods standing on their merits as meat alternatives. *Future Foods*, *6*, 100181. https://doi.org/10.1016/j.fufo.2022.100181

Boukid, F., Rosell, C. M., Rosene, S., Bover-Cid, S., & Castellari, M. (2022). Non-animal proteins as cutting-edge ingredients to reformulate animal-free foodstuffs: Present status and future perspectives. *Critical Reviews in Food Science and Nutrition*, *62*(23), 6390–6420. https://doi.org/10.1080/10408398.2021.1901649

Bourne. (2002). *Texture, Viscosity, and Food*. https://doi.org/10.1016/B978-012119062-0/50001-2

Boye, J. I., Aksay, S., Roufik, S., Ribéreau, S., Mondor, M., Farnworth, E., & Rajamohamed, S. H. (2010). Comparison of the functional properties of pea, chickpea and lentil protein concentrates processed using ultrafiltration and isoelectric precipitation techniques. *Food Research International, Molecular, Functional and Processing Characteristics of Whole Pulses and Pulse Fractions and Their Emerging Food and Nutraceutical Applications*, *43*(2), 537–546. https://doi.org/10.1016/j.foodres.2009.07.021

Brishti, F. H., Zarei, M., Muhammad, S. K. S., Ismail-Fitry, M. R., Shukri, R., & Saari, N. (2017). Evaluation of the functional properties of mung bean protein isolate for development of textured vegetable protein. *International Food Research Journal*, *24*(4), 1595–1605.

De Angelis, D., Opaluwa, C., Pasqualone, A., Karbstein, H. P., & Summo, C. (2023). Rheological properties of dry-fractionated mung bean protein and structural, textural, and

rheological evaluation of meat analogues produced by high-moisture extrusion cooking. *Current Research in Food Science*, *7*, 100552. https://doi.org/10.1016/j.crfs.2023.100552

Flory, J., & Alavi, S. (2024). Use of hydration properties of proteins to understand their functionality and tailor texture of extruded plant-based meat analogues. *Journal of Food Science*, *89*(1), 245–258. https://doi.org/10.1111/1750-3841.16804

Flory, J., Xiao, R., Li, Y., Dogan, H., Talavera, M. J., & Alavi, S. (2023). Understanding Protein Functionality and Its Impact on Quality of Plant-Based Meat Analogues. *Foods*, *12*(17), 3232. https://doi.org/10.3390/foods12173232

Grabowska, K. J., Zhu, S., Dekkers, B. L., de Ruijter, N. C. A., Gieteling, J., & van der Goot, A. J. (2016). Shear-induced structuring as a tool to make anisotropic materials using soy protein concentrate. *Journal of Food Engineering*, *188*, 77–86. https://doi.org/10.1016/j.jfoodeng.2016.05.010

Guerrero, M., Stone, A. K., Singh, R., Lui, Y. C., Koksel, F., & Nickerson, M. T. (2025). Effect of Extrusion Conditions on the Characteristics of Texturized Vegetable Protein from a Faba Bean Protein Mix and Its Application in Vegan and Hybrid Burgers. *Foods*, *14*(4), 547. https://doi.org/10.3390/foods14040547

Herz, E., Herz, L., Dreher, J., Gibis, M., Ray, J., Pibarot, P., Schmitt, C., & Weiss, J. (2021). Influencing factors on the ability to assemble a complex meat analogue using a soy-protein-binder. *Innovative Food Science & Emerging Technologies*, *73*, 102806. https://doi.org/10.1016/j.ifset.2021.102806

Hong, S., Shen, Y., & Li, Y. (2022). Physicochemical and Functional Properties of Texturized Vegetable Proteins and Cooked Patty Textures: Comprehensive Characterization and Correlation Analysis. *Foods*, *11*(17), 2619. https://doi.org/10.3390/foods11172619

Ikuse, M., Marchus, C. R., Schiele, N. R., & Ganjyal, G. M. (2024). Extruded plant protein two-dimensional scaffold structures support myoblast cell growth for potential applications in cultured meat. *Food Research International (Ottawa, Ont.)*, *195*, 114981. https://doi.org/10.1016/j.foodres.2024.114981

Jarpa-Parra, M. (2018). Lentil protein: A review of functional properties and food application. An overview of lentil protein functionality. *International Journal of Food Science & Technology*, *53*(4), 892–903. https://doi.org/10.1111/ijfs.13685

Jia, F., Wang, J., Wang, Q., Zhang, X., Di Chen, Chen, Y., & Zhang, C. (2020). Effect of extrusion on the polymerization of wheat glutenin and changes in the gluten network. *Journal of Food Science and Technology*, *57*(10), 3814–3822. https://doi.org/10.1007/s13197-020-04413-6

Kaale, L. D., Siddiq, M., & Hooper, S. (2023). Lentil (Lens culinaris Medik) as nutrient-rich and versatile food legume: A review. *Legume Science*, *5*(2), e169. https://doi.org/10.1002/leg3.169

Kantrong, H., Charunuch, C., Limsangouan, N., & Pengpinit, W. (2018). Influence of process parameters on physical properties and specific mechanical energy of healthy mushroom-rice snacks and optimization of extrusion process parameters using response surface methodology. *Journal of Food Science and Technology*, *55*(9), 3462–3472. https://doi.org/10.1007/s13197-018-3271-2

Karkle, E. L., Alavi, S., & Dogan, H. (2012). Cellular architecture and its relationship with mechanical properties in expanded extrudates containing apple pomace. *Food Research International*, *46*(1), 10–21. https://doi.org/10.1016/j.foodres.2011.11.003

Lee, J.-S., Oh, H., Choi, I., Yoon, C. S., & Han, J. (2022). Physico-chemical characteristics of rice protein-based novel textured vegetable proteins as meat analogues produced by low-moisture extrusion cooking technology. *LWT*, *157*, 113056. https://doi.org/10.1016/j.lwt.2021.113056

Lyu, J. S., Lee, J.-S., Chae, T. Y., Yoon, C. S., & Han, J. (2022). Effect of screw speed and die temperature on physicochemical, textural, and morphological properties of soy protein isolate-based textured vegetable protein produced via a low-moisture extrusion. *Food Science and Biotechnology*, *32*(5), 659–669. https://doi.org/10.1007/s10068-022-01207-8

Ma, K. K., Grossmann, L., Nolden, A. A., McClements, D. J., & Kinchla, A. J. (2022). Functional and physical properties of commercial pulse proteins compared to soy derived protein. *Future Foods*, *6*, 100155. https://doi.org/10.1016/j.fufo.2022.100155

Mattice, K. D., & Marangoni, A. G. (2020). Evaluating the use of zein in structuring plant-based products. *Current Research in Food Science*, *3*, 59–66. https://doi.org/10.1016/j.crfs.2020.03.004

Maung, T.-T., Gu, B.-Y., & Ryu, G.-H. (2021). Influence of extrusion process parameters on specific mechanical energy and physical properties of high-moisture meat analog. *International Journal of Food Engineering*, *17*(2), 149–157. https://doi.org/10.1515/ijfe-2020-0042

McClements, D. J., Weiss, J., Kinchla, A. J., Nolden, A. A., & Grossmann, L. (2021). Methods for Testing the Quality Attributes of Plant-Based Foods: Meat- and Processed-Meat Analogs. *Foods*, *10*(2), 260. https://doi.org/10.3390/foods10020260

Novaković, S., & Tomašević, I. (2017). A comparison between Warner-Bratzler shear force measurement and texture profile analysis of meat and meat products: A review. *IOP Conference Series: Earth and Environmental Science*, *85*(1), 012063. https://doi.org/10.1088/1755-1315/85/1/012063

Osen, R., Toelstede, S., Wild, F., Eisner, P., & Schweiggert-Weisz, U. (2014). High moisture extrusion cooking of pea protein isolates: Raw material characteristics, extruder responses, and texture properties. *Journal of Food Engineering*, *127*, 67–74. https://doi.org/10.1016/j.jfoodeng.2013.11.023

Plattner, B., Strahm, B., & Rausch, K. (2001). The phase transition AnalyzerT and its impact on extrusion processing of foodstuffs. *2001 Sacramento, CA July 29-August 1,2001*. 2001 Sacramento, CA July 29-August 1,2001. https://doi.org/10.13031/2013.4744

Pulivarthi, M. K., Rajpurohit, B., Chakraborty, S., Li, Y., Bean, S. R., & Siliveru, K. (2025). Comparative Analysis of Physicochemical and Functional Properties of Dry and Wet Fractionated Red Lentil Proteins. *Sustainable Food Proteins*, *3*(3), e70030. https://doi.org/10.1002/sfp2.70030

Sathe, S. K., & Salunkhe, D. K. (1981). Functional Properties of the Great Northern Bean (*Phaseolus vulgaris* L.) Proteins: Emulsion, Foaming, Viscosity, and Gelation Properties. *Journal of Food Science*, *46*(1), 71–81. https://doi.org/10.1111/j.1365-2621.1981.tb14533.x

Schopf, M., Wehrli, M. C., Becker, T., Jekle, M., & Scherf, K. A. (2021). Fundamental characterization of wheat gluten. *European Food Research and Technology*, *247*(4), 985–997. https://doi.org/10.1007/s00217-020-03680-z

Singh, R., Guerrero, M., Nickerson, M. T., & Koksel, F. (2024). Effects of extrusion screw speed, feed moisture content, and barrel temperature on the physical, techno-functional, and microstructural quality of texturized lentil protein. *Journal of Food Science*, *89*(4), 2040–2053. https://doi.org/10.1111/1750-3841.16991

Sumner, A. K., Nielsen, M. A., & Youngs, C. G. (1981). Production and Evaluation of Pea Protein Isolate. *Journal of Food Science*, *46*(2), 364–366. https://doi.org/10.1111/j.1365-2621.1981.tb04862.x

Tang, X., Shen, Y., Zhang, Y., Schilling, M. W., & Li, Y. (2021). Parallel comparison of functional and physicochemical properties of common pulse proteins. *LWT*, *146*, 111594. https://doi.org/10.1016/j.lwt.2021.111594

Teobaldi, A. G., Carrillo Parra, E. J., Barrera, G. N., & Ribotta, P. D. (2025). Effect of Food Proteins on Wheat Starch Pasting and Thermal Properties. *Foods*, *14*(22), 3865. https://doi.org/10.3390/foods14223865

Unlu, E., & Faller, J. F. (2002). RTD in twin-screw food extrusion. *Journal of Food Engineering*, *53*(2), 115–131. https://doi.org/10.1016/S0260-8774(01)00148-0

van Esbroeck, T., Sala, G., Stieger, M., & Scholten, E. (2024). Effect of structural characteristics on functional properties of textured vegetable proteins. *Food Hydrocolloids*, *149*, 109529. https://doi.org/10.1016/j.foodhyd.2023.109529

Webb, D., Dogan, H., Li, Y., & Alavi, S. (2023). Physico-Chemical Properties and Texturization of Pea, Wheat and Soy Proteins Using Extrusion and Their Application in Plant-Based Meat. *Foods*, *12*(8), 1586. https://doi.org/10.3390/foods12081586

Webb, D., Plattner, B. J., Donald, E., Funk, D., Plattner, B. S., & Alavi, S. (2020). Role of chickpea flour in texturization of extruded pea protein. *Journal of Food Science*, *85*(12), 4180–4187. https://doi.org/10.1111/1750-3841.15531

Yuliarti, O., Kiat Kovis, T. J., & Yi, N. J. (2021). Structuring the meat analogue by using plant-based derived composites. *Journal of Food Engineering*, *288*, 110138. https://doi.org/10.1016/j.jfoodeng.2020.110138

Chapter 4 - Role of Protein Formulation and Processing Conditions in Shaping Texture and Fibrousness of Soy-Based High-Moisture Meat Analogs

Abstract

Driven by demand for sustainable meat alternatives, this research investigated how protein type, functionality and extrusion processing conditions influence the structure, texture and performance of plant-based meat produced using high-moisture extrusion. High-moisture meat analog (HMMA) based on soy proteins was the focus of this study.

Before evaluating the different process technologies and plant-based meat products, the functionality of various plant proteins was characterized because it strongly influenced structure development and product quality. Based on water absorption capacity (WAC) and rapid visco-analysis (RVA), soy protein isolate (SPI) and one type of soy protein concentrate (SPC1) were classified as cold swelling proteins due to their high WAC (SPI: 5.05 g/g; SPC1: 4.35 g/g) and/or low-temperature peak viscosity (30-42°C). In contrast, another type of soy protein concentrate (SPC2) behaved as non-cold swelling ingredient, showing lower hydration and/or requiring higher temperatures to develop viscosity. Cold swelling proteins generally lead to more viscous melts and also exhibit high cross-linking and greater film-forming ability, which leads to more expanded and porous plant-based meat structures, whereas non-cold swelling proteins are often

associated with denser, more fibrous products. These functional differences helped explain variation in processing behavior, texture and final structure of HMMA.

Soy protein formulations were processed using high-moisture extrusion with a special cooling die, and the impact of formulation, feed rate, and barrel temperature on the resultant HMMA products and their fibrous structure was studied. A blended standard formulation (STD) consisting of SPC1, SPC2, SPI, tapioca starch, canola oil and salt was compared with a single-protein formulation (SP) consisting of SPC2, canola oil and salt, under different feed rate and barrel temperature conditions. STD showed greater hydration, lower gelation concentration, and higher viscosity development than SP, consistent with the expected functionality differences between the formulations. Higher barrel temperature reduced SME (from 685 to 537 kJ/kg in STD and from 745 to 542 kJ/kg in SP) due to lower melt viscosity. Higher feed rate under low-temperature conditions increased die pressure, while SME changed only slightly. However, the low-feed, high-temperature condition produced the highest (up to 2.37) anisotropy index (AI; a measure of directional fiber alignment), supporting the hypothesis that stronger thermal treatment and longer residence time improved protein alignment and fibrous structure. Low-temperature conditions produced the firmest texture (hardness up to 183.72 N), showing that firmer products were not necessarily more fibrous. Visual fibrosity was higher in STD (7.35-8.11) than SP (4.02-6.75). These results supported the formulation hypothesis that STD showed stronger hydration and higher visual fibrosity, but AI did not differ significantly between STD and SP under matched processing conditions, indicating that processing conditions, particularly low-feed and high-temperature, were the main drivers of structural anisotropy. Fiberlyzer, an image-based method that quantifies fibrousness from elongated structures in macro images, showed a strong positive correlation with AI ($r = 0.93$), and an expert-guided deep-learning

model based on a modified ResNet-18 demonstrated strong agreement with expert visual fibrosity scores (r = 0.89).

This research showed that the quality of HMMAs processed using high moisture extrusion depended on the processing and combination of protein functionality. Differences in hydration, viscosity, temperature, feed rate and formulation shaped processing, structure, and texture, providing an improved theoretical and scientific framework and practical guidance for designing better quality plant-based meat products.

4.1 Introduction

The growing demand for plant-based meat products is being driven by concerns related to environmental sustainability, human health, animal welfare, and the need to provide alternative protein sources that can better meet future food demands (McClements, 2022; Zahari et al., 2022). This shift in consumer demand has led to rapid growth in the plant-based meat sector, which is projected to increase from $7.2 billion in 2023 to $24.8 billion by 2030 (Plant-Based Meat Market Size, Share & Growth Report, 2030, n.d.). However, the continued growth of this category depends not only on nutritional or sustainability benefits, but also on the ability of these products to reproduce the sensory experience of meat, particularly its texture (Michel et al., 2021). Among all quality attributes, the development of a fibrous, muscle-like structure is one of the most important determinants of consumer acceptance in meat analogues (Elzerman et al., 2011).

High-moisture extrusion is one of the most effective technologies for producing meat analogues with a fibrous structure similar to whole-muscle meat (Dekkers et al., 2016; McClements, 2022). During extrusion, plant proteins are exposed to heat, shear, pressure, and

cooling, which together promote protein denaturation, alignment, aggregation, and phase separation, leading to anisotropic structures in the final product (Ferawati et al., 2021; Grabowska et al., 2014). The final texture of high-moisture meat analogues (HMMAs), however, is not determined by processing alone. It also depends strongly on ingredient functionality, including hydration behavior, swelling characteristics, viscosity development, and gelation capacity, all of which influence melt flow, energy transfer, and structural setting during extrusion (Osen et al., 2014; Plattner et al., 2024).

Soy and pea proteins are among the most widely used raw materials for HMMAs, but soy remains especially attractive because of its strong functionality, protein quality, and well-established use in structured protein formulations (Asgar et al., 2010). In particular, soy protein concentrates and isolates can differ markedly in solubility, water absorption, and gelation behavior depending on their composition and processing history, and these differences can substantially affect extrusion processability and final product texture (Flory et al., 2023; Plattner et al., 2024). Previous work has shown that raw material properties such as cold swelling, heat-induced viscosity development, and gel-forming ability are closely related to extrusion behavior and texturization performance (Flory et al., 2023; Webb et al., 2020). For example, proteins with greater water absorption generally show stronger hydration and swelling. Mechanical energy is especially important in promoting protein transformation and texturization during extrusion (Webb et al., 2020).

In addition to ingredient functionality, extrusion conditions such as barrel temperature and feed rate play a major role in defining HMMA structure. Higher barrel temperatures generally reduce melt viscosity and die pressure by increasing thermal softening, whereas feed rate affects barrel fill, compression, and flow resistance (Chen et al., 2010; Osen et al., 2014;

Riaz, 2000). These process responses ultimately influence the balance between dense structure formation and directional fiber alignment. As a result, the texture of HMMAs is multidimensional and cannot be fully described by a single measurement. Mechanical properties such as hardness and chewiness reflect resistance to compression, while anisotropy measurements provide information about directional alignment and fibrousness (Barbut, 2015; Schreuders et al., 2019). Therefore, a more complete understanding of HMMA quality requires linking raw material functionality, extrusion responses, and multiple structural measurements in the final product.

Another important challenge in this field is the objective evaluation of fibrous structure. Many HMMA studies still rely on visual inspection of macrostructure, even though this approach is subjective and qualitative (Dekkers et al., 2016; Jia et al., 2021; Osen et al., 2014). At the same time, mechanical anisotropy does not always fully match visual observations of fibrousness (Barbut, 2015; Schreuders et al., 2019). This has created a need for more robust, quantitative tools that can characterize visual fiber formation in a reproducible way. Computer vision has recently emerged as a promising approach for this purpose, offering automated analysis of structural features from product images (Fan et al., 2013; Ma et al., 2024).

Although previous studies have separately examined ingredient functionality, extrusion performance, and texture development in meat analogues, fewer studies have evaluated these factors together within one HMMA product. In addition, limited work has compared whether a mixed protein-starch formulation and a simplified single-protein system respond differently to the same extrusion conditions, and whether visually quantified fibrousness agrees with mechanical anisotropy in these products. This represents an important gap, because

manufacturers need formulation strategies that are not only processable, but also capable of producing consistent and objectively measurable fibrous structures.

Therefore, the aim of this study was to investigate how formulation composition and extrusion conditions influence the functionality, processability, and final structure of soy-based HMMAs.

It was hypothesized that formulation functionality would strongly influence both extrusion behavior and final HMMA structure. More specifically, the blended formulation, because of its higher hydration and viscosity-building potential, was expected to show different process responses and produce a denser, more fibrous structure than the single-protein formulation (Flory et al., 2023; Plattner et al., 2024). It was further hypothesized that low-feed, high-temperature conditions would promote greater fiber development by enhancing protein transformation and alignment during extrusion (Osen et al., 2014; Plattner et al., 2024). Finally, it was expected that the image-based fibrosity score would positively correspond with mechanical anisotropy, supporting the practical value of computer vision as a complementary tool for evaluating fibrous structure in HMMAs (Ma et al., 2024).

4.2 Materials and Methods

4.2.1 Ingredients and formulation

In this study, plant protein concentrates and isolates were used to develop formulations for HMMA production. Soy protein concentrates, SPC1 (Arcon SM, ADM, Quincy, IL, USA; 70% protein, dry basis) and SPC2 (Arcon F, ADM, Quincy, IL, USA; 60% protein, dry basis) were used as the primary protein concentrates due to their functional properties in structured

protein formulations. Soy protein isolate (SPI; Profam 974, ADM, Quincy, IL, USA; 90% protein, dry basis) was incorporated as an additional high-protein ingredient to enhance the overall protein content and support structure formation during processing.

Additional ingredients included tapioca starch (Windmill Company; Meelunie B.V., Amsterdam, The Netherlands), canola frying oil (Fry & Fry Frying Oil, Memphis, TN, USA), and salt (Cargill, Wayzata, MN, USA). Similar formulation strategies combining plant proteins with starches and lipids have been reported in previous studies to support structure formation and functionality in extruded plant-based meat (Plattner et al., 2024; Webb et al., 2020).

Two formulations were prepared to evaluate the influence of protein composition. The first and Standard formulation (STD) consisted of blended proteins, containing 50% SPC1, 30% SPC2, and 10% SPI. Other ingredients in this formulation included 6.5% tapioca starch, 2.5% canola frying oil, and 1% salt. Based on the protein contents provided by the manufacturers, the calculated net protein content of this formulation was approximately 62.0% (dry basis).

The second formulation represented a simplified and Single Protein (SP) formulation consisting of 96.5% SPC2 as the only protein ingredient, with 2.5% canola frying oil and 1% salt. The calculated net protein content of this formulation was approximately 57.9% (dry basis).

All formulations were prepared in 180 lb. batches. The composition of the formulations and their calculated protein contents are summarized in Table 4.1.

Table 4.1. Ingredient composition for each HMMA formulation

	Recipes (%)	
Ingredients	Standard (STD)	Single Protein (SP)
SPC1	50	
SPC2	30	96.5

SPI	10	
Tapioca Starch	6.5	
Canola Frying Oil	2.5	2.5
Salt	1	1
Net protein content %	62	57.9

4.2.2 Raw Material Analysis

4.2.2.1 Moisture Content

The moisture content of raw ingredients was assessed following the AACC 44-19.01 method. Duplicate samples, each weighing approximately 2 g, underwent a drying process at 135°C for 2 hours as per the described procedure.

4.2.2.2 Water Absorption Capacity (WAC)

WAC was measured following the procedure described by Webb et al., (2023), with minor adjustments. Briefly, 2.5 g of each sample was weighed into centrifuge tubes, and 30 mL of deionized water was added. The mixtures were vortexed for 30 s to ensure uniform dispersion of the material in water. Samples were then allowed to hydrate at room temperature for 30 min, with occasional mixing during this period to promote consistent water contact.

After hydration, the tubes were centrifuged at 3000 × g for 30 min. The supernatant was carefully removed, and the amount of water retained by the sample was determined. WAC was expressed as grams of water absorbed per gram of dry sample.

WAC was calculated using the following equation:

$$WAC\left(\frac{g_{water}}{g_{protein}}\right) = \frac{W_f - W_i}{W_i} \quad (4.1)$$

Where W_f is the weight of the sediment, and W_i is the initial weight of the sample.

4.2.2.3 Least Gelation Concentration (LGC)

The LGC was determined following the methods of Kamani et al. (2024) and Sathe & Salunkhe (1981), with minor modifications. Protein slurries were prepared by dispersing the samples in distilled water to obtain concentrations ranging from 8% to 20% (w/v). For each concentration, 10 mL of distilled water was mixed with the appropriate amount of protein and blend powder in clean, dry glass test tubes. The suspensions were manually stirred to ensure uniform hydration and dispersion.

The test tubes were then heated in a boiling water bath (90-100°C) for 1 hour to promote gel formation. After heating, the tubes were cooled under running water for 10 minutes and subsequently refrigerated at 4°C for 2 hours to allow complete gel setting.

Gel formation was evaluated by inverting the test tubes. The LGC was defined as the lowest protein concentration at which a stable gel was formed that remained intact and did not flow or slip down the tube upon inversion. All measurements were performed in duplicate.

4.2.2.4 Rapid Visco Analyzer (RVA)

The thermal viscosity characteristics of individual protein ingredients and the formulations were analyzed using a Rapid Visco Analyzer (RVA 4800, Perten Instruments). The analysis followed the general procedure described in AACC International Method 76-21.02 (STD1), with a modification to the initial temperature setting. Viscosity was monitored continuously as a function of time and temperature to evaluate both cold and non-cold swelling behavior of the samples.

For each test, approximately 3.5 g of sample (dry basis) was weighed. The exact sample mass was adjusted according to the moisture content of each ingredient or formulation to achieve a final solids concentration of 14% (w/v). The samples were dispersed in 25 mL of distilled water in the RVA canister. The slurry was first equilibrated at 30 °C under high shear (960 rpm) for 10 s, followed by a 50 s holding period at the same temperature with the paddle speed reduced to 160 rpm. The temperature was then increased from 30 to 95 °C between 1:00 and 4:42 min at a constant shear rate of 160 rpm, followed by a holding stage at 95 °C from 4:42 to 7:12 min. Subsequently, the sample was cooled from 95 to 30 °C between 7:12 and 11:00 min and finally held at 30 °C from 11:00 to 13:00 min.

Viscosity values were recorded continuously during the heating and cooling cycle to generate thermal viscosity profiles for each sample. All measurements were performed in triplicate.

4.2.3 Extrusion Parameters and Calculations

Before extrusion, the dry ingredients for each formulation were blended using a double-ribbon mixer (Wenger Manufacturing, Sabetha, KS, USA) for approximately 5 min to ensure a homogeneous mixture. The prepared blends were then processed using a pilot-scale co-rotating twin-screw extruder (TX-52, Wenger Manufacturing, Sabetha, KS, USA). Two formulations were evaluated in this study: a standard formulation (STD) and a formulation containing a single protein, SPC2 (SP). A 2×3 factorial experimental design was applied to examine the combined effects of formulation type and extrusion conditions on product characteristics. The first factor was formulation (STD or SP), while the second factor was extrusion condition, which included three processing settings: high feed rate - low temperature (HF-LT), low feed rate - low

temperature (LF-LT), and low feed rate - high temperature (LF-HT). These factors produced six treatments in total. Detailed processing parameters for each treatment are summarized in Table 4.2.

Table 4.2. Experimental Design and Treatment ID

Treatment	Formulation	Feed Rate (kg/h)	Barrel Temperature (°C)	Treatment ID
1	STD	35	40, 80, 110, 110, 130	STD-HF-LT
2	STD	25	40, 80, 110, 110, 130	STD-LF-LT
3	STD	25	40, 100, 130, 150, 155	STD-LF-HT
4	SP	35	40, 80, 110, 110, 130	SP-HF-LT
5	SP	25	40, 80, 110, 110, 130	SP-LF-LT
6	SP	25	40, 100, 130, 150, 155	SP-LF-HT

During processing, the dry blends were first fed into the preconditioner at feed rates of either 25 or 35 kg/h and subsequently conveyed into the extruder, where the screw speed was maintained at 446 rpm for all treatments. Water was added to the preconditioner at either 10.5 or 14.9 kg/h and further injected into the extruder at rates of 17 or 24 kg/h, depending on the treatment conditions. Steam was not used at any stage of the process.

The screw configuration (Figure 4.1) was designed to progressively compress and mix the material as it moved through the barrel. The configuration included five double-flighted screw sections with decreasing pitch from the feed inlet toward the discharge end. In addition, the screw assembly incorporated four forward-conveying kneading blocks, five reverse-conveying kneading blocks, and a conical cut-flight element positioned near the discharge to assist with final material compression and flow. The screw diameter was 52 mm, and the extruder had a length-to-diameter (L/D) ratio of 25.5. The barrel consisted of five independently

controlled heating zones. For the low-temperature treatments, the barrel temperature profile was set to 40, 80, 110, 110, and 130 °C, whereas for the high-temperature treatments, the profile was adjusted to 40, 100, 130, 150, and 155 °C from the inlet toward the die end of the barrel.

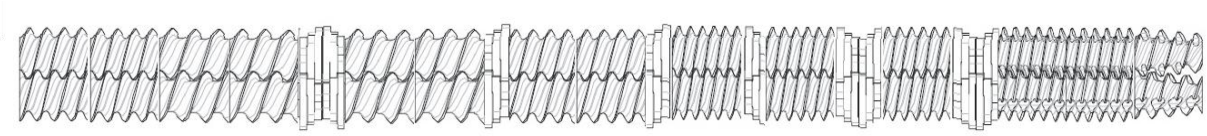

1	1	2	2	3	4	2	2	3	1	1	3	5	6	5	6	7	5	6	7	8	9	10
11	11	2	2	3	4	2	2	3	1	1	3	5	6	5	6	7	5	6	7	8	9	10

Figure 4.1. Screw Profile

The screw elements shown in the figure include a ¾-pitch, double-flight element with 9 units (1); a full-pitch, double-flight element with 9 units (2); a forward kneading block with 3 units (3); a backward-oriented forward kneading block with 3 units (4); a ½-pitch, double-flight element with 9 units (5); a reverse kneading block with 3 units (6); a backward-oriented reverse kneading block with 3 units (7); a ½-pitch, double-flight cut-flight element with 9 units (8); a ½-pitch, double-flight cut-flight element with 6 units (9); a ¾-pitch, double-flight cut-flight cone screw (10); and a ¾-pitch, single-flight element with 9 units (11).

Extruded materials exited the barrel through a 5/16-inch three-section cooling slit die designed to facilitate protein alignment, texturization, and cooling of the product. The first section of the die operated without forced cooling, allowing the protein matrix to align, set, and form fibrous structures. The subsequent two die sections were water-cooled, with cooling intensity manually controlled through a throttle valve. The water flow was adjusted as needed during processing to promote optimal product structuring, typically ranging between 30 and 31 kg/min.

After exiting the die, the HMMA products were manually cut using a kitchen knife. The freshly produced samples were immediately transferred into zip-lock bags and stored in a freezer until further analyses were conducted.

Barrel moisture during extrusion was calculated using the following equation:

$$IBM\ (\%wb) = \frac{(m_f \times (x_{wf}) + m_{ps} + m_{pw} + m_{es} + m_{ew})}{m_f + m_{ps} + m_{pw} + m_{es} + m_{ew}} \quad (4.2)$$

Where m_f is the dry feed rate, X_{wf} is the moisture content of the dry feed material (expressed as wet basis fraction), and m_{ps} and m_{pw} are the steam and water injection rate into the preconditioner; also, the m_{es} and mew are the steam and water injection rate into the extruder (in kg/h), respectively.

Specific mechanical energy (SME) was used as an indicator of the mechanical energy transferred from the screws to the material during extrusion on a dry-feed basis. This parameter reflects the level of mechanical work applied to the material and is closely related to melt viscosity and the degree of structural transformation occurring during processing. SME (kJ/kg) was calculated using the following equation:

$$Specific\ Mechanical\ Energy\ \left(\frac{kJ}{kg}\right) = \frac{W - W_0}{m} \quad (4.3)$$

where W is motor power reading in kW, W_0 is the no-load motor power reading, and m is mass flow rate in kg/sec.

Processing conditions were monitored throughout extrusion using a data acquisition system that recorded operational parameters at 1-s intervals. The system logged multiple variables, including downspot temperature (temperature of the material leaving the preconditioner), temperatures of each barrel zone, die temperature, bin feeder speed (rpm), preconditioner cylinder speed (rpm), motor load, screw speed (rpm), water addition rates to both the preconditioner and extruder, and motor power consumption (kW).

4.2.4 Extrudate Analysis

4.2.4.1 Cutting Test and Anisotropy Index (AI)

Frozen extrudate samples were thawed by placing them in a 2% (w/v) salt solution for 20 min. After thawing, the samples were manually cut into 2 × 2 cm square pieces using a knife. These pieces were used for the cutting test.

Texture analysis was performed using a TA-XT2 Texture Analyzer (Texture Technologies Corp., Scarsdale, NY, USA). A guillotine knife blade (70 mm width × 100 mm height × 3 mm thickness) was used for all measurements. The test speed was set to 2 mm/s, and samples were cut to 75% of their original thickness (75% strain) with a 50 g trigger force.

For each treatment, samples were taken from two locations across the slab: the sides (edge) and the middle. A total of 12 samples from the sides and 12 samples from the middle were tested. Within each location, half of the samples were cut parallel to the extrusion flow direction, and the other half were cut perpendicular to the extrusion flow direction. The sampling locations and cutting orientations are shown in Figure 4.2.

The maximum shear force recorded during cutting was used to calculate the Anisotropy Index (AI), defined as:

$$AI = \frac{F_{Perpendicular}}{F_{Parallel}} \tag{4.4}$$

Where $F_{Perpendicular}$ is the maximum force required to cut the sample perpendicular to the extrusion flow, and $F_{Parallel}$ is the maximum force required to cut it parallel to the flow. The procedure was adapted from (Bondu et al., 2025) with modifications in sample preparation and test settings.

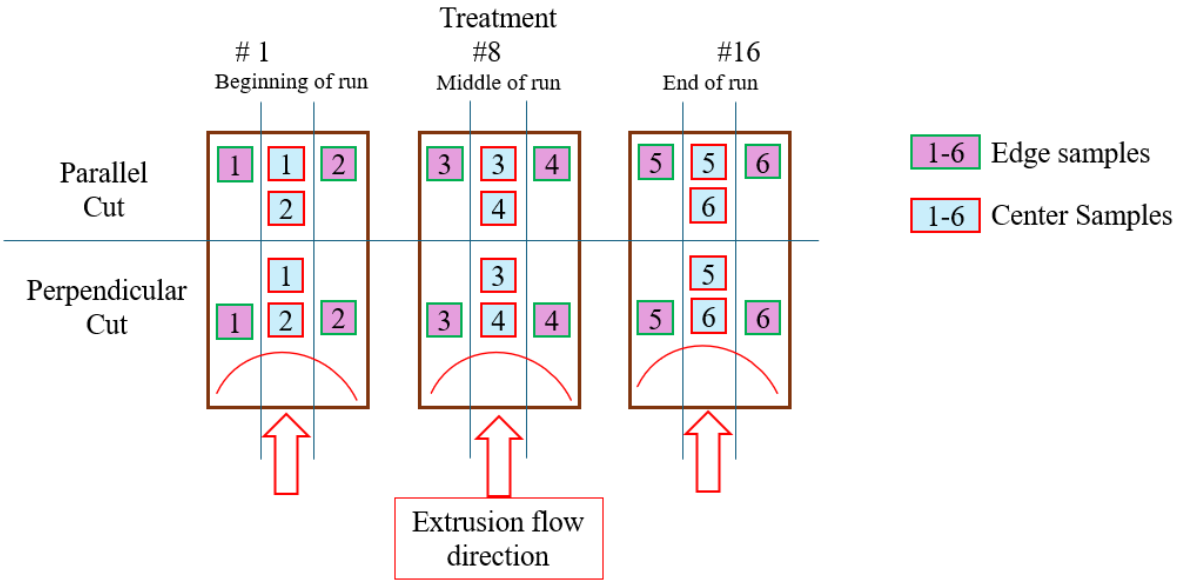

Figure 4.2. Schematic illustration of the sampling procedure used for the cutting test and anisotropy index determination. Samples were collected from the beginning, middle, and end of the extrusion run and from both the edge and center regions of the extrudate. Samples were cut either parallel or perpendicular to the extrusion flow direction.

4.2.4.2 Texture Profile Analysis (TPA)

TPA was used to evaluate the mechanical texture properties of the HMMA samples. A two-cycle compression test was performed to simulate the chewing process and to generate force-time curves from which textural parameters were calculated (Bourne, 2002).

Frozen HMMA samples were first thawed in a 2% (w/v) salt solution for 20 min. After thawing, samples were manually cut into 2 × 2 cm square pieces using a knife. For each treatment, a total of 12 replicates were prepared, with half of the samples taken from the two sides (edges) of the slab and the other half from the middle region in order to obtain representative samples across the extrudate cross-section and ensure that the measured textural properties reflected the overall structure of the product rather than a single localized region.

All TPA measurements were carried out using a TA-XT2 Texture Analyzer (Texture Technologies Corp., Scarsdale, NY, USA), following the general approach described by

(Webb et al., 2020). A 25 mm diameter cylindrical compression probe was used for all tests. Samples were compressed twice to 50% of their original height with a trigger force of 5 g. The pre-test and test speeds were set to 1 mm/s, and the post-test speed was set to 5 mm/s.

Hardness was defined as the maximum force recorded during the first compression cycle. Springiness was calculated as the ratio of the distance recovered between the end of the first compression and the start of the second compression. Chewiness was calculated as the product of hardness and springiness, multiplied by the ratio of the area under the second compression curve to that under the first compression curve (Bourne, 2002; McClements et al., 2021).

4.2.4.3 Visual Analysis

The internal fibrous structure of the HMMAs was evaluated using high-resolution macro imaging. Sample preparation followed the general approach described by (Bondu et al., 2025). For each treatment, three slabs were selected from different points of the extrusion run (beginning, middle, and end) to account for potential variability during processing. Each slab was cut into 3 × 3 cm square pieces using a sharp knife to obtain samples from both the edge and central regions of the product.

To reveal fiber orientation, each square sample was partially cut to approximately 50% of the total sample thickness in two directions: parallel to the extrusion flow and perpendicular to the extrusion flow. The samples were then manually pulled apart and gently folded along the cut surface to expose the internal fibrous network. The open structures were fixed in position using toothpicks to maintain the exposed structure during imaging. In addition, a transverse cross-section of each slab (1 cm thickness) was cut and prepared to visualize the overall internal structure across the product thickness.

From each slab, five images were obtained: two from edge regions (parallel and perpendicular cuts), two from the center region (parallel and perpendicular cuts), and one transverse cross-section of the slab. This procedure was repeated for all three slabs within each treatment, resulting in a total of 15 images per treatment. The same sampling protocol was applied to all treatments.

Images were captured using a Nikon Z 7II digital camera equipped with a 105 mm NIKKOR Z macro lens and a Godox MF-R76N TTL macro ring flash. A Kaiser RS1 copy stand and an 18% grey card were used to ensure consistent camera positioning, lighting conditions, and color balance across all images. Image acquisition was performed using Nikon NX Tether software (version 2.4.0) with a tether profile (version 9.0) under standardized shooting conditions.

4.2.4.4 Image-Based Fibrosity Score Analysis

To quantify the degree of fibrous structure in the HMMA samples, the captured macro images were analyzed using Fiberlyzer, an automated image analysis tool introduced by Ma et al. (2024). Fiberlyzer is a Python-based image analysis tool to automatically quantify fibrous structures in meat analogue products. The software identifies potential fibrous regions within the images and calculates a fibrous score (F) based on the geometric characteristics of the detected structures. The average fibrous score obtained from each image was used as a quantitative indicator of fiber development in the samples, and a higher fiber score indicates a more pronounced and elongated fibrous structure. Detailed information about the algorithm and image analysis procedure can be found in Ma et al., (2024).

4.2.4.5 Expert-Guided Deep Learning-Based Fibrosity Estimation

In addition to the Fiberlyzer-based analysis, an expert-guided deep learning approach based on Aljishi et al. (2026) was used to estimate fibrosity scores from HMMA macro images. A total of 90 images representing the six treatments were included in this analysis. Before model development, two experts independently scored all images on a scale from 0 to 10, where 0 indicated no visible fibrous structure and 10 indicated a highly fibrous structure. The average of the two visual expert scores was used as the reference value for each image. The dataset was then divided into a training set consisting of 66 randomly selected images and an independent test set consisting of 24 images. A modified ResNet-18 deep convolutional neural network, originally pretrained for image classification, was adapted for regression to generate continuous fibrosity scores. Using a modified version of the model and image-processing procedure described by Aljishi et al. (2026), the network was trained to learn the relationship between the visual features of the images and the visual expert-assigned fibrosity scores. The trained model was then applied to the independent test images to generate estimated fibrosity scores. These estimated scores were used as an additional quantitative indicator of fibrous structure.

4.2.5 Statistical Analysis

Statistical analyses were performed based on the structure of each dataset. Treatment means were compared using one-way ANOVA when appropriate. Homogeneity of variance was assessed using Levene's test. When the equal-variance assumption was met, Tukey's HSD test was used for post hoc comparisons; when this assumption was violated, Welch's ANOVA followed by Games-Howell post hoc comparisons was applied. Two-way ANOVA was also

used to evaluate the effects of formulation and sample location, as well as their interaction. Differences were considered statistically significant at $p < 0.05$.

4.3 Results and Discussion

4.3.1 Raw Material Characteristics

4.3.1.1 Water Absorption Capacity (WAC)

The WAC of the ingredients and formulations is shown in Figure 4.3. Significant differences were observed among samples, and SPI and SPC1 exhibited the highest WAC values and did not differ significantly from each other. Both proteins formed the highest WAC values of 5.05 ± 0.03 and 4.35 ± 0.17 g/g, respectively. SPC2 and the STD formulation showed moderate WAC values (2.81 ± 0.06 and 2.76 ± 0.05 g/g) and were not significantly different from each other. SP formulation displayed a slightly lower WAC (2.41 ± 0.01 g/g), while tapioca starch had the lowest value (0.72 ± 0.01 g/g), significantly lower than all other samples.

These results are consistent with previous studies showing that WAC is closely related to protein solubility and the availability of hydrophilic binding sites. Proteins with higher solubility generally absorb more water because more polar groups are available to interact with water molecules (Hong et al., 2022; Webb et al., 2020). This explains the high WAC observed for SPI and SPC1. SPI is known to be highly water-soluble, while SPC1 is described as having high protein solubility and good water-binding ability, which supports the relatively high hydration capacity observed in this study.

The relatively lower WAC of SPC2 compared with SPC1 can be attributed to differences in protein functionality resulting from processing conditions during ingredient production.

Although both ingredients are soy protein concentrates with similar protein contents, their functional properties differ because isolation and processing methods can modify protein structure, folding, and solubility (Flory et al., 2023). SPC2 has a lower protein dispersibility index (PDI) and lower solubility, which reduces its ability to absorb water compared with more soluble ingredients such as SPI or SPC1.

The differences in hydration behavior can also be interpreted using the cold swelling and non-cold swelling concept described by (Flory et al., 2023). Proteins with WAC values above approximately 4 g/g were classified as cold swelling proteins, meaning they are able to absorb water and swell at room temperature. In contrast, ingredients with lower WAC values (< 4 g/g) behave more as non-cold swelling proteins and require heating to fully hydrate. The WAC values observed in this study follow a similar pattern, where SPI and SPC1 showed strong hydration behavior, while SPC2 and the other samples exhibited lower water absorption.

The very low WAC observed for tapioca starch is expected because native starch granules do not readily absorb water at room temperature. Starch granules must first undergo gelatinization, during which the crystalline structure of the granules is disrupted, and water can penetrate the granule matrix. For tapioca starch, gelatinization typically occurs at approximately 63-84 °C (Naz et al., 2014). Because the WAC test was conducted at room temperature, the starch granules remained largely intact and therefore absorbed minimal water.

Overall, the WAC values measured in this study fall within the range commonly reported for plant proteins and reflect differences in protein solubility, polarity of amino acid residues, and structural modifications during ingredient processing (Webb et al., 2023). These differences in hydration behavior may also influence processing behavior during extrusion, since ingredients

that absorb more water generally require less mechanical energy during processing (Webb et al., 2020).

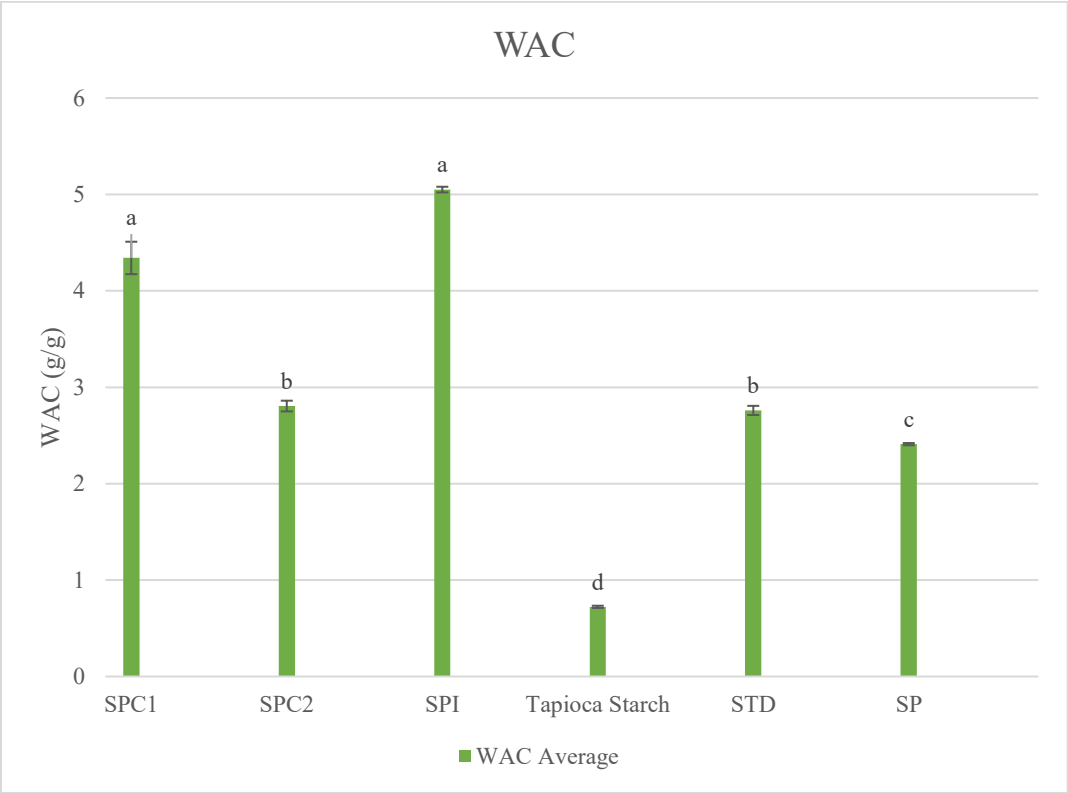

Figure 4.3. Water Absorption Capacity. Bars represent mean ± SD (n = 3). Different letters indicate significant differences among samples according to the Games-Howell post hoc test ($p < 0.05$).

4.3.1.2 Least Gelation Concentration (LGC)

LGC was used to evaluate the heat-induced gelation ability of the individual ingredients and formulations (Figure 4.4). LGC represents the minimum concentration required for a protein dispersion to form a self-supporting gel after heating, with lower values indicating stronger gel-forming ability (Boye et al., 2010; Jones, 2016). Protein gelation occurs when heating causes proteins to unfold and subsequently aggregate during cooling, forming a three-dimensional network capable of entrapping water (Jarpa-Parra, 2018). This network is stabilized through

protein-protein interactions and electrostatic forces while holding water within the gel matrix (Florence O. Uruakpa, 2012).

Among the individual ingredients, tapioca starch showed the lowest LGC (8%), followed by SPC1 (12%), SPI (15%), and SPC2 (18%). Lower LGC values indicate a stronger ability to form a heat-induced gel; therefore, tapioca starch and SPC1 exhibited relatively stronger gel-forming behavior compared with the other protein ingredients. The lower LGC observed for SPC1 suggests a greater ability to contribute to gel network formation and hydration, while the higher LGC of SPC2 indicates that a higher concentration was required before a stable gel could form.

For the formulations, the STD exhibited a lower LGC (16%) than the SP (21%). This difference likely reflects the additive effects of multiple protein sources and the presence of starch in the STD formulation. The inclusion of SPC1 and tapioca starch appears to contribute to gel network formation and improved hydration, whereas SPC2 tends to dilute gel-forming capacity within the blend. In contrast, the SP formulation contained only SPC2 as the protein source and did not include starch. Although SPC2 alone showed an LGC of 18%, the SP formulation required a higher concentration (21%) to form a gel, suggesting that the addition of oil and salt reduced the effective protein-protein interactions required for stable gel formation.

The LGC values observed in this study were somewhat higher than those reported by Flory et al. (2023), who found LGC values of approximately 11% for SPI and Arcon-S (another soy protein concentrate with broader food applications, whereas SPC1 is specifically designed for meat) and 13% for SPC2. Differences between studies may be attributed to variations in ingredient source, protein processing history, and composition, since protein isolation and treatment methods can significantly alter protein structure and gelation behavior (Mession et al.,

2015; Webb et al., 2023). Processing conditions such as pH, ionic strength, and enzymatic treatment can influence protein solubility and aggregation behavior, which ultimately affects the concentration required for gel formation (Webb et al., 2023).

Although LGC provides useful insight into heat-induced gelation behavior, it does not fully predict extrusion performance. The LGC test evaluates gel formation in relatively dilute dispersions, whereas protein network formation during extrusion occurs under much lower moisture conditions and higher heat, pressure, and shear (Webb et al., 2023). Therefore, while LGC helps characterize differences in protein functionality, it should be interpreted alongside other measurements such as WAC and RVA when evaluating ingredient performance for plant-based meat analogues.

Overall, the LGC results showed a general relationship with the WAC findings. Ingredients with higher water absorption capacity, such as SPI and SPC1, tended to support gel network formation more effectively, while ingredients with lower hydration capacity required higher concentrations to form stable gels. The relationship between gelation behavior and swelling properties is discussed further in the RVA section.

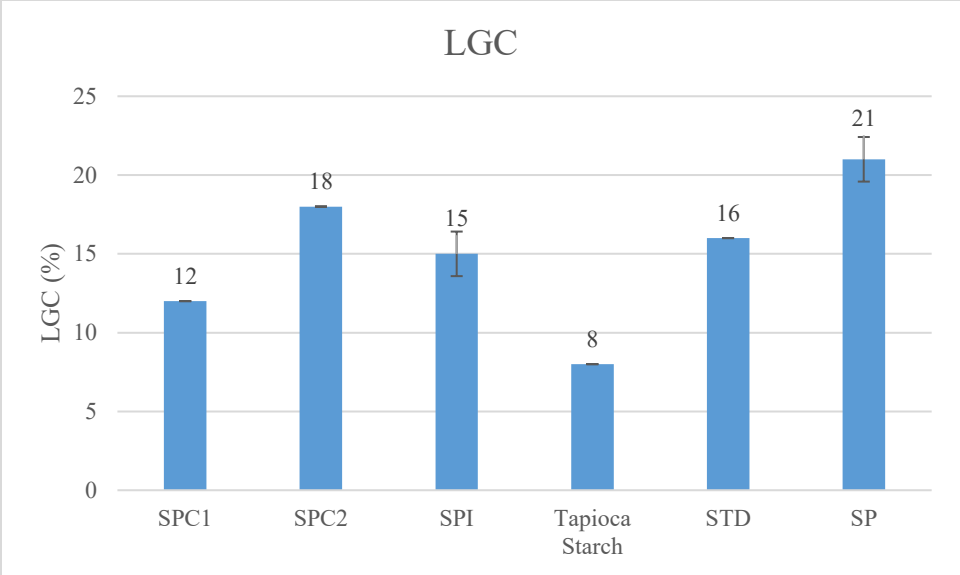

Figure 4.4. The least gelation concentration of individual ingredients and formulations. Bars represent mean ± SD.

4.3.1.3 Rapid Visco Analyzer (RVA)

The RVA pasting profiles revealed clear differences in viscosity development among the individual proteins and formulations, reflecting variations in hydration, swelling behavior, and heat-induced gelation (Table 4.3, Figures 4.5 and 4.6). These rheological responses are closely related to the functional properties of the proteins, particularly WAC and LGC, which together determine how proteins interact with water and respond to thermal processing (Osen et al., 2014; Plattner et al., 2024)

Among the ingredients, SPI exhibited the highest peak viscosity (1551.3 ± 323.2 cP), reaching its maximum very early in the RVA cycle (0.3 min at 30.07 °C). According to the classification proposed by Flory et al. (2023), peaks occurring before 4 min indicate cold swelling behavior, meaning that the material hydrates and develops viscosity rapidly without requiring significant heating. This observation is consistent with the high WAC of SPI (5.18 g/g), indicating strong water-binding capacity and rapid hydration. Similar behavior has been

reported for highly soluble soy proteins, where globular protein structures readily absorb water and unfold under shear, promoting aggregation and gel formation that increases viscosity (Flory et al., 2023; Webb et al., 2023). The relatively moderate LGC of SPI (15%) further supports this interpretation, suggesting a good ability to form heat-induced protein networks once hydrated.

SPC1 showed a similar behavior, reaching a peak viscosity of 488.3 ± 48.1 cP at 1.71 min and 41.87 °C. This peak occurred before the 4 min threshold, indicating cold swelling characteristics, although the viscosity was substantially lower than that of SPI. The relatively high WAC of SPC1 (4.35 g/g) likely contributed to this early swelling behavior. Previous studies have also reported that proteins with higher water absorption capacities tend to generate higher viscosities during RVA testing because greater water uptake promotes swelling and network formation (Webb et al., 2023).

The substantially higher and earlier viscosity peak of SPI compared with SPC1 may be related to differences in protein purity, solubility, degree of denaturation, molecular structure, and processing history. As a protein isolate, SPI contains a higher proportion of hydratable protein and fewer non-protein components, whereas the concentrate may contain residual carbohydrates and more extensively processed or aggregated proteins that limit swelling and viscosity development (Flory et al., 2023).

In contrast, SPC2, STD, and SP exhibited peak viscosities much later in the RVA cycle (5.24-6.96 min), all occurring at high temperatures (94.87-94.97 °C). Based on the same criteria, these profiles indicate non-cold swelling behavior, where proteins require thermal energy before significant viscosity development occurs.

SPC2 showed a relatively low peak viscosity (33 ± 1 cP) despite having a moderate WAC (2.83 g/g) and a relatively high LGC (18%). The high LGC indicates a lower gelation

ability compared to the other protein ingredients, meaning that higher protein concentrations are required to form a stable gel network. This behavior is consistent with its RVA profile, where viscosity development occurred only after heating, reaching the peak at 6.96 min and 94.97 °C. Similar patterns have been reported for some soy protein concentrates, where lower solubility delays hydration and swelling during RVA testing (Plattner et al., 2024).

The STD formulation showed a peak viscosity of 213 ± 23.1 cP occurring at 5.24 min and 94.87 °C, which classifies it as a non-cold swelling blend. This delayed viscosity development likely reflects the combined effects of multiple ingredients in the formulation. As reported by (Plattner et al., 2024), mixtures containing protein concentrates, starch, and other components often exhibit lower initial viscosities than isolated proteins because the additional ingredients reduce overall protein solubility and interfere with early hydration. Similarly, Ketnawa et al. (2024) noted that mixed formulations for high moisture extrusion often require more time and higher temperatures to reach peak viscosity because proteins must first denature and aggregate before forming viscous networks.

The cold viscosity results further distinguished the cold swelling ingredients from the heat-dependent samples. SPI and SPC1 showed cold viscosities of 1551.3 ± 323.2 cP and 488.3 ± 48.1 cP, respectively, which were identical to their peak viscosities because maximum viscosity development occurred during the initial low-temperature stage of the RVA cycle. In contrast, SPC2, STD, and SP exhibited lower cold viscosities of 24 ± 1, 57 ± 1, and 13.3 ± 0.6 cP, respectively, indicating limited viscosity development before heating. These results further confirm that SPI and SPC1 readily hydrated and developed viscosity under cold conditions, whereas the other samples required thermal treatment to achieve their maximum viscosity.

Overall, the RVA profiles demonstrate that viscosity development in these materials is strongly influenced by both cold swelling capacity (related to WAC) and heat-induced gelation (related to LGC). Ingredients such as SPI, which possess high WAC, showed rapid cold swelling and high early viscosity, whereas ingredients with lower cold water solubility required heating before viscosity increased.

RVA viscosity profiles provide insight into how proteins behave under conditions of heat, shear, and hydration that resemble those in extrusion (Osen et al., 2014). In extrusion processing, viscosity strongly influences flow behavior and mechanical energy input. Materials with low viscosity may require greater mechanical energy to promote protein alignment and network formation, whereas materials with higher viscosity may reach the desired structure with lower additional mechanical input in HMMAs (Plattner et al., 2024).

Therefore, understanding the cold swelling and non-cold swelling properties of protein ingredients through RVA, in combination with WAC and LGC, provides valuable insight into their expected behavior during HMMA processing and their potential contribution to final product structure.

Table 4.3. Rapid Visco Analyzer Results

Sample	Peak Viscosity (cP)	Temp at Peak Visc (°C)	Time at Peak Visc (min)	Cold Peak Viscosity (cP)	Temp at Cold Peak Visc (°C)	Time at Cold Peak Visc (min)
SPC1	488.3 ± 48.1	41.87 ± 1.99	1.71 ± 0.1	488.3 ± 48.1	41.87 ± 1.99	1.71 ± 0.1
SPC2	33 ± 1	94.97 ± 0.03	6.96 ± 0.14	24.0 ± 1	30.15 ± 0.05	0.33 ± 0

SPI	1551.3 ± 323.2	30.07 ± 0.06	0.33 ± 0	1551.3 ± 323.2	30.07 ± 0.06	0.33 ± 0
STD	213 ± 23.1	94.87 ± 0.03	5.24 ± 0.04	57 ± 1	32.33 ± 1.79	1.22 ± 0.1
SP	19.3 ± 1.2	94.87 ± 0.08	6.84 ± 0.37	13.3 ± 0.6	30.1± 0.05	0.64 ± 0.27

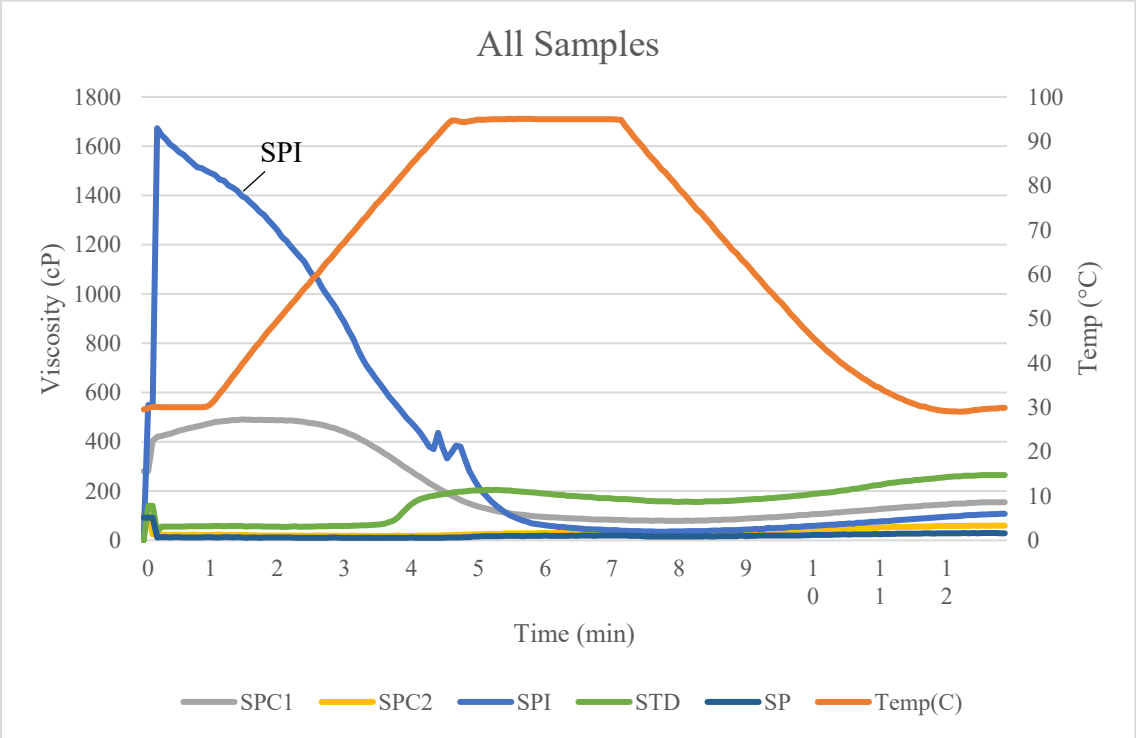

Figure 4.5. Rapid Visco Analyzer (all raw materials, with emphasis on the differences between SPI and the other raw materials)

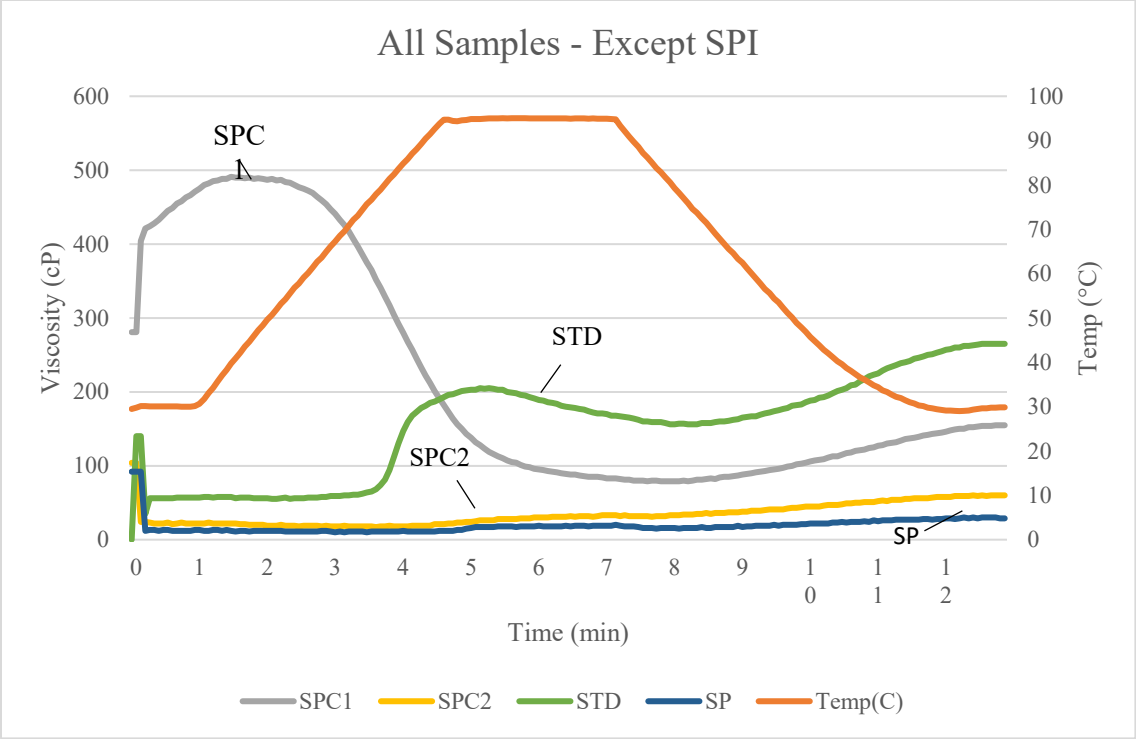

Figure 4.6. Rapid Visco Analyzer (raw materials, except SPI)

4.3.2 Extrusion Parameters and Calculations

As shown in Table 4.4, extrusion responses for the HMMA formulations showed that the main processing effects were driven more clearly by feed rate and barrel temperature than by large shifts in IBM, which remained controlled across all treatments (54.92-56.16% wb). This narrow IBM range indicates that water addition was optimized to maintain stable high-moisture processing for both formulations, despite their compositional differences. A similarly small variation in IBM has been reported when formulations were adjusted to obtain acceptable HMMA processing conditions, with final extruder responses then reflecting not only moisture level, but also the interaction between formulation functionality and process settings (Plattner et al., 2024).

The clearest trend was observed in SME and die pressure. Within both formulations, increasing barrel temperature from LT to HT at the low feed rate sharply reduced SME and die pressure. For STD, SME decreased from 684.98 to 536.78 kJ/kg and die pressure from 318.06 to 209.61 psi when moving from LF-LT to LF-HT, while for SP, SME decreased from 744.88 to 542.31 kJ/kg and die pressure from 328.26 to 204.77 psi. At the same time, die temperature increased substantially, from 133.9 to 151.2 °C for STD and from 137.8 to 155.8 °C for SP. This pattern is consistent with previous HMMA studies showing that higher barrel temperatures reduce melt viscosity, thereby lowering mechanical energy demand and pressure buildup (Osen et al., 2014; Plattner et al., 2024). Similar behavior has also been reported during soy protein extrusion, where increasing cooking temperature reduced in-line viscosity and generally lowered SME because more thermal energy was supplied to the system and less mechanical work was needed to maintain flow (Chen et al., 2010). The same interpretation fits the present data well; under HT conditions, the protein melt likely became more mobile, reducing resistance to screw rotation and flow through the die.

Feed rate also had a strong effect under LT conditions. For both formulations, the higher feed rate treatment produced higher die pressure than the low-feed condition. In STD, pressure increased from 318.06 psi at LF-LT to 419.55 psi at HF-LT, and in SP, from 328.26 to 446.02 psi. This agrees with the general extrusion principle that a higher feed rate increases barrel fill, compression, and friction, which in turn raises pressure and mechanical input (Riaz, 2000).

Under LT conditions, increasing the feed rate affected die pressure much more clearly than SME. In STD, SME changed only from 684.98 to 690.76 kJ/kg, indicating that the mechanical energy demand remained stable despite the increase in feed rate. The SP showed a slight decrease in SME, from 744.88 to 726.67 kJ/kg, while the die pressure increased

substantially. This suggests that the effect of feed rate on SME was formulation-dependent and much smaller than its effect on die pressure.

In HMMAs, such extruder responses are valuable because SME, die pressure, and die temperature are recognized predictors of melt viscosity, degree of cook, and ultimately texturization performance even before examining the final product structure (Palanisamy et al., 2019; Plattner et al., 2024).

A significant overall formulation effect was also observed for SME, with the SP formulation showing a higher mean SME than the STD formulation when data were averaged across extrusion conditions (Figure 4.7). Under matched processing conditions, SP generally showed higher SME and die pressure than STD. At HF-LT, SP had an SME of 726.67 kJ/kg and die pressure of 446.02 psi, compared with 690.76 kJ/kg and 419.55 psi for STD. At LF-LT, the contrast was even clearer, with SP reaching 744.88 kJ/kg versus 684.98 kJ/kg for STD. Even under HT conditions, where both formulations became easier to flow, SP still maintained slightly higher SME than STD (542.31 vs. 536.78 kJ/kg). This difference likely reflects formulation-dependent melt resistance during extrusion. The STD formulation contained SPC1, SPC2, SPI, and tapioca starch, whereas SP consisted only of SPC2. The presence of starch in the STD contributed to improved plasticization and flow of the melt, reducing resistance within the extruder. In contrast, the protein-rich SP formulation may have produced a more resistant protein melt, resulting in higher die pressure and mechanical energy requirements.

Therefore, the functionality of the proteins appears to be important. Previous studies have emphasized that SME reflects not just composition level, but also ingredient-specific traits such as solubility, swelling behavior, gelation, and viscosity-building capacity (Aslam et al., 2026; Osen et al., 2014).

Webb et al. (2023) reported that materials with higher resistance to flow and stronger viscosity tend to require greater SME during extrusion, while Aslam et al. (2026) similarly showed that soy-rich formulations can produce higher SME because their melts exhibit stronger network formation and greater resistance to deformation. In the present study, the SP formulation, which relied only on SPC2 as its protein base, developed a more resistant melt during processing than the STD blend. This can explain why SP required more mechanical input and generated higher pressure, especially under LT conditions where thermal softening was limited.

Overall, the extrusion results showed that both formulations were processed within a similar IBM range, but their behavior during HMMA extrusion was different. Higher barrel temperature reduced SME and die pressure for both formulations, confirming that thermal energy decreased the melt viscosity and partially replaced mechanical energy during processing. Higher feed rate increased pressure, consistent with greater barrel fill. Most importantly, SP showed consistently stronger resistance to flow than STD, indicating that formulation functionality had a clear impact on system response. This interpretation aligns well with the HMMA literature, where extruder response variables are understood as combined outcomes of recipe functionality and process conditions rather than simple reflections of protein content alone (Plattner et al., 2024).

Table 4.4. Screw Speed, IBM, SME, and Die Pressure and Die Temp Data

	STD HF-LT	STD LF-LT	STD LF-HT	SP HF-LT	SP LF-LT	SP LF-HT
Feed Rate (kg/hr)	35.7	25.7	25.15	35.62	25.76	25.69
IBM (%wb)	55.35	54.92	55.45	56.16	55.61	55.68

SME (kJ/kg)	690.76	684.98	536.78	726.67	744.88	542.31
Die Pressure (psi)	419.55	318.06	209.61	446.02	328.26	204.77
Die Temp (°C)	129.9	133.9	151.2	132.6	137.8	155.8

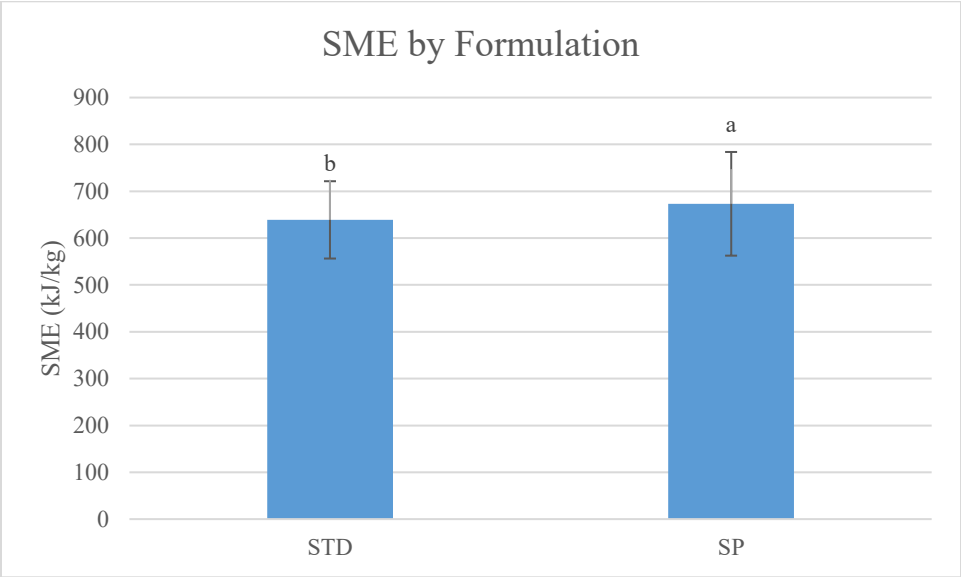

Figure 4.7. Overall mean SME of the STD and SP formulations across extrusion conditions. Bars represent mean ± standard deviation. Different letters indicate a significant difference between formulations ($p < 0.05$).

4.3.3 Extrudate Analysis

4.3.3.1 Cutting Test and Anisotropy Index (AI)

Cutting force and anisotropy index (AI) were clearly affected by extrusion treatment (Table 4.5 and Figure 4.8). In the STD formulation, perpendicular cutting force at the edges increased from 6.98 ± 2.72 kg in STD-HF-LT to 10.70 ± 1.60 kg in STD-LF-LT and 11.16 ± 2.62 kg in STD-LF-HT. A similar trend was observed in the center, where the highest

perpendicular values were also found in the STD samples (8.31-9.80 kg). In the SP formulation, the LT treatments produced much lower cutting forces, especially SP-HF-LT (2.25 ± 0.18 kg at the edge), whereas SP-LF-HT showed a strong increase in cutting force (11.23 ± 1.76 kg at the edge; 7.30 ± 1.77 kg at the center). Overall, the LF-HT treatments in both formulations showed the highest resistance to cutting. Also, in both STD-LF-HT and SP-LF-HT, perpendicular cutting force was much higher than parallel cutting force, suggesting a more directionally aligned and fibrous structure. The cutting force values obtained in this study are comparable to the firmness values reported in similar cutting tests in the literature, where firmness is defined as the force required to cut the sample (Plattner et al., 2024).

The AI results supported the cutting force data. Treatment had a significant effect on AI ($p < 0.001$), and location also had a smaller but significant effect ($p = 0.025$), whereas the treatment × location interaction was not significant ($p = 0.079$). Tukey-adjusted pairwise comparisons showed that, within the STD formulation, STD-LF-HT had significantly higher overall AI than both STD-HF-LT and STD-LF-LT ($p < 0.001$), while STD-HF-LT and STD-LF-LT did not differ significantly ($p = 0.940$). Similarly, within the SP formulation, SP-LF-HT had significantly higher AI than both SP-HF-LT and SP-LF-LT ($p < 0.001$), whereas SP-HF-LT and SP-LF-LT did not differ significantly ($p = 1.000$). Comparisons between STD and SP under matched processing conditions were not significant for HF-LT ($p = 0.728$), LF-LT ($p = 0.180$), or LF-HT ($p = 0.910$). These results indicate that the LF-HT processing condition, rather than formulation, was primarily responsible for the increase in structural anisotropy. This agrees with previous reports showing that thermal input is critical for protein transformation, alignment, and crosslinking during HMMA extrusion (Ferawati et al., 2021). It also suggests that temperature

had a stronger influence on fibrous structure than feed rate alone, because changing feed rate under LT conditions did not significantly affect AI within either formulation.

Although AI differed slightly between the edge and center locations, this difference was relatively small compared with the effect of treatment. In most treatments, AI values were slightly higher in the center than at the edges, which may be related to differences in flow and cooling conditions across the extrudate. The center of the extrudate typically experiences more uniform flow and slightly slower cooling, which may allow better development of aligned fibrous structures. Similar spatial variations in anisotropy across extrudates have been reported by Bondu et al. (2025), who attributed these differences to structural heterogeneity within the extrudate. Overall, the LF-HT treatments produced the highest AI values, indicating a more developed fibrous structure, whereas the LT treatments showed lower AI and therefore a less anisotropic structure.

Table 4.5. Cutting forces and anisotropy index of extrudates produced under different formulations. Values represent mean ± standard deviation.

	STD HF-LT	STD LF-LT	STD LF-HT	SP HF-LT	SP LF-LT	SP LF-HT
Perpendicular Cutting Force – Edges (kg)	6.98 ± 2.72	10.70 ± 1.60	11.16 ± 2.62	2.25 ± 0.18	4.15 ± 0.80	11.23 ± 1.76
Parallel Cutting Force – Edges (kg)	7.30 ± 1.35	7.64 ± 1.51	4.71 ± 2.50	3.14 ± 0.20	5.02 ± 0.75	4.54 ± 1.39
Perpendicular Cutting Force - Center (kg)	8.31 ± 1.83	9.80 ± 2.67	8.78 ± 3.19	2.63 ± 0.34	4.31 ± 1.77	7.30 ± 1.77

Parallel Cutting Force – Center (kg)	7.40 ± 2.07	8.77 ± 2.02	4.78 ± 1.44	3.05 ± 0.39	5.77 ± 1.25	4.29 ± 0.56
AI (Overall Mean)	1.10 ± 0.43[b]	1.30 ± 0.37[b]	2.37 ± 1.09[a]	0.80 ± 0.14[b]	0.78 ± 0.17[b]	2.14 ± 0.63[a]

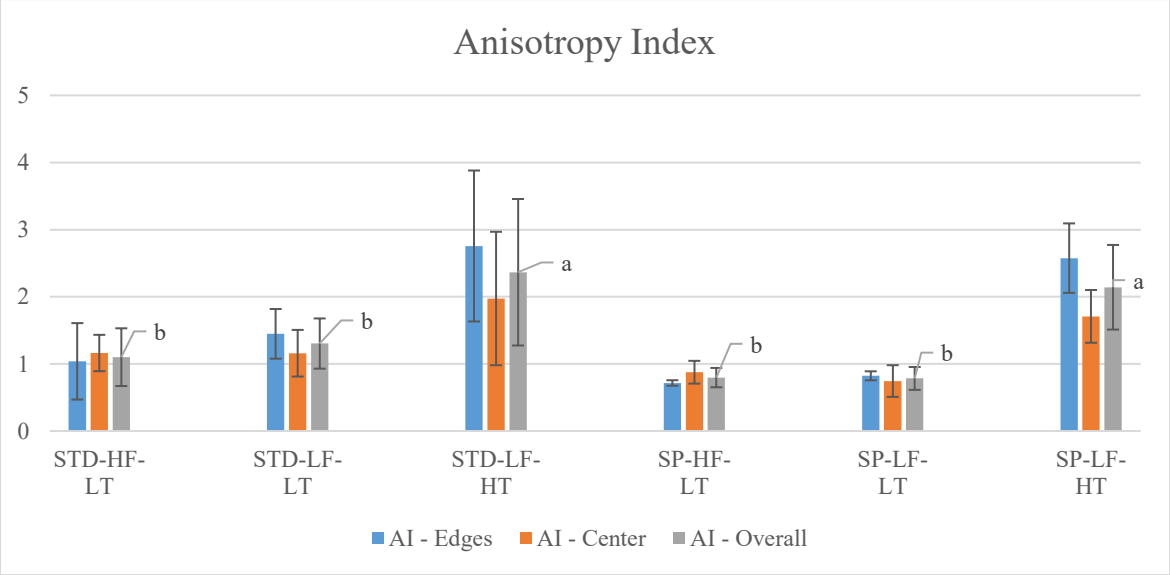

Figure 4.8. Anisotropy Index (AI) at Edge, Center, and Overall Locations of Extrudates. AI was calculated as the ratio of perpendicular cutting force to parallel cutting force relative to the extrusion flow direction. Bars represent mean ± standard deviation (n = 6 for edge and center measurements). Grey bars (third bar in each treatment group) represent overall AI values calculated from combined edge and center data (n = 12). Different letters above the overall bars indicate significant differences among treatments according to Tukey's post hoc test ($p < 0.05$).

4.3.3.2 Texture Profile Analysis (TPA)

Textural properties of the extrudates, including hardness, springiness, and chewiness, differed significantly among the six treatment combinations (Table 4.6 and Figure 4.9). Because the objective of this analysis was to compare the overall texture of the products rather than spatial variation within the cross-section, measurements from the edge and center were pooled within each treatment to provide an overall representation of the texture of the complete

extrudate slab. Three TPA results from STD-LF-HT treatment were excluded before analysis because structural separation in the extrudate caused unrealistically low compression values that did not reflect the true mechanical behavior of the samples.

Pairwise comparisons showed clear treatment-dependent differences in hardness. Within the STD formulation, STD LF-LT had significantly greater hardness than STD HF-LT ($p = 0.033$), and both treatments had significantly greater hardness than STD LF-HT ($p = 0.010$ and $p < 0.001$, respectively). Within the SP formulation, SP LF-LT had significantly greater hardness than both SP HF-LT ($p < 0.001$) and SP LF-HT ($p = 0.049$), whereas SP HF-LT and SP LF-HT did not differ significantly ($p = 0.924$). Under matched processing conditions, STD had significantly greater hardness than SP under HF-LT and LF-LT conditions ($p < 0.001$), whereas the formulations did not differ significantly under LF-HT conditions ($p = 0.690$). Among all treatments, STD-LF-LT showed the highest hardness (183.72 ± 30.94 N), indicating the greatest resistance to compression. In contrast, the LF-HT treatments showed relatively low hardness, particularly STD LF-HT (66.32 ± 49.90 N) and SP LF-HT (94.96 ± 35.62 N). Structural separation between the core and outer layers was observed in these samples, and the lower hardness may therefore be partly attributed to internal delamination and slippage during compression rather than uniform deformation of the extrudate.

Springiness varied less than hardness. Within the STD formulation, STD LF-HT had significantly greater springiness than both STD HF-LT ($p = 0.035$) and STD LF-LT ($p = 0.004$), whereas the two LT treatments did not differ significantly ($p = 0.244$). Within the SP formulation, springiness did not differ significantly among processing conditions. Comparisons between STD and SP under matched processing conditions were also not significant for HF-LT,

LF-LT, or LF-HT ($p \geq 0.091$). STD LF-HT had the highest numerical springiness value (93.27 ± 6.21%), suggesting greater elastic recovery after compression.

Chewiness also differed among treatment combinations. Within the STD formulation, STD LF-LT had significantly greater chewiness than STD LF-HT ($p = 0.007$), whereas STD HF-LT did not differ significantly from either STD LF-LT ($p = 0.291$) or STD LF-HT ($p = 0.067$). Within the SP formulation, SP HF-LT had significantly lower chewiness than both SP LF-LT ($p < 0.001$) and SP LF-HT ($p = 0.034$), whereas SP LF-LT and SP LF-HT did not differ significantly ($p = 0.979$). Under matched processing conditions, STD had significantly greater chewiness than SP under HF-LT and LF-LT conditions ($p < 0.001$), whereas no significant formulation difference was observed under LF-HT conditions ($p = 0.641$). STD LF-LT showed the highest chewiness value (98.98 ± 23.59), indicating a firm and compression-resistant structure.

The pairwise comparisons showed that texture development depended on the specific combination of formulation and processing condition. Under LT conditions, reducing the feed rate from HF to LF significantly increased hardness in both formulations. Similarly, at the low feed rate, increasing barrel temperature from LT to HT significantly reduced hardness in both STD and SP. However, the effect on chewiness was formulation-dependent. Increasing temperature significantly reduced chewiness in STD, whereas SP LF-LT and SP LF-HT did not differ significantly. The response of springiness was also formulation-dependent, because LF-HT increased springiness within STD but not within SP. These findings agree with previous HMMA studies showing that textural outcomes are influenced by the combined effects of formulation and extrusion conditions rather than by one processing variable alone (Plattner et al., 2024).

Differences between the two formulations were most evident under the HF-LT and LF-LT conditions, where STD had significantly greater hardness and chewiness than SP. However, these formulation differences were no longer significant under LF-HT conditions. This pattern may reflect differences in ingredient functionality between the formulations. STD contained a combination of SPC1, SPC2, SPI, and tapioca starch, whereas SP relied only on SPC2. Differences in hydration, viscosity development, plasticization, and network formation may therefore have contributed to the greater compression resistance of STD under LT conditions. However, the relationship between water absorption and final texture is not necessarily linear, because increased hydration may either support network formation or soften the structure depending on water distribution and the degree of plasticization within the matrix (Gulzar et al., 2025; Wagner & Ganjyal, 2024).

The TPA results should also be interpreted together with the cutting test and AI results without assuming that the measurements must follow the same trend. The LF-HT treatments showed the highest AI values for both formulations, indicating greater directional anisotropy, while also exhibiting relatively low hardness. These findings are not contradictory because AI and TPA hardness represent different structural characteristics. AI is derived from directional cutting resistance and reflects fiber alignment, whereas TPA hardness reflects resistance to compression and is influenced by matrix density, internal voids, adhesion between layers, and structural separation. A sample may therefore have a highly aligned fibrous structure and high AI while showing relatively low hardness if its internal matrix is more open or partially delaminated. In the present study, the LF-HT treatments appeared more structured in terms of alignment but less resistant to compression, whereas LF-LT, particularly STD LF-LT, produced a denser and firmer texture. Descriptively, treatments with lower hardness also tended to show

greater springiness, suggesting that a less dense internal structure may allow greater elastic recovery during compression.

Overall, the TPA results demonstrated that the six formulation-processing combinations produced distinct textural responses. STD had greater hardness and chewiness than SP under HF-LT and LF-LT conditions, but these formulation differences were not observed under LF-HT conditions. At the same time, the LF-HT treatments showed greater anisotropy but relatively low compression resistance. Together, these findings showed that fiber alignment and matrix firmness represent different structural attributes and that both should be considered when evaluating the texture of HMMA products.

Table 4.6. Texture profile parameters of HMMA extrudates produced under different formulation and processing-condition combinations. Values represent mean ± standard deviation.

	STD HF-LT	STD LF-LT	STD LF-HT	SP HF-LT	SP LF-LT	SP LF-HT
Hardness (N)	146.5 ± 23.08 ^{b}	183.72 ± 30.94 ^{a}	66.32 ± 49.9 ^{c}	105.45 ± 13.28 ^{c}	130.85 ± 11.51 ^{b}	94.96 ± 35.62 ^{c}
Springiness (%)	85.16 ± 1.8 ^{b}	82.08 ± 4.22 ^{b}	93.27 ± 6.21 ^{a}	84.74 ± 3.96 ^{b}	83.84 ± 3.42 ^{b}	85.48 ± 6.03 ^{ab}
Chewiness	81.1 ± 11.85 ^{ab}	98.98 ± 23.59 ^{a}	42.26 ± 33.23 ^{bcd}	37.84 ± 5.44 ^{c}	57.32 ± 8.91 ^{d}	62.27 ± 22.99 ^{bd}

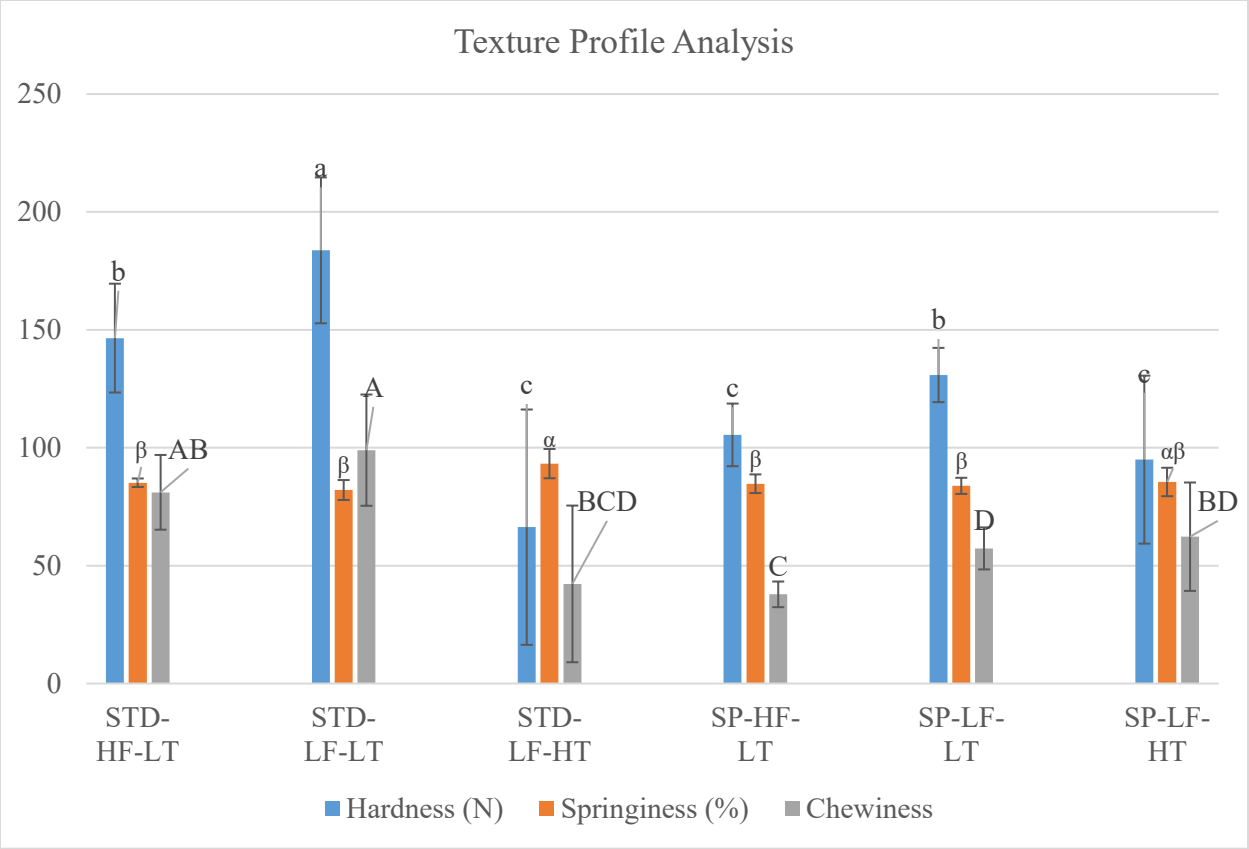

Figure 4.9. Texture profile parameters of HMMA extrudates produced under different formulation and processing-condition combinations. Bars represent mean ± standard deviation. Different letters within each texture parameter indicate significant differences among treatments according to Games-Howell post hoc comparisons ($p < 0.05$).

4.3.3.3 Visual Analysis

Visual inspection of extrudates showed clear differences in internal structure (Table 4.7). In general, the STD treatments appeared more fibrous and organized than the SP treatments, which agrees with their higher visual fibrosity scores (Table 4.8). In the images, these treatments exhibited more layered internal structure, especially in the parallel cuts, where elongated fibrous strands were more visible. In contrast, the SP treatment had a lower visual score and showed a more disrupted, less aligned structure with weaker visible fiber formation.

The images also suggest that the extrusion condition influenced structure development within each formulation. For both STD and SP, the LF-HT condition produced the most visibly oriented and separated fibrous structure, particularly in the parallel-cut images, indicating better alignment along the flow direction. This pattern is consistent with the higher AI values measured for STD-LF-HT (2.37) and SP-LF-HT (2.14). However, the relationship between visual fibrosity score and AI was moderate (r = 0.5, Figure 4.10). In other words, samples that looked more fibrous did not always show proportionally higher anisotropy values. This is reasonable because visual scoring reflects the overall appearance of fibrousness, whereas AI is a more specific quantitative measure of structural orientation.

Overall, the visual analysis supported the main structural trends observed across treatments: STD samples generally exhibited a stronger fibrous appearance than SP samples, and the LF-HT condition promoted the best structural alignment in both formulations. Similar to the descriptive approach used in previous studies, the images were useful for confirming treatment-related differences in product structure and for showing how processing conditions influenced the development of visible fibrous layers and strand separation (Plattner et al., 2024).

Table 4.7. Macro Images of hydrated chunk final products

Treatments	Perpendicular Cut	Parallel Cut
STD-HF-LT		
STD-LF-LT		

STD-LF-HT		
SP-HF-LT		
SP-LF-LT		
SP-LF-HT		

Table 4.8. Visual Fibrosity Score

Sample	Fibrosity Score
STD-HF-LT	8.11 ± 0.59
STD-LF-LT	7.35 ± 0.63
STD-LF-HT	7.63 ± 0.77
SP-HF-LT	4.02 ± 0.96
SP-LF-LT	5.95 ± 0.7
SP-LF-HT	6.75 ± 1

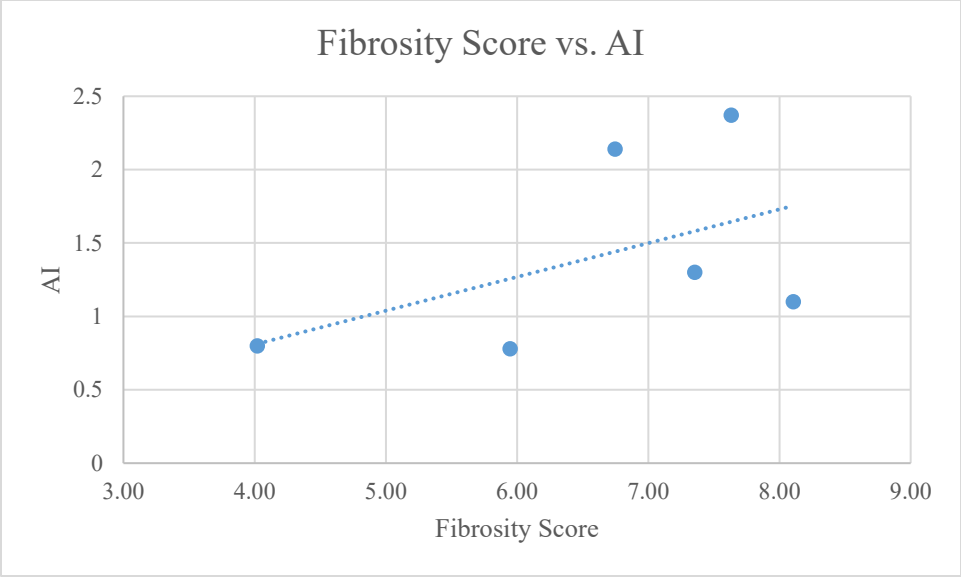

Figure 4.10. Correlation between visual fibrosity score and anisotropy index (AI) across treatments (r = 0.50).

4.3.3.4 Image-Based Fibrosity Score Analysis

Because visual analysis alone is subjective, Fiberlyzer scores were further compared with the AI to determine whether visually detected fibrous structures were also reflected in mechanical behavior. For this purpose, the mean Fiberlyzer scores (Table 4.9) were compared with the overall AI values of the corresponding treatments. A strong positive correlation was found between the two parameters (r = 0.93), indicating that treatments with higher visually quantified fibrous structure also tended to show higher mechanical anisotropy (Figure 4.11). The highest Fiberlyzer scores were observed for the LF-HT treatments in both formulations (STD-LF-HT and SP-LF-HT), which also exhibited the highest AI values. In contrast, the HF-LT treatments showed the lowest Fiberlyzer scores and comparatively lower AI values.

Fiberlyzer, as described by (Ma et al., 2024), quantifies fibrousness based on the geometry of elongated structures detected in macro images, where higher scores reflect more developed and elongated fibrous regions. The strong association observed here suggests that the

visually aligned structures detected in the images were accompanied by greater directional texture development in the extrudates. This finding is valuable because visual fibrousness and mechanical anisotropy are not always reported to correspond closely. In the present study, however, both measurements followed a similar trend across treatments, suggesting that the processing conditions that enhanced visual fiber formation also promoted anisotropic mechanical behavior. This comparison can support the use of Fiberlyzer as a useful complementary approach for assessing fibrous structure development in HMMA products.

Table 4.9. Fiberlyzer Score. Values represent mean ± standard deviation (n = 15 images per treatment). Higher scores indicate a more developed and elongated fibrous structure.

Treatments	Fiberlyzer
STD-HF-LT	5.83 ± 1.63
STD-LF-LT	6.79 ± 3.16
STD-LF-HT	7.83 ± 2.3
SP-HF-LT	5.01 ± 1.58
SP-LF-LT	6.07 ± 2.01
SP-LF-HT	7.64 ± 2.94

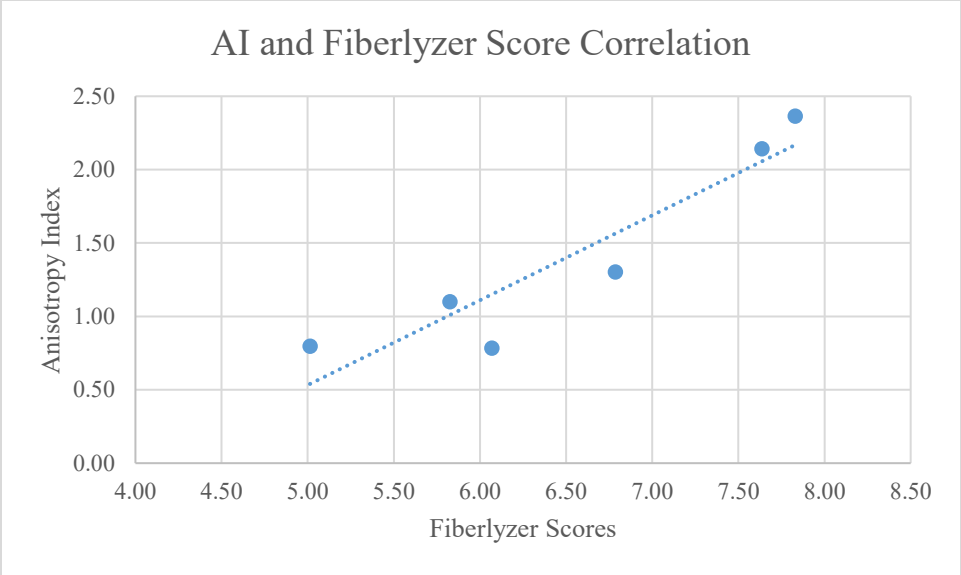

Figure 4.11. Correlation between Fiberlyzer score and anisotropy index (AI) across treatments. A strong positive correlation was observed (r = 0.93).

4.3.3.5 Expert-Guided Deep Learning-Based Fibrosity Estimation

Model performance was assessed using the independent test set of 24 images. The estimated fibrosity scores were strongly correlated with the true mean visual expert scores (r = 0.89; Figure 4.12 and Table 4.10), showing that the deep learning model was generally able to reproduce visual expert evaluations of fibrous structure. While some deviation was observed for individual samples, the estimated scores followed the overall pattern of visual expert scoring across the test images. This indicates that the modified deep learning approach, based on Aljishi et al. (2026), provided a useful additional quantitative measure of fibrosity in HMMA samples.

.

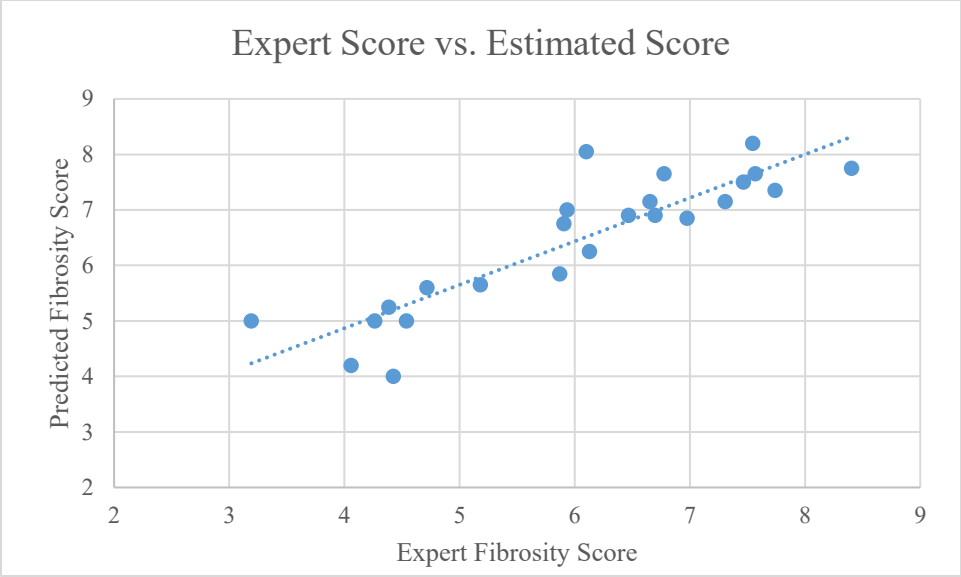

Figure 4.12. Relationship between expert fibrosity scores and estimated fibrosity scores for the test images. Each point represents one image from the test set (n = 24). The strong positive correlation (r = 0.89) indicates good agreement between model predictions and expert evaluation.

Table 4.10. Comparison of visual expert-assigned and estimated fibrosity scores for HMMA images in the test set across all treatments. Visual expert scores represent the mean of two expert ratings (0 = not fibrous, 10 = highly fibrous), and estimated scores were obtained using the modified image-based estimation approach.

Treatments	Visual expert Fibrosity Scores	Estimated Fibrosity Scores		Treatments	Visual expert Fibrosity Scores	Estimated Fibrosity Scores
STD-HF-LT	7.5	7.46		SP-HF-LT	4.2	4.06
	7.65	7.57			4	4.43
	7.35	7.74			5	4.54
	8.05	6.10			5	4.26
STD-LF-LT	6.85	6.97		SP-LF-LT	7	5.93
	6.25	6.13			5.25	4.39
	7.15	7.31			5.6	4.72
	7.15	6.65			5	3.19

STD-LF-HT	6.9	6.47		SP-LF-HT	5.65	5.18
	7.65	6.78			7.75	8.40
	6.9	6.70			5.85	5.87
	8.2	7.54			6.75	5.91

4.4 Conclusion

In summary, both formulation and extrusion conditions played important roles in determining the functionality, processability, and final structure of the soy-based HMMAs. The standard formulation generally showed better hydration, lower gelation concentration, and higher viscosity development than the single-protein formulation, which helped it form a denser and more structured product. During extrusion, high-temperature and low-feed-rate conditions reduced SME and die pressure in both formulations, while also promoting greater structural alignment and fiber formation.

Overall, the LF-HT condition produced the highest anisotropy and the most developed fibrous structure in both formulations, whereas the STD formulation tended to produce firmer and chewier products, especially under low-temperature conditions. These findings show that fibrousness and mechanical texture do not always develop in the same way, and both need to be considered when evaluating HMMA quality. In addition, the strong correlation between Fiberlyzer score and anisotropy index suggests that image-based analysis can be a useful complementary tool for objectively assessing fibrous structure in plant-based meat analogues.

4.5 References

Aljishi, A., Sheikhizadeh, S., Das, S., & Alavi, S. (2026). Estimating Fibrosity Scores of Plant-Based Meat Products from Images: A Deep Neural Network Approach. *Foods, 15*(4), 665. https://doi.org/10.3390/foods15040665

Asgar, M. a., Fazilah, A., Huda, N., Bhat, R., & Karim, A. a. (2010). Nonmeat Protein Alternatives as Meat Extenders and Meat Analogs. *Comprehensive Reviews in Food Science and Food Safety, 9*(5), 513–529. https://doi.org/10.1111/j.1541-4337.2010.00124.x

Aslam, R., Sheikhizadeh, S., Alavi, S., Zhou, W., & Maqsood, S. (2026). Mechanistic evaluation of pea-soy protein isolate and concentrate based high moisture meat analogues: Evaluation of protein blends and extrudate quality. *Journal of Food Engineering, 406*, 112802. https://doi.org/10.1016/j.jfoodeng.2025.112802

Barbut, S. (2015). *The Science of Poultry and Meat Processing.*

Bondu, C., Rouilly, A., Labonne, L., & Evon, P. (2025). Combination of Different Methods, Including Image Analysis, to Define the Fibrous Structure of High-Moisture Extrusion-Cooking Extrudates. *Journal of Texture Studies, 56*(2), e70022. https://doi.org/10.1111/jtxs.70022

Bourne. (2002). *Texture, Viscosity, and Food.* https://doi.org/10.1016/B978-012119062-0/50001-2

Boye, J. I., Aksay, S., Roufik, S., Ribéreau, S., Mondor, M., Farnworth, E., & Rajamohamed, S. H. (2010). Comparison of the functional properties of pea, chickpea and lentil protein concentrates processed using ultrafiltration and isoelectric precipitation techniques. *Food*

Research International, Molecular, Functional and Processing Characteristics of Whole Pulses and Pulse Fractions and Their Emerging Food and Nutraceutical Applications, 43(2), 537–546. https://doi.org/10.1016/j.foodres.2009.07.021

Chen, F. L., Wei, Y. M., Zhang, B., & Ojokoh, A. O. (2010). System parameters and product properties response of soybean protein extruded at wide moisture range. *Journal of Food Engineering, 96*(2), 208–213. https://doi.org/10.1016/j.jfoodeng.2009.07.014

Dekkers, B. L., Nikiforidis, C. V., & van der Goot, A. J. (2016). Shear-induced fibrous structure formation from a pectin/SPI blend. *Innovative Food Science & Emerging Technologies, 36*, 193–200. https://doi.org/10.1016/j.ifset.2016.07.003

Elzerman, J. E., Hoek, A. C., Boekel, M. A. J. S. van, & Luning, P. A. (2011). Consumer acceptance and appropriateness of meat substitutes in a meal context. *Food Quality and Preference, 22*(3), 233–240. https://doi.org/10.1016/j.foodqual.2010.10.006

Fan, F. H., Ma, Q., Ge, J., Peng, Q. Y., Riley, W. W., & Tang, S. Z. (2013). Prediction of texture characteristics from extrusion food surface images using a computer vision system and artificial neural networks. *Journal of Food Engineering, 118*(4), 426–433. https://doi.org/10.1016/j.jfoodeng.2013.04.015

Ferawati, F., Zahari, I., Barman, M., Hefni, M., Ahlström, C., Witthöft, C., & Östbring, K. (2021). High-Moisture Meat Analogues Produced from Yellow Pea and Faba Bean Protein Isolates/Concentrate: Effect of Raw Material Composition and Extrusion Parameters on Texture Properties. *Foods, 10*(4), 843. https://doi.org/10.3390/foods10040843

Florence O. Uruakpa. (2012). Gelling Behavior of Plant Proteins and Polysaccharides in Food Systems. *Journal of Food Science and Engineering, 2*(5). https://doi.org/10.17265/2159-5828/2012.05.001

Flory, J., Xiao, R., Li, Y., Dogan, H., Talavera, M. J., & Alavi, S. (2023). Understanding Protein Functionality and Its Impact on Quality of Plant-Based Meat Analogues. *Foods, 12*(17), 3232. https://doi.org/10.3390/foods12173232

Grabowska, K. J., Tekidou, S., Boom, R. M., & van der Goot, A.-J. (2014). Shear structuring as a new method to make anisotropic structures from soy–gluten blends. *Food Research International, 64*, 743–751. https://doi.org/10.1016/j.foodres.2014.08.010

Gulzar, S., Tagrida, M., Martín-Belloso, O., & Soliva-Fortuny, R. (2025). Optimizing high-moisture meat analogue textures through Artificial Intelligence: The effect of sorbitol in soy protein concentrate blends. *LWT, 217*, 117416. https://doi.org/10.1016/j.lwt.2025.117416

Hong, S., Shen, Y., & Li, Y. (2022). Physicochemical and Functional Properties of Texturized Vegetable Proteins and Cooked Patty Textures: Comprehensive Characterization and Correlation Analysis. *Foods, 11*(17), 2619. https://doi.org/10.3390/foods11172619

Jarpa-Parra, M. (2018). Lentil protein: A review of functional properties and food application. An overview of lentil protein functionality. *International Journal of Food Science and Technology, 53*(4), 892–903. https://doi.org/10.1111/ijfs.13685

Jia, W., Curubeto, N., Rodríguez-Alonso, E., Keppler, J. K., & van der Goot, A. J. (2021). Rapeseed protein concentrate as a potential ingredient for meat analogues. *Innovative Food Science & Emerging Technologies, 72*, 102758. https://doi.org/10.1016/j.ifset.2021.102758

Jones, O. G. (2016). Recent advances in the functionality of non-animal-sourced proteins contributing to their use in meat analogs. *Current Opinion in Food Science, Food Chemistry and Biochemistry • Food Bioprocessing, 7*, 7–13. https://doi.org/10.1016/j.cofs.2015.08.002

Kamani, M. H., Liu, J., Fitzsimons, S. M., Fenelon, M. A., & Murphy, E. G. (2024). Determining the influence of fava bean pre-processing on extractability and functional quality of protein isolates. *Food Chemistry: X, 21*, 101200. https://doi.org/10.1016/j.fochx.2024.101200

Ketnawa, S., Chaijan, M., Grossmann, L., & Rawdkuen, S. (2024). High-moisture soy protein-mushroom-based meat analogue: Physicochemical, structural properties and its application. *International Journal of Food Science and Technology, 59*(1), 596–614. https://doi.org/10.1111/ijfs.16595

Ma, Y., Schlangen, M., Potappel, J., Zhang, L., & van der Goot, A. J. (2024). Quantitative characterizations of visual fibrousness in meat analogues using automated image analysis. *Journal of Texture Studies, 55*(1), e12806. https://doi.org/10.1111/jtxs.12806

McClements, D. J. (with Grossmann, L.). (2022). *Next-generation plant-based foods: Design, production, and properties.* Springer.

McClements, D. J., Weiss, J., Kinchla, A. J., Nolden, A. A., & Grossmann, L. (2021). Methods for Testing the Quality Attributes of Plant-Based Foods: Meat- and Processed-Meat Analogs. *Foods, 10*(2), 260. https://doi.org/10.3390/foods10020260

Mession, J.-L., Chihi, M. L., Sok, N., & Saurel, R. (2015). Effect of globular pea proteins fractionation on their heat-induced aggregation and acid cold-set gelation. *Food Hydrocolloids, 46*, 233–243. https://doi.org/10.1016/j.foodhyd.2014.11.025

Michel, F., Hartmann, C., & Siegrist, M. (2021). Consumers' associations, perceptions and acceptance of meat and plant-based meat alternatives. *Food Quality and Preference.* https://www.semanticscholar.org/paper/Consumers%E2%80%99-associations%2C-perceptions-and-acceptance-Michel-Hartmann/5850bdf8b73f42a256c16f75125365000d8744dc

Naz, M. Y., Sulaiman, S. A., Ariwahjoedi, B., & Shaari, K. Z. K. (2014). Characterization of Modified Tapioca Starch Solutions and Their Sprays for High Temperature Coating Applications. *The Scientific World Journal, 2014*, 375206. https://doi.org/10.1155/2014/375206

Osen, R., Toelstede, S., Wild, F., Eisner, P., & Schweiggert-Weisz, U. (2014). High moisture extrusion cooking of pea protein isolates: Raw material characteristics, extruder responses, and texture properties. *Journal of Food Engineering, 127*, 67–74. https://doi.org/10.1016/j.jfoodeng.2013.11.023

Palanisamy, M., Franke, K., Berger, R. G., Heinz, V., & Töpfl, S. (2019). High moisture extrusion of lupin protein: Influence of extrusion parameters on extruder responses and product properties. *Journal of the Science of Food and Agriculture, 99*(5), 2175–2185. https://doi.org/10.1002/jsfa.9410

Plant-based Meat Market Size, Share & Growth Report, 2030. (n.d.). Retrieved March 17, 2026, from https://www.grandviewresearch.com/industry-analysis/plant-based-meat-market

Plattner, B. J., Hong, S., Li, Y., Talavera, M. J., Dogan, H., Plattner, B. S., & Alavi, S. (2024). Use of Pea Proteins in High-Moisture Meat Analogs: Physicochemical Properties of Raw

Formulations and Their Texturization Using Extrusion. *Foods, 13*(8), 1195. https://doi.org/10.3390/foods13081195

Riaz, M. N. (Ed.). (2000). *Extruders in Food Applications.* CRC Press. https://doi.org/10.1201/9781482278859

Sathe, S. K., & Salunkhe, D. K. (1981). Functional Properties of the Great Northern Bean (*Phaseolus vulgaris* L.) Proteins: Emulsion, Foaming, Viscosity, and Gelation Properties. *Journal of Food Science, 46*(1), 71–81. https://doi.org/10.1111/j.1365-2621.1981.tb14533.x

Schreuders, F. K., Dekkers, B., Bodnár, I., Erni, P., Boom, R., & Goot, A. J. van der. (2019). Comparing structuring potential of pea and soy protein with gluten for meat analogue preparation. *Journal of Food Engineering.* https://www.semanticscholar.org/paper/Comparing-structuring-potential-of-pea-and-soy-with-Schreuders-Dekkers/9ba98fa7a6b096d7e066b5c206904de061876dfd

Wagner, C. E., & Ganjyal, G. M. (2024). Impact of functional dietary fiber incorporation on the appearance and mechanical properties of extruded high moisture meat analogs. *Journal of Food Science, 89*(8), 4953–4968. https://doi.org/10.1111/1750-3841.17164

Webb, D., Dogan, H., Li, Y., & Alavi, S. (2023). Physico-Chemical Properties and Texturization of Pea, Wheat and Soy Proteins Using Extrusion and Their Application in Plant-Based Meat. *Foods, 12*(8), 1586. https://doi.org/10.3390/foods12081586

Webb, D., Plattner, B. J., Donald, E., Funk, D., Plattner, B. S., & Alavi, S. (2020). Role of chickpea flour in texturization of extruded pea protein. *Journal of Food Science, 85*(12), 4180–4187. https://doi.org/10.1111/1750-3841.15531

Zahari, I., Östbring, K., Purhagen, J. K., & Rayner, M. (2022). Plant-Based Meat Analogues from Alternative Protein: A Systematic Literature Review. *Foods, 11*(18), 2870. https://doi.org/10.3390/foods11182870

Chapter 5 - Printability and Structural Properties of Plant-Based Meat Analogs in Extrusion-Based 3D Food Printing: Role of Protein Type, Methylcellulose, and Pea Fiber

Abstract

Driven by demand for sustainable meat alternatives, this research investigated how protein type and functionality influence the structure, texture and performance of plant-based meat produced using additive manufacturing. 3D printed plant-based meat, based on soy and pea protein isolates, in combination with various supplemental ingredients, was the focus of this study.

Before evaluating the different process technologies and plant-based meat products, the functionality of various plant proteins was characterized because it strongly influenced structure development and product quality. Based on water absorption capacity (WAC) and rapid visco-analysis (RVA), soy protein isolate (SPI) was classified as cold swelling protein due to its high WAC (5.75 g/g) and/or low-temperature peak viscosity (30 °C). In contrast, pea protein isolate (PPI) behaved as non-cold swelling ingredient, showing lower hydration and/or requiring higher temperatures to develop viscosity. Cold swelling proteins generally show higher viscosity. These functional differences helped explain variation in processing behavior, texture and final structure of 3D printed plant-based meat.

This study explored extrusion-based 3D printing of plant-based meat using PPI and SPI with different levels of methylcellulose (MC) and pea fiber (PF). SPI (cold swelling) hydrated faster than PPI (non-cold swelling) and produced plant protein ink with higher viscosity. SPI

formulations were firmer, reaching hardness up to 23.47 N, likely because faster hydration and higher viscosity formed a stronger, more cohesive printed network. MC showed very high WAC (9.93 g/g) and increased viscosity, which helped to print filaments that set quickly after deposition. However, at higher MC levels, this strong thickening made the ink overly viscous and elastic, limiting relaxation after extrusion and reducing dimensional stability, reflected by more negative dimensional distortion ratio (DDR) values (as low as -0.27), where DDR compares the measured printed dimensions with the intended design, and values closer to zero indicate better shape fidelity. In contrast, PF improved shape retention by providing more gradual water binding and physical support, reducing deformation and bringing DDR closer to zero.

This research showed that the quality of plant-based meat processed using an extrusion-based 3D printer depended on the combination of protein functionality, supplemental ingredients and processing. Differences in hydration, viscosity and formulation shaped structure and texture, providing an improved theoretical and scientific framework and practical guidance for designing better quality plant-based meat products.

5.1 Introduction

Three-dimensional (3D) printing, also known as additive manufacturing, refers to the fabrication of solid objects through the layer-by-layer deposition of materials based on a digital model (Dankar et al., 2018; Z. Liu et al., 2017). Since its early development in the 1980s, this technology has evolved from a rapid prototyping tool into a versatile manufacturing platform used across aerospace, medical, automotive, and advanced materials industries (Lipson et al.,

2013). Compared with conventional molding or subtractive manufacturing, 3D printing enables complex geometries, internal structural control, material integration, and reduced material waste (Z. Liu et al., 2017; Sun et al., 2015). These advantages have positioned additive manufacturing as a transformative production approach with broad industrial implications.

The application of this technology to food, known as 3D food printing, adapts the principles of additive manufacturing to edible materials such as dough, chocolate, and protein-based pastes (Mantihal et al., 2017; Sun et al., 2015; Wang et al., 2017). In extrusion-based food printing, the most widely used method in the food sector, materials are deposited in successive layers to create customized shapes and structures (Godoi, Prakash, and Bhandari 2016). Successful printing depends primarily on two key material properties: extrudability, which allows continuous flow through the nozzle, and shape stability, which ensures structural fidelity after deposition (Schwab et al., 2020). Therefore, the rheological and physicochemical characteristics of the printing material are central to product quality and process reliability.

Beyond geometric flexibility, 3D food printing offers additional advantages compared to traditional food processing. It enables personalized nutritional design, incorporation of functional ingredients, utilization of cosmetically imperfect raw materials, and potential reduction of food waste (An et al., 2019; Dankar et al., 2018; Lipton et al., 2015). These capabilities are particularly relevant in the context of increasing demand for plant-based and sustainable food products. Several reviews have summarized the principles, applications, and advantages of 3D food printing, as well as the effects of material properties, process parameters, and post-processing on product quality (Z. Liu et al., 2017; Shah et al., 2024; Varvara, Szabo, and Vodnar 2021; Zhang et al., 2021). However, despite this growing body of literature, important knowledge gaps remain.

Specifically, limited research has examined how individual formulation components, such as plant protein type, methylcellulose concentration, and fiber inclusion, interact to influence both printing behavior and the physicochemical performance of plant-based meat inks. Although previous studies highlight the importance of material characteristics in determining printing precision and structural stability (Dankar et al., 2018; Zhang et al., 2021) the direct relationship between composition, rheological behavior, and post-print structural integrity remains insufficiently understood. In particular, comparative evaluation of different plant proteins under controlled variations of structuring agents and fiber levels is still lacking. This gap restricts the ability to rationally design formulations that achieve both smooth extrusion and dimensional stability after printing.

Plant proteins such as pea protein isolate (PPI) and soy protein isolate (SPI) are widely used in extrusion-based meat analogue development due to their gelation capacity and ability to form a structured matrix (Aghababaei et al., 2025; Bhuiyan, Yeasmen, and Orsat 2025). Methylcellulose (MC) is frequently incorporated as a thermo-reversible binder that forms a heat-induced gel network and improves moisture retention and structural cohesion (Wen, Kim, and Park 2022; Yuliarti et al., 2023). Pea fiber (PF), due to its good water-holding capacity and porous structure, may enhance water distribution and shape retention in printed pastes (Venkatachalam et al., 2026). While each of these ingredients has been individually associated with improved functionality in plant-based ingredients, their combined and comparative effects within 3D printing formulations have not been comprehensively evaluated using integrated analyses of water absorption capacity (WAC), rapid visco analyzer (RVA), least gelation concentration (LGC), dimensional deformation rate (DDR), and texture profile analysis.

Therefore, the objective of this study was to investigate the effects of plant protein type (PPI vs. SPI), methylcellulose concentration, and pea fiber inclusion on the printability and structural stability of plant-based meat formulations designed for extrusion-based 3D printing. Two formulation sets were developed: one varying methylcellulose concentration within each protein and another varying pea fiber inclusion while maintaining constant total solids. By combining physicochemical measurements (WAC, RVA, LGC) with printing performance indicators (DDR) and post-print texture analysis, this study aims to clarify how compositional adjustments influence both flow behavior during extrusion and structural integrity after deposition.

It was hypothesized that increasing methylcellulose concentration would enhance structural stability and reduce dimensional deformation due to its gel-forming and binding properties (Wen et al., 2022). It was further hypothesized that inclusion of pea fiber would improve water management and shape retention, but excessive fiber levels might disrupt matrix cohesion and negatively affect extrusion continuity (Venkatachalam et al., 2026). Additionally, differences between PPI and SPI-based blends were expected due to variations in protein structure and hydration behavior, particularly in relation to cold swelling capacity and water-protein interactions. Proteins with higher cold swelling behavior (such as SPI) can hydrate and expand more at lower temperatures, resulting in higher viscosity and stronger network formation before thermal treatment, whereas non-cold swelling proteins (such as PPI) tend to require heat or additional structuring agents to achieve comparable gel development. Differences in molecular interactions and crosslinking influence water uptake, chain mobility, and mechanical stability (Flory et al., 2023). These structural and hydration-related differences were therefore

expected to lead to distinct rheological responses and printing outcomes between PPI and SPI-based formulations.

By addressing the interaction between protein source, binder concentration, and fiber inclusion, this study seeks to contribute to the understanding of formulation design in plant-based 3D printed meat. Such insights are essential for advancing the development of structurally stable, customizable, and sustainable printed food products.

5.2 Materials and Methods

5.2.1 Ingredients and formulation

After preliminary testing involving multiple ingredient ratios, 12 final formulations were selected for evaluation in this study. The formulations were specifically designed to examine the effects of different plant proteins, Methylcellulose (MC), and pea fiber (PF) on food 3D printing behavior and the physicochemical characteristics of the formulations.

The first set of formulations was developed to examine the role of methylcellulose as a structuring and binding agent in 3D printed plant-based meat. A single base formulation was established, consisting of a plant protein isolate (either PPI or SPI), pregelatinized corn starch, vegetable oil, xanthan gum, potassium chloride, and pea fiber. Methylcellulose content was varied while all other ingredients were proportionally adjusted to maintain a constant total solids content.

Three methylcellulose ratios were tested relative to the base dry mix: 100:0 (control, no methylcellulose), 96.7:3.3, and 93.3:6.7 (base mix:methylcellulose). These ratios were selected to provide two incremental amounts of methylcellulose content. Each of these three formulations

was prepared using either PPI or SPI, for a total of six formulations. This design allowed the effect of methylcellulose concentration to be evaluated independently within each protein blend.

A second set of formulations was developed to investigate the influence of pea fiber inclusion on formulation behavior and printability. For this set, a different base formulation was used, consisting of a plant protein isolate (PPI or SPI), pregelatinized corn starch, vegetable oil, xanthan gum, potassium chloride, and methylcellulose held at a constant level. Pea fiber content was varied while the remaining dry ingredients were proportionally scaled to preserve a constant total solids content.

Three pea fiber ratios were tested relative to the base dry mix: 100:0 (control, no added pea fiber), 85.5:14.5, and 71:29 (base mix:pea fiber). Each formulation was prepared using PPI or SPI, yielding six formulations in this set. This approach enabled direct comparison of fiber effects within and across proteins.

Two intermediate formulations (3.3% methylcellulose and 14.5% pea fiber) across the two formulation sets were compositionally identical. These formulations were intentionally prepared and printed in separate experimental series to facilitate clearer and more direct comparison across formulation sets.

PPI (Puris Pea 870, PURIS Foods, Minneapolis, MN, USA) and SPI (Profam 974, Archer Daniels Midland Company, Abilene, KS, USA) were used as the main protein bases because pea and soy proteins are among the most common protein platforms reported for extrusion-based food and 3D printed meat analogue development, and they support key functions such as gelation, emulsification, or oil-binding, and structure formation (Aghababaei et al., 2025; Bhuiyan et al., 2025). Pregelatinized corn starch (Onuva, Izmir, Turkey) was included as a viscosity-building carbohydrate to support extrusion or printing behavior. Starch-based

components are widely used in printable inks because their rheology can be tuned to balance flow through the nozzle with shape retention after deposition (Bhuiyan et al., 2025). Vegetable (soybean) oil (Hy-Vee, Inc., West Des Moines, IA, USA) was incorporated as a lipid phase that can be immobilized or emulsified within the protein network and contribute to the overall functional behavior of the ink, such as lubrication during flow and fat-like functionality (Bhuiyan et al., 2025). Xanthan gum (Micro Ingredients, Montclair, CA, USA) was added at low levels to provide shear-thinning behavior, allowing the material to flow during extrusion and recover its structure after printing to help maintain the printed shape (Bhuiyan et al., 2025; Liu et al., 2023). Potassium chloride (Micro Ingredients, Montclair, CA, USA) was included as a mineral salt to facilitate smoother extrusion by reducing gel viscosity and improving flow through the nozzle, as salts have been shown to enhance water binding and enable more consistent extrusion behavior in meat analogue and 3D printing (Bhuiyan et al., 2025). However, KCl is known to produce bitter, chemical, or metallic off-tastes, particularly at higher concentrations (Ben Abu et al., 2018). Because the present study focused on physicochemical properties, printability, and final product structure, sensory acceptability was not evaluated. Therefore, optimization of the KCl concentration or the use of taste-masking strategies should be considered before consumer application.

Methylcellulose (Modernist Pantry, Portsmouth, NH, USA) is a cellulose-ether ingredient that forms a gel network when heated and can create a thermo-reversible gel (Yuliarti et al., 2023). Because it binds water effectively, it helps retain moisture and can improve sensory-related texture and eating quality. Methylcellulose is often considered a strong binder option for plant proteins, including 3D printed meat analogues, where controlled structure formation and moisture management are important (Wen et al., 2022). Finally, pea fiber (Anchor Ingredients,

Fargo, ND, USA) was included in the formulation to improve water holding capacity and structural stability of the 3D print paste. Due to its high WHC and porous fiber network, pea fiber helps regulate water distribution within the ink, supporting consistent extrusion and shape retention after deposition (Venkatachalam et al., 2026).

Although both methylcellulose and pea fiber contribute to water management and structural development, they function through different mechanisms. Methylcellulose is a thermoresponsive hydrocolloid that increases viscosity and forms a heat-induced gel network, thereby acting primarily as a binder within the protein matrix. In contrast, pea fiber functions mainly as a particulate structural filler, absorbing water, swelling, and physically reinforcing the matrix. Therefore, methylcellulose primarily modifies rheology and thermal gelation, whereas pea fiber mainly contributes to physical reinforcement and post-deposition shape retention.

Dietary fiber can be classified into soluble and insoluble fractions based on its behavior in water. Soluble dietary fiber dissolves or disperses in the aqueous phase and can contribute more directly to viscosity and gel-like behavior, whereas insoluble dietary fiber remains as hydrated particles and primarily contributes through water retention, swelling, and physical reinforcement (Wang et al., 2024). Pea fiber fractions are generally dominated by insoluble non-starch polysaccharides, particularly cellulose-rich material, although smaller soluble fractions containing pectic polysaccharides may also be present (Ralet, Della Valle, and Thibault 1993). Accordingly, insoluble pea fiber may primarily reinforce the food matrix through particle hydration and swelling, while its soluble fraction may additionally contribute to continuous-phase viscosity. The soluble and insoluble fractions of the commercial pea fiber used in the present study were not separately quantified.

The detailed composition of base formulations and final percentages of each formulation are provided in Tables 5.1 to 5.3.

Table 5.1. Composition of base formulations

Base formulation - for varied methylcellulose concentration (%db)			Base formulation - for varied pea fiber concentration (%db)	
PPI or SPI	62.67		PPI or SPI	70.87
Pregel starch	8.67		Pregel starch	9.79
Vegetable oil	6.33		Vegetable oil	7.17
Xanthan Gum	0.73		Xanthan Gum	0.83
Potassium Chloride (KCl)	6.60		Potassium Chloride (KCl)	7.45
Pea Fiber	15.00		Methylcellulose	3.90

Table 5.2. Methylcellulose inclusion level treatments ratios

	Treatment 1, PPI	Treatment 2, PPI	Treatment 3, PPI	Treatment 4, SPI	Treatment 5, SPI	Treatment 6, SPI
Base Formulation	100	96.7	93.3	100	96.7	93.3
Methylcellulose	0	3.3	6.7	0	3.3	6.7

Table 5.3. Pea Fiber inclusion level treatments ratios

	Treatment 7, PPI	Treatment 8, PPI	Treatment 9, PPI	Treatment 10, SPI	Treatment 11, SPI	Treatment 12, SPI
Base Formulation	100	85.5	71	100	85.5	71
Pea Fiber	0	14.5	29	0	14.5	29

5.2.2 Raw Material Analysis

5.2.2.1 Moisture Content

The moisture content of the raw materials was determined using the AACC Method 44-19.01. Briefly, duplicate samples (2 g each) were dried at 135 °C for 2 h according to the standard protocol.

5.2.2.2 Water Absorption Capacity (WAC)

WAC was measured following the procedure reported by Webb, Dogan, et al. (2023). In brief, 2.5 g of each sample (individual material and blends) was transferred to centrifuge tubes and mixed with 30 mL of deionized water. The suspensions were vortexed for 30 s to promote uniform mixing and then left at room temperature for 30 min, with occasional gentle agitation. Samples were subsequently centrifuged at 3000 g for 30 min, and the excess water was carefully decanted. WAC was expressed as the amount of water retained per gram of dry sample.

WAC was calculated using the following equation:

$$WAC\ \left(\frac{g_{water}}{g_{protein}}\right) = \frac{W_f - W_i}{W_i} \quad (5.1)$$

Where W_f is the weight of the sediment and W_i is the initial weight of the sample.

5.2.2.3 Least Gelation Concentration (LGC)

LGC was evaluated based on the method of Sathe and Salunkhe (1981), with minor modifications. Protein slurries were prepared by dispersing samples (individual raw materials and blends) in 10 mL of distilled water to achieve concentrations ranging from 8% to 20% (w/v). The mixtures were manually stirred in clean, dry glass test tubes to ensure complete hydration. The tubes were then heated in a boiling water bath (90 - 100 °C) for 1 hour, cooled under

running water for 10 minutes, and subsequently refrigerated at 4 °C for 2 h. LGC was defined as the lowest protein concentration at which the gel remained firm and did not flow when the test tube was inverted. This test was conducted in duplicate.

5.2.2.4 Rapid Visco Analyzer (RVA)

The thermal viscosity behavior of individual protein ingredients and formulated blends was evaluated using a Rapid Visco Analyzer (RVA 4800, Perten Instruments), following the general procedure outlined in AACC Method 76-21.02 (STD1) with a modified initial temperature. Viscosity changes were monitored as a function of time and temperature, allowing for the assessment of both cold swelling and non-cold swelling behavior. These viscosity changes provide insight into functional changes that are relevant to the extrusion and extruding material during 3D printing (Osen et al., 2014).

For each measurement, approximately 3.5 g of sample (dry basis) was weighed, with the exact amount adjusted based on the moisture content of each ingredient or formulation to obtain a final solids concentration of 14% (w/v). Samples were dispersed in 25 mL of distilled water and transferred to the RVA canister. The slurry was initially equilibrated at 30 °C under high shear (960 rpm) for 10 seconds, followed by a 50-second holding period at the same temperature with the reduced paddle speed to 160 rpm. The temperature was then increased from 30 to 95 °C (under 160 rpm shear rate) between 1:00 and 4:42 min, followed by a holding period at 95 °C from 4:42 to 7:12 min. The sample was subsequently cooled from 95 to 30 °C between 7:12 and 11:00 min, and finally held at 30 °C from 11:00 to 13:00 min, marking the end of the test.

Viscosity was recorded continuously throughout the heating and cooling cycle to generate thermal viscosity profiles for each sample. All measurements were conducted in duplicate.

5.2.3 Ink Preparation

The inks were prepared as follows. Potassium chloride was first dissolved in the total amount of water required for ink preparation. The water phase constituted 70% of the final formulation, while the remaining 30% consisted of the dry ingredient blend. All dry ingredients were then added to the saline solution and combined using a laboratory scale food blender (NutriBullet, Capital Brands Holdings Inc., Los Angeles, CA, USA) and mixed for 30 s. After each 30 s mixing cycle, the material was manually scraped and remixed to ensure uniform dispersion. This process was repeated three times to achieve homogeneous mixing and consistent ingredient distribution.

The resulting raw formulation was transferred into a special plastic syringe designed for food 3D printing. The filled syringes were then stored at 4 °C for 24 hours to allow hydration and penetration. Previous tests indicated that a 24 h refrigeration period improves printability by promoting uniform water distribution and reducing the formation of agglomerates that could lead to nozzle clogging.

Prior to printing, the syringes were removed from refrigeration and equilibrated at room temperature for 2 h. Finally, the syringe containing the prepared ink was loaded into the food 3D printer for printing.

5.2.4 3D Printing Process

Three-dimensional printing was performed using a Foodbot S2 multi-ingredient food 3D printer (Changxing Shiyin Technology Co., Ltd., Hangzhou, China). The system utilizes a motor-driven plunger mechanism with a maximum extrusion force of 3 kg, depositing material through disposable, food-grade syringe or tube assemblies to minimize direct contact between the formulation and printer hardware and support hygienic operation. The printer provides a maximum build volume of 150 × 150 × 73 mm (X × Y × Z) and supports a nominal printing speed range of 15 - 70 mm/s. During printing, the effective speed was adjusted using the on-device speed control, enabling lower operating speeds when required by formulation flow behavior. Interchangeable nozzles with internal diameters spanning 0.3 - 1.5 mm were available and selected based on the required feature resolution and formulation rheology. Printing was started and managed directly on the printer using pre-generated G-code files loaded from a USB flash drive.

For printing, the previously equilibrated, ink-filled syringes were used and loaded into the printer syringe holder. The extrusion temperature was set to 30 °C, as preliminary tests indicated this temperature provided optimal material flow and printability for the formulations. Printing speed was adjusted according to ink viscosity based on prior optimization trials, ranging from 3.75 mm/s for highly viscous inks to 15 mm/s for formulations with lower viscosity. Printing was performed using a nozzle with an internal diameter of 1.2 mm. The printed model had dimensions of 22.9 × 41.8 × 14.3 mm, with a layer height of 0.72 mm. Print duration varied depending on the selected printing speed. All samples were printed onto wax paper substrates. Five replicates per treatment were printed for formulations with varying methylcellulose levels,

and seven replicates per treatment were printed for formulations with varying pea fiber levels. Representative 2D and 3D views of the printed model are shown in Figures 5.1 and 5.2.

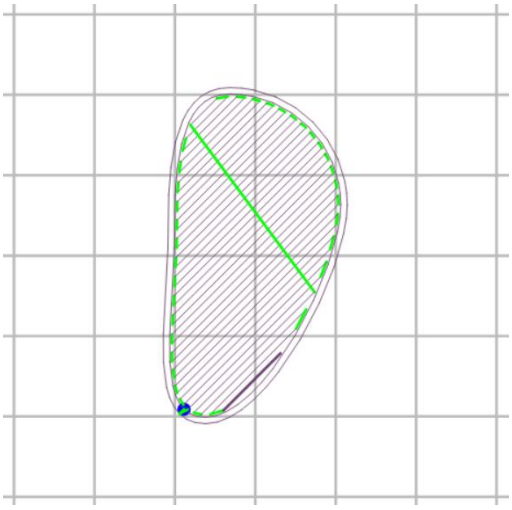

Figure 5.1. 2D View of Printed Model

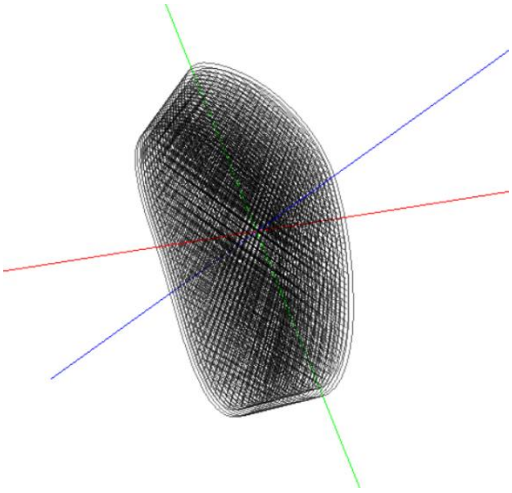

Figure 5.2. 3D View of Printed Model

5.2.5 Post-Printing Process

Printed samples, together with the wax paper substrate, were transferred to covered metal Petri dishes to minimize moisture loss and were immediately placed in a freezer. After 24 hours, samples were removed, and their dimensions were measured while frozen using a digital caliper to reduce deformation during handling. Samples were placed in covered Petri dishes and then steamed in a Black&Decker Flavor Scenter steamer (Stanley Black & Decker, USA) for 3 hours to avoid direct exposure to steam. This steaming time was selected based on preliminary trials showing that shorter times resulted in an undercooked, paste-like interior, whereas 3 hours produced a cooked internal texture with no additional observable change upon further steaming. Following steaming, samples (still on wax paper) were placed into a sealed, threaded 316 stainless-steel metal chamber (2-inch, Class 150) to limit moisture loss during baking, and were heated in an oven at 150 °C for 65 min to achieve final cooking and light surface browning. All cooking conditions (steam and oven temperatures and times) were determined based on preliminary optimization trials conducted prior to the main experiments. After final cooking, sample dimensions were measured again using a caliper, transferred back to covered metal Petri dishes, and stored in the freezer until subsequent analyses.

5.2.6 Extrudate Analysis

5.2.6.1 Distortion Dimension Ratio (DDR)

Dimensional accuracy of the printed samples was evaluated using the dimensional distortion ratio (DDR), adapted from the approach proposed by Asadi-Eydivand et al. (2016). Because the printed samples were not perfectly symmetric, lateral dimensions were defined using the major axis length and the maximum width rather than a single circular diameter. The

sample length (A_l) was measured along the longest direction of the printed sample, and the width (A_w) was defined as the lateral dimension at the location where the printed sample reached its maximum width. The sample height (A_h) was measured as the vertical dimension of the printed sample. All measurements were obtained using a digital caliper. The corresponding dimensions from the .stl file were used as reference values.

The DDR was calculated as:

$$DDR = \frac{\frac{A_l + A_w}{2}}{A_h} - \frac{\frac{stl_l + stl_w}{2}}{stl_h} \quad (5.2)$$

where A_l represents the measured length, A_w is the measured maximum width, and A_h is the measured height of the printed sample, while stl_l, stl_w, and stl_h represent the corresponding dimensions defined in the .stl file.

A DDR value of zero indicates no distortion relative to the designed geometry. Positive DDR values indicate lateral expansion relative to height, whereas negative DDR values indicate relative elongation in the vertical direction.

5.2.6.2 Texture Profile Analysis (TPA)

TPA was used to evaluate the mechanical texture properties of the final products. A two-cycle compression test was applied to simulate the chewing process and to generate force–time curves from which textural parameters were calculated (Bourne 2002).The primary parameters evaluated were hardness, springiness, and chewiness.

Before TPA measurements, cooked samples that had been stored frozen in Petri dishes were transferred to the refrigerator and allowed to thaw for 24 h under refrigerated conditions. After thawing, samples were subjected to TPA analysis.

All TPA measurements were performed using a TA-XT2 Texture Analyzer (Texture Technologies Corp., Scarsdale, NY, USA), following the general methodology described by Webb et al. (2020) with minor modifications to account for differences in sample type and preparation. A cylindrical compression probe with a diameter of 25 mm was used for all measurements. Samples were subjected to two consecutive compressions to 25% strain with a hold time of 1 s between compressions, using a trigger force of 2.5 g. The pre-test speed was set to 1 mm/s, while the test and post-test speeds were set to 3 mm/s.

Hardness was defined as the maximum force recorded during the first compression cycle. Springiness was calculated as the ratio of the recovered distance between the end of the first compression and the start of the second compression. Chewiness was calculated as the product of hardness and springiness multiplied by the ratio of the area under the second compression curve to that of the first (Bourne 2002). The number of replicates was determined by the number of samples tested, with five for the formulations with varying methylcellulose levels and seven for the formulations prepared with varying pea fiber levels.

5.2.6.3 Visual Analysis

The structure of the 3D printed samples was evaluated after cooking using high-resolution macro imaging. Images of the printed products were captured with a Nikon Z 7II digital camera equipped with a 105 mm NIKKOR Z macro lens and a Godox MF-R76N TTL macro ring flash to ensure uniform and shadow-minimized illumination. A Kaiser RS1 copy stand was used to maintain a fixed camera position and working distance. The distance between the camera and the sample was maintained at approximately 50 cm using the copy stand scale to ensure consistent framing across samples. Samples were positioned on the stand's non-reflective

matte gray baseboard with a printed 1-cm grid, which provided a consistent background and scale reference across all images. Image acquisition was performed using Nikon NX Tether software (version 2.4.0) with a tether profile (version 9.0) under consistent shooting conditions.

5.2.7 Statistical Analysis

Statistical analyses were performed using analysis of variance (ANOVA) according to the experimental design. For experiments involving a single factor, one-way ANOVA was applied, whereas factorial experiments were analyzed using two-way ANOVA to evaluate the effects of each factor and their interaction. Assumptions of normality and homogeneity of variance were assessed prior to analysis. When significant differences were detected, post-hoc multiple comparisons were conducted to identify differences among treatments. Results are reported as mean ± standard deviation or estimated marginal means ± standard error, as appropriate. Statistical significance was determined at $p < 0.05$.

5.3 Results and Discussion

5.3.1 Raw Material Characteristics

5.3.1.1 Water Absorption Capacity (WAC)

WAC differed markedly among the individual ingredients (Figure 5.3). Xanthan gum exhibited the highest WAC (12.18 g/g), followed by methylcellulose (9.93 g/g). Pea fiber showed a WAC of 6.45 g/g, while pregelatinized corn starch and SPI demonstrated moderate values of 5.81 and 5.75 g/g, respectively. PPI had the lowest WAC among the tested materials (2.98 g/g). The high WAC of pea fiber is consistent with values reported by Webb et al. (2023),

where pea fiber exhibited nearly twice the WAC of PPI. This behavior can be attributed to the hydrophilic polysaccharide structure of the fiber, which promotes water binding through hydrogen bonding (De Angelis et al., 2020). Similarly, the elevated WAC of pregelatinized corn starch aligns with findings by Gerçekaslan (2021), who reported significantly higher water absorption for pregelatinized starch compared to native starch due to disruption of crystalline regions and improved water accessibility. Methylcellulose also showed high WAC, likely due to the presence of numerous hydroxyl groups and its strong hydration capacity. As described by Ghadermazi et al. (2019), methylcellulose is soluble in cold water and forms hydrogen-bond-stabilized networks that facilitate water uptake. Xanthan gum demonstrated the highest WAC overall, in agreement with Sánchez, Bartholomai, and Pilosof (1995), who identified xanthan as one of the strongest water binding food gums. In the present study, 2.5 g of xanthan absorbed approximately all 30 mL of water and formed a stable gel, confirming its exceptional hydration ability.

In the formulation series containing methylcellulose (Figure 5.4), increasing MC content significantly increased WAC in both protein blends ($p < 0.05$). In PPI-based formulations, WAC increased from 2.26 g/g in the absence of MC to 3.31 g/g at 6.7% MC inclusion. A similar trend was observed in SPI-based formulations, where WAC increased from 3.07 g/g to 4.36 g/g with increasing MC level. The interaction between protein type and MC level was not significant ($p = 0.587$), indicating that methylcellulose affected WAC similarly in both PPI and SPI. This suggests that the effect of MC is largely additive rather than protein specific. The increase in WAC can be explained by the hydrophilic nature of methylcellulose, which increases the number of available sites for hydrogen bonding within the matrix and enhances overall water retention, regardless of protein type.

In contrast, the effect of pea fiber depended on protein type (Figure 5.5), as indicated by a significant protein-PF interaction ($p = 0.004$). In PPI-based formulations, increasing pea fiber level from 0% to 29% did not significantly change WAC, with values remaining in the range of 2.70 - 2.79 g/g. Although pea fiber alone exhibited high WAC, its incorporation into the PPI matrix did not increase water retention in the composite. This suggests that while the fiber absorbs water, the mixture may not retain that water strongly during the WAC test, leading to no measurable increase. In SPI-based formulations, however, increasing pea fiber content significantly reduced WAC. The highest value was observed in SPI 100:0 PF (4.25 g/g), and inclusion of 29% PF significantly decreased WAC to 3.40 g/g ($p = 0.002$). SPI alone appears capable of forming a cohesive protein network that effectively entraps water. The addition of pea fiber may disrupt this protein network, weakening its structural integrity and reducing the ability of the matrix to retain water. Although pea fiber has a high water absorption capacity, its presence in the SPI blend reduced overall water retention. These findings showed that the intrinsic water absorption of an individual ingredient does not necessarily predict its behavior within a composite protein-fiber matrix, where structural interactions and network integrity play a critical role in determining effective water retention.

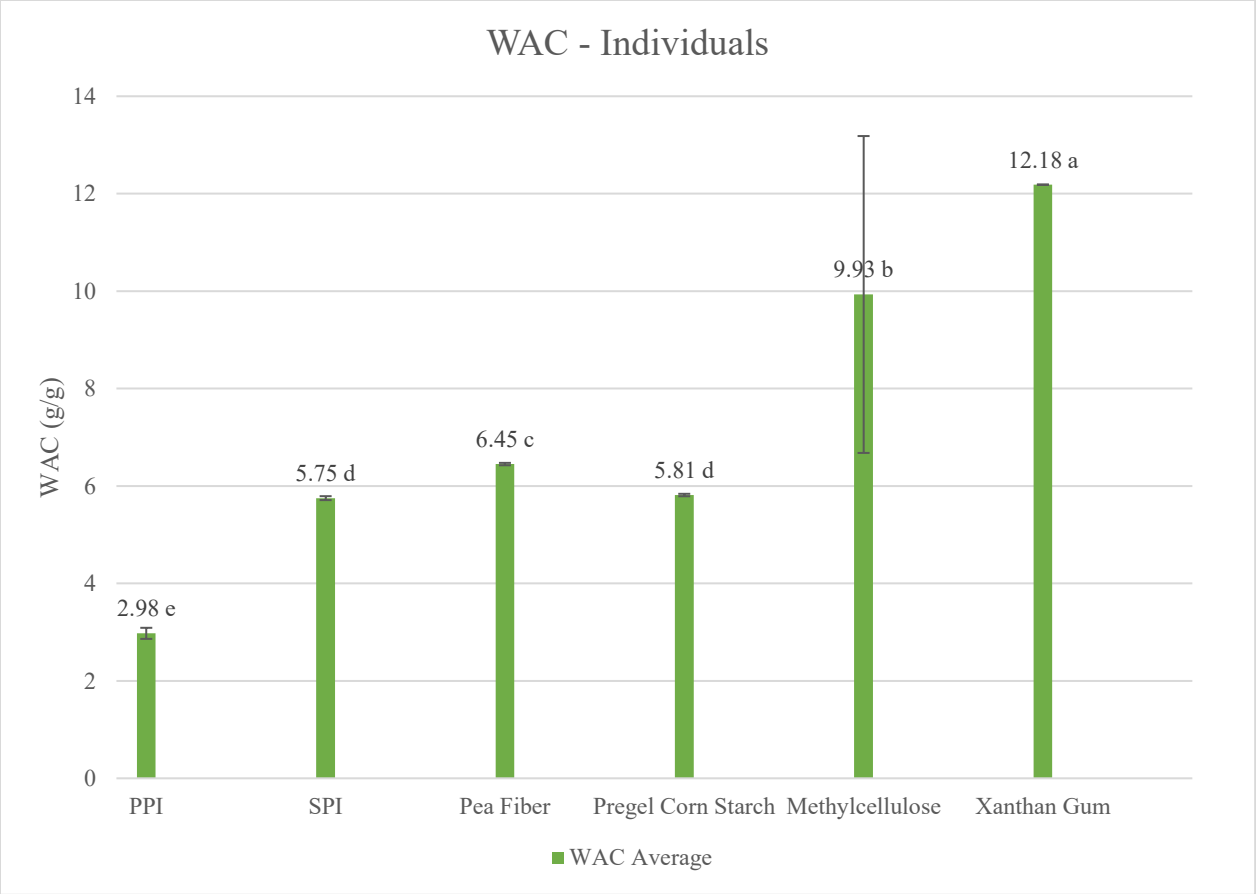

Figure 5.3. Water Absorption Capacity (Individual Materials). Bars represent mean ± SD (n = 3). Different letters indicate significant differences among samples according to the Games-Howell Post-Hoc Test ($p < 0.05$)

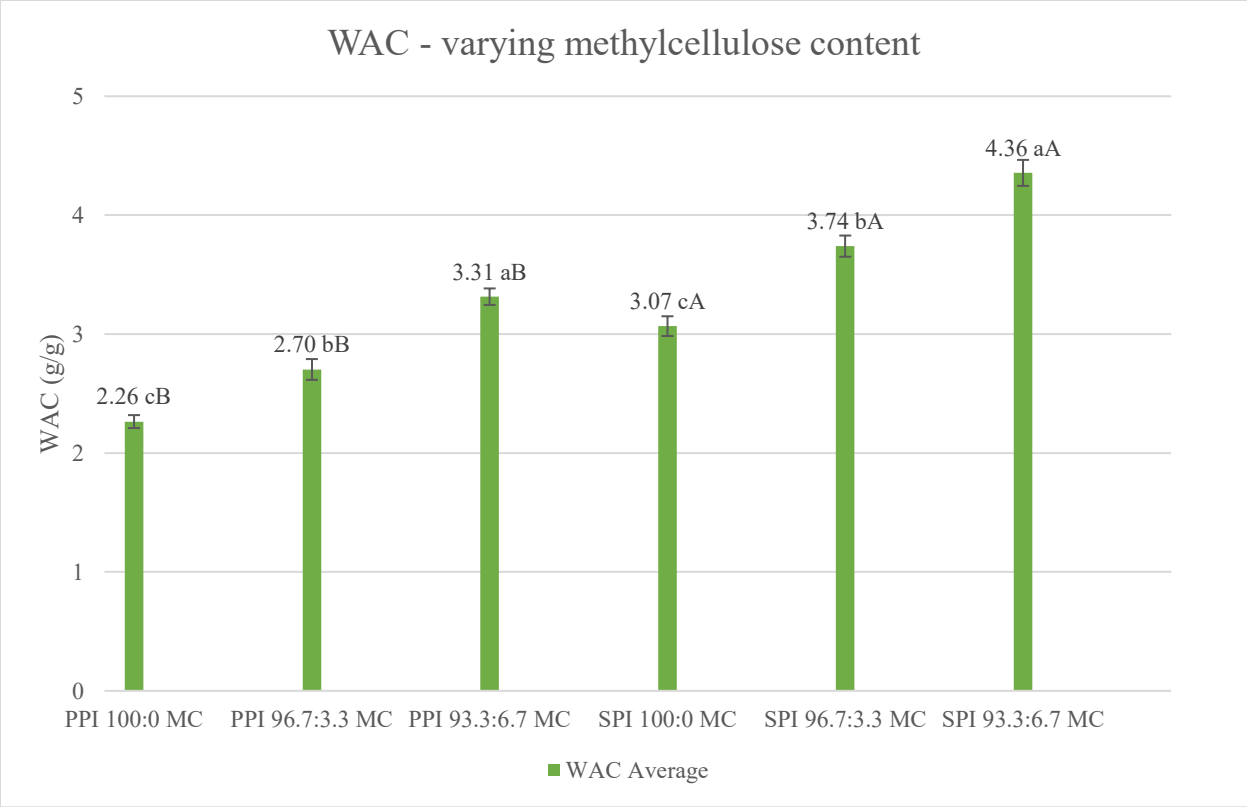

Figure 5.4. Water Absorption Capacity (Formulation with varying MC content). Bars represent mean ± SD (n = 3). Different lowercase letters show significant differences among methylcellulose levels, while different uppercase letters indicate significant differences between protein types, according to Tukey's test ($p < 0.05$).

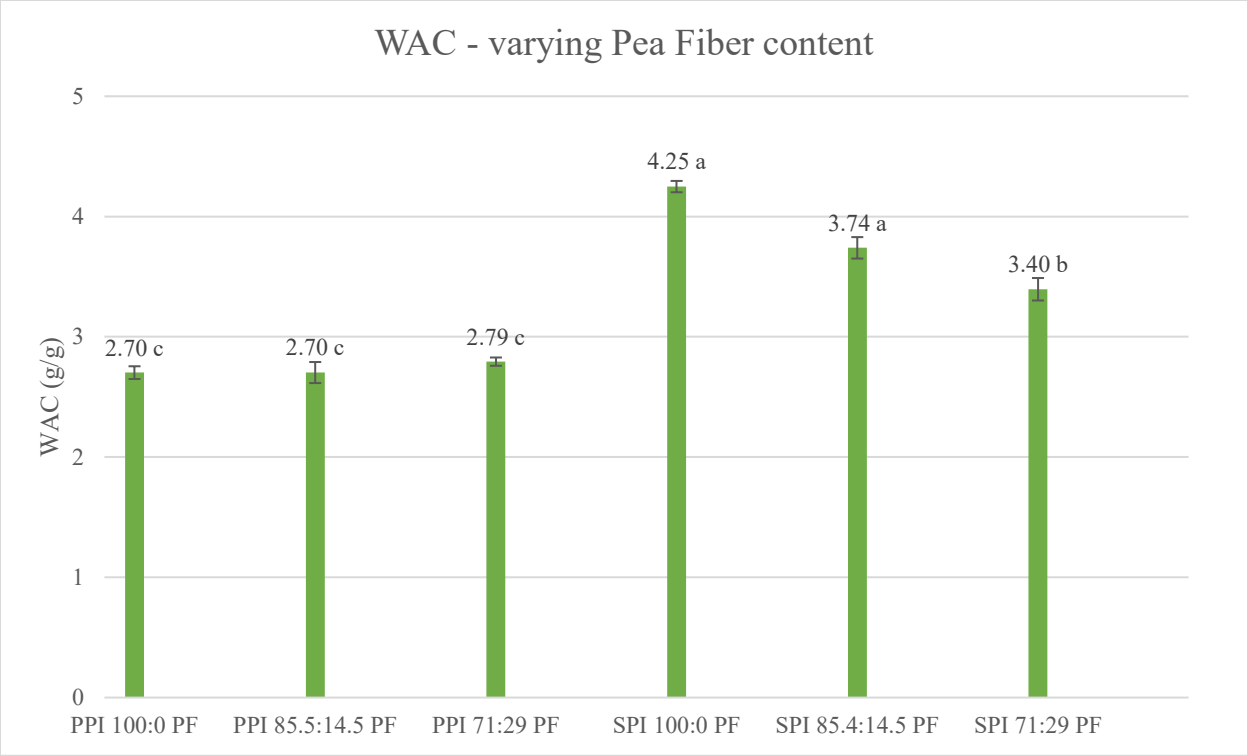

Figure 5.5. Water Absorption Capacity (Formulation with varying PF content). Different letters indicate significant differences among protein-pea fiber combinations according to Tukey's post hoc test ($p < 0.05$).

5.3.1.2 Least Gelation Concentration (LGC)

Gel formation in food reflects the development of a continuous three-dimensional network that immobilizes water and yields a self-supporting structure. In protein-based gels, this network typically emerges when heating above the denaturation temperature unfolds the protein, and subsequent cooling promotes aggregation and network setting, driven mainly by hydrophobic interactions and sometimes reinforced by disulfide bonding (Brishti et al., 2017; Jarpa-Parra 2018). LGC is commonly used as an index of gelling ability, and lower LGC values indicate that a material can reach a no-flow, self-supporting state at a lower concentration (Boye et al., 2010). Here, LGC was assessed across 8-20% (w/w) dispersions, and because testing

began at 8%, any ingredient that gelled at 8% may also be capable of gelling below this level, but concentrations lower than 8% were not evaluated in the present dataset.

Across the single ingredient, the two protein isolates showed higher LGC values than the hydrocolloid and fiber ingredients (Figure 5.6). PPI required 14% to form a self-supporting gel, whereas SPI gelled at 12%. This pattern is consistent with the broader observation that pea proteins often show weaker gelling behavior than soy proteins, and that reported LGC values for legume proteins commonly fall within the 8-14% range depending on extraction method and composition (Jarpa-Parra 2018). In contrast, pregelatinized corn starch, methylcellulose, pea fiber, and xanthan gum all reached a gel structure at the lowest concentration tested (8%). For pregelatinized starch, this behavior aligns with the fact that pregelatinized starches are engineered to disperse and swell readily, developing viscosity and structure more efficiently than native starches, and they are widely used as thickening or texturizing agents in instant and rehydrated foods (Chakraborty et al., 2022). Methylcellulose similarly showed gelation at 8%, which is compatible with its well-known thermoresponsive behavior. Heating promotes dehydration and hydrophobic association of methoxyl groups and polymer-polymer interactions, and a stable gel network is typically observed upon cooling (Thirumala, Gimble, and Devireddy 2013). Although LGC is usually used for proteins, the gel structure observed for pea fiber at 8% can be explained by its strong ability to absorb water and swell. As the fibers take up water, they expand, which increases the effective volume of particles. This promotes closer fiber-fiber interactions and the formation of a continuous physical network that traps water and prevents flow. Similar behavior has been reported for pea hull fiber, where greater swelling and water binding lead to increased viscosity and a more solid-like structure at higher concentrations (Ytterberg et al., 2026). Xanthan gum also gelled at 8%, consistent with its established role as a

strong thickener or stabilizer and with literature describing temperature-dependent structural rearrangements that yield firm gel networks upon cooling after sufficient thermal treatment (Palaniraj and Jayaraman 2011; Petri 2015).

The blend results further indicate that apparent gelation behavior is not simply additive and can shift when materials are combined (Figures 5.7 and 5.8). In protein-MC formulations, PPI 100:0 MC and PPI 96.7:3.3 MC both exhibited LGC = 12%, but increasing MC to 6.7% raised LGC to 14%. For SPI, the base formulation (SPI 100:0) gelled at 8%, while adding MC increased LGC to 10% at both 3.3% and 6.7% MC. These trends are consistent with the idea that, although MC can form its own network, incorporating MC into a protein matrix can dilute the effective protein concentration and interfere with protein-protein connectivity, meaning a higher total solids level may be required before a continuous, self-supporting network is achieved under the same heating and cooling protocol (Thirumala et al., 2013). In protein and pea fiber blends, LGC values are around 10 to 12%. PPI 100:0 PF showed LGC = 10%, increased to 12% at the intermediate PF level (85.5:14.5), and returned to 10% at the higher PF level (71:29), while SPI-PF formulations remained at 10% across the tested ratios. Pea fiber helps build structure mainly by swelling and forming contacts between fibers. However, when it is mixed with protein, the fibers are more spread out, so fiber-fiber contacts decrease (a dilution effect). At the same time, the fiber particles can interrupt the protein network (a network interference effect). Because of this, the blend may need the same or even a higher total concentration to reach a no-flow, self-supporting gel compared with the strongest individual ingredient. Still, due to the high swelling and water holding capacity of pea fibers, a gel-like structure can form once the overall particle concentration becomes sufficiently high (Ytterberg et al., 2026).

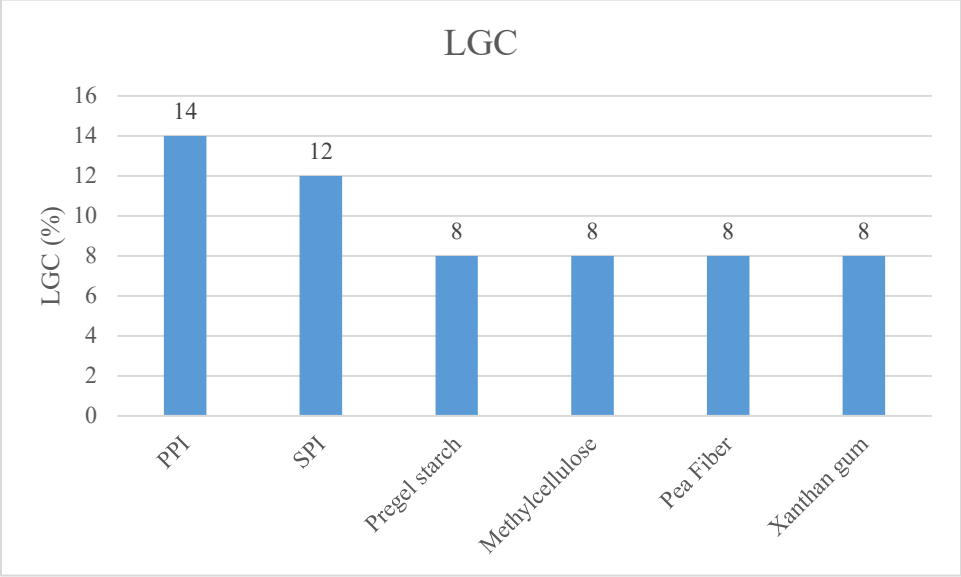

Figure 5.6. Least Gelation Concentration (Individual Materials). The standard deviation was zero for all samples

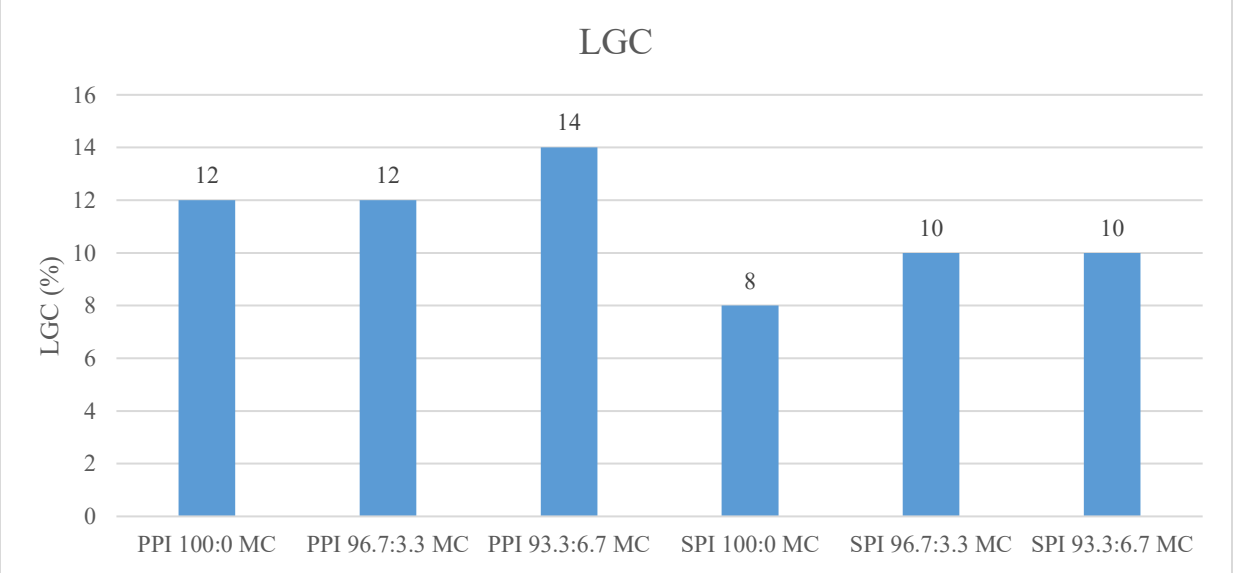

Figure 5.7. Least Gelation Concentration (Formulation with varying MC content). The standard deviation was zero for all samples

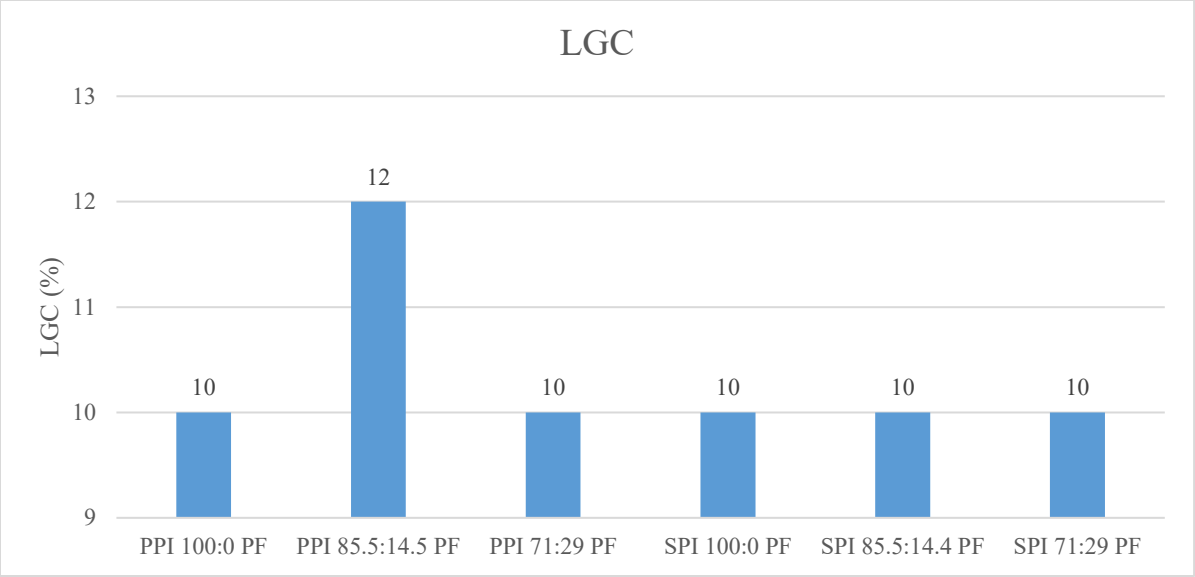

Figure 5.8. Least Gelation Concentration (Formulation with varying PF content). The standard deviation was zero for all samples

5.3.1.3 Rapid Visco Analyzer (RVA)

RVA was used to observe how viscosity developed during a heating, holding, and then cooling cycle, and based on when viscosity built up, to infer whether each material behaved more like a cold swelling material or a non-cold swelling one (Table 5.4). Cold swelling is typically reflected by an early viscosity maximum (often before 4 min), whereas viscosity that develops later in the run more often reflects heat induced structuring or aggregation rather than rapid hydration at low temperature (Flory et al., 2023).

To distinguish cold swelling behavior from the absolute maximum viscosity reached during the complete RVA cycle, the cold swelling peak was evaluated separately. The cold swelling peak was defined as a distinct local viscosity maximum occurring between 30 and 60 °C. Therefore, the overall peak viscosity and the cold-swelling peak do not necessarily represent the same point in the RVA profile.

In this study, the clearest cold swelling behavior was observed for SPI (Figure 5.9), pregelatinized corn starch, and xanthan gum. SPI reached a high peak viscosity very early (1718.5 ± 17.7 cP at 0.33 min and 30.05 °C). Pregelatinized corn starch showed a similarly early viscosity peak (2056 ± 305.5 cP at 1.53 min and 39.8 °C), consistent with cold swelling behavior (Figure 5.10). Xanthan gum also peaked early, reaching 3986.5 ± 379.7 cP at 1.53 min and 38.23 °C (Figure 5.10). This pattern is consistent with fast hydration and rapid network development under shear at relatively low temperature, a behavior often described for cold swelling globular proteins (Flory et al., 2023) and for highly hydrophilic gums that thicken quickly in the continuous phase. In pregelatinized starch, earlier viscosity rise at low temperature is often interpreted as evidence of increased water accessibility and faster swelling compared to native starch (Y. Liu et al., 2017), but the exact timing still depends on the degree of gelatinization, residual granular structure, and molecular degradation.

In contrast, PPI showed a much lower peak viscosity and a late peak (80.5 ± 10.61 cP at 5.9 min, 95 °C), indicating that PPI did not express cold swelling and instead behaved more like an ingredient whose viscosity develops only after substantial heating (Figure 5.9). This is not contradictory to the other literature. PPI has been reported to vary widely in swelling intensity, and that variability is strongly shaped by solubility and processing history (Osen et al., 2014). This PPI appears to have limited early viscosity build and minimal resistance to shear until the high-temperature phase.

Pea fiber reached a relatively high peak (5538.5 ± 767.2 cP) but still at a late stage (4.83 min, 93.82 °C), suggesting that its maximum thickening emerged mainly during the high-temperature portion (Figure 5.10). Methylcellulose showed by far the highest peak viscosity on average (18248 ± 190.9 cP) with a mid-run peak (3.77 ± 2.03 min) and a broad peak temperature

estimate (74.05 ± 29.49 °C), consistent with its strong thickening capacity and temperature-dependent hydration behavior reported for cellulose derivatives in starch and biopolymers (Figure 5.10). Importantly, it was also observed that a measurement artifact for MC in the 9-min RVA runs, the instrument reported 0 cP even though the sample had formed a clearly viscous mass that adhered to the paddle and rotated freely with it. Mechanistically, that observation fits a wall slip or rotation situation where the paste moves as a cohesive body with minimal relative shear between paddle, sample, and canister; the RVA torque signal can collapse even when the material is highly viscous, simply because the material loses frictional coupling rather than because viscosity truly vanishes. So, any near-zero MC trace in these runs is considered an artifact of the instrument interacting with the sample, rather than a true loss of structure.

When moved from individual ingredients to protein-hydrocolloid (Figure 5.11) and protein-fiber (Figure 5.12) blends, the timing and magnitude of peak viscosity shifted in ways that are informative for formulation design. In PPI-MC blends, adding MC increased peak viscosity and shifted the peak earlier and to a lower peak temperature relative to PPI alone. PPI 100:0 MC peaked at 295 ± 5.7 cP at 7.07 min and 94.95 °C, while increasing MC to 6.7% (PPI 93.3:6.7 MC) raised the peak viscosity to 482.5 ± 44.5 cP and shifted the peak to 1.27 min and 33 °C. This pattern is consistent with an additive thickening effect from MC in the continuous phase, with viscosity developing earlier in the heating cycle, which is commonly observed when hydrocolloids are incorporated into concentrated biopolymer suspensions (Techawipharat, Suphantharika, and BeMiller 2008). Moreover, as MC concentration increased, the formulation behavior shifted from a non-cold swelling profile toward a cold swelling one at the highest MC levels, likely reflecting the additive thickening and rapid hydration characteristics of methylcellulose in the blend.

In SPI-MC formulations, SPI already showed relatively strong viscosity development, and increasing MC further increased peak viscosity while shifting the peak to earlier times at the highest inclusion level. SPI 100:0 MC peaked at 953.5 ± 0.7 cP at 6.17 min and 95.03 °C. At the intermediate level, SPI 96.7:3.3 MC increased to 1229 ± 73.5 cP, although the peak still occurred relatively late (5.13 min, 94.78 °C). At the highest level, SPI 93.3:6.7 MC reached 1233 ± 8.5 cP at 1.33 min and 34.45 °C, indicating a clear shift toward cold swelling behavior. This suggests that higher MC levels gradually changed the formulation from a more non-cold swelling profile to a clearer cold swelling profile, likely due to the additive thickening and rapid hydration effect of methylcellulose. Because SPI itself has a greater viscosity-building capacity than PPI, the overall viscosities of SPI-MC formulations remained higher than those of the corresponding PPI-MC formulations.

The pea fiber blends showed a different pattern. In PPI-PF formulations, PPI 100:0 PF peaked at 271.5 ± 71.4 cP at 2.67 min and 59.08 °C, showing clear cold swelling behavior. At the intermediate level, PPI 85.5:14.5 PF reached 398.5 ± 87 cP at 4.03 min and 82.82 ± 4.21 °C, and at the highest level, PPI 71:29 PF reached 630.5 ± 20.5 cP at 6.37 min and 95 °C.

For SPI-PF formulations, peak viscosity remained relatively high across all fiber levels, but the position of the peak changed with increasing PF. SPI 100:0 PF peaked at 1261.5 ± 0.71 cP at 1.2 min and 35 °C, showing cold swelling behavior. At the intermediate level, SPI 85.5:14.5 PF reached 1329.5 ± 6.36 cP at 4.33 min and 83.43 °C, indicating that the early cold swelling peak was no longer present. At the highest level, SPI 71:29 PF reached 1367 ± 275.77 cP at 5.2 min and 94.8 °C, showing that viscosity remained high but developed later and under stronger heating.

These results suggest that increasing PF gradually reduced the cold swelling character of the formulations. As the PF level increased, the early cold swelling peak disappeared, and viscosity development shifted to later times and higher temperatures. This trend likely reflects an additive effect of pea fiber, since PF alone behaved as a non-cold swelling material in the RVA. In other words, although the protein blends initially showed early viscosity development, increasing PF progressively suppressed this behavior and shifted the blends toward a more heat-dependent viscosity profile. This type of shift in viscosity behavior has also been reported in legume protein blends, where adding other ingredients can change how the components interact and influence whether it behaves more like a cold swelling or a non-cold swelling material (Webb et al., 2023), and fiber can redistribute water and change the viscosity of the continuous phase, which may cause a shift in the peak.

Overall, the RVA results were generally consistent with the WAC and LGC observations, but they also highlight that hydration alone does not fully determine viscosity development. At the ingredient level, materials with strong water-binding capacity, such as xanthan gum and MC, produced the highest viscosities, which is consistent with the idea that swelling and viscosity development depend on water absorption and solubility of the components (Webb et al., 2023).

However, it is important to note that the WAC test is performed at room temperature and without heating, whereas the RVA test involves a heating cycle. Because of this difference, the ability of an ingredient to absorb water in the WAC test does not always translate directly to viscosity development in RVA. In the blended formulations, the RVA behavior therefore depended not only on how much water each ingredient could absorb, but also on how the ingredients interacted and formed a structure during heating. For example, methylcellulose increased WAC and also promoted earlier viscosity development in the RVA, indicating that its

strong hydration contributed to faster thickening. At the same time, the LGC results showed that increasing MC required higher concentrations for gel formation, suggesting that although MC thickens the blend, it can also interfere with the protein network.

In contrast, pea fiber showed high WAC as an individual ingredient but did not always increase viscosity in the blends. This is consistent with the LGC results, where fiber particles can interrupt protein-protein contacts and weaken the continuous network. As a result, even though pea fiber absorbs water, the mixture does not necessarily develop higher viscosity during RVA.

Taken together, these results suggest that RVA behavior in these formulations is controlled by both hydration and structural interactions within the mixture, rather than water absorption alone.

Table 5.4. Rapid Visco Analyzer Results

Sample	Peak Viscosity (cP)	Temp at Peak Visc (°C)	Time at Peak Visc (min)	Cold Peak Viscosity (cP)	Temp at Cold Peak Visc (°C)	Time at Cold Peak Visc (min)
PPI	80.5 ± 10.6	95 ± 0	5.90 ± 0.05	43.5 ± 7.8	37.38 ± 10.29	1.17 ± 0.99
SPI	1718.5 ± 17.7	30.05 ± 0	0.33 ± 0	1718.5 ± 17.7	30.05 ± 0	0.33 ± 0
Pregel Corn Starch	2323 ± 582.7	93.85 ± 1.27	4.87 ± 0.38	2056 ± 305.5	39.8 ± 13.86	1.53 ± 0.85
Methylcellulose	18248 ± 190.9	74.05 ± 29.49	3.77 ± 2.03	15128 ± 4603.3	48.35 ± 6.86	2.07 ± 0.38

Pea Fiber	5538.5 ± 767.2	93.82 ± 1.10	4.83 ± 0.33	2911 ± 291.3	59.12 ± 0.04	2.67 ± 0
Xanthan Gum	3986.5 ± 379.7	38.23 ± 1.8	1.53 ± 0.09	3986.5 ± 379.7	38.23 ± 1.8	1.53 ± 0.09
PPI 100:0 MC	295 ± 5.7	94.95 ± 0	7.07 ± 0	85.5 ± 0.7	36.95 ± 0	1.47 ± 0
PPI 96.7:3.3 MC *	398.5 ± 87	82.82 ± 4.21	4.03 ± 0.24	168.5 ± 87	35.15 ± 6.15	1.37 ± 0.33
PPI 93.3:6.7 MC	694.5 ± 36.1	86.60 ± 0.78	4.23 ± 0.05	482.5 ± 44.5	33 ± 0.07	1.27 ± 0
SPI 100:0 MC	953.5 ± 0.7	95.03 ± 0.04	6.17 ± 0.05	227.5 ± 9.2	57.3 ± 0.78	2.57 ± 0.05
SPI 96.7:3.3 MC **	1229 ± 73.5	94.78 ± 0.18	5.13 ± 0.19	799.5 ± 37.5	33.05 ± 0.07	1.27 ± 0
SPI 93.3:6.7 MC	1671.5 ± 186	80.45 ± 0.71	3.90 ± 0.05	1233 ± 8.5	34.45 ± 1.91	1.33 ± 0.09
PPI 100:0 PF	480.5 ± 16.3	89.95 ± 7.14	5.17 ± 1.46	271.5 ± 71.4	59.08 ± 0.11	2.67 ± 0
PPI 85.5:14.5 PF *	398.5 ± 87	82.82 ± 4.21	4.03 ± 0.24	168.5 ± 87	35.15 ± 6.15	1.37 ± 0.33
PPI 71:29 PF	630.5 ± 20.5	95 ± 0.07	6.37 ± 0.14	219 ± 8.5	33.77 ± 0.74	1.3 ± 0.05

SPI 100:0 PF	1261.5 ± 0.71	35 ± 0	1.2 ± 0	1260 ± 5.7	31.85 ± 0.14	1.20 ± 0
SPI 85.5:14.5 PF **	1329.5 ± 6.36	83.43 ± 16.16	4.33 ± 1.32	799.5 ± 37.5	33.05 ± 0.07	1.27 ± 0
SPI 71:29 PF	1367 ± 275.77	94.8 ± 0.14	5.2 ± 0.19	613.5 ± 125.2	32.45 ± 0.92	1.23 ± 0.05
* Same formulations ** Same formulations						

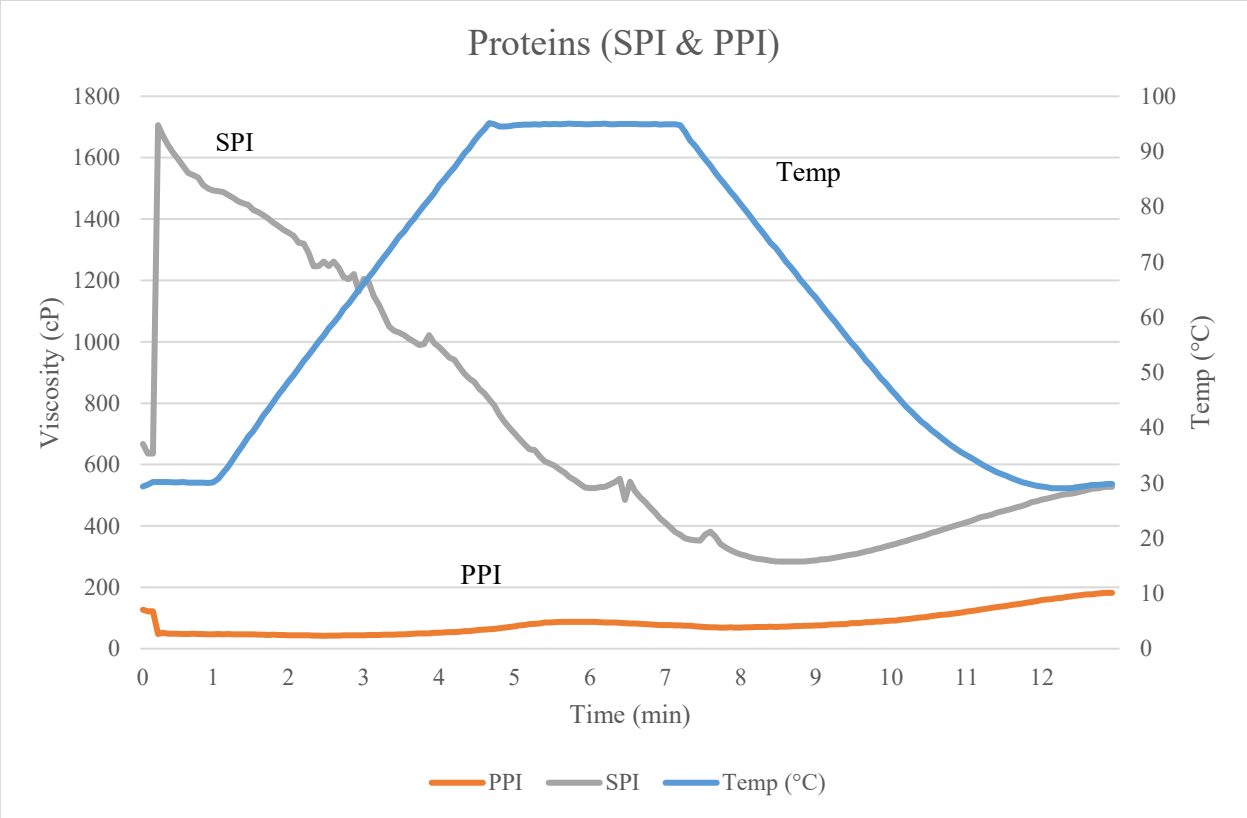

Figure 5.9. Rapid Visco Analyzer (Proteins: SPI and PPI)

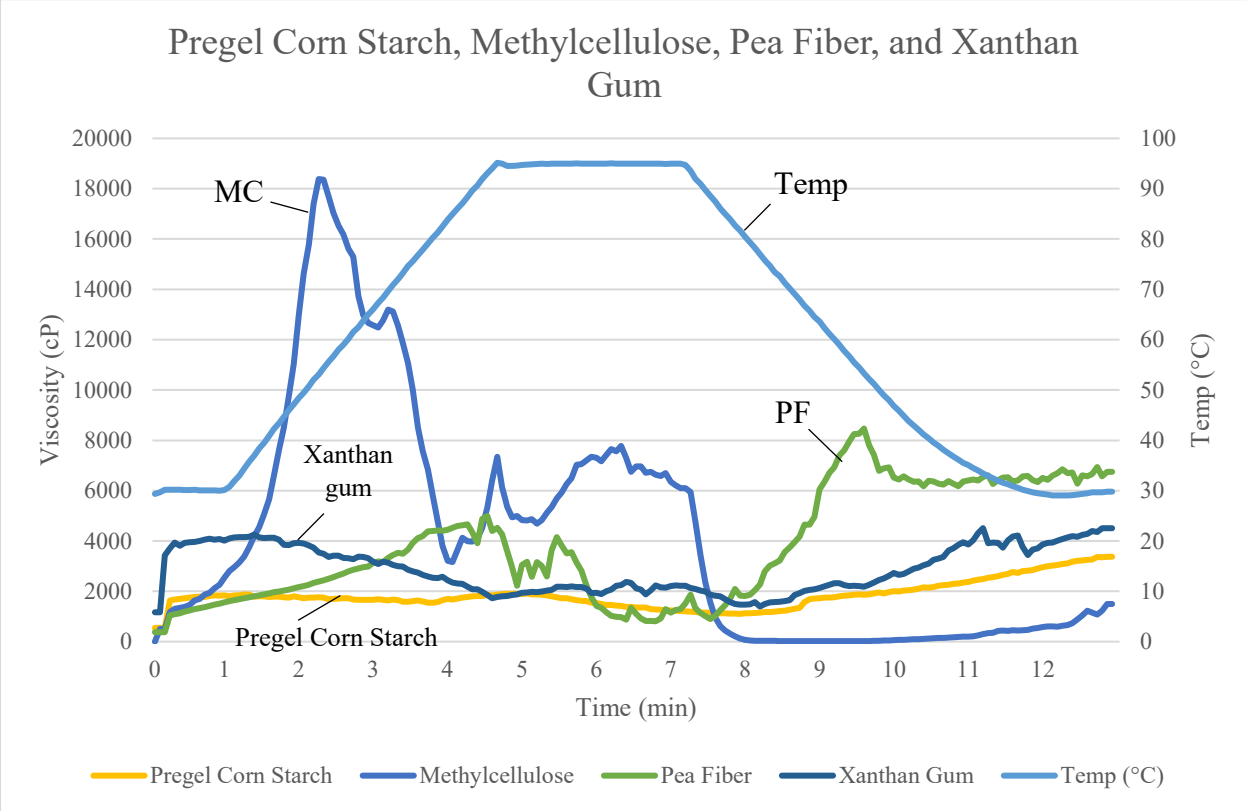

Figure 5.10. Rapid Visco Analyzer (Methylcellulose, Pea Fiber, Pregel Corn Starch, and Xanthan Gum)

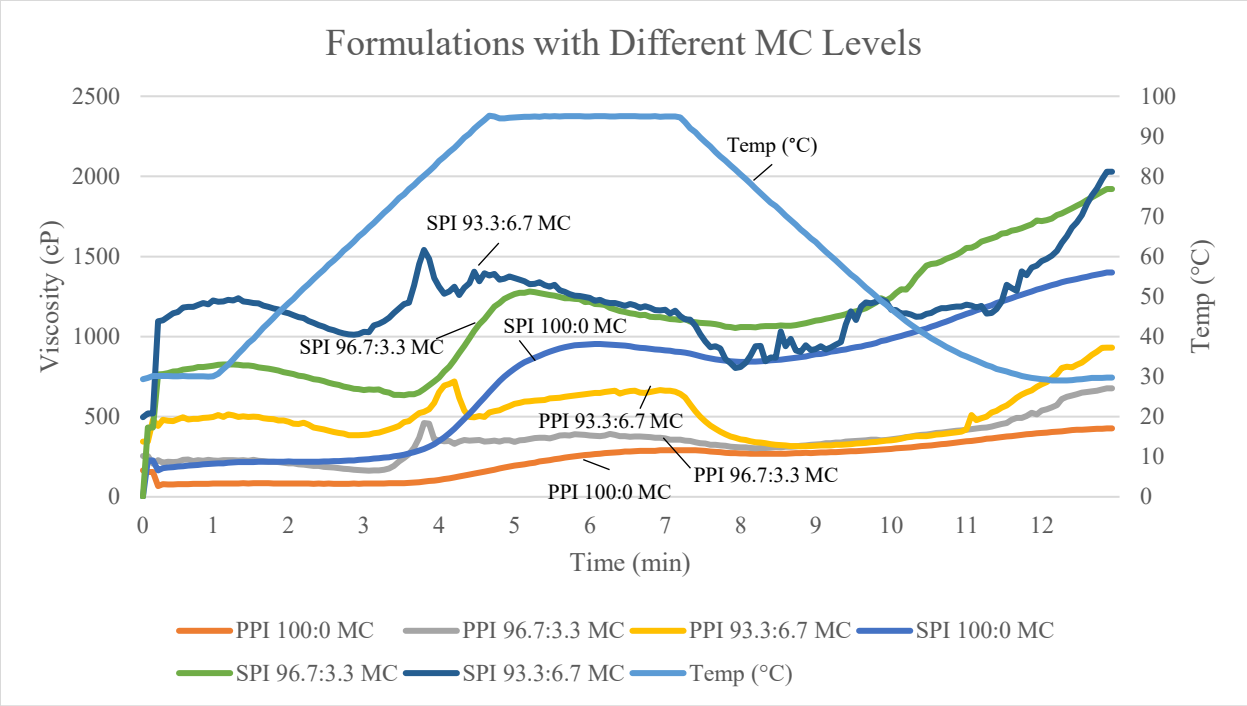

Figure 5.11. Rapid Visco Analyzer (Formulations with different MC levels)

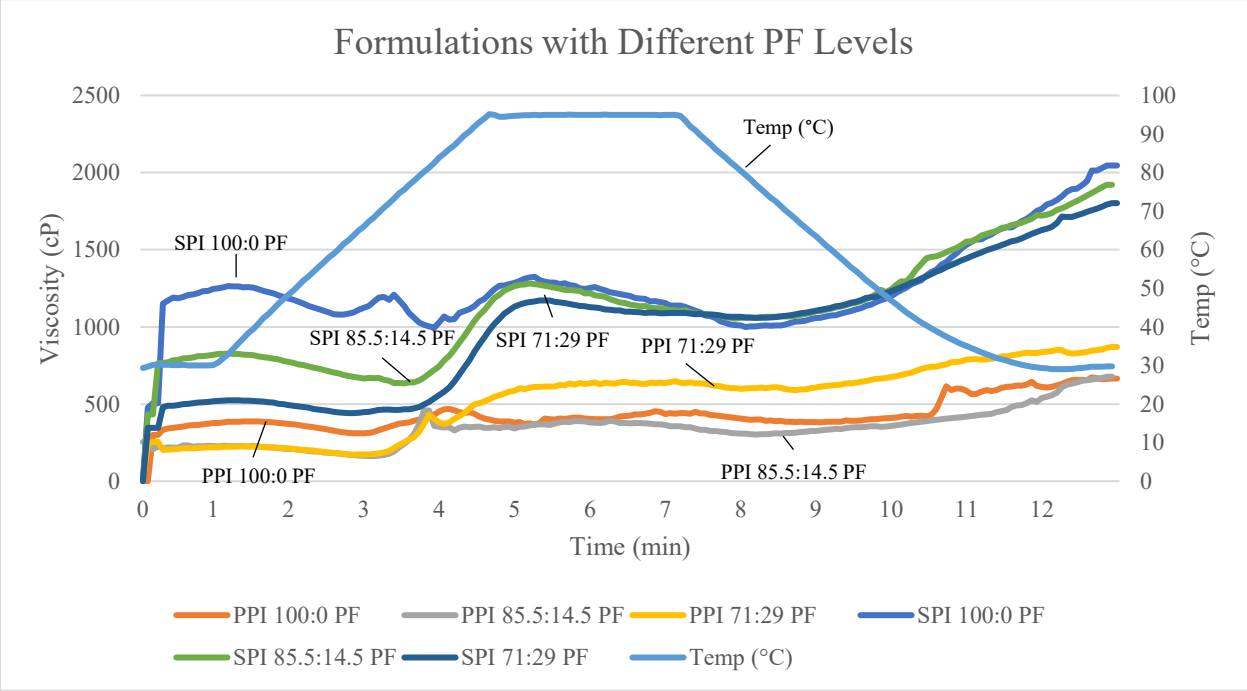

Figure 5.12. Rapid Visco Analyzer (Formulations with different PF levels)

5.3.2 Extrudate Analysis

5.3.2.1 Distortion Dimension Ratio (DDR)

In extrusion-based 3D food printing, printability refers to the ability of a material to flow through the nozzle while maintaining its intended geometry after deposition. Successful printable inks must balance extrusion flow with sufficient structural stability to support their own weight and resist post-deposition deformation (Liu et al., 2018; Steenhuis, Fang, and Ulusemre 2018). Dimensional stability is commonly quantified using the dimensional distortion ratio (DDR), which compares measured printed dimensions to the original CAD design. A DDR value of 0 indicates no distortion, whereas non-zero values reflect asymmetric deviation between height and diameter (Asadi-Eydivand et al., 2016). Thus, values closer to zero indicate higher shape fidelity and better structural retention after printing.

As shown in Tables 5.5 and 5.6, DDR was significantly influenced by both protein type and MC level, with a significant Protein-MC interaction, indicating that the effect of MC differed between PPI and SPI-based formulations.

For PPI formulations, DDR remained statistically unchanged between 100:0 and 96.7:3.3 MC (0 ± 0.02 and -0.03 ± 0.01, respectively), suggesting that moderate MC incorporation did not substantially change dimensional fidelity. However, at 93.3:6.7 MC, DDR decreased markedly (-0.18 ± 0.02), indicating significantly greater dimensional distortion relative to the higher MC levels.

In contrast, SPI formulations exhibited a progressive decrease in DDR across all MC levels (100:0 = 0.1 ± 0.02; 96.7:3.3 = - 0.17 ± 0.01; 93.3:6.7 = - 0.27 ± 0.02), with each level differing significantly from the others. This indicates that SPI-based inks were more sensitive to MC addition in terms of dimensional stability.

These results align with previous findings that formulation composition strongly influences post-deposition stability (Hussain, Arora, and Malakar 2021). While structural reinforcement can enhance shape retention, excessive modification of the ink formulation may disrupt the balance between extrusion flow and structural setting. In extrusion-based printing, higher viscosity can improve structural support but may also cause geometric deviations if extrusion conditions are not optimally matched (Liu et al., 2018). In this study, printing speed was adjusted according to formulation viscosity to prevent filament breakage; nevertheless, the shift in DDR, particularly in SPI-based formulations, suggests that compositional changes altered the material's ability to maintain dimensional fidelity after printing. For example, PPI formulations were printed at 15, 10.5, and 6 mm/s for 100:0, 96.7:3.3, and 93.3:6.7 MC, respectively, whereas SPI formulations required even lower speeds (10.5, 6, and 3.75 mm/s). Despite these adjustments, the shift in DDR, particularly in SPI formulations, indicates that compositional changes, rather than printing speed alone, governed dimensional stability.

The greater sensitivity of SPI formulations may reflect differences in structure and water interactions compared to PPI blends. SPI is known to exhibit cold swelling behavior, leading to substantially higher viscosity even at lower temperatures, which is consistent with the RVA results observed in this study. In contrast, PPI formulations generally showed lower viscosity profiles, indicating a less pronounced hydration-driven thickening effect. The higher initial viscosity of SPI may have made them more prone to dimensional distortion during and after deposition, resulting in the more negative DDR values observed with increasing MC levels. Similar formulation-dependent responses have been reported in starch-based inks, where ingredient modifications affected water absorption and structural setting behavior, ultimately

influencing DDR (Kabus 2024). These findings indicate that MC incorporation influences dimensional fidelity in protein blends, with SPI-based formulations showing greater distortion.

For PF-containing formulations, both protein type and PF level significantly influenced DDR, although the Protein-PF interaction was not statistically significant, indicating a comparable overall pattern across proteins (Table 5.7).

For PPI formulation, the 100:0 formulation exhibited a DDR of - 0.14 ± 0.02, whereas both 85.5:14.5 (- 0.03 ± 0.01) and 71:29 (0 ± 0.02) showed significantly improved dimensional fidelity (values closer to zero). Notably, the two PF-containing formulations did not significantly differ from one another, suggesting that the primary shift in dimensional behavior occurred upon initial fiber incorporation, with no additional statistically detectable change at higher fiber levels.

Similarly, SPI formulations showed a significant shift from - 0.35 ± 0.02 (100:0) to - 0.17 ± 0.01 (85.5:14.5) and - 0.12 ± 0.02 (71:29), with both PF-containing formulations differing from the control but not from each other. Across all PF levels, SPI samples consistently exhibited more negative DDR values than PPI samples, consistent with the main effect of protein type.

These findings indicate that pea fiber incorporation improved dimensional fidelity relative to the control formulation, but further increasing fiber content beyond the intermediate level did not produce statistically distinct changes. Such behavior is consistent with the literature demonstrating that formulation adjustments can enhance post-deposition stability by modifying structural integrity (Hussain et al., 2021). Once a threshold of structural reinforcement is reached, additional inclusion may not yield proportional gains in shape fidelity.

In this study, higher fiber levels were associated with lower viscosity during printing, and printing speed was adjusted accordingly (15 mm/s for PPI 100:0 and 71:29 PF; 10.5 mm/s for

PPI 85.5:14.5 PF; 10.5, 6, and 10.5 mm/s for SPI formulations). Although higher fiber levels were associated with lower viscosity and allowed higher printing speeds in some cases, the improved DDR values in PF-containing formulations suggest that fiber mainly enhanced shape stability after printing, rather than simply changing how easily the material flowed through the nozzle.

Prior work has shown that dimensional distortion is strongly influenced by formulation-dependent rheology and structural behavior (Kabus 2024; Liu et al., 2018). Materials that are too fluid may collapse, whereas excessively viscous inks may exhibit extrusion defects. The current results showed that fiber incorporation shifted the formulations toward a more favorable balance between extrusion and structural retention, thereby improving DDR.

Overall, DDR values across formulations demonstrate that dimensional stability in 3D printed protein-based ink is highly formulation dependent. Both MC and PF altered post-deposition fidelity, but their effects differed in magnitude and pattern across protein types. Consistent with prior research (Asadi-Eydivand et al., 2016; Steenhuis et al., 2018), achieving optimal printability requires balancing extrusion behavior with structural stability after deposition. In the present research, moderate compositional adjustments improved or maintained dimensional fidelity, whereas higher levels, particularly of MC in SPI formulations, resulted in increased geometric distortion.

Table 5.5. DDR of PPI-based Samples at Different MC Levels. Values are estimated marginal means (±SE). Different superscript letters within each protein indicate significant differences among MC levels (Tukey-adjusted, $p<0.05$)

3D Printed Samples	PPI 100:0 MC	PPI 96.7:3.3 MC	PPI 93.3:6.7 MC
DDR (Estimated Marginal Means ± SE)	0 ± 0.02^{a}	-0.03 ± 0.01^{a}	-0.18 ± 0.02^{b}

Table 5.6. DDR of SPI-based Samples at Different MC Levels. Values are estimated marginal means (±SE). Different superscript letters within each protein indicate significant differences among MC levels (Tukey-adjusted, p<0.05)

3D Printed Samples	SPI 100:0 MC	SPI 96.7:3.3 MC	SPI 93.3:6.7 MC
DDR (Estimated Marginal Means ± SE)	0.1 ± 0.02 [a]	-0.17 ± 0.01 [b]	-0.27 ± 0.02 [c]

Table 5.7. DDR for Formulations with Different PF Levels. Different letters indicate significant differences among PF levels (Tukey-adjusted, p<0.05), collapsed across protein type.

3D Printed Samples	PPI 100:0 PF	PPI 85.5:14.5 PF	PPI 71:29 PF
DDR (Estimated Marginal Means ± SE)	-0.14 ± 0.02 [a]	-0.03 ± 0.01 [b]	0 ± 0.02 [b]
3D Printed Samples	SPI 100:0 PF	SPI 85.5:14.5 PF	SPI 71:29 PF
DDR (Estimated Marginal Means ± SE)	-0.35 ± 0.02 [a]	-0.17 ± 0.01 [b]	-0.12 ± 0.02 [b]

5.3.2.2 Texture Profile Analysis (TPA)

TPA was used to evaluate the mechanical properties of the printed formulations, including hardness, springiness, and chewiness. These parameters are commonly used to assess the structural strength and stability of plant-based meat and provide insight into how formulation and rheological properties influence the final texture (Bhuiyan et al., 2025).

For the MC blends, hardness and chewiness were strongly affected by both protein type and MC level, whereas springiness was mainly influenced by protein type (Figures 5.13 and 5.14). Hardness values of the PPI formulations remained relatively stable across MC levels (about 10 N), indicating that increasing MC concentration did not substantially strengthen the PPI matrix. In contrast, SPI formulations exhibited pronounced variation. The SPI 96.7:3.3 MC formulation showed the highest hardness (21.3 N) and chewiness (12.98), significantly higher

than the other treatments. Increasing MC to 6.7% reduced these values again, although they remained higher than those of PPI formulations.

These results suggest that SPI formulations responded more strongly to MC incorporation than PPI. This behavior is consistent with the different hydration and swelling characteristics observed in the RVA data. SPI blends exhibited substantially higher peak viscosities than PPI blends, indicating stronger thickening. Importantly, SPI behaves as a cold swelling protein, meaning that it hydrates and develops viscosity at relatively low temperatures, whereas PPI behaves as a non-cold swelling protein that requires higher temperatures to swell and form structure. As a result, SPI can develop a more structured matrix earlier in the process, which can later be reinforced by hydrocolloids such as methylcellulose.

The highest hardness and chewiness observed at the intermediate MC level (3.3%) likely reflect a synergistic interaction between the SPI network and the gelation behavior of methylcellulose. Methylcellulose forms a thermo-reversible gel upon heating and is known to strengthen the structure of plant-based meat ink by binding water and reinforcing the protein matrix (Bhuiyan et al., 2025). At moderate levels, MC can therefore contribute additional network connectivity and increase resistance to compression. However, at higher concentrations (6.7%), the hydrocolloid phase may begin to interfere with protein-protein crosslinking or compete for water, which can reduce the efficiency of the protein network and lead to slightly lower mechanical strength.

Springiness was less sensitive to MC concentration and was primarily determined by protein type. SPI formulations consistently showed higher springiness values (approximately 83-85%) than PPI formulations (approximately 77-82%). Because the Protein-MC interaction was

not significant, these differences appear to reflect intrinsic differences in the elastic behavior of the two protein matrices rather than the influence of MC concentration.

The observed trends also align with the hydration characteristics measured by WAC. Water absorption capacity increased with MC concentration in both protein blends, but the increase was much larger in SPI blends (3.07 to 4.36 g/g) than in PPI blends (2.26 to 3.31 g/g). This suggests that SPI matrices immobilized larger amounts of water within the structured network formed by the protein and MC. When water becomes immobilized rather than remaining free, it can contribute to structural rigidity instead of acting as a plasticizer, which helps explain the higher hardness and chewiness observed in the SPI formulations.

LGC values did not directly follow the same pattern as hardness. Although PPI blends showed slightly higher LGC values (12-14%) than SPI blends (8-10%), LGC primarily reflects the concentration required to initiate gel formation rather than the swelling behavior of plant proteins. Flory et al. (2023) noted that LGC is not the most reliable indicator of swelling functionality, and tests such as WAC or RVA provide better insight into hydration and thickening behavior. Instead, LGC can indicate differences in protein functionality and gelation capacity, which may contribute to the formation of layered structures in meat analogues but do not necessarily predict final mechanical strength. Therefore, the higher hardness observed in SPI blends likely results from their stronger viscosity development and hydration behavior rather than differences in gelation concentration alone.

For the pea fiber blends, increasing PF content affected hardness, springiness, and chewiness (Figures 5.15 and 5.16). Hardness increased progressively with PF level in both protein blends, but the effect was much stronger in SPI formulations. The highest hardness

values were observed in SPI samples containing 14.5% and 29% PF (21.34 and 23.47 N), whereas PPI formulations showed a more gradual increase, reaching 16.38 N at 29% PF.

This pattern indicates that the fiber acted primarily as a structural filler within the matrix. The incorporation of fiber can reinforce the matrix by increasing resistance to deformation. Because the SPI matrix already exhibits higher viscosity at low temperature, the reinforcing effect of fiber becomes more pronounced in SPI blends.

Springiness showed an opposite trend. Increasing PF reduced springiness, particularly at the highest fiber level. Samples containing 29% PF exhibited significantly lower springiness than those without fiber. This decrease in elastic recovery likely occurred because the fiber particles disrupted the continuity of the elastic protein network and crosslinking, limiting the ability of the matrix to recover after deformation.

Chewiness followed a similar pattern to hardness. SPI formulations with 14.5% and 29% PF exhibited the highest chewiness values (approximately 13), while PPI samples without fiber or with moderate PF showed the lowest values. Since chewiness reflects the energy required to break down the structure during chewing, the increased chewiness in fiber-rich SPI blends indicates a denser and more resistant matrix.

The trends observed in the TPA measurements were also consistent with the hydration and swelling behavior of the formulations. RVA results indicated that SPI-PF blends maintained relatively high viscosities, whereas PPI blends showed lower and less consistent viscosity values. This difference is consistent with the cold swelling behavior of SPI compared with the non-cold swelling behavior of PPI. In cold swelling protein (SPI), hydration and matrix development occur earlier, allowing the protein network to form before extensive heating. This early structuring can improve the mechanical integration of insoluble components such as fiber within

the matrix, leading to more effective reinforcement and higher resistance to compression. In contrast, PPI behaves as a non-cold swelling protein and develops structure at higher temperatures. This leads to a weaker and less structured matrix during processing, which may reduce the effectiveness of fiber reinforcement. As a result, the strengthening effect of pea fiber was more pronounced in SPI formulations than in PPI formulations.

The WAC data further support this interpretation. In the PPI-PF blends, WAC remained relatively constant (around 2.7 to 2.8 g/g), suggesting that the increase in hardness was mainly due to structural reinforcement by fiber rather than changes in hydration. In contrast, SPI-PF blends showed a decrease in WAC as PF increased (4.25 to 3.40 g/g). This reduction may indicate redistribution of water within the materials or reduced availability of free water. Lower levels of free water can reduce plasticization of the matrix and therefore increase hardness.

LGC values in the PF blends were relatively stable across treatments, indicating that fiber addition did not strongly influence the gelation threshold. This suggests that the mechanical strengthening observed in the TPA results was primarily driven by fiber reinforcement and matrix structure rather than differences in gel formation.

Overall, SPI-based blends consistently exhibited higher hardness and chewiness than PPI blends. This difference can be attributed to the stronger viscosity development and hydration behavior of SPI, which behaves as a cold swelling protein and forms a structured matrix at lower temperatures. This early structuring enhances the reinforcing effects of both methylcellulose and pea fiber. In contrast, PPI behaves as a non-cold swelling protein that requires higher temperatures to develop structure, which limits the degree of improvement achieved through hydrocolloid or fiber addition. These results highlight how differences in protein functionality,

hydration behavior, and rheological properties collectively determine the final mechanical texture of plant-based formulations (Bhuiyan et al., 2025; Osen et al., 2014).

Detailed numerical results, including estimated marginal means, standard errors, and Tukey-adjusted significance groupings for the MC and PF formulations, are provided in Appendix Tables B.1 and B.2.

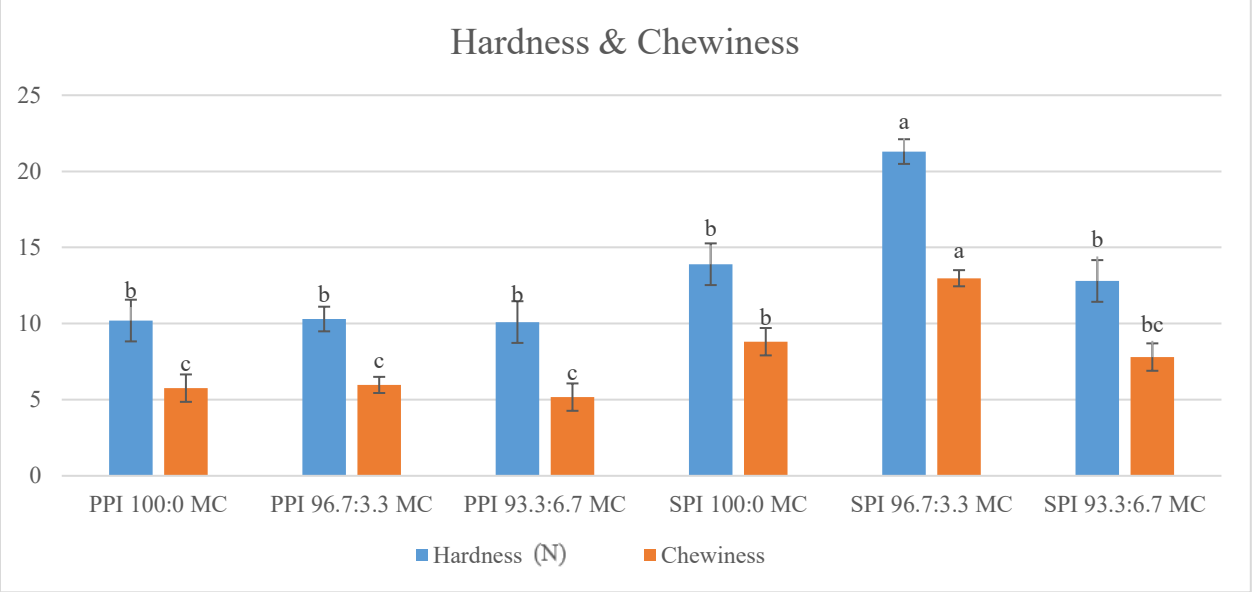

Figure 5.13. Hardness and chewiness of the printed MC formulations. Values are presented as estimated marginal means ± standard error (EMM ± SE). Different lowercase letters indicate significant differences among Protein × MC treatments based on Tukey-adjusted pairwise comparisons ($p < 0.05$).

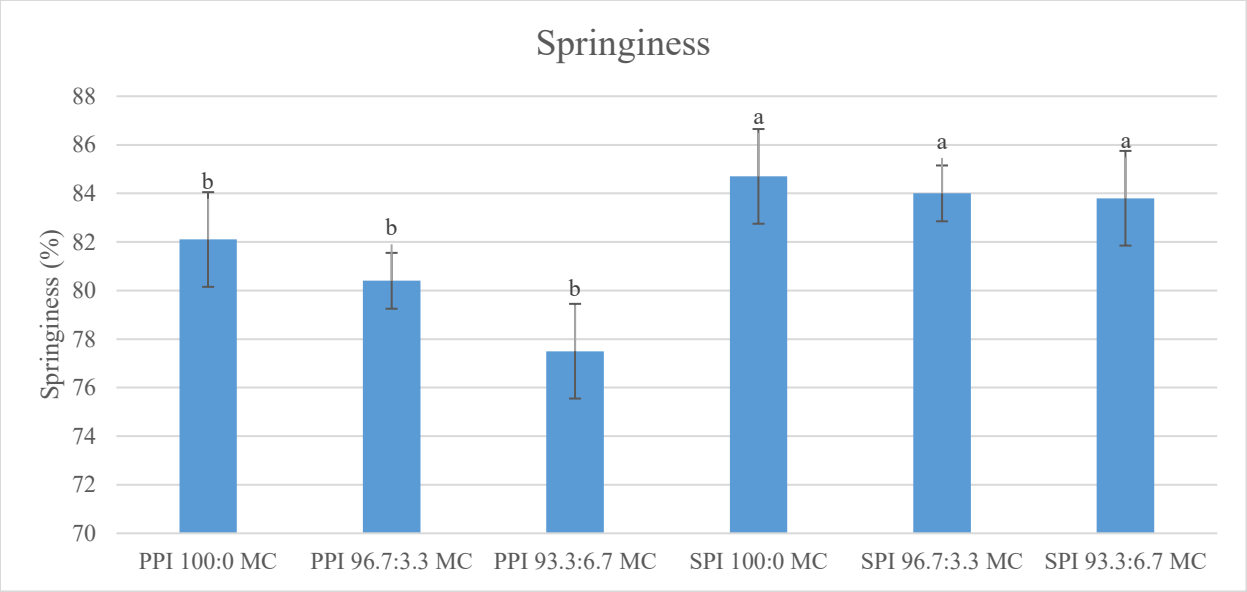

Figure 5.14. Springiness of the printed MC formulations. Values are presented as estimated marginal means ± standard error (EMM ± SE). Different lowercase letters indicate significant differences between protein types based on Tukey-adjusted pairwise comparisons ($p < 0.05$).

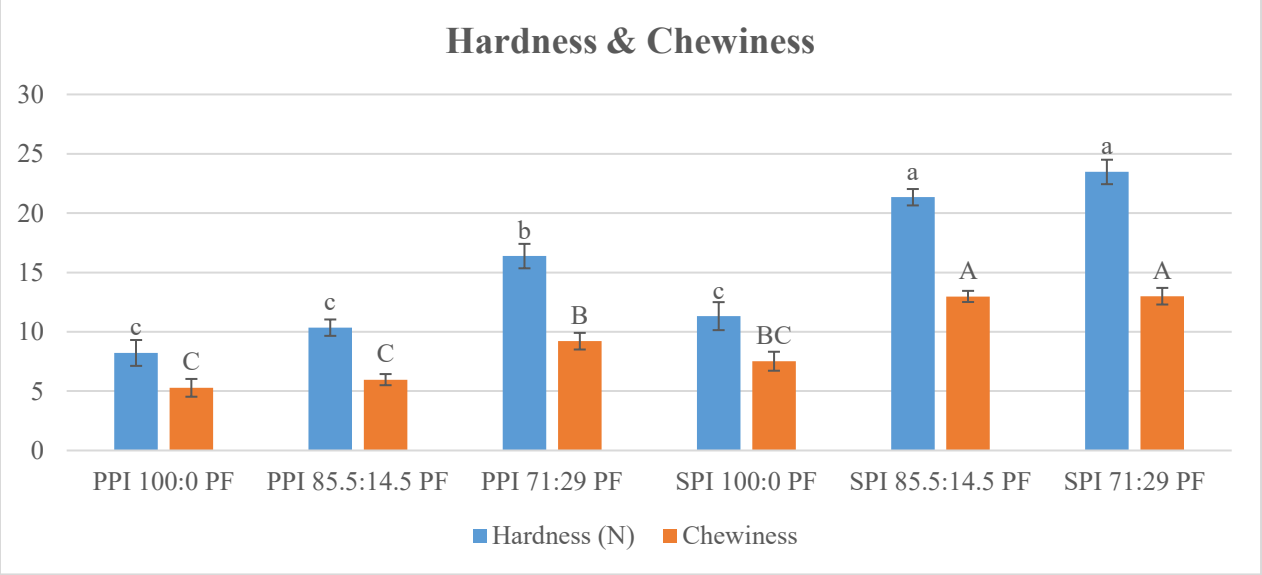

Figure 5.15. Hardness and chewiness of the printed PF formulations. Values are presented as estimated marginal means ± standard error (EMM ± SE). Different lowercase letters indicate significant differences among Protein × PF treatments based on Tukey-adjusted pairwise comparisons ($P < 0.05$).

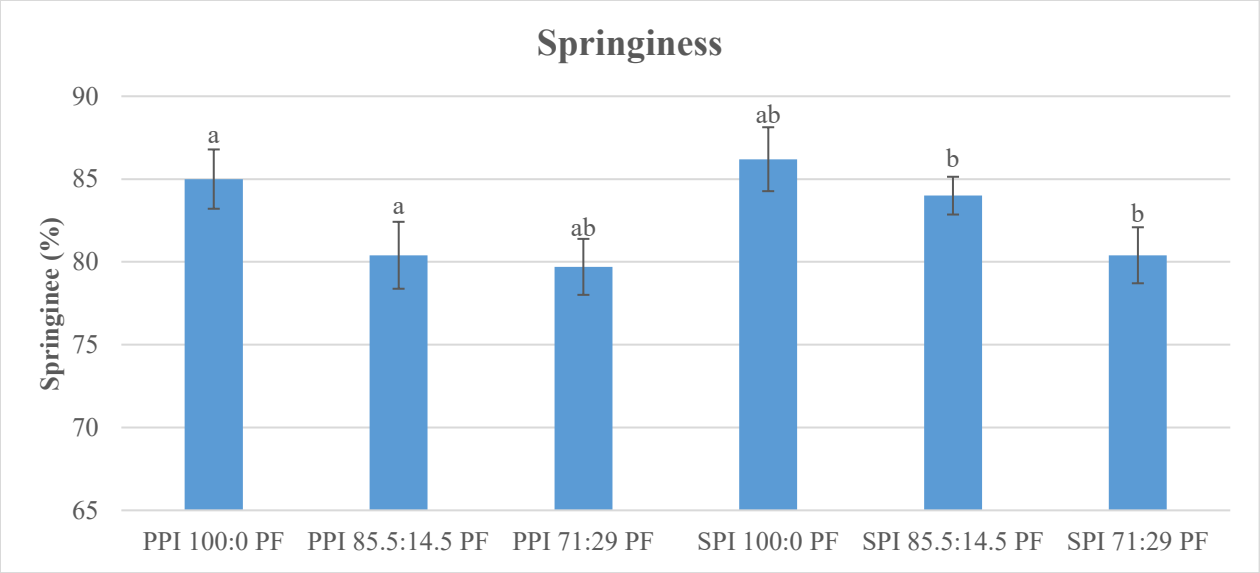

Figure 5.16. Springiness of the printed PF formulations. Values are presented as estimated marginal means ± standard error (EMM ± SE). Different lowercase letters indicate significant differences associated with PF level based on Tukey-adjusted pairwise comparisons ($p < 0.05$).

5.3.2.3 Visual Analysis

The visual appearance of the printed samples generally followed the same pattern observed in the DDR measurements (Figure 5.17). Samples with DDR values closer to zero tended to maintain their intended shape more clearly, whereas samples with more negative DDR values showed greater deformation and less structural definition after printing.

For the MC-containing formulations, the PPI samples maintained generally consistent shapes across all MC levels, although differences in surface texture were visible. The control sample (100:0 MC) and the moderate MC level (96.7:3.3) showed somewhat uneven and slightly rough surface textures, particularly visible in the side view. Despite this surface roughness, the overall geometry of the printed structures remained relatively stable, which is consistent with the

DDR values close to zero. At the higher MC level (93.3:6.7), the printed structures appeared slightly more uniform in surface texture, although some geometric thickening of the printed strand was visible in the side view. This change corresponds with the more negative DDR value observed for this formulation, indicating greater dimensional deviation despite the relatively smoother surface appearance.

A similar but more pronounced trend was observed in the SPI-based formulations. While the SPI control sample still maintained a recognizable shape, the surfaces appeared rougher and less uniform than in the PPI samples. As MC content increased, the printed structures showed progressively greater distortion. The side views revealed more irregular edges and reduced structural definition, particularly at the highest MC level. These observations are consistent with the DDR results, where SPI formulations exhibited a stronger decrease in dimensional fidelity as MC increased.

For the PF-containing formulations, visual observations generally supported the DDR results, although differences in surface texture were evident. In PPI formulations, the addition of 14.5% PF produced slightly more compact structures with better defined edges compared with the control. However, at the highest PF level (29%), the surface became more uneven and irregular despite the overall shape remaining stable. A similar pattern was observed in SPI formulations, where moderate PF addition improved structural definition, while the highest PF level resulted in rougher and more irregular surfaces. Overall, these observations align with the DDR values shifting closer to zero after PF incorporation, indicating improved dimensional fidelity despite increased surface roughness at higher fiber levels.

Overall, the qualitative visual analysis supported the quantitative DDR measurements. Samples with DDR values closer to zero generally maintained better shape fidelity and structural

stability after printing, whereas samples with more negative DDR values showed greater deformation and less defined printed structures. This agreement between visual observations and dimensional measurements further confirms that formulation composition plays a key role in determining structural stability in extrusion-based 3D printing (Liu et al., 2018; Steenhuis et al., 2018).

Figure 5.17. Macro Images of 3D printed final products

Treatments	Front View	Side View
PPI 100:0 MC		
PPI 96.7:3.3 MC		
PPI 93.3:6.7 MC		
SPI 100:0 MC		
SPI 96.7:3.3 MC		
SPI 93.3:6.7 MC		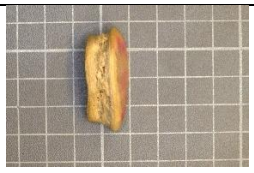

PPI 100:0 PF		
PPI 85.5:14.5 PF		
PPI 71:29 PF		
SPI 100:0 PF		
SPI 85.5:14.5 PF		
SPI 71:29 PF		

5.4 Conclusion

This study showed that the performance of plant-based inks for extrusion-based 3D printing depends strongly on the combination of protein source and added structuring ingredients. Although both methylcellulose and pea fiber changed hydration, viscosity, dimensional stability, and texture, their effects were not the same in pea and soy protein blends.

Overall, SPI-based formulations performed better than PPI-based formulations in terms of viscosity development and final texture. SPI showed stronger cold swelling behavior, higher viscosity, and generally produced samples with greater hardness and chewiness. These properties appear to have helped SPI form a more structured matrix during processing, which made it more responsive to formulation changes. In contrast, PPI behaved as a non-cold swelling protein and required more thermal input to develop structure, resulting in weaker viscosity development and less pronounced textural improvement.

Methylcellulose increased water absorption in both protein formulations and promoted earlier viscosity development, but its effect on final print quality depended on the protein source and inclusion level. In SPI formulations, a moderate level of MC improved texture, especially hardness and chewiness, but higher MC levels led to greater dimensional distortion. In PPI formulations, MC had less effect on texture and, at the highest level, also reduced dimensional fidelity. These findings suggest that MC can be useful for strengthening the ink, but excessive amounts may disturb the balance between extrusion behavior and shape retention.

Pea fiber had a different effect on printability. Fiber addition improved dimensional fidelity in both protein formulations, with DDR values moving closer to zero after PF incorporation. This indicates that pea fiber helped the printed structures better maintain their intended shape after deposition. At the same time, PF increased hardness and chewiness, especially in SPI blends, showing that it also contributed to a stronger final structure. However, its effect on water retention was not always positive, which confirms that the behavior of an ingredient alone does not necessarily predict its function in a blend.

The results showed that printability and final product quality cannot be explained by a single property such as WAC, LGC, or RVA alone. Instead, successful 3D printing performance

emerged from the combined effects of hydration, viscosity development, ingredient interactions, and matrix formation. Among the tested treatments, SPI formulations containing moderate MC or added PF showed the most promising balance between structural strength and printing performance.

Overall, this research provides insight into how protein type, methylcellulose, and pea fiber can be used to design more stable and functional plant-based 3D printing inks. These findings can support the future development of customized plant-based meat with improved shape retention, texture, and processing performance.

5.5 References

Aghababaei, F., McClements, D. J., Pignitter, M., & Hadidi, M. (2025). Plant protein edible inks: Upgrading from 3D to 4D food printing. *Food Chemistry: X*, *26*, 102280. https://doi.org/10.1016/j.fochx.2025.102280

An, Y.-J., Guo, C.-F., Zhang, M., & Zhong, Z.-P. (2019). Investigation on characteristics of 3D printing using Nostoc sphaeroides biomass. *Journal of the Science of Food and Agriculture*, *99*(2), 639–646. https://doi.org/10.1002/jsfa.9226

Asadi-Eydivand, M., Solati-Hashjin, M., Farzad, A., & Abu Osman, N. A. (2016). Effect of technical parameters on porous structure and strength of 3D printed calcium sulfate prototypes. *Robotics and Computer-Integrated Manufacturing*, *37*, 57–67. https://doi.org/10.1016/j.rcim.2015.06.005

Ben Abu, N., Harries, D., Voet, H., & Niv, M. Y. (2018). The taste of KCl – What a difference a sugar makes. *Food Chemistry*, *255*, 165–173. https://doi.org/10.1016/j.foodchem.2018.01.175

Bhuiyan, Md. H. R., Yeasmen, N., & Orsat, V. (2025). Plant-proteins based 3D meat analog printing: A review. *Food Chemistry*, *482*, 144157. https://doi.org/10.1016/j.foodchem.2025.144157

Bourne. (2002). *Texture, Viscosity, and Food*. https://doi.org/10.1016/B978-012119062-0/50001-2

Boye, J. I., Aksay, S., Roufik, S., Ribéreau, S., Mondor, M., Farnworth, E., & Rajamohamed, S. H. (2010). Comparison of the functional properties of pea, chickpea and lentil protein concentrates processed using ultrafiltration and isoelectric precipitation techniques. *Food Research International, Molecular, Functional and Processing Characteristics of Whole Pulses and Pulse Fractions and Their Emerging Food and Nutraceutical Applications*, *43*(2), 537–546. https://doi.org/10.1016/j.foodres.2009.07.021

Brishti, F. H., Zarei, M., Muhammad, S. K. S., Ismail-Fitry, M. R., Shukri, R., & Saari, N. (2017). Evaluation of the functional properties of mung bean protein isolate for development of textured vegetable protein. *International Food Research Journal*, *24*(4), 1595–1605.

Chakraborty, I., N, P., Mal, S. S., Paul, U. C., Rahman, Md. H., & Mazumder, N. (2022). An Insight into the Gelatinization Properties Influencing the Modified Starches Used in Food Industry: A review. *Food and Bioprocess Technology*, *15*(6), 1195–1223. https://doi.org/10.1007/s11947-022-02761-z

Dankar, I., Haddarah, A., Omar, F. E. L., Sepulcre, F., & Pujolà, M. (2018). 3D printing technology: The new era for food customization and elaboration. *Trends in Food Science & Technology*, *75*, 231–242. https://doi.org/10.1016/j.tifs.2018.03.018

De Angelis, D., Kaleda, A., Pasqualone, A., Vaikma, H., Tamm, M., Tammik, M.-L., Squeo, G., & Summo, C. (2020). Physicochemical and Sensorial Evaluation of Meat Analogues Produced from Dry-Fractionated Pea and Oat Proteins. *Foods*, *9*(12), 1754. https://doi.org/10.3390/foods9121754

Flory, J., Xiao, R., Li, Y., Dogan, H., Talavera, M. J., & Alavi, S. (2023). Understanding Protein Functionality and Its Impact on Quality of Plant-Based Meat Analogues. *Foods*, *12*(17), 3232. https://doi.org/10.3390/foods12173232

Gerçekaslan, K. E. (2021). Hydration level significantly impacts the freezable—And unfreezable -water contents of native and modified starches. *Food Science and Technology*, *41*, 426–431. https://doi.org/https://doi.org/10.1590/fst.04520

Ghadermazi, R., Hamdipour, S., Sadeghi, K., Ghadermazi, R., & Khosrowshahi Asl, A. (2019). Effect of various additives on the properties of the films and coatings derived from hydroxypropyl methylcellulose—A review. *Food Science & Nutrition*, *7*(11), 3363–3377. https://doi.org/10.1002/fsn3.1206

Godoi, F. C., Prakash, S., & Bhandari, B. R. (2016). 3d printing technologies applied for food design: Status and prospects. *Journal of Food Engineering*, *179*, 44–54. https://doi.org/10.1016/j.jfoodeng.2016.01.025

Hussain, S., Arora, V. K., & Malakar, S. (2021). Formulation of protein-enriched 3D printable food matrix and evaluation of textural, rheological characteristics, and printing stability. *Journal of Food Processing and Preservation*, *45*(2), e15182. https://doi.org/10.1111/jfpp.15182

Jarpa-Parra, M. (2018). Lentil protein: A review of functional properties and food application. An overview of lentil protein functionality. *International Journal of Food Science & Technology*, *53*(4), 892–903. https://doi.org/10.1111/ijfs.13685

Kabus, C. J. (2024). *Starch-based food inks in extrusion 3D printing: Formulation, physico-chemical properties and printing performance* [Kansas State University]. https://hdl.handle.net/2097/44469

Lipson, H., Kurman, M., Lipson, H., & Safari, an O. M. C. (2013). *Fabricated: The new world of 3D printing*. John Wiley & Sons. https://tind.wipo.int/record/27587

Lipton, J. I., Cutler, M., Nigl, F., Cohen, D., & Lipson, H. (2015). Additive manufacturing for the food industry. *Trends in Food Science & Technology*, *43*(1), 114–123. https://doi.org/10.1016/j.tifs.2015.02.004

Liu, Y., Chen, J., Luo, S., Li, C., Ye, J., Liu, C., & Gilbert, R. G. (2017). Physicochemical and structural properties of pregelatinized starch prepared by improved extrusion cooking technology. *Carbohydrate Polymers*, *175*, 265–272. https://doi.org/10.1016/j.carbpol.2017.07.084

Liu, Z., Chen, X., Dai, Q., Xu, D., Hu, L., Li, H., Hati, S., Chitrakar, B., Yao, L., & Mo, H. (2023). Pea protein-xanthan gum interaction driving the development of 3D printed dysphagia diet. *Food Hydrocolloids*, *139*, 108497. https://doi.org/10.1016/j.foodhyd.2023.108497

Liu, Z., Zhang, M., Bhandari, B., & Wang, Y. (2017). 3D printing: Printing precision and application in food sector. *Trends in Food Science & Technology*, *69*, 83–94. https://doi.org/10.1016/j.tifs.2017.08.018

Liu, Z., Zhang, M., Bhandari, B., & Yang, C. (2018). Impact of rheological properties of mashed potatoes on 3D printing. *Journal of Food Engineering, 3D Printed Food – Design and Technology*, *220*, 76–82. https://doi.org/10.1016/j.jfoodeng.2017.04.017

Mantihal, S., Prakash, S., Godoi, F. C., & Bhandari, B. (2017). Optimization of chocolate 3D printing by correlating thermal and flow properties with 3D structure modeling. *Innovative Food Science & Emerging Technologies, Emerging Technologies with Reference to IUFoST*, *44*, 21–29. https://doi.org/10.1016/j.ifset.2017.09.012

Osen, R., Toelstede, S., Wild, F., Eisner, P., & Schweiggert-Weisz, U. (2014). High moisture extrusion cooking of pea protein isolates: Raw material characteristics, extruder responses, and texture properties. *Journal of Food Engineering*, *127*, 67–74. https://doi.org/10.1016/j.jfoodeng.2013.11.023

Palaniraj, A., & Jayaraman, V. (2011). Production, recovery and applications of xanthan gum by *Xanthomonas campestris*. *Journal of Food Engineering*, *106*(1), 1–12. https://doi.org/10.1016/j.jfoodeng.2011.03.035

Petri, D. F. S. (2015). Xanthan gum: A versatile biopolymer for biomedical and technological applications. *Journal of Applied Polymer Science*, *132*(23). https://doi.org/10.1002/app.42035

Ralet, M.-C., Della Valle, G., & Thibault, J.-F. (1993). Raw and extruded fibre from pea hulls. Part I: Composition and physico-chemical properties. *Carbohydrate Polymers*, *20*(1), 17–23. https://doi.org/10.1016/0144-8617(93)90028-3

Sánchez, V. E., Bartholomai, G. B., & Pilosof, A. M. R. (1995). Rheological properties of food gums as related to their water binding capacity and to soy protein interaction. *LWT - Food Science and Technology*, *28*(4), 380–385. https://doi.org/10.1016/0023-6438(95)90021-7

Sathe, S. K., & Salunkhe, D. K. (1981). Functional Properties of the Great Northern Bean (*Phaseolus vulgaris* L.) Proteins: Emulsion, Foaming, Viscosity, and Gelation Properties. *Journal of Food Science*, *46*(1), 71–81. https://doi.org/10.1111/j.1365-2621.1981.tb14533.x

Schwab, A., Levato, R., D'Este, M., Piluso, S., Eglin, D., & Malda, J. (2020). Printability and Shape Fidelity of Bioinks in 3D Bioprinting. *Chemical Reviews*, *120*(19), 11028–11055. https://doi.org/10.1021/acs.chemrev.0c00084

Shah, P., Shah, V., Shrestha, S., & Mitra, P. (2024). A Review on 3D Food Printing Technology in Food Processing. *Journal of Food Industry*, *8*(1), 17–34. https://doi.org/10.5296/jfi.v8i1.22468

Steenhuis, H.-J., Fang, X., & Ulusemre, T. (2018). Strategy in 3D Printing of Food. *2018 Portland International Conference on Management of Engineering and Technology (PICMET)*, 1–6. https://doi.org/10.23919/PICMET.2018.8481817

Sun, J., Zhou, W., Huang, D., Fuh, J. Y. H., & Hong, G. S. (2015). An Overview of 3D Printing Technologies for Food Fabrication. *Food and Bioprocess Technology*, *8*(8), 1605–1615. https://doi.org/10.1007/s11947-015-1528-6

Techawipharat, J., Suphantharika, M., & BeMiller, J. N. (2008). Effects of cellulose derivatives and carrageenans on the pasting, paste, and gel properties of rice starches. *Carbohydrate Polymers*, *73*(3), 417–426. https://doi.org/10.1016/j.carbpol.2007.12.019

Thirumala, S., Gimble, J. M., & Devireddy, R. V. (2013). Methylcellulose Based Thermally Reversible Hydrogel System for Tissue Engineering Applications. *Cells*, *2*(3), 460–475. https://doi.org/10.3390/cells2030460

Varvara, R.-A., Szabo, K., & Vodnar, D. C. (2021). 3D Food Printing: Principles of Obtaining Digitally-Designed Nourishment. *Nutrients*, *13*(10), 3617. https://doi.org/10.3390/nu13103617

Venkatachalam, A., Wilms, P. F. C., Patón Baeza, J., Schutyser, M. A. I., & Zhang, L. (2026). Formulation of pea-based inks with different starches to produce customized 3D printed and baked snacks. *Current Research in Food Science*, *12*, 101320. https://doi.org/10.1016/j.crfs.2026.101320

Wang, L., Wang, J., Wang, J., Guo, Z., Li, Z., Qiu, J., & Wang, L. (2024). Soluble and insoluble dietary fiber at different ratios: Hydration characteristics, rheological properties, and ameliorative effects on constipation. *Food Chemistry: X*, *24*, 101996. https://doi.org/10.1016/j.fochx.2024.101996

Wang, W., Yao, L., Zhang, T., Cheng, C.-Y., Levine, D., & Ishii, H. (2017). Transformative Appetite: Shape-Changing Food Transforms from 2D to 3D by Water Interaction through Cooking. *Proceedings of the 2017 CHI Conference on Human Factors in Computing Systems, CHI '17*, 6123–6132. https://doi.org/10.1145/3025453.3026019

Webb, D., Dogan, H., Li, Y., & Alavi, S. (2023). Physico-Chemical Properties and Texturization of Pea, Wheat and Soy Proteins Using Extrusion and Their Application in Plant-Based Meat. *Foods*, *12*(8), 1586. https://doi.org/10.3390/foods12081586

Webb, D., Plattner, B. J., Donald, E., Funk, D., Plattner, B. S., & Alavi, S. (2020). Role of chickpea flour in texturization of extruded pea protein. *Journal of Food Science*, *85*(12), 4180–4187. https://doi.org/10.1111/1750-3841.15531

Wen, Y., Kim, H. W., & Park, H. J. (2022). Effects of transglutaminase and cooking method on the physicochemical characteristics of 3D-printable meat analogs. *Innovative Food Science & Emerging Technologies*, *81*, 103114. https://doi.org/10.1016/j.ifset.2022.103114

Ytterberg, J., Krona, A., Pereira, P. F. de M., Jimenez-Quero, A., Lopez-Sanchez, P., & Ström, A. (2026). Rheological behaviour of pea hull fibres treated with pectate lyase. *Future Foods*, 100945. https://doi.org/10.1016/j.fufo.2026.100945

Yuliarti, O., Ng, L., Koh, W. M., Abdullah Tan, M. F. B. M. F., & Dwi Sentana, A. (2023). Structural properties of meat analogue with added konjac gels. *Food Hydrocolloids*, *142*, 108716. https://doi.org/10.1016/j.foodhyd.2023.108716

Zhang, Y.-F., Li, Z., Li, H., Li, H., Xiong, Y., Zhu, X., Lan, H., & Ge, Q. (2021). Fractal-Based Stretchable Circuits via Electric-Field-Driven Microscale 3D Printing for Localized Heating of Shape Memory Polymers in 4D Printing. *ACS Applied Materials & Interfaces*, *13*(35), 41414–41423. https://doi.org/10.1021/acsami.1c03572

Chapter 6 - Conclusion

Overall, this research showed that raw material functionality, formulation design, and processing conditions all play critical roles in determining the final structure, texture, and performance of plant-based meat analogs. Across the different systems studied, protein hydration behavior, especially the distinction between cold swelling and non-cold swelling ingredients, was consistently linked to extrusion behavior and final product quality. Soy-containing formulations generally promoted higher hydration, viscosity development, and more expanded structures, whereas pea, lentil, and faba-containing blends often produced denser and firmer textures unless formulation and processing conditions were carefully adjusted. These findings highlight that the success of plant-based meat products does not depend on ingredient selection alone, but on the interaction between ingredient functionality and process design.

This work also showed that alternative plant proteins, such as faba, lentil, and pea, have strong potential in plant-based meat applications when their functional limitations are better understood and properly managed. By adjusting moisture level, screw speed, feed rate, temperature, or adding structuring components such as fiber and methylcellulose, it was possible to improve texture development, fibrousness, and structural stability. In this way, the research helps bridge an important gap between raw material properties, extrusion behavior, and final product texture.

While this study helps clarify several important relationships, several areas still need further development. At present, texture, visual analysis, and sensory evaluation are commonly used to judge texturization, but more direct and quantitative methods for measuring protein network formation would strengthen future research. In addition, further work should examine post-processing, including cooking methods, color development, and sensory optimization, to

better match the appearance and eating quality of animal meat. Finally, a more detailed investigation of extrusion hardware, screw configuration, die design, and cooling systems would help clarify how equipment design contributes to fibrous structure formation.

In conclusion, this research provides a framework for linking ingredient functionality and processing conditions to final product quality in plant-based meat. This foundation can support future efforts to develop more consistent, structured, and commercially competitive meat analogs.

Appendix A - Supplementary Materials for Chapter 3

This appendix presents supplementary tables and figures related to Chapter 3.

Appendix Table A.1. Water Holding Capacity of milled and chunk final products

Formulations	LPC + SPI (High IBM, High rpm)	LPC + SPI (Low IBM, High rpm)	LPC + SPI (Low IBM, Low rpm)	LPC + PPI (Low IBM, High rpm)	LPC + PPI (High IBM, Low rpm)	LPC + PPI (High IBM, High rpm)
WHC – Chunk (%)	214.15 ± 22.76	330.46 ± 7.39	233.11 ± 22.6	313.1 ± 36.47	174.71 ± 9.24	235.76 ± 26.96
WHC – Milled (%)	258.7 ± 13.49	379.3 ± 12.9	277.9 ± 13.7	345.9 ± 2.25	178.3 ± 7.23	257.7 ± 9.62

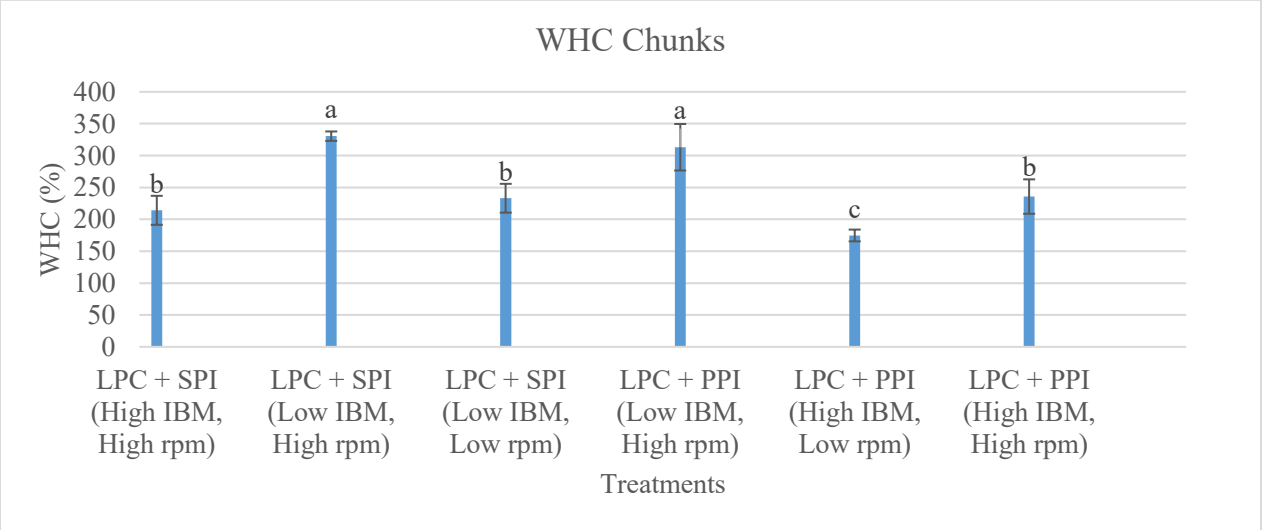

Appendix Figure A.1. Water Holding Capacity – Chunks. Bars represent mean ± standard deviation. Different letters indicate statistically significant differences among formulations

based on one-way ANOVA followed by Games-Howell post hoc test, applied due to violation of homogeneity of variances ($p < 0.05$)

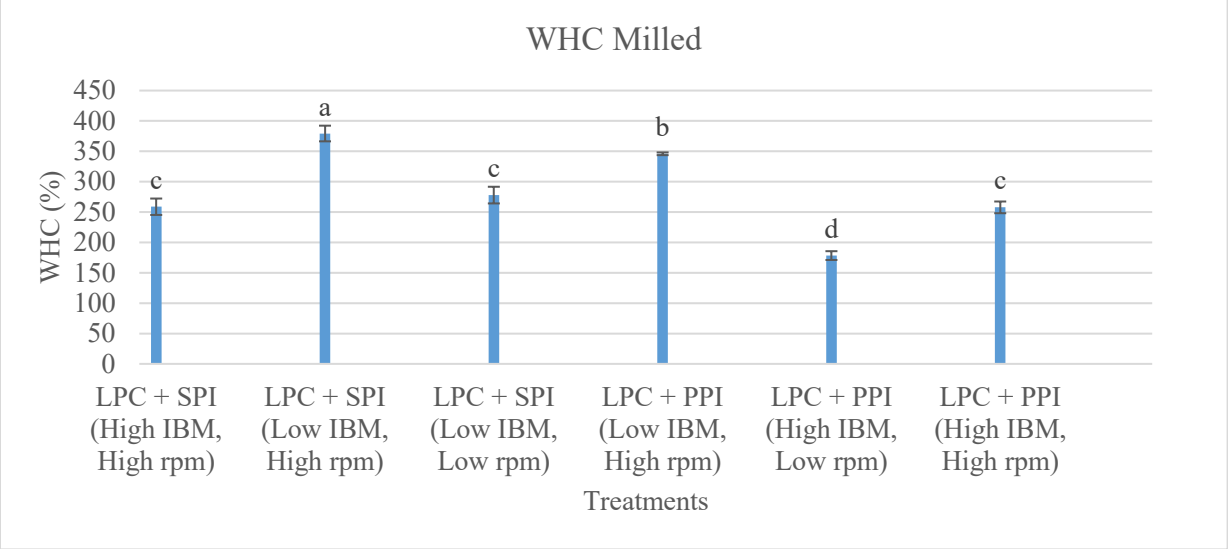

Appendix Figure A.2. Water Holding Capacity – Milled. Bars represent mean ± standard deviation. Different letters indicate statistically significant differences among formulations based on one-way ANOVA (assuming equal variances), followed by Tukey's HSD post hoc test.

Appendix Table A.2. Texture Profile Analysis Results - Hardness

Treatment	Hardness (N) - Chunk	Hardness (N) - Patty without Binder	Hardness (N) - Patty with Binder
LPC + SPI (High IBM, High rpm)	7.85 ± 2.38 [a]	6.03 ± 0.85 [b]	23.09 ± 6.29 [a]
LPC + SPI (Low IBM, High rpm)	3.09 ± 0.97 [b]	5.23 ± 0.57 [c]	26.62 ± 4.27 [a]
LPC + SPI (Low IBM, Low rpm)	5.89 ± 3.07 [b]	5.9 ± 0.7 [b]	31.78 ± 9.98 [a]
LPC + PPI (Low IBM, High rpm)	2.62 ± 0.78 [b]	6.91 ± 1.26 [b]	28.21 ± 11.25 [a]
LPC + PPI (High IBM, Low rpm)	6.45 ± 4.73 [b]	12.26 ± 2.86 [a]	33.61 ± 9.95 [a]
LPC + PPI (High IBM, High rpm)	3.18 ± 1.24 [b]	7.95 ± 2.05 [b]	29.67 ± 12.19 [a]

Appendix Table A.3. Texture Profile Analysis Results - Springiness

Treatment	Springiness % - Chunk	Springiness % – Patty without Binder	Springiness % – Patty with Binder
LPC + SPI (High IBM, High rpm)	88.95 ± 3.24 ^{ab}	87.54 ± 3. 04 ^{a}	63.9 ± 5.49 ^{a}
LPC + SPI (Low IBM, High rpm)	91.12 ± 2.75 ^{a}	87.07 ± 2.02 ^{a}	66.95 ± 7.45 ^{a}
LPC + SPI (Low IBM, Low rpm)	89.74 ± 7.29 ^{ab}	87.66 ± 3.54 ^{a}	59.16 ± 6.68 ^{ab}
LPC + PPI (Low IBM, High rpm)	83.86 ± 5.86 ^{b}	85.56 ± 2.75 ^{ab}	55.92 ± 5.33 ^{b}
LPC + PPI (High IBM, Low rpm)	85.93 ± 6.01 ^{ab}	81.87 ± 3.77 ^{b}	65.3 ± 10.33 ^{ab}
LPC + PPI (High IBM, High rpm)	83.84 ± 4.41 ^{b}	81.53 ± 4.42 ^{b}	58.78 ± 12.56 ^{ab}

Appendix Table A.4. Texture Profile Analysis Results - Chewiness

Treatment	Chewiness - Chunk	Chewiness – Patty without Binder	Chewiness – Patty with Binder
LPC + SPI (High IBM, High rpm)	5.44 ± 1.78 ^{a}	3.99 ± 0.71 ^{b}	5.14 ± 2.25 ^{a}
LPC + SPI (Low IBM, High rpm)	2.23 ± 0.7 ^{bc}	3.5 ± 0.34 ^{b}	7.76 ± 1.61 ^{a}
LPC + SPI (Low IBM, Low rpm)	3.91 ± 1.86 ^{b}	4 ± 0.6 ^{b}	8 ± 3.61 ^{a}
LPC + PPI (Low IBM, High rpm)	1.62 ± 0.5 ^{c}	4.39 ± 0.9 ^{b}	6.14 ± 4.2 ^{a}
LPC + PPI (High IBM, Low rpm)	3.79 ± 2.83 ^{bc}	6.74 ± 1.91 ^{a}	8.29 ± 3.67 ^{a}
LPC + PPI (High IBM, High rpm)	1.8 ± 0.68 ^{bc}	4.55 ± 1.5 ^{b}	6.99 ± 4.52 ^{a}

Final Products		Longitudinal cut			
LPC+ SPI	High IBM, High rpm	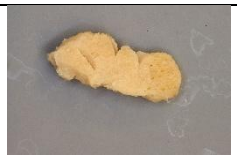			
	Low IBM, High rpm		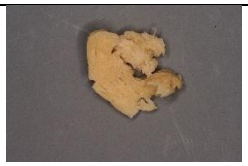		
	Low IBM, Low rpm				
LPC+ PPI	Low IBM, High rpm	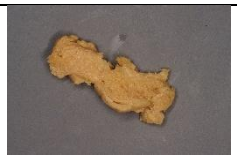		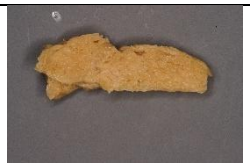	
	High IBM, Low rpm				

	High IBM, High rpm	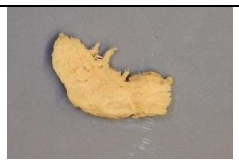	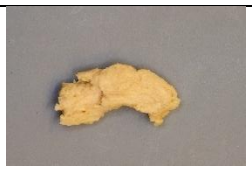	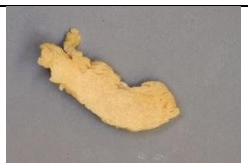	

Appendix Figure A.3. Macro Images of hydrated chunk final products

Appendix Table A.5. Fibrosity Expert Score

Sample	Fibrosity Expert Score
LPC + SPI (High IBM, High rpm)	5.6 ± 1.08
LPC + SPI (Low IBM, High rpm)	5.65 ± 0.96
LPC + SPI (Low IBM, Low rpm)	6.75 ± 1.07
LPC + PPI (Low IBM, High rpm)	6.07 ± 0.94
LPC + PPI (High IBM, Low rpm)	6.06 ± 1.03
LPC + PPI (High IBM, High rpm)	6.26 ± 0.89

Appendix Table A.6. Fibrosity Scores Across Treatments. Fibrosity scores were obtained from expert visual, computer vision-based, and machine learning-based evaluations.

Treatments	Expert Score	CV Score	ML Score
LPC + SPI (High IBM, High rpm)	5.6 ± 1.08	6.58 ± 0.84	5.75 ± 0.68
LPC + SPI (Low IBM, High rpm)	5.65 ± 0.96	6.41 ± 1.02	5.83 ± 0.59
LPC + SPI (Low IBM, Low rpm)	6.75 ± 1.07	6.64 ± 2.05	6.60 ± 0.58
LPC + PPI (Low IBM, High rpm)	6.07 ± 0.94	7.29 ± 0.55	5.98 ± 0.56
LPC + PPI (High IBM, Low rpm)	6.06 ± 1.03	5.02 ± 1.25	6.21 ± 0.63
LPC + PPI (High IBM, High rpm)	6.26 ± 0.89	4.37 ± 1.27	6.14 ± 0.57

Appendix B - Supplementary Materials for Chapter 5

Appendix Table B.1. Texture Profile Analysis Results – MC Blends. Values are presented as estimated marginal means ± standard error (EMM ± SE). Different letters within each column indicate significant differences among treatments based on Tukey-adjusted comparisons ($p < 0.05$). For hardness and chewiness, letters reflect Protein × MC differences; for springiness, letters indicate differences between protein types only.

Treatment	Hardness (N)	Springiness (%)	Chewiness
PPI 100:0 MC	10.2 ± 1.37 ^{b}	82.1 ± 1.95 ^{b}	5.76 ± 0.9 ^{c}
PPI 96.7:3.3 MC	10.3 ± 0.81 ^{b}	80.4 ± 1.15 ^{b}	5.97 ± 0.53 ^{c}
PPI 93.3:6.7 MC	10.1 ± 1.37 ^{b}	77.5 ± 1.95 ^{b}	5.17 ± 0.9 ^{c}
SPI 100:0 MC	13.9 ± 1.37 ^{b}	84.7 ± 1.95 ^{a}	8.81 ± 0.9 ^{b}
SPI 96.7:3.3 MC	21.3 ± 0.81 ^{a}	84 ± 1.15 ^{a}	12.98 ± 0.53 ^{a}
SPI 93.3:6.7 MC	12.8 ± 1.37 ^{b}	83.8 ± 1.95 ^{a}	7.8 ± 0.9 ^{bc}

Appendix Table B.2. Texture Profile Analysis Results – PF Blends. Values are presented as estimated marginal means ± standard error (EMM ± SE). Different lowercase letters within each column indicate significant differences among treatments based on Tukey-adjusted comparisons ($p < 0.05$). For hardness and chewiness, letters reflect differences among Protein × PF combinations, whereas for springiness, letters indicate differences associated with PF level.

Treatment	Hardness (N)	Springiness (%)	Chewiness
PPI 100:0 PF	8.22 ± 1.09 ^{c}	85 ± 1.79 ^{a}	5.28 ± 0.75 ^{c}
PPI 85.5:14.5 PF	10.35 ± 0.69 ^{c}	80.4 ± 2.02 ^{a}	5.97 ± 0.47 ^{c}
PPI 71:29 PF	16.38 ± 1.03 ^{b}	79.7 ± 1.69 ^{ab}	9.21 ± 0.7 ^{b}
SPI 100:0 PF	11.32 ± 1.18 ^{c}	86.2 ± 1.93 ^{ab}	7.52 ± 0.8 ^{bc}
SPI 85.5:14.5 PF	21.34 ± 0.69 ^{a}	84 ± 1.14 ^{b}	12.98 ± 0.47 ^{a}
SPI 71:29 PF	23.47 ± 1.03 ^{a}	80.4 ± 1.69 ^{b}	13 ± 0.7 ^{a}